

# **NUMERICAL MODELLING OF JOULE HEATED CERAMIC MELTER**

*By*

**G SUNEEL**

(Enrollment Number: ENGG02201204018)

**Indira Gandhi Centre for Atomic Research, Kalpakkam**

*A thesis submitted to the Board of Studies in Engineering Sciences  
in partial fulfilment of requirements for the Degree of*

**DOCTOR OF PHILOSOPHY**

*of*

**HOMI BHABHA NATIONAL INSTITUTE**



**June 2019**

# Homi Bhabha National Institute (HBNI)

## Recommendations of the Viva Voce Committee

As members of the Viva Voce Committee, we certify that we have read the dissertation prepared by Mr. G. Suneel entitled "Numerical Modelling of Joule Heated Ceramic Melter" and recommend that it may be accepted as fulfilling the thesis requirement for the award of Degree of Doctor of Philosophy.

Chairman – Dr. K. Velusamy



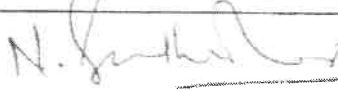
Date: 25/9/2020

Guide / Convener – Dr. C.P.Kaushik



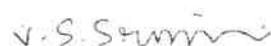
Date: 25/09/2020

Examiner– Dr. Sendhil Kumar



Date: 25-09-2020

Member 1- Dr. V.Srinivasan



Date: 25/09/2020

Member 2- Dr. T.V.Krishna Mohan



Date: 25/09/2020

Final approval and acceptance of this thesis is contingent upon the candidate's submission of the final copies of the thesis to HBNI.

I hereby certify that I have read this thesis prepared under my direction and recommend that it may be accepted as fulfilling the thesis requirement.

Date: 25/09/2020

Place: Indira Gandhi Centre for Atomic Research  
Kalpakkam



Dr. C.P. Kaushik  
(Guide)

## STATEMENT BY AUTHOR

---

This dissertation has been submitted in partial fulfilment of requirements for an advanced degree at Homi Bhabha National Institute (HBNI) and is deposited in the Library to be made available to borrowers under rules of the HBNI.

Brief quotations from this dissertation are allowable without special permission, provided that proper acknowledgement of the source is made. Requests for permission for extended quotation from or reproduction of this manuscript in whole or in part may be granted by the Competent Authority of HBNI when in his or her judgment the proposed use of the material is in the interests of scholarship. In all other instances, however, permission must be obtained from the author.

**Kalpakkam**  
**June, 2019**

  
**G. Suneel**

# DECLARATION

---

I, hereby declare that the investigation presented in the thesis has been carried out by me. The work is original and has not been submitted earlier as a whole or in part for a degree/diploma at this or any other Institution/University.

**Kalpakkam**

**June, 2019**



**G. Suneel**

## List of Publications Arising from the Thesis

---

### Journal

1. Gattu Suneel, PM Satya Sai, Chetan P Kaushik, JK Gayen, KV Ravi and Amitava Roy. "Experimental Investigations and Numerical Modelling of Joule Heated Ceramic Melter for Vitrification of Radioactive Waste. Journal of Hazardous, Toxic and radioactive waste, 23(2019)
2. Gattu Suneel, S Rajasekharan, J Selvakumar, Chetan P Kaushik, JK Gayen and KV Ravi. "Determination of Reaction Kinetics during Vitrification of Radioactive Liquid Waste for Different Types of Base Glass." Journal of Nuclear Engineering and Technology, 51(3), 2019.
3. Gattu Suneel, C. P.Kaushik, P.M Satya Sai, J. K. Gayen, K V Ravi," Remote Start-Up Of Joule Heated Ceramic Melter – Optimization of Design Parameters Based on Experimental and Numerical Investigations", Journal of Nuclear Science and Technology, 57(3), 2020
4. G. Suneel, C. P.Kaushik, JK Gayen, KV Ravi, "Enhancement of Glass Production Rate in Joule Heated Ceramic Melter ", Proceedings of 2<sup>nd</sup> International Conference on New Frontiers in Chemical, Energy and Environmental Engineering Proceedings, Chemical Product and Process Modelling, 2020, DOI: <https://doi.org/10.1515/cppm-2019-0068>.

## Conferences

1. G. Suneel, Santosh Kumar C.T., J.K. Gayen, "Simulation and Validation of Thermal Profile in and Industrial Scale Joule Melter" , Proceedings of the 23<sup>rd</sup> National Heat and Mass Transfer Conference and 1<sup>st</sup> International ISHMT-ASTFE Heat and Mass Transfer Conference, 17-20<sup>th</sup>, Dec 2015, India. (IHMTTC-2015-084).
2. G. Suneel, C. P.Kaushik, JK Gayen, KV Ravi, "Enhancement of Glass Production Rate in Joule Heated Ceramic Melter", 2<sup>nd</sup> International Conference on New Frontiers in Chemical, Energy and Environmental Engineering (INCEEE-2019) 15-16<sup>th</sup> Feb 2019, NITW, India
3. G. Suneel, R. Raja, C. P.Kaushik, JK Gayen, KV Ravi, "Heat Transfer Enhancement study in Glass Furnace", CHEMCON-2017.
4. Santhosh Kumar C.T, G. Suneel, J.K. Gayen, P.M. SatyaSai, Amitava Roy, "Numerical Simulation of Heat Transfer in a Melter Cavity", CHEMENT-2014.

**Kalpakkam**  
**June, 2019**



**G. Suneel**

Dedicated to my beloved **family**  
**members**, very supportive **guides** for all  
those scientific discussions,  
encouragement of  
my dear father, Late Shri. **G. Narayana**,  
Without his dedication and sacrifice,  
I would not have reached this stage.

# ACKNOWLEDGEMENTS

---

Scientific research is a collective effort of motivated individuals and research organisations towards an improved understanding, enhancing the safety and progress of the society. Without continuous guidance and involvement of supervisors, colleagues and the support of family, significant progress in any field of research is difficult. Therefore, with humbleness and gratitude, I am extremely grateful to my research guide **Dr. C.P. Kaushik** for his valuable guidance, constant support, encouragement, motivation and sincere interest throughout my Ph.D. His foresight and keen scientific intuition were vital for the progress of this work and led to the timely completion of the thesis. I am extremely thankful to my superior and guide **Dr. P.M. Satya Sai** without his support and guidance this Ph.D would not have been possible. I am highly obliged to him for his constructive criticism, valuable suggestions, and sharing his abundance of knowledge with me. I am thankful to **Mr. K. V. Ravi, CE, NRB** for his continuous encouragement and constant support in pursuit of my research work. His probing questions encouraged me to work further on the subject. I am thankful **Mr. Biplob Paul, FD, BARCF** for his support.

I wish to thank the honourable members of my doctoral advisory committee **Dr. K. Velusamy, Dr. M. Saibaba, Dr. K. Nagarajan, Dr. V. Srinivasan, and Dr. T. V. Krishna Mohan** for their scientific discussions and helpful suggestions at different time throughout my research, which helped me in redirecting my thinking and kept me motivated and focused.

I am grateful to all of those with whom I have had the pleasure to work during this and other related projects. I would like to thank my immediate superior **Mr. J. K. Gayen**, for his suggestions and continuous support since the beginning of my doctoral program. I thank **Mr. Amitava Roy** for encouragement and support. I would also utilize this opportunity to thank **Dr. S. Basu** for giving me an opportunity to work in this field and pursue my Doctoral program.

I would also like to thank **Mr. H. R. Pimparkar, Mr. Sangam Gupta, Mr. M. P. Pradeep, Mr. M. Thamaraiselvan, Mr. Nitin Kumar Sharma, Mr. S. Rajasekaran, Dr. Selva Kumar, Mr. Jaiprakash Mishra, Mr. Y.T. Revanth Kumar**, and all others colleagues from Waste Immobilisation Plant for the fruitful scientific

discussions and for creating scientific atmosphere. I have been benefited one way or the other from their association and timely help.

I would also like to thank **Mr. S. Mandal**, from Central Glass and Ceramic Research Institute, Kolkata for his friendly support, suggestions and guidance. I would like to mention special thanks to **Mr. M. Balamuragan** and **Mr. R. Rajendran**, from Indira Gandhi Centre for Atomic Research IGCAR for their support and guidance.

Nobody has been more important to me in the pursuit of the project than the members of my family. I would like to express the sincerest gratitude to my parents **Mr. G. Narayana** and **Mrs. G. Lakshmi** and to my uncle **Mr. P. Rajababu** and aunty **Mrs. P. Sumathi** whose love and guidance are with me in whatever I pursue. They are a constant source of inspiration for me. Most importantly, I wish to thank my loving and very supportive wife **Kalpana** and my two wonderful children, **Jithin** and **Krithik** for providing cheerful atmosphere at home.

There are many people that I wish to thank who have helped me to complete this thesis. Although I do not mention you all by name, you are not forgotten - thank you all! Last but not least, I thank the almighty for protecting all of us from harm and blessing with health and happiness, and for helping me reach this far.

**Kalpakkam**

**June, 2019**

  
**G. Suneel**

# ABSTRACT

---

Fossil fuels contribute to greenhouse gas emissions and there is a global consensus on the need for limiting CO<sub>2</sub> emissions. Reduction of the share of fossil fuels in the energy generation is not sustainable with currently available renewable energy sources like wind, solar, hydroelectric and tidal. Analyses are conclusive that nuclear power shall be an important stakeholder of any sustainable energy portfolio of national policy. While opting for nuclear energy, concerns are expressed about nuclear waste management. Modern nuclear fuel recycling and recent advances in nuclear waste vitrification technology offer effective solutions to the nuclear waste issues faced by the world today.

Radioactive liquid waste (RLW) generated in the closed nuclear fuel cycle is immobilised by fixing the radionuclides in a borosilicate-based glass matrix by a process known as "Vitrification". The liquid fed Joule Heated Ceramic Melter (JHCM) is an electric furnace, which takes advantage of the good electrical conductivity of glass at high temperatures. Presently this equipment is globally used due to its high throughput and good product quality.

In the present work, a numerical model based on Computational Fluid Dynamics, using COMSOL MULTIPHYSICS<sup>®</sup> software, is developed to predict the performance of a plant scale JHCM. The model is validated with temperature profiles, concentration profiles of a key component and electrical parameters, generated from experiments on a plant scale JHCM. Three different stages of operation of JHCM, viz., start-up heating, glass melting and vitrification have been modelled. The validated model was used for simulation and suggesting modifications of the melter design for better energy

efficiency. For providing accurate inputs for the model, thermo-physical and kinetic properties of glass ( $\text{SiO}_2$ -48%,  $\text{B}_2\text{O}_3$ -26.3%,  $\text{Na}_2\text{O}$ -11.7%,  $\text{TiO}_2$ -9.5%,  $\text{Fe}_2\text{O}_3$ -4.5%) with simulated waste oxides viz., co-efficient of thermal expansion, viscosity and electrical conductivity are determined experimentally. Simulation of batch-to-glass conversion was carried out by determining the kinetic parameters like activation energies, pre-exponential factors and order of reaction of waste nitrates in the presence of other waste nitrates and glass beads used in the study using Kissinger method. A mathematical model incorporating the electric, temperature, velocity fields, and reaction kinetics in an industrial scale JHCM is developed, and scope for further investigations in this field of research is outlined. A hybrid method for estimating the effective thermal conductivity of molten glass inside the JHCM is discussed.

The effective thermal conductivity is estimated for different stages of melter operation, indicating strong natural convective currents in the molten glass. The effect of different parameters during operation of melter at different stages of operation was studied. A numerical, 1:1, 3D model of the glass furnace was developed, and heat flow patterns, electrical field, convection pattern, and concentration profiles of oxides in JHCM were analysed. The agreement between theoretical predictions and experimental data demonstrates that the simulation code is a useful tool for design, optimisation, and evaluation of the performance of a JHCM with a variation of  $\pm 10\%$ . The current study will be used as a design refinement tool for future designs, to improve the thermal efficiency and product quality. The present study provides a basis for predicting the processing capacities based on model-based designs. The future studies can include the effect of bubbling on JHCM by integrating Multiphase models within the glass pool.

# TABLE OF CONTENTS

---

<b>ACKNOWLEDGEMENTS</b> .....	<b>I</b>
<b>ABSTRACT</b> .....	<b>III</b>
<b>LIST OF FIGURES</b> .....	<b>XI</b>
<b>LIST OF TABLES</b> .....	<b>XVII</b>
<b>NOMENCLATURE</b> .....	<b>XIX</b>
<b>1 INTRODUCTION</b> .....	<b>2</b>
<b>1.1 NUCLEAR POWER AND RADIOACTIVE WASTE</b>	<b>2</b>
1.1.1 Nuclear Fuel Cycle & Generation of Radioactive Waste	2
1.1.2 Characterisation of Radioactive Wastes	9
1.1.3 Radioactive Wastes Management Approach	10
1.1.4 Strategy for Management of HLW	12
1.1.5 Necessity for Immobilisation of High Level Waste	15
1.1.6 Vitrification of HLW	17
1.1.7 Types of Glass Used for Vitrification	21
1.1.8 Processing of vitreous waste forms	23
1.1.9 Vitrification Equipment	26
1.1.10 Alternate Waste Forms	31
<b>1.2 ORGANISATION OF THE THESIS</b>	<b>32</b>
<b>1.3 CLOSURE</b>	<b>33</b>
<b>2 REVIEW OF LITERATURE</b> .....	<b>35</b>
<b>2.1 GLASS MELTING PROCESS</b>	<b>36</b>

2.1.1	Determination of rate kinetics	37
2.1.2	Effect of Design Parameters	38
2.2	EXPERIMENTAL STUDIES ON JHCM	40
2.3	REVIEW OF MODELLING ON COMMERCIAL GLASS FURNACES	42
2.4	MODELLING APPROACHES TO JHCM	44
2.5	COMPUTER CODES FOR JHCM PROCESSING OF RADIOACTIVE WASTE	46
2.6	MODELLING OF START-UP HEATING	49
2.7	MODELLING OF MOLTEN GLASS	52
2.8	MELT POOL CONVECTION MODEL	55
2.9	COLD CAP MODELLING	56
2.10	CFD ANALYSIS OF GLASS FURNACES	60
2.11	GAP AREAS IN LITERATURE	62
2.12	MOTIVATION	63
2.13	SCOPE OF STUDY	64
2.14	RESEARCH OBJECTIVES	65
2.15	METHODOLOGY FOR MODELLING	66
2.16	CLOSURE	67
<b>3</b>	<b>EXPERIMENTAL STUDY .....</b>	<b>69</b>
3.1	DETERMINATION OF GLASS PROPERTIES	69
3.1.1	Viscosity of Glass	69
3.1.2	Thermal Expansion of Glass	70
3.1.3	Reaction Kinetics during Vitrification of RLW	70
3.2	EXPERIMENTAL SET UP - JOULE MELTER	73
3.2.1	Refractory & Insulation Layers	75

3.2.2	Inconel® Alloy 690 Electrodes	75
3.2.3	Feed Nozzle & Off-gas Nozzle	75
3.2.4	Temperature Measurement in JHCM	77
3.2.5	Level Measurement	77
3.2.6	Measurement of Heat Losses from the Melter Surface	78
3.2.7	Plenum Heaters	78
3.2.8	Freeze Valves & Induction Heating Coils	79
3.3	PILOT SCALE EXPERIMENTS FOR DETERMINATION OF HEAT TRANSFER MECHANISMS	79
3.3.1	Pilot Scale Experimental Set-Up	79
3.3.2	Experimental procedure	81
3.4	EXPERIMENTS ON INDUSTRIAL SCALE JHCM	82
3.4.1	Stage – I Operation of JHCM: Start-up Heating	83
3.4.2	Stage – II Operation of JHCM: Glass Melting	84
3.4.3	Stage – III Operation of JHCM: Vitrification	84
3.5	CLOSURE	87
<b>4</b>	<b>COMPUTATIONAL MODELLING AND SIMULATIONS .....</b>	<b>89</b>
4.1	MODELLING APPROACH	89
4.2	PROBLEM FORMULATION	89
4.3	ESTIMATION OF THE PROPERTIES OF THE MATERIALS	90
4.4	UNIT PROBLEMS	92
4.4.1	Electrical	93
4.4.2	Heat Transfer	94
4.4.3	Cold cap Model	95

4.4.4	Rate Kinetics	100
4.5	<b>MATHEMATICAL MODELLING OF JOULE HEATED CERAMIC MELTER</b>	<b>103</b>
4.5.1	Assumptions	103
4.5.2	Model Geometry	104
4.5.3	Domain Specification of the model	104
4.5.4	Mesh independence Studies	106
4.5.5	Measurements for validation	108
4.6	<b>MODEL DEVELOPMENT FOR JOULE HEATED CERAMIC MELTER</b>	<b>108</b>
4.6.1	Modelling of stage – I and stage – II	109
4.6.2	Governing Equations	110
4.6.3	Boundary Conditions	110
4.6.4	Assumptions made for modelling of stage – I and stage – II	110
4.7	<b>MODELLING OF STAGE - III</b>	<b>113</b>
4.7.1	Assumptions made for modelling of Stage – III	113
4.7.2	Governing equations for the model	114
4.7.3	Boundary Conditions for Stage - III	117
	Numerical Simulations	118
4.8	<b>CLOSURE</b>	<b>119</b>
<b>5</b>	<b>RESULTS AND DISCUSSION.....</b>	<b>121</b>
5.1	<b>ESTIMATION OF THE PHYSICAL AND CHEMICAL PROPERTIES OF GLASS</b>	<b>121</b>
5.1.1	Viscosity	121
5.1.2	Thermal Expansion of Glass	122
5.1.3	Resistivity of Glass	122
5.1.4	Determination of Reaction Kinetics for Vitrification of RLW	124

5.1.5	Determination of kinetic parameters	128
5.2	PILOT PLANT STUDIES FOR DETERMINATION OF THE CONTRIBUTION OF DIFFERENT MODES OF HEAT TRANSFER TO THE GLASS FRIT	135
5.3	TEMPERATURE PROFILES IN VARIOUS STAGES OF INDUSTRIAL SCALE JHCM OPERATION	137
5.3.1	Temperature Profile for Stage-I Operation of JHCM	137
5.3.2	Temperature Profile for Stage – II Operation of JHCM	139
5.3.3	Temperature Profile for Stage – III Operation of JHCM	142
5.3.4	Energy Distribution	148
5.3.5	Product Glass Characterisation	149
5.4	VALIDATION OF THE MODEL	151
5.4.1	Temperature Profiles at Various Power Inputs in Stage-I	151
5.4.2	Temperature Profile in Stage – II Operation of JHCM	153
5.4.3	Temperature Profiles In Stage – III Of Melter Operation - Simulation and Validation	159
5.4.4	Electrical Prameters validation in Stage – III operation of JHCM	164
5.4.5	Concentration Distribution in Stage – III of JHCM	167
5.5	STUDY OF DESIGN AND OPERATING PARAMETER REFINEMENTS IN JHCM BASED ON MODEL	171
5.5.1	Parameters influencing start-up heating efficiency	171
5.5.2	Parameters influencing Processing Capacity	177
5.6	CLOSURE	181
<b>6</b>	<b>CONCLUSIONS AND RECOMMENDATIONS .....</b>	<b>183</b>
6.1	CONCLUSIONS	183

6.2 RECOMMENDATIONS

186

**REFERENCES ..... 187**

## LIST OF FIGURES

---

<b>Figure 1.1:</b> Closed Fuel Cycle	4
<b>Figure 1.2:</b> Comparative energy density of fuels [6]	7
<b>Figure 1.3:</b> Strategy for management of radioactive waste	11
<b>Figure 1.4:</b> Indian strategy for waste management	15
<b>Figure 1.5:</b> Immobilization of waste - dissolution vs encapsulation	16
<b>Figure 1.6:</b> Formation of crystalline and amorphous material	18
<b>Figure 1.7:</b> Random network structure of the vitrified waste product	20
<b>Figure 1.8:</b> Typical flowchart for producing glass waste form	24
<b>Figure 1.9:</b> Schematic of the HLW Vitrification Process in French AVM [16]	25
<b>Figure 1.10:</b> Metallic Melter	26
<b>Figure 1.11:</b> Joule Heated Ceramic Melter [18]	28
<b>Figure 1.12:</b> Cold Crucible Induction Melter	30
<b>Figure 2.1:</b> Schematic of Cold Cap	37
<b>Figure 2.2:</b> Images of the cold cap [83]	57
<b>Figure 3.1:</b> Anton Paar Rheometer for measuring viscosity of glass	69
<b>Figure 3.2:</b> Dilatometer for measuring coefficient of thermal expansion of glass	70
<b>Figure 3.3:</b> Block diagram of TGA system	71
<b>Figure 3.4:</b> Schematic of JHCM	74
<b>Figure 3.5:</b> Temperature measurement in JHCM	76
<b>Figure 3.6:</b> Schematic of the RADAR Level Measurement	77
<b>Figure 3.7:</b> Thermal Image of top surface of JHCM	78
<b>Figure 3.8:</b> Plenum Heaters	79

<b>Figure 3.9:</b> Schematic of experiment used for determination of mode of heat transfer	81
<b>Figure 3.10:</b> Melter Operation Stages – a) Stage I : Empty cavity b) Stage – II: Glass Melting c) Stage – III : Vitrification	85
<b>Figure 4.1:</b> Pyramidal hierarchy for model development	92
<b>Figure 4.2:</b> Cold Cap during Steady State Conditions	95
<b>Figure 4.3:</b> Geometrical replica of the actual melter used in the model	104
<b>Figure 4.4:</b> Silicon Carbide resistance heaters as power source in color	105
<b>Figure 4.5:</b> Cavity of melter	105
<b>Figure 4.6:</b> Refractory layer-1 in color	105
<b>Figure 4.7:</b> Insulation layer 1 in highlighted state	105
<b>Figure 4.8:</b> Insulation layer 2 in highlighted state	106
<b>Figure 4.9:</b> Insulation layer 3 in highlighted state	106
<b>Figure 4.10:</b> Mesh independence studies	107
<b>Figure 4.11:</b> Meshing of the model	108
<b>Figure 4.12:</b> 3D Geometry of JHCM used in the model and boundary conditions for stage- I & II	109
<b>Figure 4.13:</b> Finer Meshing for the Plenum heater Domain	112
<b>Figure 4.14:</b> Mesh Element size distribution	112
<b>Figure 4.15:</b> 16 thermocouples in model used for validation of the model	113
<b>Figure 4.16:</b> 3D Geometry of JHCM used in the model and boundary conditions for stage- III	118
<b>Figure 5.1:</b> Variation of viscosity with temperature	121
<b>Figure 5.2:</b> Thermal Expansion of Glass in the Temperature Range 570–730 K	122

<b>Figure 5.3:</b> Variation of Resistivity with temperature	123
<b>Figure 5.4:</b> Variation of resistivity with Sodium concentration	123
<b>Figure 5.5:</b> Mass loss with temperature for waste constituents in sRLW	124
<b>Figure 5.6:</b> Mass loss with temperature of all the individual waste constituents, 5C & 7C glasses and base glass loaded with sRLW	125
<b>Figure 5.7:</b> DTG Curves of the individual waste constituents using TGA	125
<b>Figure 5.8:</b> DTG Curves of the individual waste constituents and 5C & 7C glass with sRLW	126
<b>Figure 5.9:</b> DTG curves at different heating rates for 5C glass with sRLW	129
<b>Figure 5.10:</b> Kissinger plot for 5C glass with sRLW	129
<b>Figure 5.11:</b> DTG curves at different heating rates for 7C glass with sRLW	130
<b>Figure 5.12:</b> Kissinger plot for 7C glass with waste constituents	131
<b>Figure 5.13:</b> Measured and fitted TGA curves and deconvolution peaks for individual heating rates for 5C loaded with waste nitrates for different heating rates (a) 10 K.min <sup>-1</sup> , (b) 20 K.min <sup>-1</sup> , (c) 30 K.min <sup>-1</sup> & (d) 40 K.min <sup>-1</sup>	133
<b>Figure 5.14:</b> Measured and fitted TGA curves and deconvolution peaks for individual heating rates for 7C loaded with waste nitrates for different heating rates (a) 10 K.min <sup>-1</sup> , (b) 20 K.min <sup>-1</sup> , (c) 30 K.min <sup>-1</sup> and (d) 40 K.min <sup>-1</sup>	134
<b>Figure 5.15:</b> Validation of model with experimental data on Pilot scale for simulating Stage - II	136
<b>Figure 5.16:</b> Spread of the cold cap with sRLW - 50 L.hr <sup>-1</sup> , 2.0 kg.hr <sup>-1</sup>	145

<b>Figure 5.17:</b> Energy distribution of JHCM with a) with 28 g.L <sup>-1</sup> and b) with 56 g.L <sup>-1</sup> of total dissolved salt	148
<b>Figure 5.18:</b> Slice Plot for transient analysis of empty cavity at t = 65 hr (Kelvin scale)	151
<b>Figure 5.19:</b> Validation of model with experimental data for an empty cavity	152
<b>Figure 5.20:</b> Slice plot depicting temperature profile inside the melter for 629 W on each heater (Color Legend: Temperature in Kelvin scale)	153
<b>Figure 5.21:</b> Industrial scale JHCM used for experiments (a) Start-up heating using plenum heaters; (b) Electrode heating	154
<b>Figure 5.22:</b> Model to predict effective thermal conductivity of packed bed of glass	154
<b>Figure 5.23:</b> Slice plot depicting temperature profile inside the melter for 1198 W on each heater (Color Legend: Temperature in Kelvin scale)	156
<b>Figure 5.24:</b> Apportionment of heat losses from JHCM	157
<b>Figure 5.25:</b> Validation of model for Temperature profile in Melter charged with packed bed of glass beads	158
<b>Figure 5.26:</b> Parity plot of the experimental values of Temperature and temperature predicted by the Model for stage-I & II	159
<b>Figure 5.27:</b> Velocity distribution in molten glass (Velocity in m.s <sup>-1</sup> )	161
<b>Figure 5.28:</b> Model validation for Stage - III with 28 g.L <sup>-1</sup> at 50 L.hr <sup>-1</sup> feed rate	162
<b>Figure 5.29:</b> Model validation for Stage - III with 56 g.L <sup>-1</sup> at 30 L.hr <sup>-1</sup> feed rate	162
<b>Figure 5.30:</b> 3D Volume plot depicting temperature contours (Rainbow Legend- Celsius scale) inside the JHCM including molten glass and cold cap	163

<b>Figure 5.31:</b> Temperature profile between the refractory and insulation layers	163
<b>Figure 5.32:</b> Parity plot of the experimental values of temperature and temperature predicted by the Model with HLW for stage-3	164
<b>Figure 5.33:</b> Current density arrow map for 3D melter model at 60 V potential drop (Rainbow legend current density in $A.m^{-2}$ )	165
<b>Figure 5.34:</b> Validation of model with electrical properties	166
<b>Figure 5.35:</b> Temperature profile inside the melter cavity (Rainbow Color legend with Temperature in Kelvin for 60 V input)	166
<b>Figure 5.36:</b> Concentration profile of $CsNO_3$ (Rainbow legend in $mol.m^{-3}$ )	168
<b>Figure 5.37:</b> Validation of model with concentration profiles	169
<b>Figure 5.38:</b> Cold cap covering 60 % of melter top surface	170
<b>Figure 5.39:</b> Cold cap covering 80 % of melter top surface	170
<b>Figure 5.40:</b> Cold cap covering 90 % of melter top surface	170
<b>Figure 5.41:</b> Comparison of experimental result with simulated result for 60% cold cap spread	170
<b>Figure 5.42:</b> Comparison of experimental result with simulated result for 80% cold cap spread	170
<b>Figure 5.43:</b> Comparison of experimental result with simulated result for 90% cold cap spread	170
<b>Figure 5.44:</b> Parity plot of temperature profile	171
<b>Figure 5.45:</b> Off gas ingress and heat losses vs negative pressure in the melter	172
<b>Figure 5.46:</b> (a) Prefabricated square slots for placing of PH with a gap 6 – 26 mm. (b) Circular Slots for placing of PH	174

<b>Figure 5.47:</b> (a) Total Energy Flux Vs Thickness of the air gap; (b) Change in temperature with time for different air gap thickness between refractories and Kanthal© tubes	174
<b>Figure 5.48:</b> Heat flux vs Distance in the prefabricated in the square and circular designs	175
<b>Figure 5.49:</b> 3D Volume plot depicting temperature profile (Rainbow Legend – Kelvin scale) inside the melter for with modified Plenum Heaters	176
<b>Figure 5.50:</b> Melter electrodes one above the other	179
<b>Figure 5.51:</b> Simulated model of electrodes placed one above the other	180
<b>Figure 5.52:</b> Vertical orientation of electrodes	180
<b>Figure 5.53:</b> Simulated model of electrodes immersed vertically (Rainbow legend Current density in $A.cm^{-2}$ )	181
<b>Figure 5.54:</b> Simulated model of electrodes immersed vertically (Rainbow legend temperature in K)	181

## LIST OF TABLES

---

<b>Table 1.1:</b> World commercial reprocessing capacity	6
<b>Table 1.2:</b> Per terawatt hour (TWh) data for key sustainability and economic- environmental impact indicators associated with 7 electricity generation options and relative ranks <sup>a</sup> of the energy [6]	8
<b>Table 1.3:</b> Categorisation of radioactive waste	10
<b>Table 1.4:</b> Typical composition of HLW generated at different reprocessing plants	12
<b>Table 1.5:</b> Half-lives of the elements present in HLW	13
<b>Table 1.6:</b> Joule Heated Ceramic Melters	29
<b>Table 2.1:</b> Summary of the detailed review of start-up heating of vitrification equipment	49
<b>Table.2.2:</b> Summary of the detailed review on cold cap modelling literature	59
<b>Table 2.3:</b> Computer codes for CFD modelling of glass furnaces	61
<b>Table 3.1:</b> Glass composition and simulated waste constituents	72
<b>Table 3.2:</b> Different Stages of Melter Operation	82
<b>Table 4.1:</b> Physical properties of glass and insulation materials used for modelling	91
<b>Table 4.2:</b> Mesh statistics of the model	107
<b>Table 5.1:</b> Thermogram of thermal decomposition	128
<b>Table 5.2.</b> Kinetic parameters of 5C base glass during thermal decomposition	132
<b>Table 5.3:</b> Kinetic parameters of 7C base glass during thermal decomposition	132
<b>Table 5.4:</b> Temperature profile in JHCM during Stage - I	140
<b>Table 5.5:</b> Temperature profile in JHCM during Stage - II	141

<b>Table 5.6:</b> Temperature profile of glass pool thermocouples in JHCM during Stage – III for estimating boil up rate	143
<b>Table 5.7:</b> Temperature profile of cold cap thermocouples in JHCM during Stage - III for estimating boil up rate	144
<b>Table 5.8</b> Variation of throughput with increased salt content	145
<b>Table 5.9:</b> Temperature profile of glass pool thermocouples in JHCM during Stage – III for determining processing capacity	146
<b>Table 5.10:</b> Temperature profile of cold cap thermocouples in JHCM during Stage - III for determining processing capacity	147
<b>Table 5.11:</b> Off-gas produced for different capacities	149
<b>Table 5.12:</b> Typical characteristic properties of VWP	150
<b>Table 5.13:</b> Throughput variation with operating level	178

# NOMENCLATURE

---

## English Symbols (in alphabetical order)

Symbol	Description	Unit
A	Pre exponential Factor	$s^{-1}$
B	Magnetic flux density vector	$Wb.m^{-2}$
C	Specific heat capacity	$J.kg^{-1}.K^{-1}$
Ce	Electrical Capacitance	F
c	Concentration of species	$mol.m^{-3}$
D	Diffusivity	$m^2.s^{-1}$
E	Activation Energy	$J.mol^{-1}$
$\vec{E}$	Electric Field Intensity	$V.m^{-1}$
e	Emissive power	$W.m^{-2}$
ep	Excess pressure over static pressure	$N.m^{-2}$
F	View factor	-
G	Surface irradiation	$W.m^{-2}$
g	Acceleration due to gravity	$m.s^{-2}$
H	Heat source or sink	$W.m^{-3}$
Hi	Height	m
h	Heat transfer coefficient	$W.m^{-2}.K^{-1}$
J	Current density	$A.m^{-2}$
J	Radiosity	$W.m^{-2}$
j	Mass flux	$kg.m^{-2}.s^{-1}$
Js	Surface radiosity	$W.m^{-2}$
k	Thermal conductivity	$W.m^{-1}.K^{-1}$
L	Height of cold cap	m
Le	Length	m
ma	Mass	kg
N	Melting rate	$kg.m^{-2}.s^{-1}$
n	Order of reaction	-
N	Concentration flux	$mol.m^{-2}.s^{-1}$
$\hat{n}$	Unit normal vector	-

nr	Refractive index	-
Q	Heat release per unit volume	J.m <sup>-3</sup>
q	Heat flux	W.m <sup>-2</sup>
q	Heating rate	K.s <sup>-1</sup>
r	Mass change rate	kg.s <sup>-1</sup>
R	Universal gas constant (8.314)	J.mol <sup>-1</sup> .K <sup>-1</sup>
Re	Resistance	Ω
Rr	Rate of reaction	mol.m <sup>-3</sup> .s <sup>-1</sup>
S <sub>1</sub>	Displacement current density	A.m <sup>-2</sup>
S <sub>2</sub>	Electric charge density	A.m <sup>-2</sup>
s	Heat transfer between gas phase and condensed phase throughout coldcap	W.m <sup>-3</sup>
t	Time	s
T	Temperature	K
v	Velocity	m.s <sup>-1</sup>
V	Voltage applied	V
w	Fraction of mass loss	-
wp	Percentage weight of Na <sub>2</sub> O in Glass	%
x	Distance in x-direction	m
y	Major reactions	-

### Greek Symbols

Symbol	Description	Unit
α	Degree of conversion of d <sup>th</sup> reaction	
β	Coefficient of expansion	K <sup>-1</sup>
δ	Distance step	m
η	Viscosity	Pa.s
λ	effective heat conductivity	W.m <sup>-1</sup> .K <sup>-1</sup>
ξ	Degree of conversion	
$\vec{\epsilon}$	composition vector at each time	
ρ	Density	kg.m <sup>-3</sup>
σ	Electrical conductivity	S.m <sup>-1</sup>
τ	Time step	s
φ	Potential	V

$\varepsilon$	Surface emissivity	
$\mu$	Magnetic permeability	$\text{H.m}^{-1}$
$\theta$	Heating rate	$\text{K.s}^{-1}$

---

### Subscripts

<b>Symbol</b>	<b>Description</b>
0	bottom
amb	ambient
b	bulk
bl	black body
Bo	Bottom of cold cap
c	condensed phase
d	particular reaction
el	electrical
ext	external
F	Final
g	gas phase
i	distance instance
J	Due to current density
L	height of cold cap
M	Species
p	at constant pressure
sb	Stefan Boltzmann
su	surface
To	Total
U	Top of cold cap
u	initial
z	Peak

---

### Superscripts

<b>Symbol</b>	<b>Description</b>
m	time instance

Tr          Transpose

---

### **Dimensionless Numbers**

<b>Symbol</b>	<b>Description</b>
<b>Nu</b>	Nusselt number
<b>Ra</b>	Rayleigh number

---

### **ACRONYMS**

---

<b>Acronym</b>	<b>Expansion</b>
2D	Two Dimensional
3D	Three Dimensional
AC	Alternate Current
ACPC	Alternating Current Power Control
ANSYS	Analysis System
APM	Advanced Powder Metallurgical
ASTM	American Standard Testing Materials
AVM	Advanced Vitrification Melter
AZS	Alumina-Zirconia-Silica
BO	Bridging Oxygen
CANDU	Canada Deuterium Uranium
CC	Cold cap
CCIM	Cold Crucible Induction Melter
CFD	Computational Fluid Dynamic

DF	Decontamination Factor
DM	Demineralized
DOM	Discrete Ordinate Method
DRS	Dynamic Rheometer System
DSC	Differential Scanning Calorimetry
DTA	Differential Thermal Analysis
DTG	Differential Thermogravimetry
DTM	Differential Transformation Method
EGA	Evolved Gas Analysis
FDM	Finite Difference Method
FEA	Finite Element Analysis
FEM	Finite Element Method
FEM	Finite Element Method
FIDAP	Fluid Dynamics and Analysis
FP	Fission products
FRS	Furnace Rheometer Systems
GC	Gas Chromatography
GP	Glass Pool
HEPA	High-Efficiency Particulate Air
HF	Hydrogen Fluoride
HLW	High-Level Liquid Waste

JHCM	Joule Heated Ceramic Melter
LAW	Low Activity Waste
LVDT	Linear Variable Differential Transformer
LWR	Light Water Reactor
MOX	Mixed Oxide
MS	Mass Spectrometer
NA	Not Applicable
NBO	Non-Bridging Oxygen
NIT	National Institute of Technology
NZP	Sodium Zirconium Phosphate
PARDISO	Parallel Sparse Direct Solver
PC	Personal Computers
PCW	Process Cooling Water
PDE	Partial Differential Equations
PH	Plenum Heaters
PHWR	Pressurized Heavy Water Reactor
PNNL	Pacific Northwest National Laboratory
PUREX	Plutonium Uranium Recovery by Extraction
RADAR	Radio Detection and Ranging
RLW	Radioactive Liquid Waste
SCADA	Supervisory Control and Data Acquisition

SIMPLER	Semi-Implicit Method for Pressure-Linked Equations Revised
sRLW	Simulated Radioactive Liquid Waste
SS	Stainless Steel
STA	Simultaneous Thermal Analysis
SW	Simulated Waste
TDS	Total Dissolved Salts
TEMPEST	Transient Energy-Momentum and Pressure Equations Solutions in Three Dimensions
TG	Thermogravimetry
TGA	Thermogravimetric analysis
TNO	The Netherlands Organization
VFT	Vogel – Fulcher – Tammann
VOF	Volume of Fluid
VRF	Volume Reduction Factor
VWP	Vitrified Waste Product
WIP	Waste Immobilization Plant
WIPK	Waste Immobilization Plant, Kalpakkam
WO	Waste Oxide
WSRC	Westinghouse Savannah River Company
XRD	X-Ray Diffraction

# CHAPTER-1

## INTRODUCTION

# CHAPTER-1

---

## 1 INTRODUCTION

### 1.1 Nuclear Power and Radioactive Waste

Power is one of the most critical components for the economic growth and welfare of nations and for ensuring a sustained growth of the global economy. Sources of power generation range from conventional sources such as coal, lignite, natural gas, oil, hydro and nuclear power to viable non-conventional sources such as wind, solar, and bio. Global electricity demand has increased rapidly and is expected to rise further in the years to come. In order to meet the increasing demand for electricity, massive addition to the installed generating capacity is required.

In 2018 for the global energy generation hydroelectric dams supplied the largest non fossil component, followed by nuclear, wind and bio and solar. The share of electricity in global energy use is going while the risk of low carbon technologies is promoting a pragmatic transformation in the way electricity is generated [1].

#### 1.1.1 Nuclear Fuel Cycle & Generation of Radioactive Waste

Nuclear Power continues to be the largest source of non – hydro and low carbon electricity globally. All forms of electricity production, whether oil, coal or gas, generates some level of CO<sub>2</sub> and other greenhouse gases. The construction phase of the plant or equipment, for example, requires cement pouring and vehicle use, each of which carries its carbon footprint. When considering the entire power generation lifecycle, including construction, mining, operation, and decommissioning, nuclear power comes out as one of the cleanest technologies available [2].

Nuclear power is generated from the fission of heavy metals like Uranium and Plutonium in a nuclear reactors. These heavy metals fabricated in the form of fuel rods are irradiated to a burn-up that ranges from 1000 MWD/T to 100000 MWD/T depending upon the type of reactor. At the end of their life cycle, these fuel rods are removed from the reactor and discarded as spent fuel.

Today, depending upon the policies of different countries, two options exist for management of spent nuclear fuel.

- Open Fuel Cycle that involves direct disposal of spent fuel in deep geological formations and,
- Closed Fuel Cycle that involves reprocessing the spent fuel using PUREX (Plutonium Uranium Recovery by Extraction) process to extract Pu and unused U for reuse in new fuel and conditioning of residual wastes that contain fission products (FP) and minor actinides in highly durable glass matrix followed by interim storage and then disposal.

The term "Nuclear fuel cycle" refers to all activities that are involved in the production of nuclear energy. The processes include ore mining and milling, conversion into oxides, fuel fabrication, power production, fuel reprocessing, waste management & disposal, and finally decontamination and decommissioning of nuclear facilities. Each step in the process involves different technical, economic, safety and environmental consequences. A vast number of fuel cycles appear in literature, and many have been utilised to some extent. The different fuel cycles can be categorised into two main classes: "open fuel cycle" and "closed fuel cycle."

In the open or once-through fuel cycle, the spent fuel discharged from the reactor is treated as waste and suitably managed by direct disposal in deep geological repositories.

In the closed fuel cycle, the spent fuel discharged from the reactor is reprocessed, and the unused Uranium and Plutonium are extracted from the fission products, as shown in Figure 1.1. This extracted solution containing Uranium and Plutonium is further partitioned to separate Uranium and Plutonium from each other. The recovered

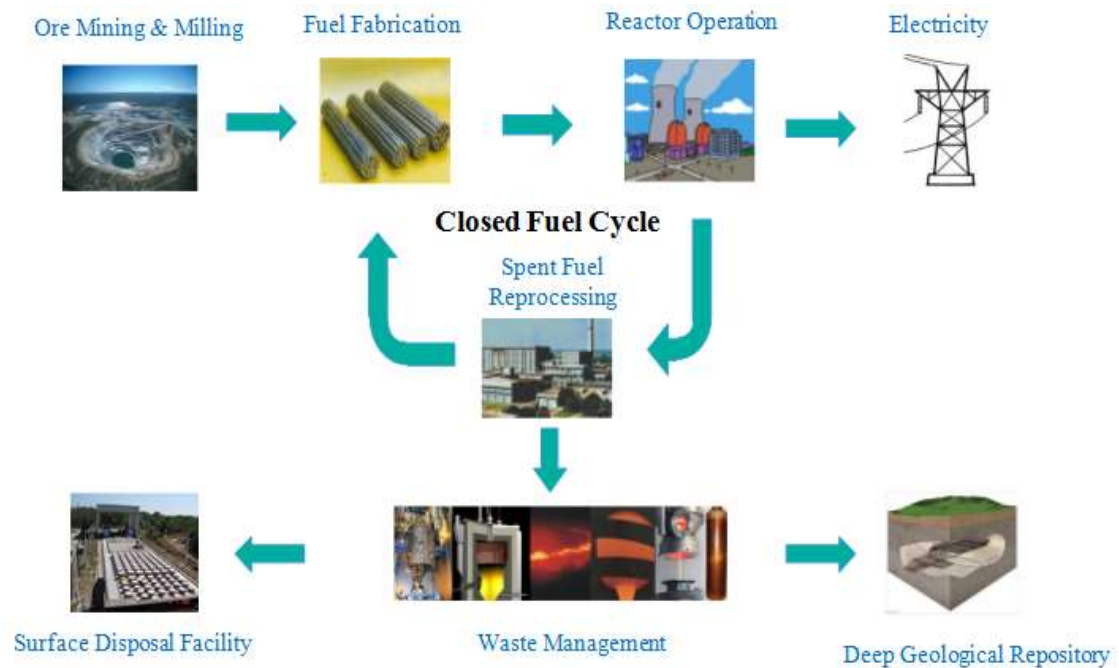


**Figure 1.1:** Closed Fuel Cycle

Uranium and Plutonium are then fabricated into oxide or mixed oxide fuel (MOX), which can be used as fuel in a reactor. The remainder of the spent fuel after the recovery of Uranium and Plutonium is treated as high-level waste (HLW). Recycling drastically reduces, not only the volume but also the long-term radiotoxicity of the final waste. Indeed, the long term toxicity of spent nuclear fuel is dominated by Plutonium. Recycling Plutonium leads to a long term radiotoxicity decrease of one order of magnitude. In other words, the waste returns to the radiotoxicity levels of the natural Uranium 10 times faster. Apart from the closed and open fuel cycle, research is also being carried out on advanced fuel cycle. The advanced fuel cycle could employ a dedicated reactor for transmuting selected isotopes separated from spent fuel. This

dedicated reactor may also be used as a breeder reactor to produce new fissile material at a rate that exceeds the consumption of fissile material by the neutron chain reaction.

In such fuel cycles, the waste streams will contain fewer actinides [3].

Partitioning (separation and recovery) of minor actinides from HLW, followed by their transmutation into short-lived nuclides will also reduce the load on future repositories.

This is of particular importance from the waste management point of view due to the problems in finding suitable geological repositories, given the reluctance on the part of the general public to allow construction of any such facility in their neighbourhood. The Partitioning & Transmutation option considerably reduces the radioactivity and reduces/eliminates the need for long-term surveillance of vitrified waste.

France, India, Russia, Japan, the United Kingdom (UK) are adopting a closed fuel cycle.

In India, a three-stage nuclear power program was formulated in the middle of the last century to exploit the full energy potential of the resources. The first stage utilises the limited natural uranium resource for both power production and also for the conversion of uranium to plutonium. The plutonium produced in the first stage will be used as a fuel in the second stage in fast breeder reactors to produce power and to enhance the fissile inventory necessary for launching the third stage of thorium-based power reactors.. Reprocessing and recycling of both fissile and fertile components back into appropriate reactor systems is an integral part of this strategy.

Globally, till date, 90,000 tonnes out of 290,000 tonnes of spent fuel from commercial power reactors have been reprocessed. The global annual reprocessing capacity is approximately 4000 tonnes for typical oxide fuels. Reprocessing capacities of various countries in the world is shown in Table 1.1[4].

**Table 1.1:** World commercial reprocessing capacity

<b>Type of fuel used</b>	<b>Country</b>	<b>Tonnes/year</b>
<b>Light Water Reactor (LWR) fuel</b>	France, La Hague	1700
	The UK, Sellafield (THORP)	600
	Russia, Ozersk (Mayak)	400
	Japan (Rokkasho)	800
	Total LWR (approx.)	3500
<b>Other nuclear fuels</b>	The UK, Sellafield (Magnox)	1500
	India (PHWR, 4 plants)	330
	Japan, Tokai MOX	40
	Total other (approx.)	1870
<b>Total civil capacity</b>		<b>5370</b>

The overall management of non-radioactive, toxic waste in the recent past has been substandard with a general disposition to dispose these directly into the environment, with little thought given to the long-term consequences of these actions on the environment. Fortunately, this had not been the case with nuclear wastes, which were produced as a result of various activities using radioactive elements. After the discovery of radioactivity and the radioactive materials in the late nineteenth century, it soon became apparent that these materials posed a unique risk to the environment and human health. Consequently, they cannot be disposed off in the same haphazard manner, which was followed for their nonradioactive counterpart and has to be suitably contained and isolated from the biosphere for a relatively more prolonged duration [5].

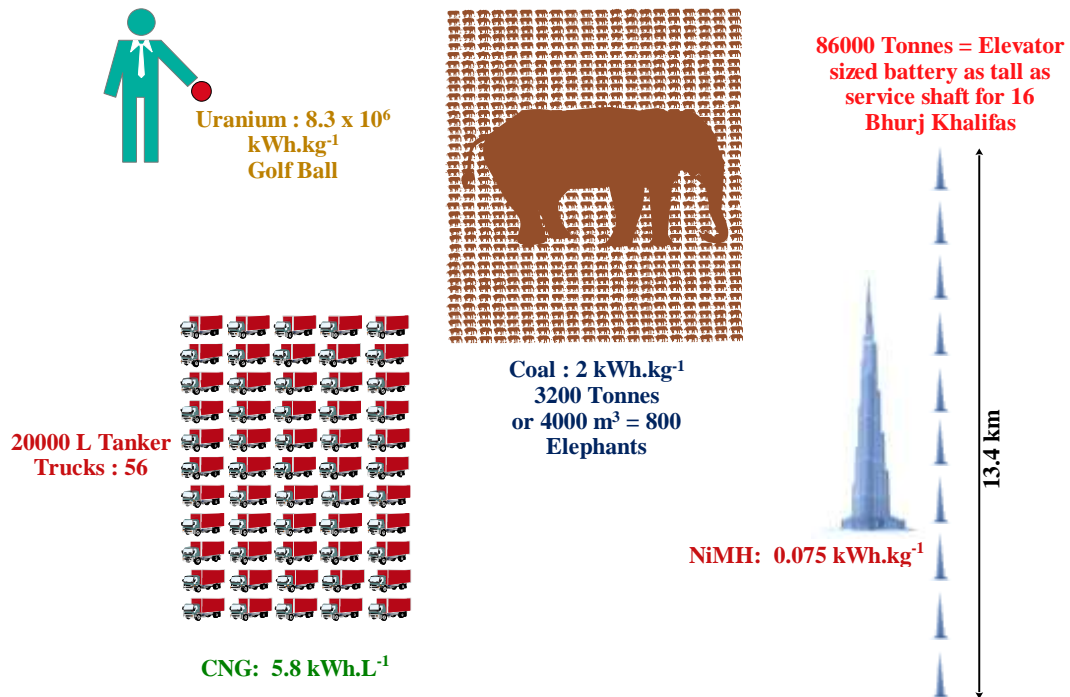


**Figure 1.2:** Comparative energy density of fuels [6]

(a) Uranium, (b) Compressed natural gas (CNG), (c) coal, and (d) Nickel-Metal-Hydride (NiMH) chemical batteries (standard type used in electric vehicles) required to supply or store approximately 220 kWh of electricity equivalent per day for 80 years (enough to service all lifetime needs for lighting, heat, transport, food production, manufacturing, etc. of a developed-world citizen. Total electrical energy embodied is calculated as 6.4 million kWh. Mass-to-volume relationship is uranium = 780 g or 40.7 cm<sup>3</sup> (golf-ball sized); compressed natural gas = 56 × 20,000-L tanker trucks; coal = 3,200 t or 4,000 m<sup>3</sup> (approximately 800 elephant equivalents); NiMH battery = 86,000 t (elevator-sized battery as tall as the service shaft for 16 Burj Khalifa sized super skyscrapers)

Figure 1.2 shows the energy density of various fuels used for power generation. Table 1.2 gives a comparative assessment of various fuels for energy generation, with respect to environment and economic factors. Although the environmental movement has historically rejected the nuclear energy option, new-generation reactor technologies that fully recycle waste and incorporate passive safety systems might resolve their concerns and be more widely understood [6].

**Table 1.2:** Per terawatt hour (TWh) data for key sustainability and economic-environmental impact indicators associated with 7 electricity generation options and relative ranks<sup>a</sup> of the energy [6]

Indicator (per TWh)	Coal		Natural Gas		Nuclear		Biomass		Hydro		Wind (onshore)		Solar	
	Value	Rank	Value	Rank	Value	Rank	Value	Rank	Value	Rank	Value	Rank	Value	Rank
GHG Emissions (t CO <sub>2</sub> ) <sup>b</sup>	10 <sup>6</sup>	7	4.7 x 10 <sup>5</sup>	6	16000	3	18000	4	4000	1	12000	2	46000	5
Electricity Cost (\$US) <sup>c</sup>	100.1	4	65.6	1	108.4	5	111	6	90.3	3	86.6	2	144.3	7
Dispatchability <sup>d</sup>	A	1	A	1	A	1	B	4	B	4	C	6	C	6
Land Use (km <sup>2</sup> ) <sup>e</sup>	2.1	3	1.1	2	0.1	1	95	7	50	6	46	5	5.7	4
Safety (fatalities) <sup>f</sup>	161	7	4	5	0.04	1	12	6	1.4	4	0.15	2	0.44	3
Solid Waste (t)	58600	7	NA	1	NA	1	9170	6	NA	1	NA	1	NA	1
Radiotoxic Waste <sup>g</sup>	Mid	6	Low	3	High	7	Low	3	Trace	1	Trace	1	Trace	1
Weighted Rank <sup>h</sup>		6		2		1.3		6.7		3.3		2.3		5.3

<sup>a</sup> Energy source with the lowest environmental or economic impact for a given indicator (e.g., greenhouse-gas emissions, cost of electricity, etc.) is assigned a rank of 1, whereas the worst performing of the 7 energy sources is assigned a rank of 7. Ties are given the same rank. All calculations and supporting data behind this table are detailed in the Supporting Information.

<sup>b</sup> Includes production-related and life-cycle-embodied emissions.

<sup>c</sup> Levelized cost of electricity, includes cost amortization for long-term waste management and plant decommissioning for nuclear energy.

<sup>d</sup> Categorical rating of capacity and availability to deliver electricity on demand.

<sup>e</sup> For fuel mining and generating footprint.

<sup>f</sup> Deaths from accidents, excluding chronic health problems.

<sup>g</sup> Categorical classification of the volume of the radiotoxic waste stream.

<sup>h</sup> Average of 3 multi-criteria decision-making analysis scenarios with multiplicative weightings applied to the indicator ranks: (1) no weighting = 1 × multiplier for all ranks; (2) economic rationalist = 1 × land use, solid waste, and radioactive waste, 2 × cost and dispatch ability, and 0.5 × greenhouse gas emissions and safety; and (3) environmentalist = 1 × safety, solid waste and radioactive waste, 2 × greenhouse gas emissions and land use, and 0.5 × cost and dispatch ability. Weightings are arbitrary but illustrative of typical viewpoints.

Nuclear waste management demands an eco-friendly process/system so that the well-being of the present and future generations are ensured. The management of wastes generated in non-nuclear industries cannot be a benchmark for the management of nuclear wastes owing to the radiation hazard and considering the public resistance to disposal of the radioactive wastes into their neighbourhood. Many treatment methods are available for the management of radioactive wastes based on considerations such as characteristics of waste, efficacy of the method, availability of material and suitability of the site to accommodate final disposal product.

### **1.1.2 Characterisation of Radioactive Wastes**

The characteristics and nature of the waste vary depending upon its origin in the nuclear fuel cycle. The radioactive wastes can be classified based on their physical states, their activity level, their salt content or the specific nature of their radioactivity. Thus, a given waste stream can be characterised in more than one way, basic parameters of classification being radionuclide concentrations and half-lives.

Classification of waste into different categories is useful in their segregation, selection of appropriate treatment process, storage, and disposal. The classification is essential from safety as well as process consideration point of view. Key parameters which are taken into account include physical, chemical, radiological, and biological properties as well as criticality aspects and origin of the waste.

Radioactive wastes are generated in various forms like solid, liquid or gaseous. The concentration of radioactivity also varies, depending upon the source of generation. Accordingly, radioactive liquid waste streams are commonly classified as Exempt Waste, Low Level Waste ( $37 \times 10^3$ - $3.7 \times 10^9$  Bq.m<sup>-3</sup>), Intermediate Level Waste ( $3.7 \times 10^9$ - $3.7 \times 10^{14}$  Bq. m<sup>-3</sup>) and High Level Waste (above  $3.7 \times 10^{14}$  Bq. m<sup>-3</sup>). The concentrations

of long-lived radionuclides and tritium are also taken into account while classifying the liquid wastes. The general categorisation of radioactive waste followed in India is presented in Table 1.3.

**Table 1.3:** Categorisation of radioactive waste

Category	Solid	Liquid	Gaseous
	Surface Dose (mGy/hr)	Activity level (Bq/m <sup>3</sup> )	Activity level (Bq/m <sup>3</sup> )
<b>I</b>	<2	<3.7 x 10 <sup>4</sup>	<3.7
<b>II</b>	2-20	3.7 x 10 <sup>4</sup> to 3.7 x 10 <sup>7</sup>	3.7 to 3.7 x 10 <sup>4</sup>
<b>III</b>	>20	3.7 x 10 <sup>7</sup> to 3.7 x 10 <sup>9</sup>	>3.7 x 10 <sup>4</sup>
<b>IV</b>	Alpha bearing waste (alpha Activity>4000 Bq/g)	3.7 x 10 <sup>9</sup> to 3.7 x 10 <sup>14</sup>	-
<b>V</b>		> 3.7 x 10 <sup>14</sup>	-

### 1.1.3 Radioactive Wastes Management Approach

Management of radioactive wastes includes management of all types of radioactive wastes generated during different steps of the nuclear fuel cycle right from the mining of uranium, fuel fabrication and reactor operations and subsequent reprocessing of the spent fuel. The four-step strategy adopted for radioactive waste management is

- Delay & Decay: Adopted for short-lived isotopes
- Dilute & Disperse: Adopted for a low-level activity where very large dilution is available
- Concentrate & Contain: Adopted for long-lived fission products
- Recover & Reuse: Isotopes that are used for the industrial purposes are recovered and reused

Effective management of radioactive wastes involves segregation, characterisation, handling, treatment, conditioning, and monitoring before final storage/disposal.

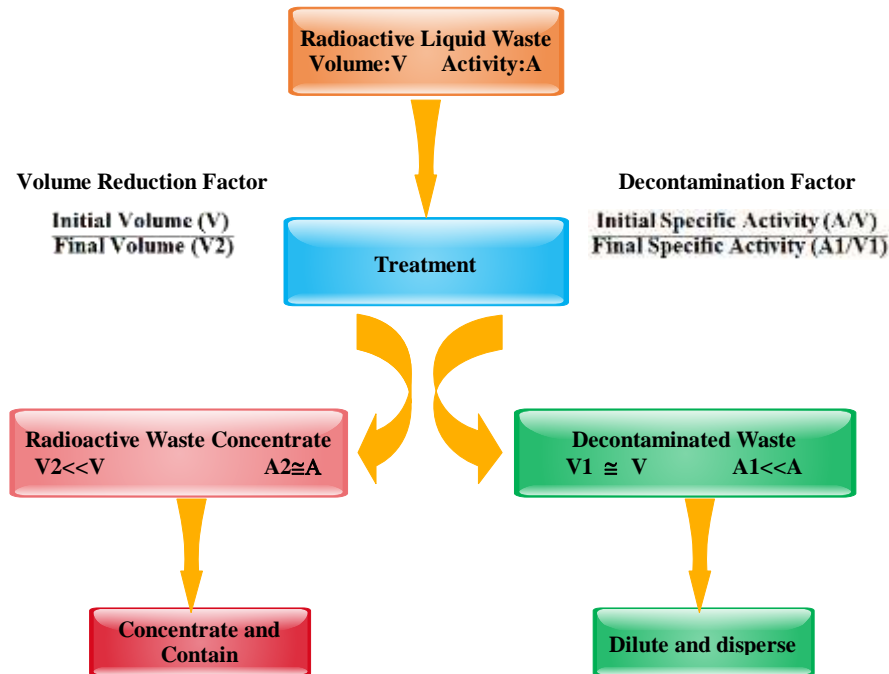


**Figure 1.3:** Strategy for management of radioactive waste

Development of strategies for the management of all types of radioactive wastes is crucial for their isolation from the human environment in a safe, sustainable, and acceptable manner. The radioactive waste after conditioning will be converted to a large volume of decontaminated waste and a small amount of concentrated waste as shown in Figure 1.3[7].

Strategy for the management of low and intermediate level wastes lies in the development of innovative treatment processes having volume reduction factor (VRF) as one of the essential parameters. The active components of radioactive wastes are separated using different chemical techniques like co-precipitation and ion-exchange, and membrane processes like, reverse osmosis, and ultra-nano filtration. The concentrates obtained from the primary treatment process are conditioned before their disposal.

### 1.1.4 Strategy for Management of HLW

Wastes with levels of activity concentration high enough to generate a significant quantity of heat by the radioactive decay process and waste with a large amount of long-lived radionuclides need to be considered in the design of a disposal facility. Disposal in deep, stable geological formations usually several hundred meters below the surface is a generally recognised option for disposal of HLW.

**Table 1.4:** Typical composition of HLW generated at different reprocessing plants

Component	Savannah river (USA)	Tokai (Japan)	Lanchow (China)	La Hague (France)	HAWC- WAK (Germany)	WIP (India)
Na (gpl)	5.9	44.5	31	-	16.0	6.6
K (gpl)	0.3	-	0.6	-	0.4	0.2
Nitrates (M)	4.2	-	-	-	-	4.1
Fission Products (gpl)	<3	49	2.7	87.0	40.5	1.1
TRUs (wt %)	<0.2	12.6	17.9	5.1	6.9	7.6

High level radioactive liquid waste is generated in the first cycle of the fuel reprocessing plant. Figure 1.3 gives the strategy adopted for the management of radioactive waste.

Table 1.4 gives the typical composition of HLW generated from different reprocessing plants across the world [8]. HLW contains almost 99% of the total radioactivity generated in the entire nuclear fuel cycle. The waste is acidic in nature (1.5-3 M nitric acid) and has activity in the range of  $3.7 \times 10^{12} - 7.5 \times 10^{14}$  Bq. m<sup>-3</sup>. The major components present in HLW are

- i. Corrosion product of Fe, Ni, Cr and Mn

- ii. Fission products such as  $^{90}\text{Sr}$ ,  $^{106}\text{Ru}$ ,  $^{137}\text{Cs}$ ,  $^{144}\text{Ce}$ ,  $^{147}\text{Pm}$ . Radio-isotopes present in HLW along with their half-lives are presented in Table 1.5
- iii. Minor actinides such as  $^{241}\text{Am}$ ,  $^{245}\text{Cm}$  and unrecovered U and Pu and
- iv. Added chemicals such as Nitric acid, Sodium Nitrate, traces of tri-butyl phosphate and its degradation products.

**Table 1.5:** Half-lives of the elements present in HLW

Fission Products	Half-Life (years)	Transuranic	Half-life (years)
$^{140}\text{Ba}$	0.035	$^{241}\text{Am}$	432.000
$^{144}\text{Ce}$	0.779	$^{243}\text{Am}$	$7.370 \times 10^3$
$^{134}\text{Cs}$	2.065	$^{245}\text{Cm}$	$8.500 \times 10^3$
$^{137}\text{Cs}$	30.170	$^{246}\text{Cm}$	$4.780 \times 10^3$
$^{140}\text{La}$	40.280	$^{247}\text{Cm}$	$1.580 \times 10^7$
$^{147}\text{Nd}$	0.030	$^{248}\text{Cm}$	$3.400 \times 10^5$
$^{107}\text{Pd}$	$6.5 \times 10^6$	$^{236}\text{Np}$	$1.200 \times 10^5$
$^{147}\text{Pm}$	2.630	$^{237}\text{Np}$	$2.100 \times 10^7$
$^{87}\text{Rb}$	$4.89 \times 10^{10}$	$^{238}\text{Np}$	$5.780 \times 10^{-3}$
$^{103}\text{Ru}$	0.107	$^{239}\text{Pu}$	$2.400 \times 10^4$
$^{106}\text{Ru}$	1.020	$^{240}\text{Pu}$	$6.560 \times 10^3$
$^{147}\text{Sm}$	$1.06 \times 10^{11}$	$^{241}\text{Pu}$	14.350
$^{148}\text{Sm}$	$7.0 \times 10^{15}$	$^{242}\text{Pu}$	$3.760 \times 10^5$
$^{149}\text{Sm}$	$1.0 \times 10^{16}$	$^{244}\text{Pu}$	$8.200 \times 10^7$
$^{151}\text{Sm}$	90.000	$^{235}\text{U}$	$7.040 \times 10^8$
$^{90}\text{Sr}$	29.000	$^{238}\text{U}$	$4.470 \times 10^9$
$^{99}\text{Tc}$	$2.13 \times 10^5$		
$^{127}\text{Te}$	$1.080 \times 10^{-3}$		
$^{90}\text{Y}$	$7.305 \times 10^{-3}$		
$^{95}\text{Zr}$	0.175		

The management and disposal of HLW from the nuclear fuel cycle are the most challenging problems faced by the nuclear industry. Today, even after fifty years of the commissioning of the first commercial nuclear power plant, no country has yet succeeded in disposing of HLW which is the longest-lived, highly radioactive and most technologically challenging waste stream.

The current practice is to store HLW from reprocessing plants in stainless steel (SS) tanks in the form of aqueous nitric acid solution. The liquid storage requires essential services like removal of decay heat with process cooling water, maintaining vacuum in the tanks, treatment of the off-gases generated from the tanks, instrumentation requirements. The failure of any of the services can have serious safety implications. Storing HLW in SS tanks is safe for the short term, but for ultimate disposal, this option cannot be considered, due to the long half-life of fission products and the susceptibility of the vessels to failure due to radiolytic and corrosion attack.

In most countries, the preferred technological approach is to dispose of the waste in repositories constructed in rock formations hundreds of meters below the earth's surface. Although several experimental and pilot facilities have been built, there are no operating high-level waste repositories. The perceived lack of progress towards successful waste disposal stands as one of the primary obstacles to the expansion of nuclear power around the world. A three-step strategy for management of HLW has been adopted in India, as shown in Figure 1.4. It involves

- I. Immobilisation of waste oxides in stable and inert solid matrices
- II. Interim storage of conditioned waste under continuous cooling and surveillance
- III. Waste disposal in deep geological formations

Immobilisation of HLW in borosilicate-based glass matrix is being practised using induction heated metallic melter in Trombay and Joule heated ceramic melter at Kalpakkam and Tarapur. An interim storage facility is fully operational for the storage of vitrified high-level waste overpacks for thirty years or even more. Nationwide

screening of potential regions and evaluation of rock mass characteristics is in progress for a geological repository program. [9]

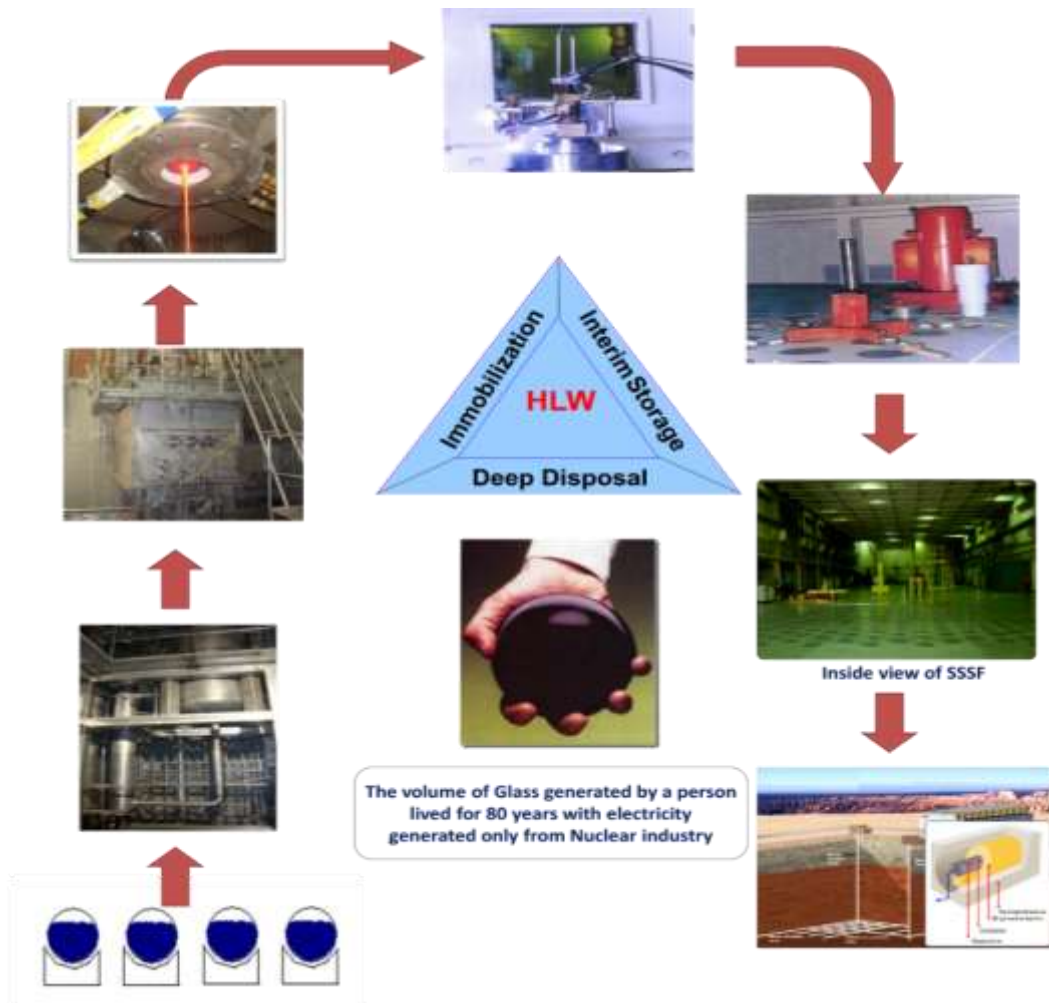


**Figure 1.4:** Indian strategy for waste management

### 1.1.5 Necessity for Immobilisation of High Level Waste

The rationale behind the immobilisation of radioactive waste materials in glass or ceramic hosts is to provide a solid, stable, and durable material that can be more easily stored, transported or disposed of than the liquid wastes. As an interim measure, HLW is stored in high integrity, large capacity stainless steel tanks. These tanks are equipped with cooling facilities for removal of decay heat and are kept under surveillance. However, given the acidic environment and heat generation because of associated radioactivity, the possibility of failure of storage tanks cannot be ruled out.

Consequently, it is essential to provide stand-by tanks for accidental or unexpected tank failures. Also, the volume of liquid waste to be stored increases with increasing production of nuclear power and the subsequent fuel reprocessing. Storage of HLW in liquid form can therefore at best can only be a temporary measure and its conversion into a suitable solid form as soon as possible, offers a distinct advantage in handling, transport, storage and ultimate disposal.

Immobilisation of the radioactive waste can be accomplished either by the dissolution of the waste elements on an atomic scale within a suitable host lattice or by encapsulation of the waste within an inert matrix as shown in Figure 1.5. Waste forms

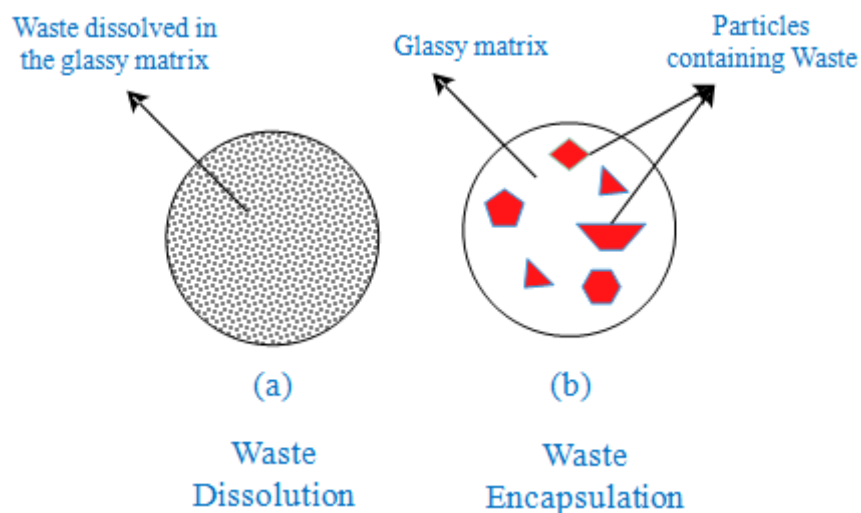


**Figure 1.5:** Immobilization of waste - dissolution vs encapsulation

can then be temporarily stored at the solidification plants (during which the heat generated by the decay of the fission products decreases). However, the long term strategy has to be their permanent disposal in an underground repository as part of a multi-barrier approach.

The selection of matrix for conditioning of any specific waste stream also depends upon the type of fuel, its history in the reactor including burn-up, the process used for

reprocessing of spent fuel and off-reactor cooling period. The characteristics of the waste, the container, repository, and the surrounding geosphere also influence the selection of the matrix. The criteria for selection of matrix for HLW immobilisation is also based on characteristics like chemical durability, thermal conductivity, radiation stability, and mechanical strength of the host material. It is also essential that the final waste product has minimum possible volume.

#### **1.1.6 Vitrification of HLW**

Glass is the material of choice for immobilising the potentially hazardous radionuclide in HLW. Vitrification of HLW has received the most considerable attention worldwide compared to any other HLW solidification process. Vitrification is the process of converting radioactive liquid waste into glass. Vitrification of radioactive waste is a desirable process as hazardous, radioactive waste constituent become bound within the molecular structure of glass, creating a substance resistant to aqueous corrosion and suitable for safe long-term geological disposal. Vitrification is conceptually attractive because of the flexibility of the process in treating a wide variety of waste streams and contaminants. Glass is an inorganic product of fusion (in the present context) which has been cooled under rigid conditions of temperatures without crystallisation. It is rigid, non-crystalline (amorphous) material. A schematic diagram, representing the formation of crystalline and amorphous material as a function of cooling rate is shown in the Figure 1.6.

Glass is often composed of constituents such as oxides of silicon, boron, aluminium, alkali and alkaline earth metals. Vitrification has significant advantages over other methods of waste management. The primary advantage is the durable and low leach waste glass product it produces.

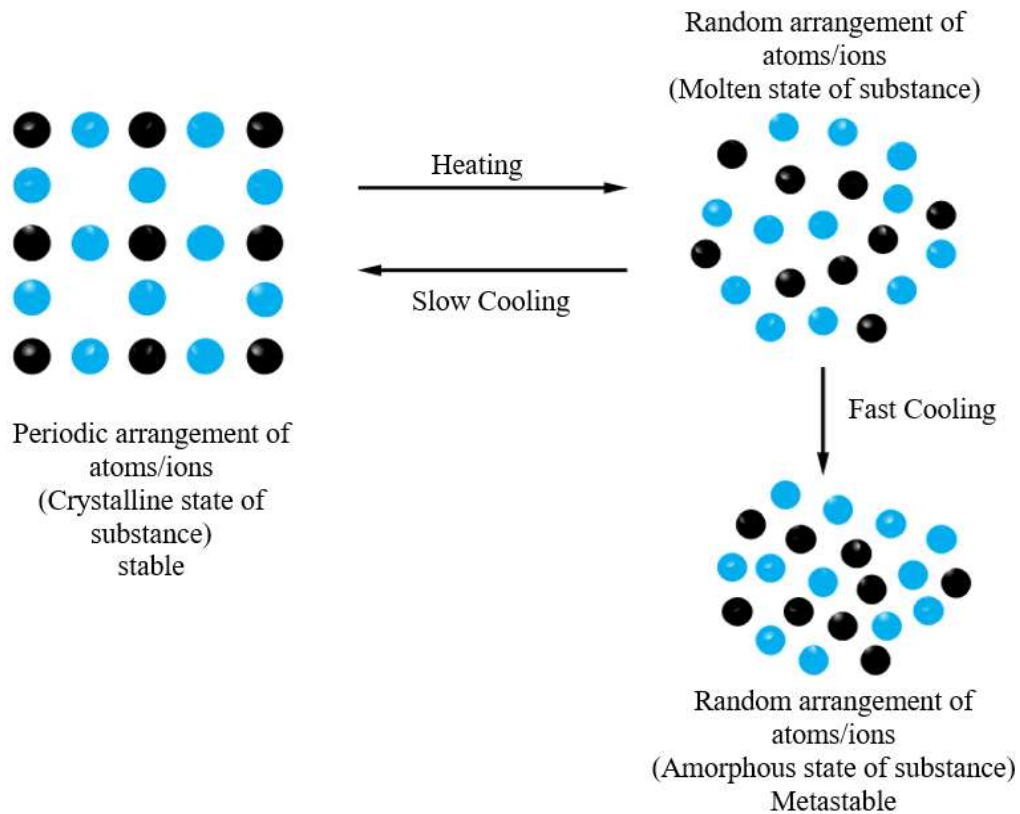


**Figure 1.6:** Formation of crystalline and amorphous material

The second advantage is the flexibility of the waste glass in incorporating a wide variety of contaminants and accompanying feed material in its structure without a significant decrease in quality. The third advantage is that the vitrification process can accommodate both inorganic and organic contaminants of different amounts. Lastly, vitrification significantly reduces the volume of waste material that needs disposal in a geological repository. However, it is an energy-intensive process, and some contaminants can volatilise. Many of these issues can be addressed amicably by suitable modifications in the process parameters. Some of the other factors that make glass one of the leading candidate matrix for immobilisation of the HLW are listed below

- Good thermal and radiation stability
- Highly corrosion resistant
- Well established manufacturing technology

- Inexpensive raw materials

Glass compositions to be used for immobilisation of HLW must be chemically stable for at least  $5 \times 10^3$  years to satisfy regulatory nuclide release limits [3]. High-level waste glasses must be able to prevent radionuclides from entering into the human environment. The solution chemistry of glass leach rate is a direct function of the glass composition. The structural resistance offered by the borosilicate glass matrix is primarily responsible for restricting the radionuclide transport in the aqueous environment [10].

Vitrification is attractive as a waste treatment process mainly because of the properties of the glass. These properties give vitrification high-quality product and flexibility in constituent proportion. To understand the advantages of vitrification as a waste treatment process, an understanding of the properties of the glass is of fundamental importance. A summary of various aspects of the glass structure is presented. An effort has also been made to discuss how this structure relates to the durability of vitrified waste product (VWP) containing hazardous waste.

#### **1.1.6.1 Glass structure**

The open random structure of glass is primarily responsible for achieving high waste loading and chemical durability. The radionuclides from the nuclear wastes are restrained in glass through primary or secondary bonding with the silicate network or both.

According to Zachariasens' view of atomic arrangement, the oxides involved in the glass formations can be categorised as glass formers, modifiers and intermediates [10]. Glass former is most essential component, without which glass network cannot be formed.  $\text{SiO}_2$  and  $\text{B}_2\text{O}_3$  are two important glass forming oxides. Modifier alone cannot

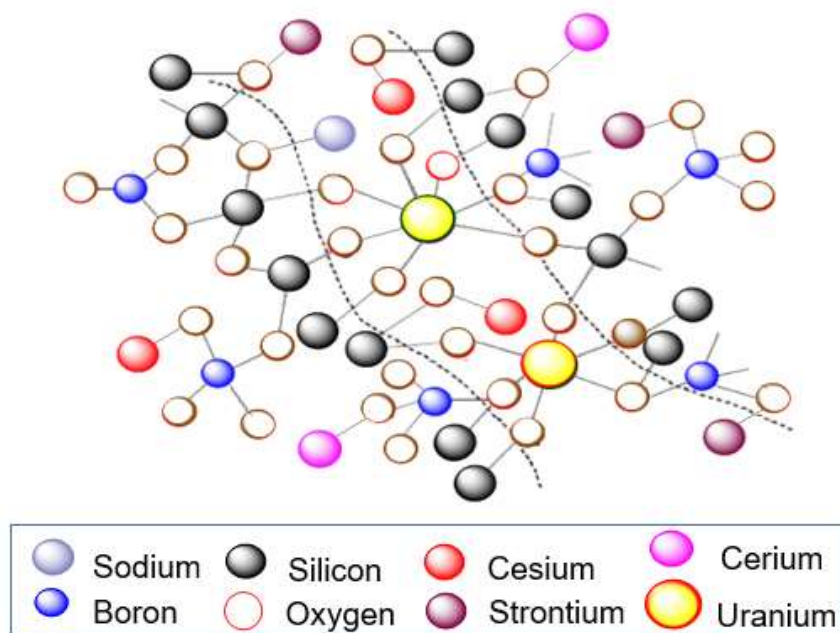


**Figure 1.7:** Random network structure of the vitrified waste product

form the glass but they are incorporated into glass structure to tailor the physical properties of glass. They convert non bridging oxygen of glass network into bridging oxygen atom thereby opening of the structure. The glass network, thus, achieves lower formation temperature and reduced viscosity. Oxides of alkali and alkaline earth metals invariably act as modifier.  $\text{Na}_2\text{O}$  is the major modifier used in the glass to bring down the viscosity. Though, many of transition elements and lanthanides present in the waste do not form glass independently, they participate in network formation unlike modifiers. These are called intermediates and are added to the matrix to fine tune the desired properties. Hazardous constituents of waste can be immobilised in the vitrification process either by primary interaction with the glass matrix (as network former) or chemical bonding (network modifier) or encapsulation, as shown in Figure 1.7. Certain waste constituents can be immobilised by chemical bonding with the glass forming materials, mainly silica present in the wastes to be vitrified. The most notable chemical bonding within vitrified materials occurs when waste constituents bond covalently with

the oxygen atoms in a silica network and become part of the network. Waste constituents like U, Fe, Al that interact in this way behave like network formers since they replace silica in the glass network structure. Other waste constituents can bond chemically with oxygen or other elements in the glass network. This ionic bonding incorporates the material into the glass but disrupts the network continuity, thereby modifying the physical and chemical properties of the vitrified materials.

A hazardous waste constituent may also be immobilised without direct chemical interaction with the glass network. Since vitrification constitutes a molten phase during some portion of the process, materials that do not interact chemically or have not completely entered into the solution are surrounded by a layer of vitrified material and thus get encapsulated, as the melt cools. This layer of vitrified material protects the encapsulated constituents from chemical attack. This structural characteristic of the glass providing three routes for immobilisation of waste constituents makes vitrification as the focal point of immobilisation of high-level radioactive waste around the world.

### **1.1.7 Types of Glass Used for Vitrification**

Two types of glasses are widely used for vitrification of nuclear wastes, the phosphate glass and the borosilicate glass.

#### **1.1.7.1 Phosphate Glass**

Interest in phosphate glasses was high during the early immobilisation studies, due to the relatively low formation temperatures required, coupled with the high solubility of sulphates and metal oxides. Sulphates are incompatible with borosilicate glasses as they cause phase separation, leading to a decrease in the durability of the product glass due to the formation of a soluble phase. Also, the solubility of actinide oxides in phosphate glasses is significantly higher than their borosilicate equivalents. However, interest in

phosphate glasses quickly declined due to a combination of factors. These included the inferior chemical durability of the early compositions coupled with their low thermal stability (de-vitrification at a relatively low temperature of around 673 K). Besides, phosphate melts usually are highly corrosive, significantly more than their silicate equivalents, and this is a factor that severely limits melter lifetime. Improvements in reprocessing flowsheet eliminated the generation of sulphate bearing HLW.

#### **1.1.7.2 Borosilicate Glass**

Silicate glasses have long been the preferred waste form for the immobilisation of HLW. This is because they readily dissolve a wide range of waste compositions and can be easily modified to optimise their properties. Also, they form the basis of the commercial glass industry and have been studied extensively for many years. They are, therefore, well characterised and their properties are well known and understood. Ideally, the most durable waste form would be vitreous silica, but this material requires very high processing temperature. Commercial glass compositions, therefore, respect a compromise between glass durability, processing ability and economics. Boric oxide is most commonly employed to lower the processing temperatures required for glass formation and workability while maintaining excellent durability within given composition ranges.

The selection was based on the flexibility of borosilicate glass with regards to waste loading and the ability to incorporate many different kinds of waste elements, coupled with excellent glass-forming ability, chemical durability, mechanical integrity, and excellent thermal and radiation stability. Based on the above detailed studies, borosilicate glass is presently the only nuclear waste form that is being produced on a plant scale. Over five hundred tonnes of highly radioactive glass have been produced

from high level radioactive liquid waste in France and Germany [11]. In India too, borosilicate-based glass matrix has been adopted for vitrification of HLW[12].

### **1.1.8 Processing of vitreous waste forms**

The primary aim of this conditioning process is to convert the HLW into an inert matrix such as glass with the help of certain additives. Hence the steps involved in the process are evaporation, denitration, calcination, the addition of glass former and modifier and finally the preparation of glass. Vitrification adopting borosilicate matrix with a minor variation of glass modifier composition on account of different waste characteristics is now an acceptable technology being pursued by many countries. Both batch and continuous processes are used for vitrification Figure 1.8 shows a typical flowchart for producing glass waste form.

In the world practice of industrial vitrification of HLW solution, two methods have been mastered. [7], [13]

- i. One step method in a ceramic electric furnace (JHCM)
- ii. Multi-step method with separate steps of evaporation, drying, and calcination-melting.

#### **1.1.8.1 Single step process**

In the single-step concept, evaporation, calcination and vitrification processes take place in a melter housed in concrete shielded hot cell. In this process, the HLW is directly fed into the melter. The off-gases generated due to the evaporation and subsequent calcination of HLW is passed through an elaborate off-gas cleaning system.

The single-step process is adopted by USA (Savannah River, West Valley, and Hanford sites), Germany, Belgium, India, former USSR, and Japan.

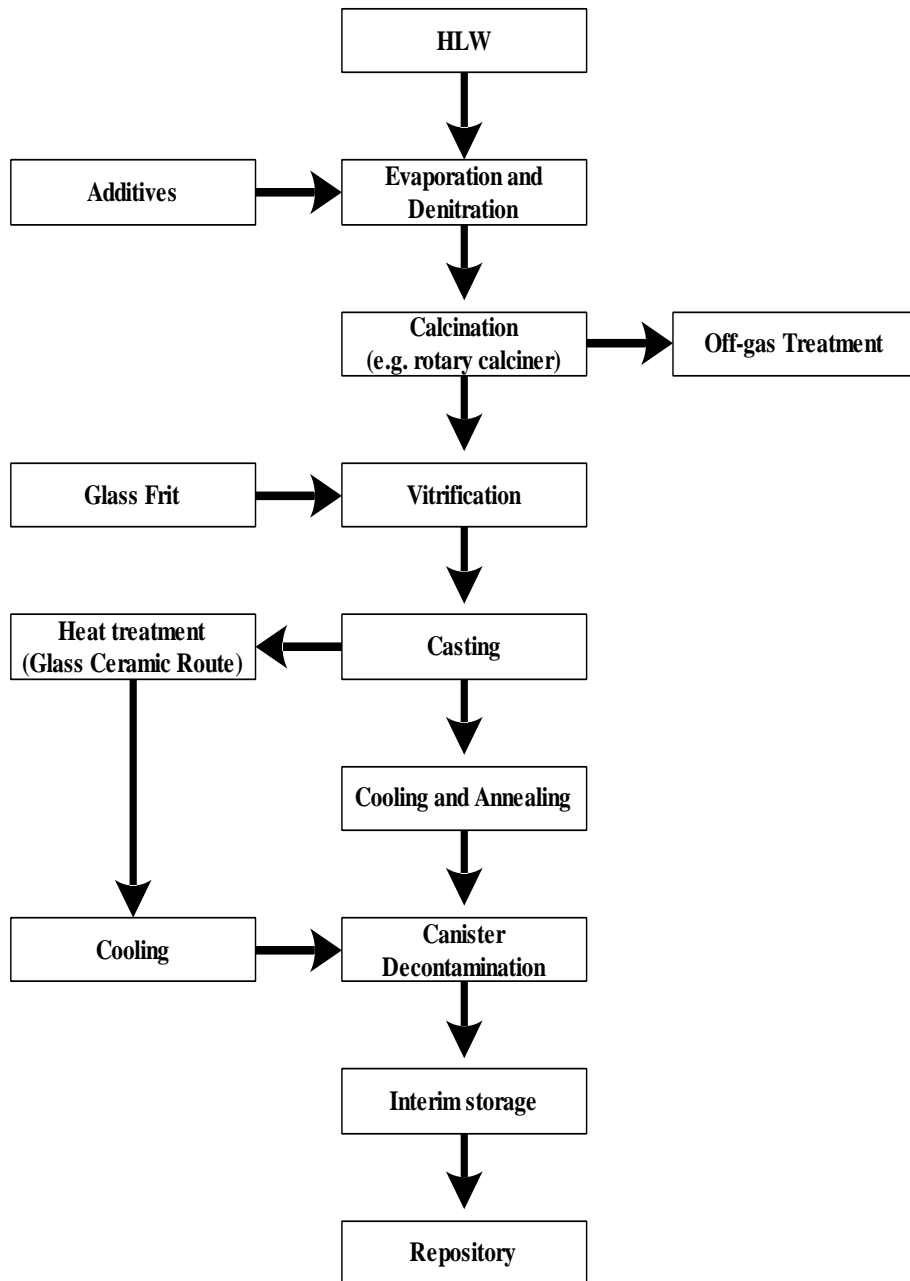


**Figure 1.8:** Typical flowchart for producing glass waste form

### 1.1.8.2 Two Step Process:

In the two-step process, the initial steps of evaporation and calcination are carried out in different equipment like rotary calciner, fluidised bed calciner, etc., followed by vitrification in metallic melter/joule melter. The two-step process is employed by France (La Hague and R7-T7 facilities) and UK (Sellafield) using a rotary calciner followed by metallic melter Mehta et al., (2008) and Baehr, (1989)[14][7]. A schematic of the French AVM process, which follows the two-step vitrification process is shown in Figure 1.9[15]. The AVM process consists of a combination of a rotary kiln and an induction-heated metal glass-melting crucible. The high-level fission product solution is fed with calcining additives into the upper end of the calciner. A slightly inclined tubular kiln which rotates at a speed of 30 revolutions per minute (rpm). The kiln is supported at each end by roller bearings. Special gas-tight seals are located at each end, allowing longitudinal expansion and maintenance of tightness. A rabble bar inside the kiln is designed to avoid possible caking. The tube is heated externally by an electric resistance furnace divided into four zones. The first two zones devoted to the

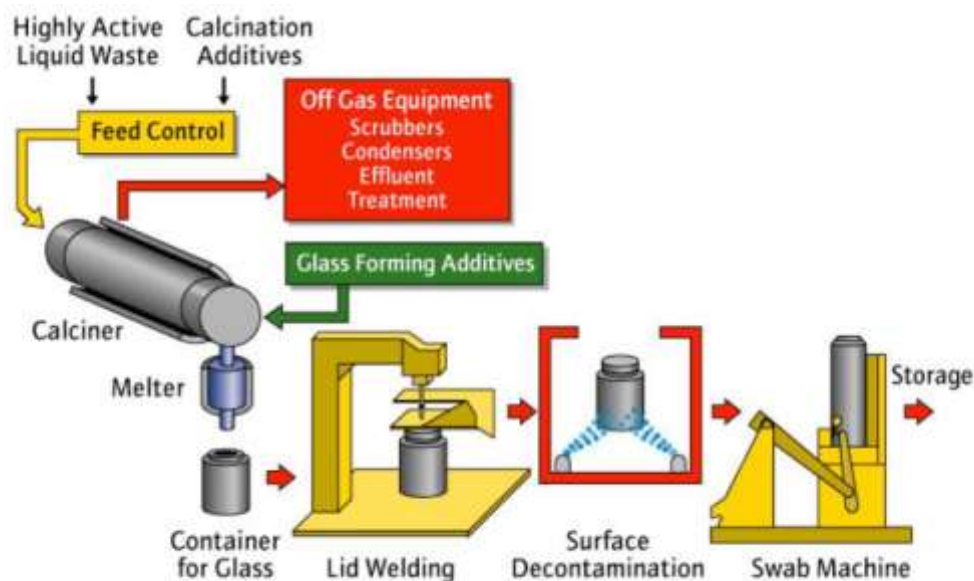


**Figure 1.9:** Schematic of the HLW Vitrification Process in French AVM [16]

evaporation have a heating capacity of 20 kW each and the others 10 kilowatts each. The temperature varies from 498 K at the feed point to a maximum of 873K [7].

## 1.1.9 Vitrification Equipment

### 1.1.9.1 Induction Heated Metallic Melter

The metallic melter is a multi-zone induction furnace. The assembly consists of a process pot, susceptor, induction coils and thermal insulation. Schematic of the metallic melter is shown in Figure 1.10.

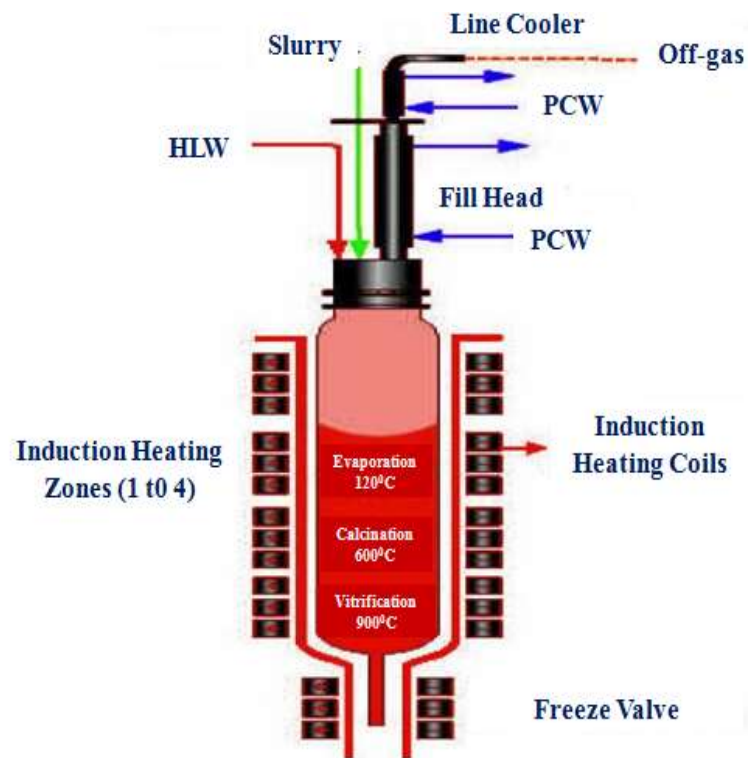


**Figure 1.10:** Metallic Melter

Process pot is the main reaction vessel where all processing steps takes place. The susceptor is a secondary containment which is heated by the furnace coils. These coils are divided into four main heating zones for better process control. There is a separate heating zone named freeze valve for draining molten glass into stainless steel canister. Process-pot and susceptor are made of high nickel chromium alloy to withstand high

processing temperature and corrosive process conditions. The essential processing steps taking place within the processing pot are, feeding of HLW & glass slurry, evaporation, calcination, melt formation, soaking, and draining.

Feeding of HLW and glass forming additives in the form of a slurry, at a pre-determined rate, is started after process pot. Feeding is continued till the solids, i.e. calcined cake, builds up to a pre-determined level indicated by temperature (873 K). The calcined mass is then fused to form glass. This mass is soaked for 6-8 hours to achieve homogeneity. VWP is drained into a stainless steel canister positioned under the processing pot. After the requisite amount of VWP is drained, the freeze valve is de-energised, and air-cooling is started. The main advantages of metallic melters are low costs and simple handling. The disadvantage is that the throughput capacity is limited to 30 to 40 litres per hour [16].

#### **1.1.9.2 Joule Heated Ceramic Melter (JHCM)**

The glass melter is heated to a maximum temperature of approx. 1273 K by the Joule principle. Application of an alternating voltage (50 Hz) between two or more paired, opposite metal power electrodes embedded in the wall causes a three-dimensional electrical potential field to develop in the glass melt and the pool areas immediately around it as shown in Figure 1.11. The local release of energy is determined by the prevailing intensity of the electric field and the local electric resistivity of the material [17].

The total power is the total of all local contributions to this power level. The electrical resistivity of the ceramic structure is approximately two orders of magnitude higher than that of the glass melt. As a consequence, the energy released outside the melt is

negligible. General levels of electric resistivity of the melt are between 4 to 20  $\Omega$ -cm, depending on the temperature.

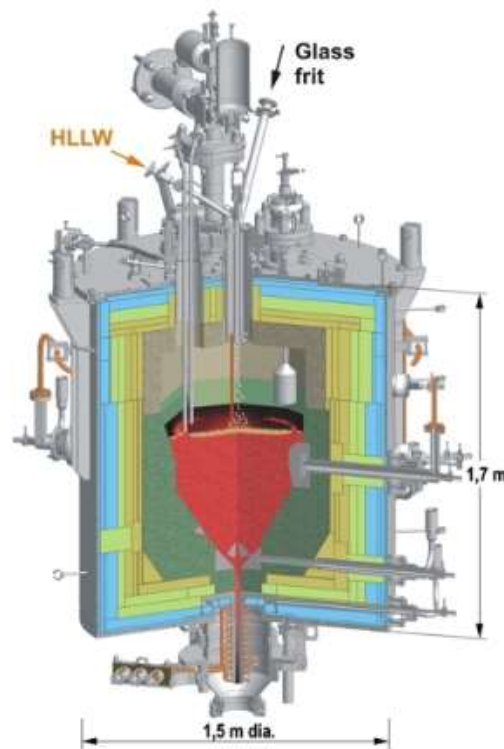


**Figure 1.11:** Joule Heated Ceramic Melter [18]

The electrode material is a high-temperature resistant chrome-nickel alloy (Ni > 58%, Cr 27-31%) commercially available under the trade name of Inconel 690<sup>®</sup>. The melting temperature of this alloy is around 1638 K. At temperatures above 1373 K, materials wear increases markedly [17]. For sufficiently long service life, the electrodes are kept at a glass contact temperature of 1273 K using air cooling.

The number and arrangement of electrodes in the melt tank are the result of criteria, such as the highest possible energy release in the glass pool, pronounced thermal convection for homogeneous mixing of the melt, and sufficient energy transport to the process zone on the surface of the molten pool, which requires large amount of energy (evaporation, melting). The melt is heated at a constant electric current. This type of power supply helps to limit the power transferred to the melt in case of excessive

temperatures of the molten pool because of the electric resistivity decreasing with temperature; in this way, temperature peaks are avoided [17]. This approach also ensures that the permissible power density load of the electrode surfaces will not be exceeded. Ceramic melters are directly heated by submerged power electrodes and hence can achieve throughput capacity of HLW greater than 100 lph. However, the ceramic melter process is so far characterized by high costs and comparatively complex remote handling operations. A list of JHCM that are being/have been operated all around the world is given in Table 1.6.

**Table 1.6:** Joule Heated Ceramic Melters

<b>Facility</b>	<b>Waste Type</b>	<b>Melting Process</b>	<b>Operational Period</b>	<b>VWP Produced</b>
<b>DWPF, Savannah River, USA</b>	HLLW	JHCM	Since 1990	1500 tons
<b>VWDP, West Valley, USA</b>	HLLW	JHCM	Since 1990	120 tons
<b>Mayak, Russia</b>	HLLW	JHCM	1987-1988	160 tons
			1991-1995	1200 tons
<b>PAMELA, Mol, Belgium</b>	HLLW	JHCM	1985-1991	64 tons
<b>India</b>	HLW	JHCM	2006	>100 tons
<b>Tokai, Japan</b>	HLLW	JHCM	Since 1995	> 100 tons
<b>WTP, Hanford,</b>	LAW	JHCM	Since 2005	

### **1.1.9.3 Cold Crucible Induction Melter (CCIM)**

In cold crucible induction glass melting, glass is directly heated by electromagnetic induction by employing a segmented crucible which is manufactured from continuous segments forming a cylindrical volume but separated by a thin layer of electrically insulating material [18]. An inductor surrounding the segmented crucible induces eddy

currents in each segment creating an electromagnetic field inside the crucible. Such an arrangement, as shown schematically in Figure 1.12, is equivalent to two air-cored transformers one formed by the induction coil and the crucible segments and the second formed between the segments and the charge. Thus, the segmented crucible acts as a field concentrator, indirectly reducing the gap between the induction coil and the charge. Direct heating of glass facilitates heating the process material to high temperatures.

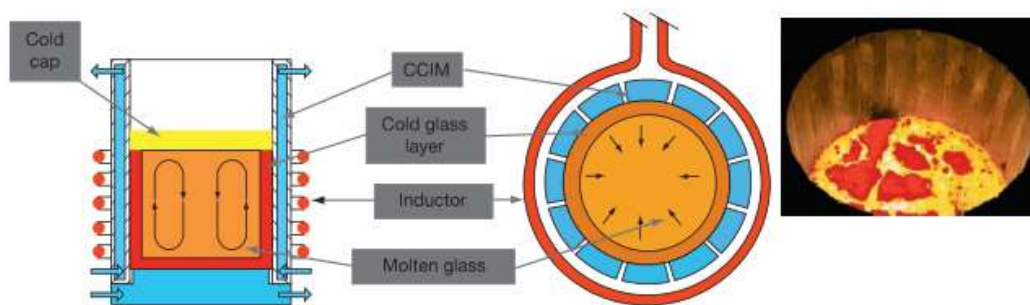


**Figure 1.12:** Cold Crucible Induction Melter

To avoid high-temperature glass corrosion of the metallic crucible, internal cooling of the segments is provided. This cooling produces a solidified glass layer, which acts as a protection against glass corrosion along the inner wall of the melter. High-temperature availability without substantial corrosion of the melter makes the CCIM a promising technology for immobilisation of HLW.

In this melter, there is no physical cavity for holding radioactive waste. The crucible/cavity is formed by cooling the outer surface of the melting charge with water. Hence, the name 'Cold Crucible'. It is similar to a metallic melter where glass is fed instead of having a susceptor pot. As glass is non-conductive at low temperatures, flexible and conductive graphite ring is used for a start-up operation. Major drawbacks

of Cold Crucible Induction Melter are its low energy efficiency and off-gas treatment system.

#### **1.1.9.4 Desirable Characteristics of Vitrification Equipment**

From the analysis of vitrification experience in the world, the recommendations on the superior design of vitrification equipment are as follows [13]:

- i. It should be a ceramic melter (JHCM)
- ii. The furnace should be small size, to make possible its evacuation to the radioactive waste repository after exhaustion of service life
- iii. The furnace bath should be one zone
- iv. The bottom discharge valve should be a cut-off valve

Considering the above facts, JHCM is the only viable option currently practised across the globe. Understanding the phenomena in JHCM plays a vital role in the safe management of radioactive waste in the nuclear fuel cycle.

#### **1.1.10 Alternate Waste Forms**

In addition to the above, various product forms such as glass ceramics, metal matrix and ceramic products have been developed. Glass ceramics are obtained by controlled crystallisation of the desired phases in the bulk glass. In metal matrix, for example, vitromet, base glass product is embedded in a metal matrix like lead to enhance the thermal conductivity of the final product. The ceramic matrix formulations, for example, Synroc, are prepared under high pressure and temperature conditions. Synroc is a titanate-based ceramic consisting of zirconolite ( $\text{CaZrTi}_2\text{O}_7$ ), hollandite ( $\text{BaAl}_2\text{Ti}_6\text{O}_{16}$ ), perovskite ( $\text{CaTiO}_3$ ) and titanium oxides ( $\text{T}_{1n}\text{O}_{2n-1}$ ) together with minor alloy phases. It is prepared by hot pressing a calcine of the precursor titanates plus waste solution at 21 MPa and temperatures between 1423 to 1473 K to obtain a dense material with less than

0.5 % porosity. Sodium Zirconium Phosphate (NZP) has been of interest because of its fast ion-transport properties. Wide variation in the composition of this structure has led the researchers to prepared NZP as a single phase ceramic waste form [3], [19]. NZPs were prepared by standard Sol-Gel and sintering techniques with waste loading varying from 10-30 wt %. The final products were checked for their desirable properties. Studies are being pursued by various researchers to see the feasibility of using NZP as a waste form.

## **1.2 Organisation of the Thesis**

The thesis is divided into six chapters, inclusive of the present chapter. The essential features of each chapter are described below.

**Chapter 1** gives a general introduction to waste management and detailed review of waste forms and equipment used for producing such waste forms. The importance of JHCM in vitrification technology is discussed. It explains the vitrification process and the different phenomena associated with it. The significance of the cold cap in JHCM equipment is described.

**Chapter 2** reviews the literature about the problems considered in the present work, along with the aim and scope of the study.

**Chapter 3** describes in detail, the experimental procedures adopted in the study. Equipment and other associated accessories used in the experiments are described.

**Chapter 4** discusses the assumptions made, and the development of the model. The governing equations for all the multiphysics associated with the system are presented in this chapter.

**Chapter 5** deals with the determination of the thermo-physical physical properties of glass. The viscosity, density, and resistivity of the glass loaded with 22 % waste oxide

were determined. A 3D model of JHCM was developed and validated with the experimental data. The kinetics of the reactions taking place in the cold cap was determined using thermogravimetric analysis and integrated into the model. The validated model was used for the design refinement studies of JHCM. The energy apportionment of different processes is also discussed in this chapter. This chapter also includes the important results of heat transfer characteristics in JHCM.

**Chapter 6** gives broad conclusions derived from these studies. The limitations of the present study and the future directions of the research are presented.

### **1.3 Closure**

In this chapter, a brief background of the problems considered in the present study has been given. Broad outlines of the thesis and salient features of the respective chapters have also been highlighted.

# CHAPTER-2

## REVIEW OF LITERATURE

## CHAPTER-2

---

### 2 REVIEW OF LITERATURE

Electric glass melting has been used industrially for over a century. An electric melting furnace was patented by Sauvegeon in France in 1907 and run first by Raeder in Norway from 1920 to 1925 and subsequently by Cornelius in Sweden in 1925 [20], [21]. Joule Heated Ceramic Melter (JHCM) is an electric melter used for vitrification of radioactive waste, in which glass is contained in the cavity of Alumina-Zirconia-Silica (AZS) refractory. The AZS refractory is backed by composite refractory materials having desirable thermal and electrical properties. The glass starts conducting electricity only at temperatures above 923 K. The resistance of the molten glass between a pair of Inconel 690<sup>®</sup> electrodes placed on opposite faces of JHCM is made use of for Joule Heating. The HLW is fed from the top at a rate determined by its composition and melter design. The quality of the VWP is greatly affected by the process parameters of the melter. To produce a high-quality product which is suitable for long term storage, a proper understanding of the parameters and their effect on the final product is very much crucial. Due to the high cost involved in the construction of melters and its non-modular design, it is difficult to vary the process parameters of an industrial melter for studying their effect on the quality of the VWP produced. The data generated on a small laboratory scale melter may not be truly representative, because of the complexities associated with scaling up. Mathematical modelling of the melter is highly effective in understanding the effects of change of process parameters, facilitating scale up of laboratory data and optimal design of a melter to meet the specifications of throughput and product quality.

As molten glass is an ionic conductor, electric melting is made possible by electric power dissipation within the melt. The heat thus produced is delivered to the cold cap, where the HLW is converted to glass, predominantly by calcination reactions [22]. The nature of the processes taking place in JHCM is complex and involves interactions between electric, thermal and flow fields. Besides, these interactions take place through strong temperature dependent glass properties, natural convection, advection, diffusion and volumetrically distributed Joule heating sources. Also, the cold feed on top of the heated glass destabilises the flow field and develops unsteady asymmetric flow motions underneath. Thus waste glass modelling requires solving a full 3-D, unsteady, momentum, energy and electric equation with temperature dependent glass properties [23].

## **2.1 Glass Melting Process**

Physical and transport properties of solid glass and glass melts are crucial for a better understanding of the temperature dependence of the industrial glass melting process. Ehrt and Flügel carried out studies on pretreated glass samples annealed to room temperature at a constant rate, to determine properties like electrical conductivity and viscosities of glasses of four different compositions [24].

Mainly borosilicate glass and phosphate glasses are used for conditioning of HLW. Among the two, borosilicate glass matrix has found wide acceptance for immobilisation of HLW [25]. Any glass formation proposed is subjected to detailed characterisation to ascertain its suitability for the given application. The properties estimated includes pouring temperature, molten glass viscosity, electrical resistivity, glass transition temperature, time-temperature transformation, and thermal conductivity.

### 2.1.1 Determination of rate kinetics

Typically, vitrification is carried out at temperatures of 1223–1523 K, depending upon the composition of base glass and characteristics of RLW. In the vitrification process,

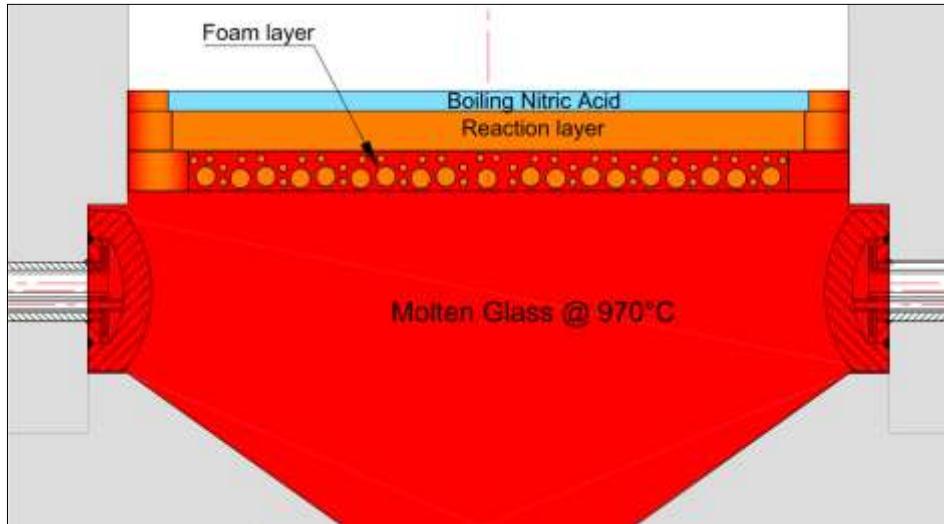


**Figure 2.1:** Schematic of Cold Cap

RLW is fed on to the top of the molten glass pool contained in JHCM. The working volume of the melter is divided into four zones and are shown in Figure 2.1[26].

Determination of heat and mass transfer rate is necessary for rational design and sizing of a melter. In order to obtain an assured product quality, knowledge of thermal decomposition reaction kinetics of waste constituents is essential [27]. In a continuously fed glass melter, RLW processing rate is controlled by the rate of heat transfer from molten glass to the cold cap and by the kinetics of various chemical reactions and phase transitions within the cold cap [28].

An understanding of thermal decomposition of the waste constituents is necessary to understand the series of phenomena occurring in cold cap. Though literature about interactions of RLW constituents with base glass in cold cap region is available, not many studies investigating the effect of different glass compositions on the physicochemical reactions taking place in the cold cap are available.

Kinetics of the reactions in a vitrification equipment of a representative waste glass feed were determined using both simultaneous thermal analysis (STA): DSC (Differential scanning calorimetry) - Thermogravimetric analysis (TGA) and thermogravimetry coupled with gas chromatography-mass spectrometer (MS) (TGA-GC-MS) as a complementary tool for performing evolved gas analysis (EGA) [29]. The results of DSC-TGA and EGA on the cold-cap reactions provide essential information for developing an advanced cold-cap model.

An iso-conversional method based on the thermal studies (TGA or DSC) at different heating rates to determine the rate kinetics of solid state reactions was reported in literature [30], [31]. Vyazovkin, (2001) & Pérez-Maqueda et al., (2011) provided guidelines for the evaluation of kinetic parameters such as activation energy, pre-exponential factor and the reaction order from the data obtained using Thermogravimetry (TG), DSC and Differential Thermal Analysis (DTA)[32], [33]. Vyazovkin, (2013) analysed the reaction kinetics using an advanced iso-conversional method for estimating activation energy [34].

Kissinger method is widely used in literature for determining the reaction kinetics of molten glass with radioactive waste constituents [35]. In the present study, the reaction kinetics were determined using the Kissinger method by carrying out TG of major constituents of sRLW. Activation energy, pre-exponential factor and order of the reaction for the decomposition of waste nitrates and oxides in RLW to VWP are estimated based on TG - Differential Thermogravimetry (DTG) analysis.

### **2.1.2 Effect of Design Parameters**

The melter mixing efficiency depends on the interactions between glass temperature, velocity and electric field in the melt pool. These interactions are governed primarily

by design parameters such as melter dimension and electrode locations and secondarily by the operating parameters such as heater power, power skewing and melt rate.

In a typical JHCM used for the treatment of RLW, the energy balance is

Joule Heat + Decay heat = Melting energy + skin losses + jacket & electrode cooling losses

JHCM used in vitrification is powered by electrical systems. From this perspective, the glass melter can be considered as a large temperature – dependent resistor. The load power, load resistance, and their variations dictate the design of the system.

#### **2.1.2.1 Joule Heating**

The power requirement of a melter is proportional to its capacity. Alternating current is passed in the molten glass pool using the submerged electrodes. Heat is generated, which is related to the resistivity of glass, current density and geometry of the cavity [36].

$$Q_j = I^2 R_e = (J)^2 L_e W H_i / \sigma$$

Where  $Q_j$ , is joule heat in Joules,  $R_e$  is resistance in  $\Omega$ ,  $I$  is current in ampere (A),  $\sigma$  is the conductivity in S/m,  $J$  is the current density in  $A\ cm^{-2}$ , and  $L_e$ ,  $W$  and  $H_i$  are the length, width, and height of the glass pool respectively in metre. The geometry of the cavity is selected based on the design throughput. Typically a JHCM used in vitrification of RLW has a throughput of  $1\ kg.hr^{-1}$  -  $50\ kg.hr^{-1}$  with melter volumes of 100 litres – 2000 litres. The electrode current density is limited to  $0.5\ amp.cm^{-2}$  for Inconel 690.

#### **2.1.2.2 Melting Energy requirement**

The melting rates of glasses having different compositions have a broad variations, associated with chemical reactions of species present in nuclear waste. The melting flux

for a given glass depends on the type of glass frit, type of salts being processed and the thermal conductivity of the calcined mass. In JHCM, the heat generated is utilized for heating RLW to boiling point, supply latent heat of vaporization, decomposition of nitric acid, heating nitrates to calcination temperature, calcination reactions, heating of oxides to fusion temperature, and supplying sensible heat to preformed glass beads fed at room temperature used for vitrification to 1273 K [37].

#### **2.1.2.3 Skin losses**

A JHCM is a multilayered structure. The layers are designed in the sequence where glass corrosion resistance & thermal conductivity decreases from the inner to the outer layer. Heat is lost to the surroundings from the outer surface of the JHCM. The higher heat losses are desirable to extend the refractory life and reduce glass corrosion. Heat losses are compensated by pumping more current, which increases the electrode current density. The skin losses from the side, bottom and top of the melter were determined.

#### **2.1.2.4 Jacket & electrode cooling losses**

RLW feed lines and off gas lines are provided with cooling provision. Air cooling to the electrode is provided to extend the life of the electrode. The geometry of the electrode cooling and PCW cooling jackets are complex and are determined by measuring the inlet and outlet temperature of the cooling medium. However, there exists a correlation for the determination of the heat transfer coefficients based on the inlet flow measurements.

### **2.2 Experimental studies on JHCM**

The vitrification technology based on the liquid fed JHCM process has been in use since the 1970s. The process development activities involved engineering facilities for

carrying out tests with simulated waste. Pilot and industrial scale melters were operated to generate data required for developmental activities of JHCM.

Chapman (1976) conducted experiments on a pilot scale and measured the temperature at different locations [38]. Experiments were conducted in 0.36 meter wide, 0.76 meters long and 0.3-meter deep melter. Molybdenum electrodes were used for pumping current into molten glass, and sacrificial electrodes were used for pre-heating the glass.

Yoshioka et al., (1992) carried out trials in Tokai Vitrification Facility in a 1.9 m x 1.9 m x 2.3 m melter having a surface area of 0.66 m<sup>2</sup> and a glass pool volume of 350 litres [39]. This JHCM utilised ten numbers of SiC heaters for pre-heating the glass. The VWP produced during this operation was composed of 75 % glass additives and 25 % waste oxide. The waste oxide consisted of 10 % fission products, 10 % Na<sub>2</sub>O and 5% other added chemicals [39].

Roth et al., (1996) presented results of the melter operated in FZK, Germany having a melt rate of 4.5 kg/hr with a melt content of 150 litres in a melter having a size of 1.5 m diameter and 1.75 m height with the inclined bottom at 50° [40].

Polyakov et al., (1994) presented the experience of operating EP – 500 / 1R melter in Mayak, Russia. Phosphate glass was used for conditioning of the RLW having 5 – 40 Ci.L<sup>-1</sup> of a specific activity. Glass with 23 % Na<sub>2</sub>O, 18.4 % Al<sub>2</sub>O<sub>3</sub>, 52 % P<sub>2</sub>O<sub>5</sub>, and other fission and corrosion products about 8 % were produced. The melter had an operating capacity of 400 lit.hr<sup>-1</sup> and it conditioned solutions with salt content of 260 g.L<sup>-1</sup>[41].

Testing of melter with different waste compositions was carried out by Matlack et al., to evaluate the effect of salt concentration. Low activity waste (LAW) streams as a source of sodium in place of chemical additives, sugar or cellulose as a reducing agent, boehmite as an aluminum source were used in the study. The objective of the study was

to enhance the waste processing rate while meeting all processing and product quality requirements.

The work also included preparation and characterisation of crucible melts in support of subsequent DuraMelter 100 (DM 100) tests designed to examine the effects of enhanced glass formulations, glass processing temperature, incorporation of the LAW waste stream as a sodium source, type of organic reductant and feed solids content on waste processing rate and product quality. They also carried out a confirmatory test on the HLW Pilot Melter (DM 1200) with a composition selected from those tested on the DM-100. The detailed test report of the glass production rate with slurry feed containing 52.2 % of water was presented in the report [42].

The experimental studies carried out on melters were limited to determination of processing capacities. No studies were carried out on different stages of melter operation like warm up heating for removal of moisture and start-up heating to raise the temperature of the charged glass to conducting zone.

### **2.3 Review of Modelling on Commercial Glass Furnaces**

Glass furnace is an enclosure designed to form the glass from the feed materials by heating feedstock to high temperature and allowing sufficient residence time. Glass furnaces dimensions for higher capacity surface area typically varies from 60 – 120 m<sup>2</sup> and for smaller plants, the area varies from 0.4 – 20 m<sup>2</sup>. Based on the type of heating, the glass furnaces are classified as fossil fuel glass furnace and electrical glass furnace. In the commercial glass industry, heating is performed by flue gases, and energy equations are solved for plenum space, glass melt and refractory temperature. Electrical heating is preferred in case of quality control of glass melts. Most of the modelling

literature about melting was available for fuel-fired furnaces compared to the models on all-electric melters[43].

Curran, (1971, 1973) performed 2D modelling of glass furnaces with electrical heating studying the influence of electrode configuration in the glass melt [44], [45]. McConnell & Goodson, (1979) and Mase & Oda, (1980) performed two-dimensional analysis on glass furnaces[46], [47]. Patankar & Spalding, (1972) and Patankar et al., (1974) developed the basis of a computer model for 3D flows with combustion and subsequently demonstrated its application to the combustion chamber[48], [49]. Viskanta (1994) reviewed the three-dimensional mathematical modelling of commercial glass melters [50]. Despite the achievements in three-dimensional modelling, the simulations still depended on lab scale melters for their validation. The validity of the results was not substantiated by practical measurements [51]. The commercial industry uses experimental and numerical modelling techniques as a tool for melt intensification of existing furnaces and developing a new glass melting furnaces.

Hrma, (1982), Schill & Chmelar, (2004), Pokorný et al., (2012) developed 1D and 2D model for batch piles charged into the furnace[43], [52], [53]. In commercial glass melting, most recent advances have been in attempting modelling of processes that affect glass quality and production. These include gas bubble transport and melt rates, redox distribution and cording.

Choudhary et al., (2010) described the characteristic features of flow and heat transfer in each of the three processes of glass melting, delivery, and forming [54]. The relevant transport and constitutive equations and boundary conditions were summarised for industrial applications of the mathematical models for furnaces and forehearths, and

forming operations were illustrated. They also presented relevant details on sub-models for various auxiliary processes associated with the primary process of melting, delivery and forming (i.e., batch melting, electric boosting, bubbling, combustion, turbulence, and radiation and viscoelastic phenomena).

The mathematical models can be constructive in studying and predicting the physical and chemical processes taking place in the melters. The models are however limited to the prediction of the glass circulation patterns and temperature patterns in the melting glass, ignoring the effect of the cold cap on melter performance[55].

The numerical modelling studies on commercial glass furnaces provide a useful tool in analysis and synthesis, primarily when these models are supported by experimental or test data on an operating furnace.

#### **2.4 Modelling Approaches to JHCM**

During the vitrification process, a molten glass pool forms, above which a partially fused calcined mass of waste oxides and nitrates along with a pool of boiling liquid, collectively called cold cap, exists [56]. The maximum spread of cold cap is limited to 90 % of the molten glass pool surface area to avoid thermal shocks to the refractory. On the other hand, limiting the spread of the cold cap to values much less than 90 % will lead to volatilisation of radionuclides thereby reducing the decontamination factor (DF) of the JHCM [57]. The VWP produced during the operation of JHCM is evaluated for long term chemical durability, homogeneity and thermal stability.

Physical phenomena taking place in a JHCM are quite complex and interrelated [58], [59]. The heat transfer in the molten glass pool is governed by natural convection caused by the body forces generated by Joule heating [58], [60]. Two types of body forces prevail in an electrically conducting liquid pool under Joule heating. These are the

gravitational body force due to non-uniform temperature field and the electromagnetic body force due to the interaction between the self-induced magnetic field and moving charge carriers in the liquid [60]. Most mathematical models developed are limited to the prediction of glass circulation patterns and temperature profiles in the melting glass. The lack of information on chemical kinetics, the reaction in glass, chemical equilibria and solubility data represent a significant roadblock in accurate prediction of the behaviour of molten glass in JHCM [50].

Numerical analysis is expected to provide an insight into the inherent process limitations of the JHCM. CFD has been applied by some researches for modelling industrial JHCMs [59], [61]. The cold cap is the most significant region of the melter, as it is this region that determines the throughput, DF and conversion rates in the melter. However, due to the complexities associated with the cold cap, it is difficult to model and is often not considered in melter simulation [8].

Pokorny et al., (2015) developed one dimensional model of the cold cap on lab scale JHCM [64]. The simulated waste used by Pokorny & Hrma, (2012) for cold cap studies was based on  $\text{Al}(\text{OH})_3$ , which tends to high foaming [43].

Hardy, (1998) modelled JHCM as quasi-steady state process in the 3D model, in which cold cap modelling was not carried out explicitly [65]. Choudhary (1988) proposed a three-dimensional model to calculate flow and heat transfer in an all-electric melting of flint glass [61]. Uchida et al., (2008) simulated the behaviour of the molten glass using a 3D model using FLUENT 6.2 without considering a cold cap [63]. Viskanta, (1994) simulated flow and heat transfer process in commercial glass melting without a cold cap [50]. Sugilal et al. (2005) predicted convective behaviour in a JHCM [58]. In this model also cold cap behaviour was not considered. Giessler & Thess, (2009) carried out

a numerical simulation of glass melt in a small scale circular crucible, which was heated using vertical electrodes [66].

The estimation of the processing capacity of furnace includes the study of thermo-physical and kinetic properties viz., density, viscosity, thermal and electrical conductivity. The simulation of batch-to-glass conversion is considered as the most complicated part of the already intricate mathematical model of glass tank [53].

Development of an integrated model of JHCM is a collaborative effort of heat transfer, mass transfer, momentum transfer and electrical phenomena and incorporating all the observations from laboratory trials, pilot plant trials and industrial scale trials into the model framework [67]. The fundamental understanding of the heat transfer, reaction kinetics, electrical field and thermal convection in a JHCM can provide a detailed insight into the complete vitrification furnace. Convection currents are the primary means of mixing in a melter. The melter mixing efficiency depends on the interactions between glass temperature, velocity and electric field in the melt pool. Physical phenomena taking place in JHCM are quite complex and interrelated. The mathematical models on HLW melters can be categorized into three broad areas

1. Start-up heating models
2. Melt pool convection models
3. Cold cap models

## **2.5 Computer codes for JHCM Processing of Radioactive Waste**

Mathematical modelling of melters, both HLW and commercial, has reached a state where the fundamental processes of buoyancy-driven, highly viscous, flow and heat transfer in melt pools can be predicted with reasonable accuracy. Eyler (1996) compiled

information on modelling capabilities for the high-temperature melter and provided glass industries modelling capability review [62].

TEMPEST electric field solution methodology is one of the most sophisticated methods available for multi-electrode, multi-phase, arbitrary waveform solution and prediction of Joule heat distribution. TEMPEST stands for "Transient Energy-Momentum and Pressure Equations Solutions in Three Dimensions." It is a powerful tool for solving engineering problems in nuclear energy, waste processing, chemical processing and environmental restoration because it analyses and illustrates three dimensional time-dependent computational fluid dynamics and heat transfer analysis. Developed by researchers at the U.S. Department of Energy's Pacific Northwest Laboratory, TEMPEST was first made available for business and industrial use in 1983. Since then, researchers at the laboratory have been continuously upgrading the code to extend its capabilities further.

The configuration-controlled N-version, which is available to the public, can be used to analyse a broad range of coupled fluid dynamic and heat transfer systems in complex three-dimensional geometries. It includes a unique combination of code features and analysis capabilities.

The developmental T-version is a vital tool for investigators at the Pacific Northwest Laboratory, who use this version of TEMPEST in sponsored research for clients (it is not currently available to the public). It has all the capabilities of the N-version; moreover, it can also be used to solve problems involving joule heating with ac/dc electric fields and joule heating models, compressible flows, marine hydrodynamics with free wave surfaces, and multi-constituent transport in curvilinear coordinates.

The TEMPEST results were within a standard deviation of 17 other computer simulations of well defined, simplistic representation of a glass melter. Several other codes reported difficulty in convergence.

TEMPEST has been successfully applied to HLW melter at Hanford Laboratories. The modelling of joule melter requires coupling of flow, heat and mass transfer and an electric field solution model to calculate joule heating distributions. Boundary conditions appropriate to the cold cap and exterior of the melter system are required. Due to the cold cap and internal heating, the melt pool is physically unstable, necessitating the transient analysis of the system.

The melt pool convection model involves solving a system of transient momentum, energy, and electric equations with temperature dependent properties. Due to the hydrothermal instability at the top of the melter pool, a full 3D model is required to capture asymmetric thermal and flow profiles. At the interface between the melt pool and cold cap where hydrothermal stability can be exceeded, multiple velocity solutions can exist due to instability induced bifurcation.

The cold cap models developed were restricted to chemical reactions of vitrifying species in the cold cap region. However, modelling efforts on the hydrothermal process in the cold cap are far from being complete due to complexity of the underlying physical phenomenon. Nobel metal deposition problem is critical in the operation of melters used for treating high-level waste. The models include size distribution, particle tracking, amalgamation, settling velocity and deposit rate. Due to the limitation on in situ experiments that can be performed on a radioactive waste melter, application of modelling as an alternative to experiment is critical.

## 2.6 Modelling of start-up heating

JHCM are located in radioactive cells with the provision of radioactive confinement. The high radioactive field does not permit personnel entry into the cell, so the cell operations and maintenance are carried out remotely. Summary of different remote start-up techniques that were employed & studied in literature is provided in Table 2.1. As glass conducts electricity only above temperatures of 873 K, resistance heaters made up of Silicon Carbide (SiC) are provided for raising the temperature of the glass frits to conducting zone. On attaining temperature, sufficient for glass to conduct current, the Inconel electrodes are energized. The total power required, depend upon type of glass, geometry of melter, and heat losses from above and below plenum zone. These heaters are also used for start-up heating of JHCM which is done to remove the moisture present in the refractory and to heat the frozen glass during regular operation.

Different heat transfer mechanisms are involved during the start-up heating of the furnace, for example, transfer of heat from the resistance heater to refractory by radiation, transfer of heat from walls of the refractory to glass frit at the bottom by radiation and conduction. The heat from the cavity due to the ingress of the air, heat losses from the outer skin of the melter by conjugate heat transfer.

Power is supplied to plenum heater that heats the refractory blocks. The refractory blocks in turn transfer heat to glass frit by radiation and conduction. The apportionments of energy transferred by these modes to glass frit were not possible in industrial scale melter. In order to determine the energy apportionment, an experimental setup was devised to study the phenomenon of start-up heating.

**Table 2.1:** Summary of the detailed review of start-up heating of vitrification equipment

<b>Investigator</b>	<b>Type of start-up technique</b>	<b>Vitrification Equipment</b>	<b>Technique and limitation</b>
Chris C. Chapman, 1982	Sacrificial Electrodes	JHCM	A start-up electrodes with a resistance heating element between them is placed in a flange which fits in the cover plate of the melter. This assembly is lowered onto the mating opening on the melter shell. Handling the operations remotely, and failure of the lowering mechanism are crucial concerns.
Weisenburger S (1982)	MoSi <sub>2</sub> heating elements	JHCM	An external source of remote start up to achieve 1173 K in plenum walls 20 kW power input required. Thermal efficiency is less.
Hardy (1998)	Resistance heaters	JHCM	Electrical current only flows in the Pt alloy shell of the melter. Therefore, the heat source for the melter and plenum model is the electrical power dissipation in the platinum alloy vessel. Corrosion of vessel and shorting of electrodes over time are major concern
Erickson, C. J. and Haideri, A. Q. (1978)	Carborundum glow bar	JHCM	A vertical configuration of electrodes was used for heating the vapour space above the melter. An external source of remote start-up to achieve 1173 K in plenum walls. Thermal efficiency is less for the system.
Suneel et al., (2018)	SiC Heating Elements	JHCM	24 numbers of SiC resistance heaters with the total combined power of 48 kW were used for a start-up. Space optimization based on the length of plenum heater space was carried out. Reliable and good for remote start up but thermal efficiency is less.

Most of the available literature focuses on the heating of a cylinder with annular spaces. Although many numerical simulation studies were carried out by researchers addressing the parametrical effect such as temperature and pressure on the heating of coaxial cylinders, the scope for focused study on the influence of the air gap on the thermal efficiency of the start-up heating exists.

Two phenomena viz., convection and radiation in and on the surfaces of the melter occur during start-up heating. Natural convection in closed enclosures is often coupled with surface radiation heat from walls of the enclosures in transparent fluid media such as air. Heat transfer analysis in enclosures and extended surfaces has been the prime concern in the analysis of heat transfer in industrial applications [68]. Yoshioka et al., (1992) used heater units that had a conventional SiC resistance heater inside the Inconel jacket for their studies[39]. Numerical and Experimental studies were carried out by Barforoush and Saedodin (2015) to analyse the effect of a cylindrical radiation shield, with temperature-dependent emissivity within concentric cylindrical enclosures in reducing heat loss[69]. Their study also included the effect of material used as a shield, position of radiation shield and pressure inside the enclosure.

Sharma, Velusamy, Balaji, & Venkateshan, (2007) studied the turbulent natural convection coupled with surface radiation numerically, in enclosures containing air and heat from the bottom [70]. Teertstra & Yovanovich (1998) reviewed the available experimental data, numerical results, analytical models and correlations for heat transfer in a horizontal circular annulus and made a comparison between different models [71]. Torabi & Zhang (2013) introduced the differential transformation method (DTM) to derive analytical solutions for the non-linear, convective-radiative, straight fins, heat transfer problems[72]. Malik, Shah, & Khushnood, (2013) studied the Computational

Fluid Dynamics (CFD) analysis of conjugate heat transfer within a bottom heated, non-convectional cylindrical enclosure [73]. Kuznetsov & Sheremet, (2011) presented a numerical study of the conjugate natural convection in a rectangular enclosure, in the presence of a heat source with heat-generating core, by assuming non-uniform heat exchange with the environment [74]. Ghauri et al., (2011) investigated experimentally, the conjugate heat transfer within an air-filled, bottom-heated vertical enclosure[75]. Rahimi & Sabernaemi (2011) studied the effect of radiation and free convection from ceiling surface temperature to other internal surfaces [76]. Sene & Narasimham, (2011) presented a numerical analysis of conjugate natural convection and surface radiation in horizontal hexagonal sheath housing 19 numbers of solid heat generating rods with cladding and argon as the fill gas [77]. Roschina, Uvarov, & Osipov (2005) investigated the natural convection of gas between two horizontal coaxial cylinders with uniform internal heat generation[78].

The behaviour of the initial heating of the glass forming oxides which are accomplished with the help of Silicon-Carbide (SiC) heaters installed in the plenum region of the JHCM has been neglected. No mathematical models are available in the literature dealing with this aspect of melter operation, possibly because of the small start-up period. However, a study of initial start-up is of paramount importance for size optimisation of JHCM. The size optimisation of the JHCM assumes importance from the fact that smaller JHCM will be much easier to de-commission.

## **2.7 Modelling of Molten glass**

The preliminary models for simulating glass furnaces only solve power distribution and convective flow in an uncoupled way. Interestingly, some have worked on an electrical conducting problem to find out the current distribution in the system. Also, a

comparison technique between an open channel and a glass melt pool was used to predict the resistance across the electrodes by using a scale of model methods. In mathematical modelling of radioactive glass melter, a 3D transient model was solved, and the effect of a boundary condition in yielding dual velocity profiles was explained in the literature.

Ungan & Viskanta, (2008) has simulated flow and heat transfer process in commercial glass melting process[79]. Here, the momentum equation was solved by considering buoyancy-driven convection with Boussinque approximation considered as a momentum source. Effective thermal conductivity was mentioned in the energy balance equation comprising convective and diffusive terms and volumetric heat generation for expressing joule heating in addition to heat from the combustion chamber. 3D simulation using finite difference discretization equations were solved using a SIMPLER technique. The bubble generation during refining due to the presence of a redox pair and its effect on buoyancy was mentioned but not included in the numerical model. The report concluded that mathematical modelling supported by small scale laboratory test and data obtained from an operating glass melter could be used to obtain an understanding of complex glass melting process.

While studying the convective behaviour of glass melts Sugilal et al., (2005) had considered a general model in which gravitational body force resulted in buoyancy-driven natural convection, and self-induced electromagnetic body force resulted in magnetohydrodynamic flow [58]. In the models for electro-slag re-melting furnace, gravitational body force was neglected when compared to electromagnetic body force. On the other hand, electromagnetic body force was ignored in models for electric glass

melts. Physical properties of electrically conductive liquids strongly govern their convective behaviour under Joule heating.

Uchida et al., (2008) carried out studies on a JHCM using CFD coupled three-dimensional model. The electric field analysis was carried out using Fluent<sup>®</sup> Version 6.2 [63]. Buoyancy forces were considered based on Boussinque approximation in momentum balance equation. In the energy balance equation, asymmetrical electric current distribution due to the arrangement of electrodes was taken into account for estimation of Joule heat generation by electrical analysis. No cold cap was considered in the modelling.

Choudhary, (1988) carried out studies of flow and heat transfer in industrial glass melter[61]. A 3D mathematical model was used to calculate flow and heat transfer in electric melting. The results indicate that the electrode orientation has a significant effect on velocity and temperature distribution. The residence time distribution was also obtained by solving the transient response to a step change in the tracer concentration. Thermal buoyancy was considered for flow field, but the effect of gas bubbles on the flow field was not accounted for. Also, glass was assumed to be optically thick so that an effective thermal conductivity was used to represent the radiative heat transfer. The model used a finite difference technique as described by Patankar & Spalding, (1972) to solve differential equations governing electric field, momentum, and heat transfer [48]. The numerical technique control volume balance approach was used to derive the finite difference equations. A power-law scheme was used to compute the contribution of convection and diffusion terms in the finite difference equations. Melting down of the glass batch was not modelled rigorously. Instead, at the batch-glass interface, constant temperature and a uniform melting rate were specified as a boundary condition.

In CFD modelling of Westinghouse Savannah River Company (WSRC) Am/Cm melter, [65] used CFX finite volume code to solve coupled momentum and energy conversion equation in three dimensions. The melter was modelled as a quasi-steady process in which glass level was constant and cold cap experienced a steady rate of evaporation equal to feed rate of the liquid. The approximation of fixed glass level is justified as the low feed rate will result in a prolonged inventory rise. Local Joule distribution estimated from a separate code was used. In this modelling, cold cap area and the temperature were fixed as a boundary. Because the heat transfer and flow within the cold cap is extremely complex, it was not explicitly modelled. Instead, the model considered cold cap thickness to be infinitesimally small and of fixed area. In reality, cold cap area will vary depending on heating and feed rate. Here, based on energy balance, the feed rate was calculated and compared with actual feed rates to determine the assumed cold cap area was approximately correct. Thus trial and error are needed to arrive at a solution. The model does not track cold cap area, and its shape, which could vary based on heating and feeding conditions and the complexities of the cold cap region was ignored. Still, the model gives reasonable estimates of glass temperature profile away from the cold cap. Gopalakrishnan & Thess, (2010) studied the variations of convective current inside a glass melt, between electrode regions by variation of electrical parameters and the relative effect of thermally induced and Magneto-hydrodynamic induced flow patterns [60].

## **2.8 Melt Pool convection model**

The melt pool convection model solves 3-D, transient, momentum, energy, and electric equations simultaneously with temperature dependent glass properties, as shown in equation (2.1) to (2.4).

$$\frac{\partial \rho}{\partial t} + \vec{\nabla} \cdot (\rho \vec{v}) = 0 \quad (2.1)$$

$$\rho \left( \frac{\partial \vec{u}}{\partial t} + \vec{v} \cdot \vec{\nabla} \vec{v} \right) = -\vec{\nabla} P + \vec{\nabla} \cdot (\mu \vec{\nabla} v) + \rho \vec{g} \{1 - \beta(T - T_u)\} \quad (2.2)$$

$$\rho \cdot C_p \left( \frac{\partial T}{\partial t} + \vec{v} \cdot \vec{\nabla} T \right) = \vec{\nabla} \cdot (\sigma \vec{\nabla} T) + \vec{\nabla} E \cdot (\sigma \vec{\nabla} E) \quad (2.3)$$

$$C_e \frac{\partial E}{\partial t} = \vec{\nabla} \cdot (\sigma \vec{\nabla} E) + I + S_1(E) + S_2(Q) \quad (2.4)$$

$\sigma$  = electric conductivity for the waste glass is in the range of 0.3-0.5 (ohm.cm)<sup>-1</sup>, hence the magnetic force of induction term was neglected in Equation (2.3).

$S_1(E)$  = displacement current and can be neglected as the frequency of AC is 60-80 hertz.

$S_2(Q)$  = electric charge density due to movement of glass and is small as compared to the unit length current density generated in glass pool by the electrode.

The energy equation is coupled to the momentum equation through advection and natural convection term in equation (2.2). The electric equation is coupled to the energy equation through a heat source term, which appears as the last term in equation (2.3).

For a 3-D, transient model of the melter, the melt pool condition can exceed a thermally induced hydrodynamic stability limit depending on boundary conditions imposed on the model. In this case, dual velocity solutions can exist at a fixed geometric location. In normal melter operating condition, flow can be more stable mainly due to the reduced temperature gradient and enhanced mixing in the melt pool. However, the oscillating solutions produced by hydrodynamic instability are still expected to exist under the cold cap.

## 2.9 Cold Cap Modelling

The goal of an efficient waste-glass melter is a sustained high volume glass throughput. Similar (all-electric) commercial melters demonstrate that electric melting can be three

to five times more rapid than that achieved in Joule-heated waste-glass melters. One of the reasons for the slow average rate of melting is an unsteady growth of the cold cap. The other issue that reduces HLW melter performance is foaming of the feed as fine bubbles from the melt are trapped under the cold cap. The foam acts as a thermal insulator that inhibits the melting process. Additionally, cold foam is reasonably stable and difficult to destroy and contributes to slow melting rates. In an HLW melter, liquid waste and glass-forming compounds are introduced into a heated tank filled with molten glass. Numerous chemical reactions take place before the waste is finally converted into glass. These reactions occur under non-isothermal conditions as the feed moves through a steep temperature gradient in the reaction zone of the cold cap. In a study of the cold cap, Pokorny & Hrma, (2012) developed a 1D model for the cold cap in a slurry-fed waste glass melter [35]. The model solves simplified balances of mass and energy using the finite difference method (FDM). Figure 2.2 shows the cold cap images [80].

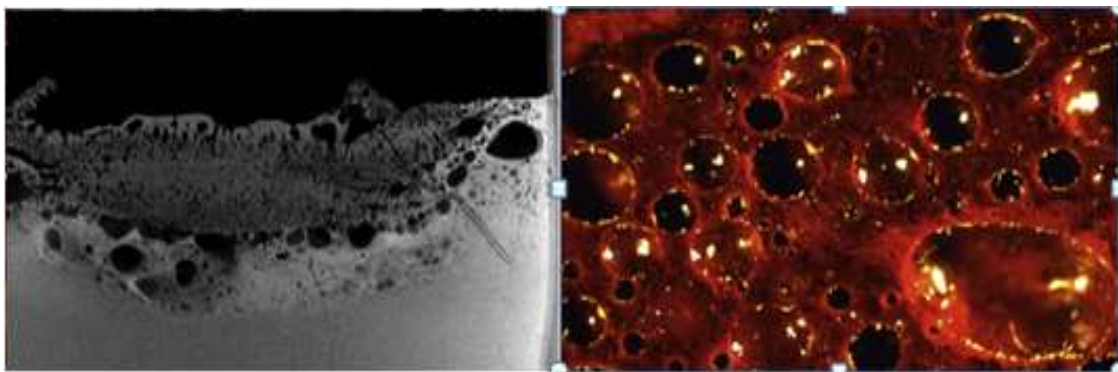


**Figure 2.2:** Images of the cold cap [83]

The temperature and velocity fields within the cold cap were predicted with reasonable accuracy. The rate of melting was determined by the total heat flux to the cold cap that occurs from below (from molten glass) and partly from above (to help evaporate water from the slurry). The response of the cold cap thickness to the boundary heat fluxes was summarized. It was already concluded that primary foam does not affect melting rate.

Effect of primary foam on heat transfer, i.e. on melting rate can become negligible only if rate of generation of gases are small or it escapes quickly. However, the validity of primary foam formation and its effect need to be checked by actual experimental data for HLW under consideration.

Vitrification of RLW is modelled based on chemical kinetics associated with all the waste constituents. For this, vitrification is mathematically expressed by a system of coupled equations involving chemical kinetics, heat transfer and mass transfer. Details of the literature available on mathematical modelling of the cold cap in JHCM are provided in Table.2.2.

As summarised in Table.2.2, various investigators studied the cold cap reactions of a representative waste glass feed using simultaneous thermal analysis. The rates of feed-to-glass conversion reactions are not the deciding factors for determining the rate of processing in an HLW glass melter. The rate of heat transfer from molten glass to the cold cap has a major impact on the forming glass rate. Such an approach is necessary because the rate of feed-to-glass conversion is controlled by phenomena that determine the heat flux to the cold cap. Thus, heat transfer predominantly controls the melting rate, i.e. the overall conversion rate is nearly as rapid as the rate of transfer of heat that can be delivered to the cold cap.

An approach followed in literature is to model the top portion, where boiling of liquid waste is taking place in a porous bed of glass frit as treated separately. The two models will be linked by supplying calculated temperatures from top portion model as a boundary condition to the bottom portion model. While heat flux calculated at bottom portion will be supplied to the top portion as a boundary condition.

**Table.2.2:** Summary of the detailed review on cold cap modelling literature

<b>Investigator</b>	<b>Type of Waste</b>	<b>Kinetic Study</b>	<b>Contributions</b>
Guerrero, et al., 2012	Glass Slurry + sRLW	No	2D & 3D model with a simplified cold cap model that assumed the foam layer void fraction as a function of temperature. Results from laboratory batch sample testing at various temperatures were used in the study
Pokorný et al., 2012	Glass Slurry + sRLW	No	1D model for the cold cap in a slurry-fed waste glass melter was developed. Temperature and velocity fields within the cold cap were predicted.
Rodriguez et al., 2014	Glass Slurry + sRLW	Yes	TGA- DSC performed with EGA. Applied Kissinger method to estimate activation energy.
Pokorny et al., 2015	Glass Slurry + sRLW	Yes	Kinetics parameters determined by Kissinger Method and 1D model developed.
S. M. Lee et al., 2017	Glass Slurry + sRLW	No	Studied different raw materials in glass making and the effect of foam on heat flow from the molten glass to cold cap
Suneel et al., 2019	Glass Beads +sRLW	No	A 3D model with a simplified cold cap model from Pokorny et al., (2015)[64]

A detailed thermo-chemical-hydraulic analysis using CFD for modelling melter will be a realistic approach for improving upon the prediction of glass melt rates and thus glass production rate. The model incorporating chemical kinetics could be utilized to predict the melt rate for different waste and base glass compositions and to optimise the melter operating conditions.

## 2.10 CFD Analysis of Glass furnaces

A model in glass technology can be defined as a description and prediction of glass furnace behaviour from the point of view of physical and chemical processes in glass space and combustion space. The early development of glass modelling is characterized by the use of scale (liquid) models which are still suitable for complicated flows, for example inside feeders. The disadvantage of these techniques is poor heat transfer simulation due to missing radiation at low model temperatures. The first period of mathematical modelling was associated with the availability of simple mechanical machines and calculators, which enabled the development of balance models. The balance models of Cooper, Nelson, Novak, etc, are still being used for furnace engineering and data preparation for true CFD.

The second period of mathematical modelling began after the appearance of mainframe computers. During this time (the 1970s and 1980s), the two-dimensional models of Chen (1976), McConnell & Goodson (1979), Mase & Oda (1980) etc. were developed [44], [45], [47]. Most of these models were based on clever algorithms, often based on Patankar (1980) concept [81]. The latest CFD generation has been initialized by the appearance of personal computers (PC), from the simple Sinclair, up to modern double processor workstations which are cheap, powerful and fast and do not need air-conditioned rooms. All these circumstances enabled the development of three-dimensional models in the 1980s and 1990s by Choudhary, Urgan, Viskanata, Simonis, Schill, Carvalho, etc. This latest period is characterized by rapid incorporation of new model features including batch melting, electrical boosting (electrode potential, Joulean heat), sub-models (particle dissolution, bubble behavior, redox), combustion space (radiation, turbulence, chemistry), complex calculation (coupling of glass and

combustions models), totally new generation of pre-processors (CAD) and post-processors (tracking, 2D- and 3D-graphics, animation), advanced control systems for glass aggregates, etc.

**Table 2.3:** Computer codes for CFD modelling of glass furnaces

<b>Name of the firm</b>	<b>Country</b>	<b>Code</b>
Corning	USA	FLUENT
TNO	Netherlands	Own code
Owens Corning Fiber Glass	USA	Own Code
PNNL	USA	TEMPEST
CFDS	USA	FLOW – 3D
Defence Waste Processing Facility	USA	FIDAP
PNNL	USA	ANSYS finite-element code combined with STAR-CD finite-volume code

CFD - Computational Fluid Dynamics, USA-United States of America, TNO - The Netherlands Organisation, PNNL - Pacific Northwest National Laboratory, FIDAP - Fluid Dynamics and Analysis, ANSYS - Analysis System

Substantial progress has been made in the development of numerical models for each component of the furnace, such as the molten glass flow, combustion space in case of commercial melters and batch layer. The radiation heat transfer from combustion space is mainly used to melt the raw material in such melters, Joule heating being the dominant energy source in HLW glass melters. The thermal, electric and flow field strongly influence each other, and hence, it is necessary to solve them simultaneously to simulate the behaviour of the melter. CFD provides a tool for inter-relating all the physics associated with a complex system like JHCM used in the current study. Fluent,

Flow 3D, Star CD and COMSOL are commercial software that can be applied for the current study. Table 2.3 shows some popular Computer codes available for CFD modelling of glass furnaces.

## **2.11 Gap Areas in Literature**

CFD studies in three-dimensional model exclude many parameters. A comprehensive cold cap modelling with appropriate boundary conditions is not considered in any of the models though this has a more significant influence in predicting melter processing capacity. Some gap areas in the field of modelling of melts that require further attention are

1. Knowledge of the rheological and thermophysical properties of glass is incomplete at operating temperature range (1100 K – 1300 K). The waste added to base glass alter the properties. The effect of these modifiers is not considered.
2. Chemical kinetics of the waste interaction with base glass is not incorporated in the models studied.
3. All the mathematical models in literature have not addressed start-up heating.
4. No integrated model incorporating heat, mass, electrical, & flow fields was studied and validated with experimental data on industrial scale JHCM.

Coupling of all the physics associated in melter such as energy, momentum, mass and electrical along with chemical kinetics will provide a better insight of the process taking place in JHCM.

## 2.12 Motivation

Prediction of the performance of JHCM to produce reliable and quality product is vital to the development of vitrification technology. As operational data obtained from the actual melter used for the vitrification of HLW is limited due to the high temperatures and radioactive environment, numerical analysis is expected to provide insights into the inherent process limitations of the melter. The mathematical models can be beneficial in studying and predicting the physical and chemical processes taking place in the melter. The mathematical models developed till date have the following limitations.

- Unable to predict the processing rates
- No 3D JHCM model is available that has been validated with pilot scale / industrial data that includes the kinetics of cold cap reactions
- Start-up heating of JHCM using resistance heaters in the plenum region has been ignored
- Unable to correlate the waste constituent concentration in glass due to insufficient data on glass chemistry and kinetics of reactions taking place in cold cap

No mathematical models are available in the literature dealing with these aspects of melter operation. The data required for developing realistic models lack coupling to the batch melting and reactions in the glass, chemical equilibria and solubility data. This motivates the need for developing a mathematical model, as there is a need for analysis and synthesis between numerical predictions and operational data to reduce the discrepancies between results of numerical calculations and actual furnace performance. This work aims at addressing the gaps in the literature and develop a model that reliably predicts the performance of melter.

Development of integrated melter model includes model framework, incorporating properties of molten glass in the temperature range of 303 K to 1273 K, cold cap model and determination of heat and mass transfer rates using data generated from pilot plant and industrial scale melters. To obtain assured product quality, knowledge of reaction kinetics associated with the waste nitrates decomposition is essential. The model thus developed will be used for maximising waste loading while improving the melting rate using customised glass composition.

### **2.13 Scope of Study**

A few systematic studies have been conducted previously on JHCM and reported to model the heat transfer predictions [54], [64], [67]. The models are however based on either heat transfer or convection currents or cold cap or electric currents. Design and operation of JHCM require a detailed understanding of all the above parameters. It is imperative to optimise the parameters during operation of melter as these melters have limited life. Operating the melter to maximise the throughput with minimum secondary waste generation is a critical factor in the operation of JHCM. Accordingly, an extensive investigation is carried out on the influence of cold cap on melter heat flux. There have been a few studies in the last decade to understand the modelling of JHCM. Nevertheless, many questions remain unsolved due to complexity of the different interactions in JHCM involving electric current distribution, resulting in natural convection in molten glass pool, heat generation by Joule heat, solid-liquid-gas phase interaction happening in the cold cap, diffusion of chemical species into glass matrix, settling of the spinels and large heat transfer by radiation, conduction and convection. The present study is primarily focused on modelling JHCM and finding the optimised design and operating parameters of a JHCM used in radioactive hot cells. Very limited

literature exists on the systematic study of the above aspects. In the present study, a three-dimensional simulation of the 1:1 model has been developed. For all numerical simulations, the industrial CFD solver COMSOL is used to solve the highly coupled multi-physics equation involving heat, flow, mass and electrical equations.

#### **2.14 Research Objectives**

The objective of this work is to build a CFD model for the industrial scale JHCM and validate the model using experimental data. JHCM has been used to generate the experimental data for validating the model. The melter used in the study is of  $2\text{ m} \times 2\text{ m} \times 2.2\text{ m}$  size, used to vitrify RLW generated from the reprocessing of spent nuclear fuel from Pressurised Heavy Water Reactors (PHWRs). Integrated CFD model with heat transfer, chemical reaction and electrical current model can reliably represent the overall melting process that can be used to predict the rate of glass processing. The aim of this study is to aid in optimizing the process of forming glasses, because even small improvements in the system can translate to crores of rupees in cost savings and years of schedule, as the cost and schedule of the vitrification campaign are highly dependent on the waste loading in glass and rate of glass production.

The technical challenges involved in vitrification of HLW in JHCM are i) physical nature of JHCM is complex and involves interactions between electric, thermal and flow fields, ii) these interactions depend on temperature-dependent glass properties, natural convection, advection, diffusion and volumetrically distributed joule heating sources, iii) the cold feed on the top of the heated glass destabilizes the flow field and develops unsteady asymmetric flow motions underneath.

The primary objective of the present work is,

- To determine experimentally physical properties in the required temperature range and use the analytical correlations for determining the properties of other materials used in the experiments
- To determine reaction kinetics of glass formation in the cold cap by Thermogravimetry (TG) - Differential Thermogravimetry (DTG)
- To carry out experiments in an industrial scale JHCM and generate data for Validation and Verification of the numerical model. To study the effect of waste composition on throughput
- Development of subsystems by decoupling the melter physics and integrating these subsystems into a complex, full-scale engineering model by incorporation of heat transfer, fluid dynamics, electrical distribution, reaction kinetics and mass transfer
- To develop a 1:1 3D model of JHCM to predict the transient temperature profile and average processing capacity of the melter based on the composition of glass and RLW

### **2.15 Methodology for Modelling**

A mathematical model will be developed to simulate the conversion of melter feed to molten glass that occurs within the cold cap. The model will be capable of relating the performance and structure of the cold cap to the input variables that will eventually become available in the overall models of the melter. These properties are bulk density, heat conductivity, effective heat capacity, melt foaminess, and kinetic equations for various feed reactions. The primary model output includes the rate of melting, cold-cap thickness, and secondary foam layer thickness. The model also yields the distribution of temperature, bulk and gas phase velocities, local heating rate and concentration

within the cold cap. Cold caps produced during inactive commissioning of JHCM being operated in Waste Immobilisation Plant, Kalpakkam (WIPK) will be compared with model predictions.

## **2.16 Closure**

An extensive review of literature relevant to the present study was presented in this chapter. The objectives and scope of the present investigation were also clearly brought out. The next chapter presents the details and methodology of the experimental work carried out for generating data which will later be used for validation of the model.

# CHAPTER-3

## EXPERIMENTAL STUDY

## CHAPTER-3

---

### 3 EXPERIMENTAL STUDY

#### 3.1 Determination of Glass Properties

After the radiochemical analysis of the HLW, a suitable glass composition is formulated for vitrification. The base glass used in the present study has a composition of SiO<sub>2</sub>-48%, B<sub>2</sub>O<sub>3</sub>-26.3%, Na<sub>2</sub>O-11.7%, TiO<sub>2</sub>-9.5% & Fe<sub>2</sub>O<sub>3</sub>-4.5%. The glass is mixed with radionuclides corresponding to 24% by weight.

##### 3.1.1 Viscosity of Glass

Viscosities of the glass loaded with 22 % waste oxide were measured with a Furnace Rheometer Systems (FRS) make viscometer “Anton Paar, FRS 1800” as shown in Figure 3.1. Measurements were performed in duplicate from 1173 K to 1323 K. Each series of measurements included two cycles that consisted of measurements made from low to high temperature, followed by measurements made from high to low temperature. The procedure followed was compliant with ASTM C 1276.



**Figure 3.1:** Anton Paar Rheometer for measuring viscosity of glass

### 3.1.2 Thermal Expansion of Glass

Thermal expansion of glass loaded with 22 % waste oxide was measured with a NETZSCH DIL 402 PC dilatometer, as shown in Figure 3.2. Measurements were performed in duplicate from 570 K to 730 K. Each series of measurements included heating cycle and comparison with Al<sub>2</sub>O<sub>3</sub> standard.



**Figure 3.2:** Dilatometer for measuring coefficient of thermal expansion of glass

### 3.1.3 Reaction Kinetics during Vitrification of RLW

The efficiency of the vitrification process is highly dependent on the loading of waste nitrates in glass and on the rate of HLW glass production. For vitrification to be economically viable, any step for increasing the rate of glass processing must also ensure lesser secondary waste generation. This implies, achieving desired spread of cold cap and its faster dissolution into the glass. The dissolution of the cold cap into glass melt is determined by the kinetics of reactions that occur in cold cap.

Melt rate studies were performed to develop a fundamental understanding of the glass conversion reactions, in particular, those that strongly influence the rate of melting. This

understanding will help in the development of models to predict the impact of composition and other critical parameters on the melting rate. This model can then be used to study methods and strategies to increase the throughput of HLW feeds [82].

Thermogravimetric technique was used to determine the extent of calcinations of various salts appearing from waste as well as glass forming additives. This technique was utilised to find the amount of material left as a function of temperature to determine the rate kinetics of RLW constituents with glass. The thermogravimetric (TG) analysis is based on the principle of monitoring the known weight of a material or a mixture as a function of temperature, using a thermo balance of high sensitivity, during a predetermined heating or cooling cycle. The weight changes can be monitored during heating as well as cooling or as a function of time (isothermal) in a specified atmosphere.

The Block diagram of TGA system is shown in Figure 3.3.

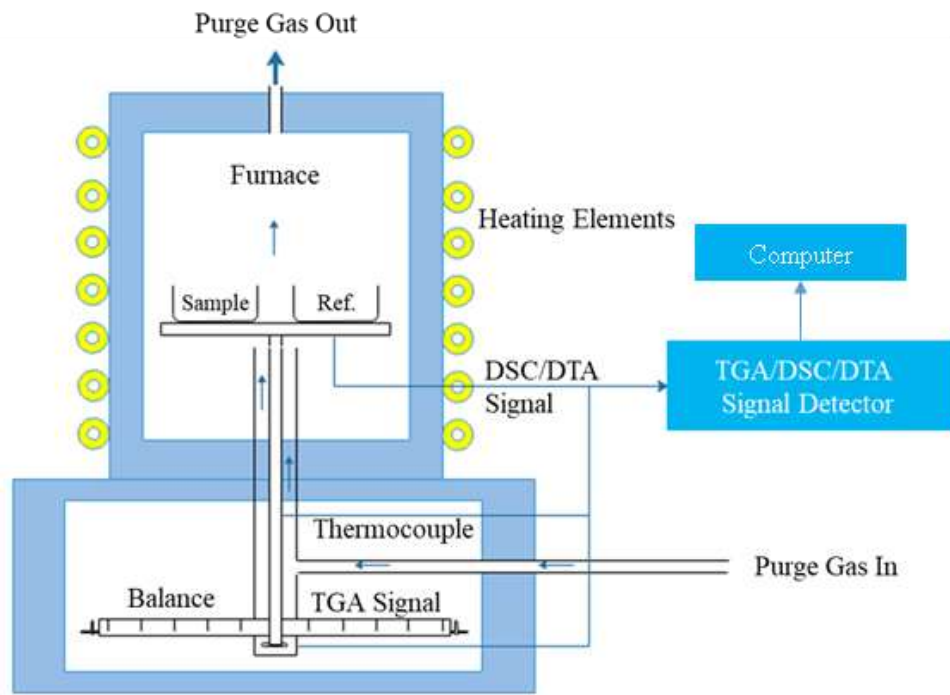


**Figure 3.3:** Block diagram of TGA system

The resulting thermogravimetric curve (change in weight versus temperature) provides information about the thermal stability and composition of the initial sample, the

thermal stability and composition of any intermediate compounds that may be formed and the composition of the residue if any.

In the present work, the investigations were carried out using simultaneous thermal analyzer (Netzsch STA 449 F1 Jupiter). The dynamic TG runs of waste constituents were carried out at different heating rates from 10 to 40 K.min<sup>-1</sup> under nitrogen atmosphere (100 cm<sup>3</sup>.min<sup>-1</sup>).

**Table 3.1:** Glass composition and simulated waste constituents

Glass Composition		Simulated Waste Constituents (24% WO)		
Component	Weight (%)		Salt	g/L
	5C	7C		
			Acidity	2 N
SiO <sub>2</sub>	48.0	54.6	CsNO <sub>3</sub>	0.233
B <sub>2</sub> O <sub>3</sub>	26.3	11.2	Sr(NO <sub>3</sub> ) <sub>2</sub>	0.081
Na <sub>2</sub> O	11.7	14.8	NaNO <sub>3</sub>	19.429
TiO <sub>2</sub>	9.5	9.7	Fe(NO <sub>3</sub> ) <sub>3</sub> .9H <sub>2</sub> O	3.617
Fe <sub>2</sub> O <sub>3</sub>	4.5	2.0	Cr <sub>2</sub> O <sub>3</sub>	0.135
CaO	-	6.2	Ni(NO <sub>3</sub> ) <sub>2</sub> .6H <sub>2</sub> O	0.248
K <sub>2</sub> O	-	1.5	Mn(NO <sub>3</sub> ) <sub>2</sub> .6H <sub>2</sub> O	0.740
			Ca(NO <sub>3</sub> ) <sub>2</sub> .4H <sub>2</sub> O	1.693
			MoO <sub>3</sub>	0.135
			BaNO <sub>3</sub>	0.350

A pierced empty platinum crucible was used as a reference. The complete process of glass production from waste nitrates and oxides to glass melt is taking place under a non-isothermal condition in the temperature range of 323 to 1273 K. Table 3.1 shows the composition of Simulated Radioactive Liquid Waste (sRLW) used in the study. These waste constituents together account for 99% of the total activity associated with RLW. The phenomena of cold cap reactions and interaction of molten glass with radioactive waste constituents and the influence of base glass composition on the

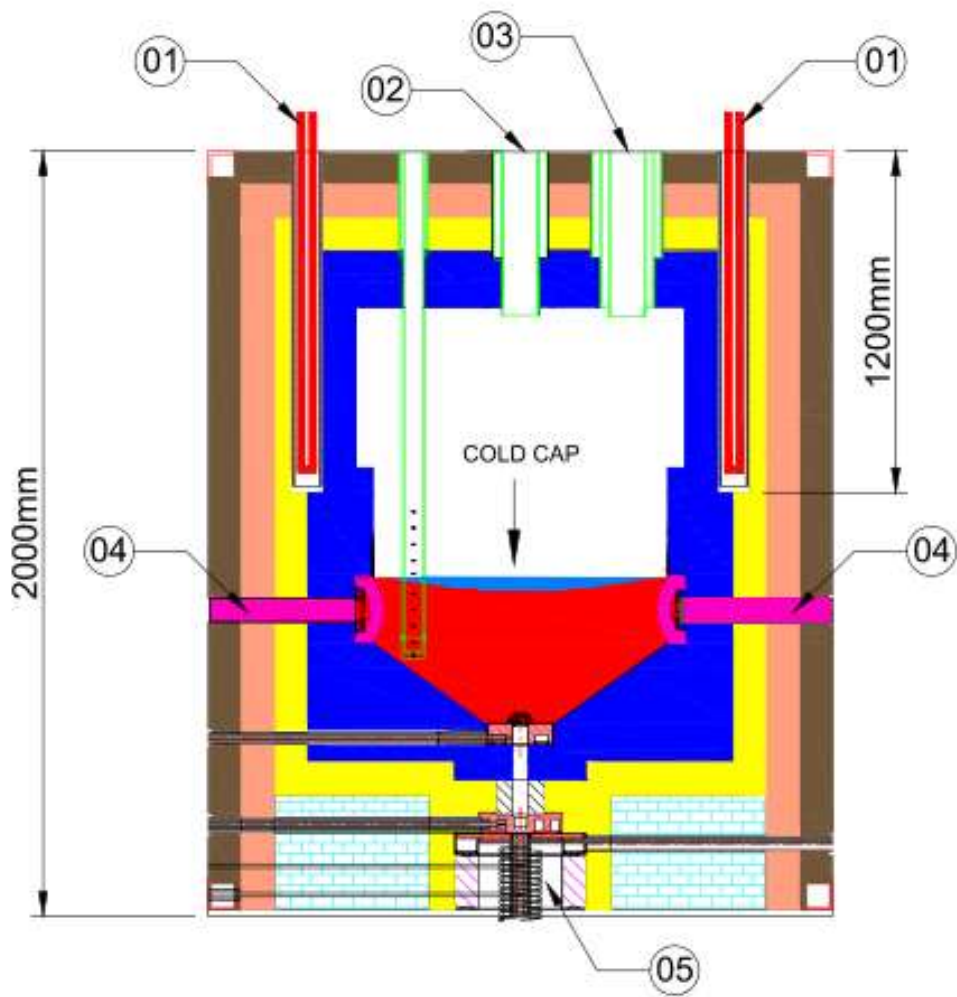
decomposition of constituents of RLW were studied by carrying out TG of ten major constituents of sRLW.

Activation energy, pre-exponential factor and order of the reaction for the decomposition of waste nitrates and oxides in RLW to VWP were estimated based on Thermogravimetry (TG) - Differential Thermogravimetry (DTG) analysis.

Waste constituents were mixed with five component (5C) and seven component (7C) glass compositions and subjected to thermal analysis. Non-isothermal weight loss measurements were carried out for the samples at different heating rates. The resulting thermogravimetric curves (change in weight versus temperature) were used to estimate activation energy (E) of the reaction by Kissinger iso-conversional method. Further, the TG curves were used to predict the rate constant and kinetic parameters for the thermally stimulated reactions.

### **3.2 Experimental Set Up - Joule Melter**

Experiments were carried out in Waste Immobilization Plant (WIP), Kalpakkam for studying the performance of the JHCM under various operating conditions. Figure 3.4 shows the schematic of the JHCM used in the studies. The glass is heated by passing alternating current between two submerged electrodes, placed opposite to each other. Electrodes are made of Inconel<sup>®</sup> alloy 690. When a current is passed through a material heat is generated inside it due to the resistivity of the material which is known as Joule Heat ( $P=I^2R$ ). Glass has a property of conducting current at a temperature starting from approximately 873 to 973 K because the resistivity of glass decreases with increase in the temperature. The heat generated is used for carrying out vitrification of HLW.



	REFRACTORY
	BACKUP REFRACTORY
	INSULATION-1
	INSULATION-2
	THERMOCOUPLES

	PLENUM HEATER
	FEED NOZZLE
	OFF GAS NOZZLE
	INCONEL ELECTRODE
	FREEZE VALVE

**Figure 3.4:** Schematic of JHCM

### **3.2.1 Refractory & Insulation Layers**

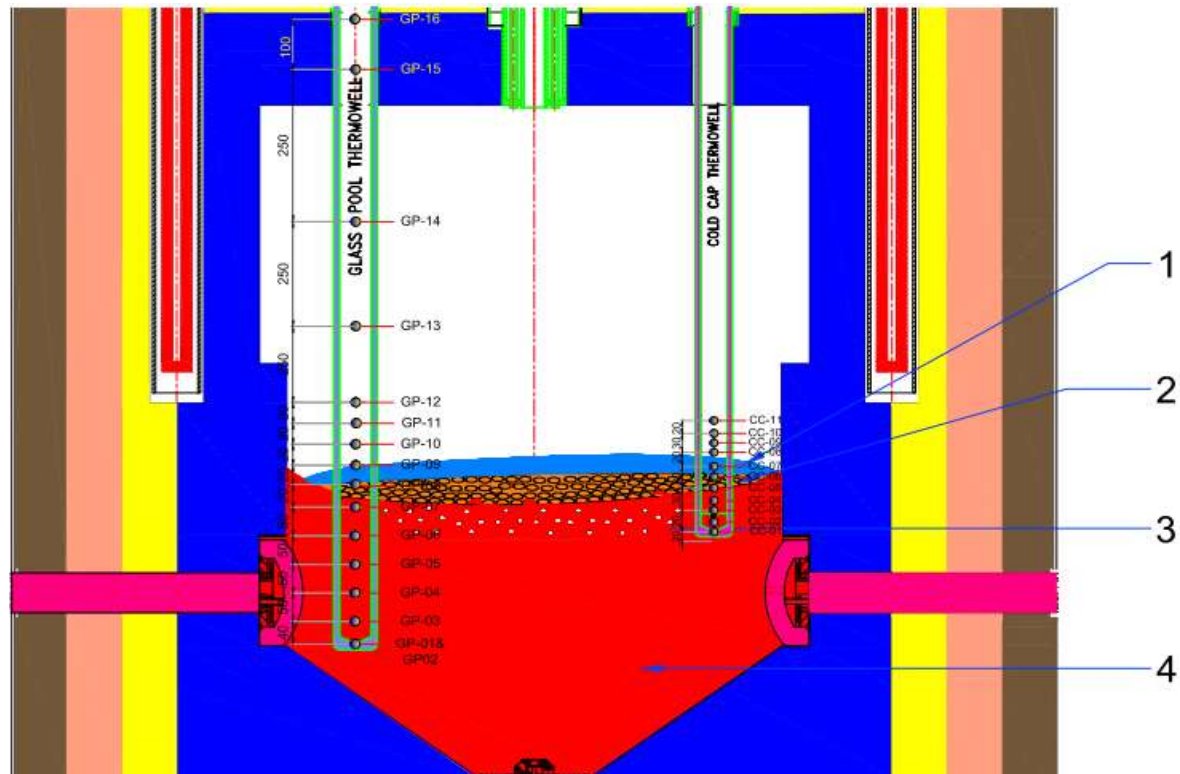
Vitrification operation is carried out in containment of refractory, which is corrosion resistant at elevated temperatures. The refractory blocks are followed by back up refractory, which is provided to prevent glass migration. The insulation layers 1 and 2 are further provided to minimise heat loss. The insulation layers are finally enveloped by a stainless steel sheet. The insulation of JHCM is designed to restrict its outer wall temperature to 343 K.

### **3.2.2 Inconel® Alloy 690 Electrodes**

Current is passed through a set of electrodes which are always dipped inside the pool. Inconel, which is a high Ni-Cr alloy, has been chosen as the material of construction as it is resistant to the highly corrosive, high-temperature nitric acid environment present in the melter.

### **3.2.3 Feed Nozzle & Off-gas Nozzle**

Feed nozzle is provided to feed the HLW and glass forming chemicals. The melter also has an off-gas nozzle meant for routing the off-gases generated during vitrification towards an elaborate treatment system. The off-gas consists of condensable and non-condensable gases along with particulates. The condensable gases are condensed in a dust scrubber & condenser. The non-condensable gases such as a nitrous oxide ( $\text{NO}_x$ ) that are generated during the decomposition of nitric acid ( $\text{HNO}_3$ ) and calcinations reactions of fission products and corrosion products are scrubbed in wet scrubbers. The residual off-gases are filtered in High-Efficiency Particulate Air filters (HEPA) before discharging to stack.



1. Boiling Nitric acid [T = 403 K, Thickness = 5-7 mm]
2. Denitration of corrosion products [T = 403-723 K, Thickness = 7-27 mm]
3. Denitration of Fission products [T = 723-873 K, Thickness = 40 mm]
4. Molten glass [T = 1223 K – 1273 K]

**Figure 3.5:** Temperature measurement in JHCM

### 3.2.4 Temperature Measurement in JHCM

JHCM is provided with 27 thermocouples (N-type and K-type) to obtain its detailed temperature profile. Out of these, 16 thermocouples are used for recording the glass pool temperatures, and 11 thermocouples for cold cap temperatures, as shown in Figure 3.5.

The temperature of the glass pool and cold cap were monitored with thermocouples placed in thermowell inside the furnace cavity. The height of the glass pool and the depth of cold cap were inferred using these thermocouples. Face temperatures of the electrodes were also monitored using thermocouples.

### 3.2.5 Level Measurement

Level in JHCM was monitored using RADAR principle. In radar level measurement, microwaves transmitted by the antenna system of the radar sensor to the measured product, are reflected by the product surface and received back by the antenna system. The time from emission to reception of the signals is proportional to the level in the vessel.

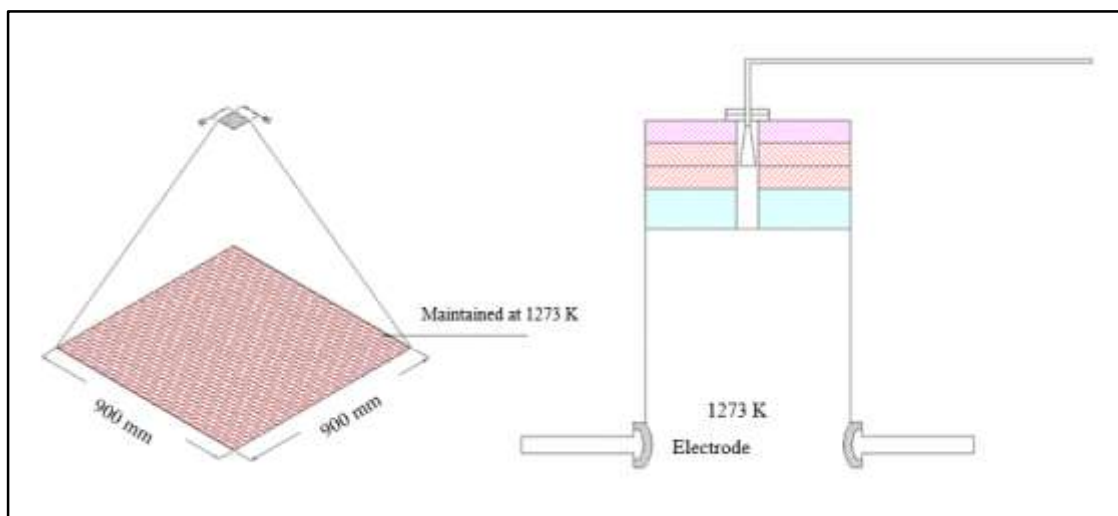


**Figure 3.6:** Schematic of the RADAR Level Measurement

The measurement is affected neither by fluctuating product properties nor by changing process conditions such as temperature, pressure or intense dust generation. Figure 3.6 shows the schematic of the RADAR level measurement used for the measurement of level in the industrial scale JHCM. RADAR level measurement instrument Model W65 of VEGA make was used for the measurement of the level of the melter.

### 3.2.6 Measurement of Heat Losses from the Melter Surface

The external face walls of the melter were monitored with thermal imaging camera TIPL C640, to determine the effectiveness of the insulation layers and detect any point of abnormal heat losses. A typical thermal image of the melter is depicted in Figure 3.7.

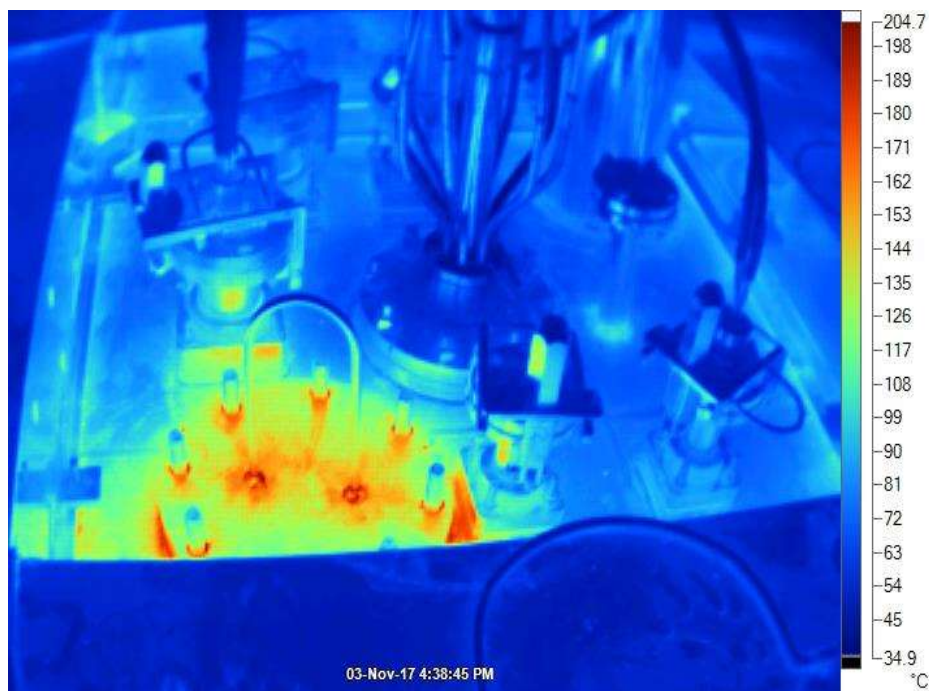


**Figure 3.7:** Thermal Image of top surface of JHCM

### 3.2.7 Plenum Heaters

Glass is an insulator at room temperature, and cannot conduct current at lower temperatures, so initial heating at the start-up is carried out by resistance heaters provided beside the refractory in the plenum region of the melter. These heaters are made up of Silicon Carbide and are placed in Kanthal ® Tubes, as shown in Figure 3.8.

As these heaters are installed in the Plenum region of the melter, they are also called Plenum heaters (PH). Once the glass starts conducting, joule heating is initiated using electrodes dipped inside the glass pool.



**Figure 3.8:** Plenum Heaters

### **3.2.8 Freeze Valves & Induction Heating Coils**

Freeze valves are provided at the bottom of the melter to facilitate pouring. To have better control on glass pouring operation, split induction coil heating system is used for heating of the freeze valve. Freeze valve consists of two sections viz., Joule Heated Section on the top, followed by an induction heated section at the bottom. The bottom section is heated by medium frequency alternating current.

## **3.3 Pilot Scale Experiments for Determination of Heat Transfer Mechanisms**

### **3.3.1 Pilot Scale Experimental Set-Up**

The efficiency of the start-up heating is affected by various parameters like the skin losses, the negative pressure of the melter, the air gap between the heater and Kanthal<sup>®</sup> tubes, and the geometries of heaters and pre-fabricated slots. Though the effect of other

parameters on the overall heat flux can be easily determined for a given system, the determination of the effect of the air gap, the geometry of the heaters, and pre-fabricated refractory slots is difficult, as mapping of temperature on inside walls of melter cavity at high temperature is difficult. This necessitates the modelling of start-up heating and its validation using experimental results.

Power is supplied to plenum heaters, which heats the refractory blocks. The refractory blocks in turn transfer this heat to glass frit. Heat is transferred to preformed glass frit by walls in the plenum region by radiation and conduction. The apportionments of energy transferred by these modes to glass frit were not possible in industrial scale melter. In order to determine the energy apportionment, an experimental setup was devised to study the phenomenon of start-up heating. The objective was to determine the contribution of different modes of heat transfer in raising the temperature of glass frit. An understanding of this fundamental phenomenon will result in devising methods that can be adopted to increase the thermal efficiency of the start-up heating. The aim was on a complete understanding of the heat transfer mechanism in continuous vitrification equipment during its start-up stage and methods of improving it.

The experimental set-up is shown in Figure 3.9. The setup consisted of stainless steel (SS) enclosure, refractory blocks, two plenum heaters of 3 kW capacity each, made up of Silicon Carbide (SiC). The heaters were enclosed in APM Kanthal<sup>®</sup> tubes and connected to Alternating Current Power Control (ACPC) panels.

The face temperature of the refractory blocks was measured at nine different locations on the hot face of the refractory blocks using K-type thermocouples having an accuracy of  $\pm 2\text{K}$  over the range of 0 to 1533K to determine the vertical and horizontal distribution

of temperature. Continuous monitoring of the temperature was carried out by connecting the output of the thermocouples to a Data Acquisition System.

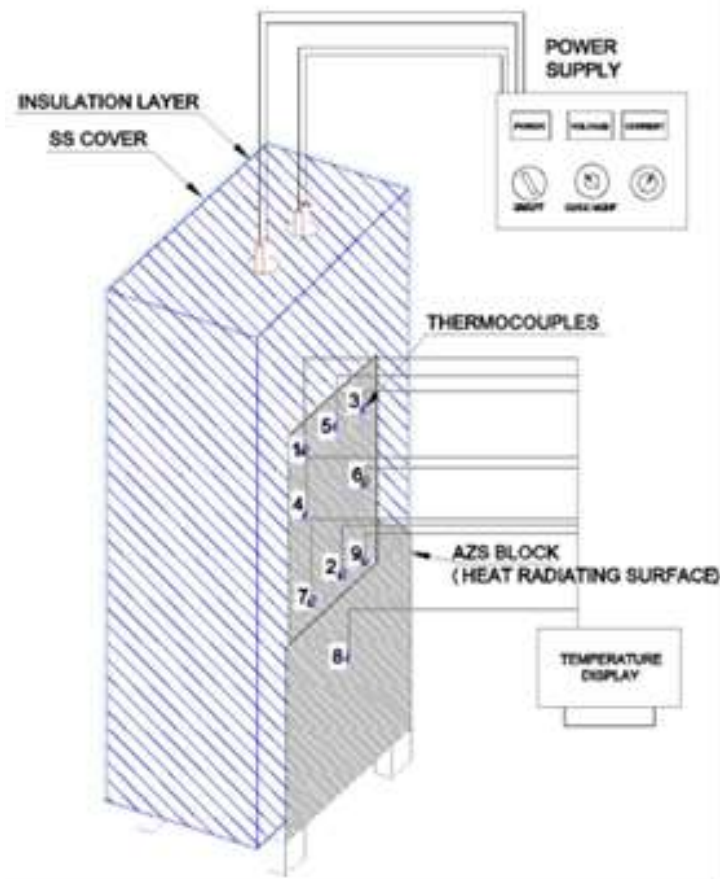


**Figure 3.9:** Schematic of experiment used for determination of mode of heat transfer

### 3.3.2 Experimental procedure

The power to the plenum heaters was increased at a rate of 0.1 kW/hr at regular intervals, and the system was allowed to achieve a steady state. The temperature of the refractory blocks increased linearly with heater power. The rise in temperature of the thermocouples and their steady state temperatures were monitored and recorded.

This experiment intended to measure the temperatures at different locations of the plenum set-up. The data generated from the experiment was used to validate the data generated from the simulation and to determine the mode of heat transfer to glass frits.

The experiment was repeated by putting glass frit in the cavity adjacent to the refractory blocks up to a height of 500 mm from the bottom.

### 3.4 Experiments on Industrial Scale JHCM

Experiments were carried out for testing the joule melter under various operating conditions. The data obtained from these experiments were used for validation of the model. Observations were made at steady state. Steady state was ensured by recording the temperatures only when the rate of rise in temperature was negligible (0.5 K/ 1 hour). The JHCM was heated gradually through different stages before charging radioactive waste to achieve the following objectives as presented in Table 3.2 and Figure 3.10

**Table 3.2:** Different Stages of Melter Operation

Stage	Name of Stage	Purpose
Stage-I	Start-up Heating	Removal of moisture from the castable backup refractory
Stage-II	Glass Melting	Charging of the glass beads and heating the glass beads to a temperature of 873 K, so that glass starts to conduct electricity.
Stage-III	Vitrification	Experimental determination of glass processing capacity of the melter and producing an inactive VWP which qualify for long term storage.

As a part of the study, experiments were carried out for establishing the temperature profiles in the melter without glass frit and with glass frit in the furnace cavity for stage – I and stage – II of furnace operations. Subsequently, experiments were conducted to estimate the processing capacity of the melter in stage-III. The response of the

thermocouples was monitored and recorded continuously using Supervisory Control and Data Acquisition (SCADA) system.

#### **3.4.1 Stage – I Operation of JHCM: Start-up Heating**

Moisture is picked up by refractory during installation. Before charging glass and radioactive waste into the melter, it is necessary to remove the moisture from the refractory. This moisture, if not removed from the refractory, can lead to shorting of electrodes during initiation of joule heating. The moisture is removed using plenum heaters. The process of removal of moisture from the refractory using plenum heaters is called “Green Heating”. As the refractory is a poor thermal conductor, the rate at which the temperature must be increased during start-up is crucial, as a sudden increase in temperature can lead to thermal stress due to a high temperature gradient across its thickness. In extreme cases, this can cause cracks in refractories. The rate of increase in heater temperature was limited to 5 K/hr. Plenum heaters were provided with thyristor control for controlled heating and thermocouples were mounted inside each heater to monitor the heater temperatures continuously. The glass pool, plenum heater, and electrode temperatures were monitored at regular intervals to control the rate of rise in temperature. The external face walls of the melter were monitored with thermal imaging cameras to determine the effectiveness of the insulation layers and detect any point of abnormal heat losses.

Stage – I of the experiments involved raise in the plenum heater power and observing the response of the system as shown in Figure – 3.10 (a). As a part of these testing, for a step increment of power input to the system, the temperature repose in melter cavity was monitored. Steady state was ensured by recording the temperatures only when the rate of rise of temperature was negligible (0.5 K/10 hours).

After completion of green heating, JHCM was fed with pre-formed glass beads in the form of granules of size 2-3 mm. The composition of the glass beads is given in Table 3.1. After charging the glass beads, the temperature of the plenum heaters was increased to 1273 K, at a rate of 5 K/hr. The temperatures were made to sustain for 150 hrs to attain a steady state.

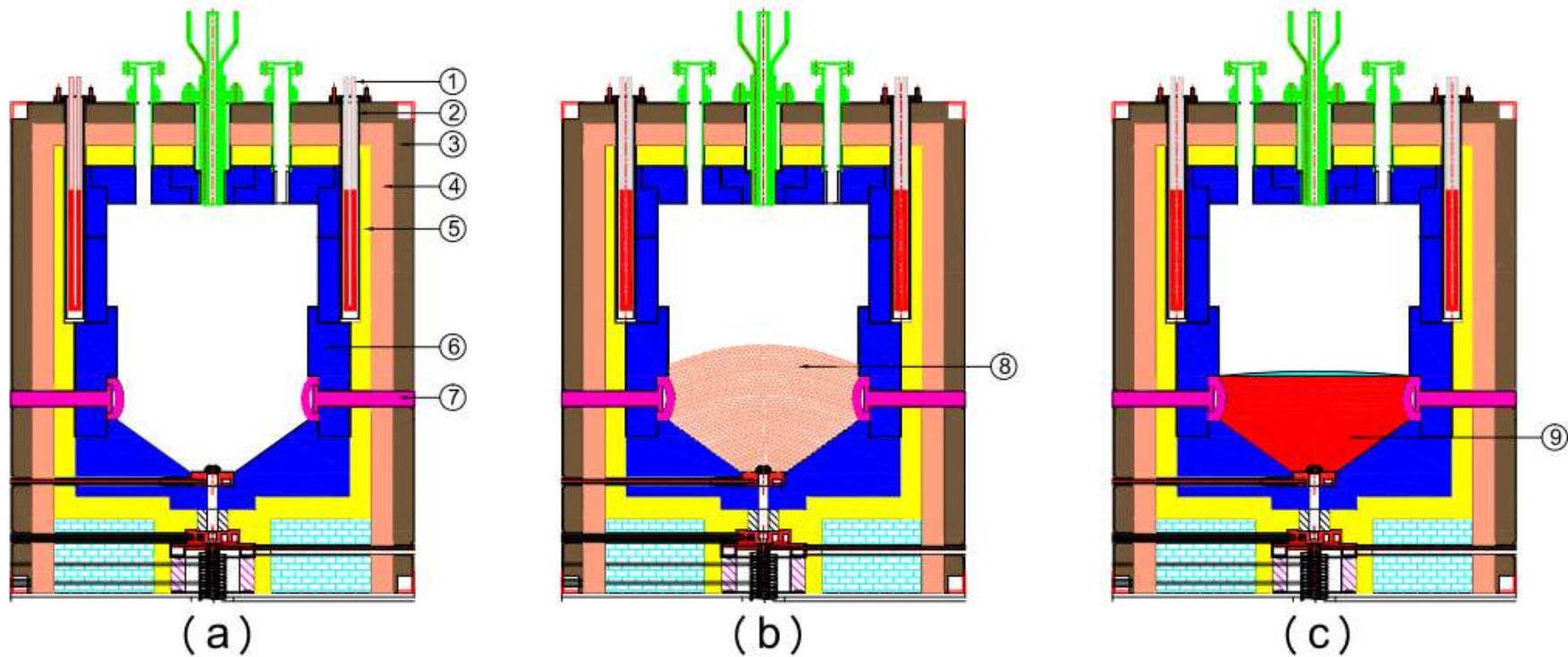
### **3.4.2 Stage – II Operation of JHCM: Glass Melting**

Pre-formed glass beads were added to the melter as shown in Figure 3.10 (b), and all the 24 numbers of plenum heaters were powered with 1198 W. The total power input to the systems through plenum heaters was 28.75 kW. The JHCM was maintained under these conditions for 160 hours. The temperature on the outer walls was measured to calculate the heat losses from the melter outer body. PCW temperatures, amount of air ingress into melter, and electrode phase temperatures were monitored.

### **3.4.3 Stage – III Operation of JHCM: Vitrification**

#### **3.4.3.1 Estimation of Boil-up rate**

The boil-up rate of JHCM was estimated using Demineralized (D.M) water at maximum and minimum operating levels. Water was fed in measured quantity from a pre-calibrated batching tank at controlled flow-rate, which was gradually increased every two hours to ensure the controlled spread of cold cap. The cold cap was recorded using a bullet camera for every increase in flow rate by 10 lph. The spread of cold cap was limited to a maximum of 90 % to prevent thermal shock to refractories. Cold cap and glass pool temperatures were recorded every hour.



1. PLENUM HEATER
2. KANTHALTUBE
3. INSULATION-2

4. INSULATION-1
5. BACKUP REFRACTORY
6. REFRACTORY

7. ELECTRODE
8. GLASS FRIT
9. MOLTEN GLASS

**Figure 3.10:** Melter Operation Stages – a) Stage – I: Empty cavity b) Stage – II: Glass Melting c) Stage – III: Vitrification

### 3.4.3.2 Estimation of Processing Capacity using Simulated Waste

Simulated waste of characteristics similar to the radioactive waste was prepared using stable isotopes of the radioactive species. Two types of SW composition with 28 g.L<sup>-1</sup> and 56 g.L<sup>-1</sup> of waste nitrates were used for estimation of processing capacity. Composition of simulated waste is given in Table 3.1.

The simulated waste and glass frit were fed simultaneously to the melter while continuously monitoring the temperature profile. To obtain a controlled and sustained spread of cold cap as shown in Figure 3.10 (c), the feed rate of simulated waste and glass frit was increased stepwise at a rate of 1 L hr<sup>-1</sup> and 80 g hr<sup>-1</sup> respectively. Continuous monitoring and recording of the glass pool and cold cap temperatures were carried out. The spread of cold cap at different glass and waste feed rate was photographed.

The electric resistivity of the ceramic structure is approximately two orders of magnitude higher than that of the glass melt. As a consequence, the energy released outside the melt is negligible. General levels of electric resistivity of the melt are between 4 and 20 Ω.cm, depending on the temperature of the melt pool.

The number and arrangement of electrodes in the melt tank are the result of criteria such as, the highest possible energy release in the glass pool, pronounced thermal convection for homogeneous mixing of the melt, and sufficient energy transport to the process zone on the surface of the molten pool, which requires a large amount of energy (evaporation, melting).

The melt is heated at a constant electric current. This type of power supply helps to limit the power transferred to the melt in case of excessive temperatures of the molten pool because of the electric resistivity decreasing with temperature. In this way, temperature

peaks are avoided. This approach also ensures that the permissible power density load of the electrode surfaces is not exceeded.

### **3.5 Closure**

Experiments were carried out on all the stages of the melter to generate data sets required for the validation of the numerical models. The contribution of different modes of heat transferred were determined. TG-DTG of the components of RLW were carried out to determine the reaction kinetics of cold cap reactions. Results of the experiments are presented in Chapter 5.

# CHAPTER-4

## MODELLING OF JHCM

# Chapter 4

---

## 4 COMPUTATIONAL MODELLING AND SIMULATIONS

### 4.1 Modelling Approach

This chapter is devoted to a complete discussion on the governing equations and the methods of solution for the heat transfer, electric currents, reaction kinetics, mass transfer, and cold cap modelling in a JHCM used for vitrification of nuclear waste. The formulation of the governing equations and the solution methodology are explained. Increase of the temperature of molten glass decreases the resistivity and this in turn increases the temperature for a given voltage input across the electrodes. To explain this, electrical and heat transfer aspects are modelled together, along with fluid dynamics. The most important physico-chemical phenomena occurring in the melter is in the cold cap, where evaporation, boiling and nitration take place. Mathematical model of cold cap reactions is developed and integrated into the holistic model of JHCM, to make it complete in all respects. This chapter also describes the grid independence test of the models.

### 4.2 Problem Formulation

A three-dimensional CFD model has been developed using the commercial software package COMSOL MULTIPHYSICS to study the electrical, heat, fluid dynamics, and mass transfer occurring in the melter. The governing equations are solved using the finite element method (FEM). In addition to conventional physics-based user-interfaces, COMSOL MULTIPHYSICS also allows for entering coupled systems of partial differential equations (PDEs). The PDEs can be entered directly or using the ‘weak form’.

Electrodes immersed in molten glass pool are subjected to an electric potential difference, and the heat generated by the current density is estimated. Joule heat generated by passing electric current is coupled with heat transfer. Multiple modes of heat transfer occur in melter during its start-up the heating, heating of glass to conducting temperature, and processing of RLW. A mathematical sub model describes the complex cold cap process (i.e., heat transfer, mass transfer, and reaction kinetics). A semi-empirical constitutive model of the cold cap is derived from pilot plant scale experiments reported in the literature and is used in the study.

The modelling of JHCM is a transient heat transfer problem with the surface to surface radiation incorporated on the interior walls of the melter cavity and is constructed using FEM. Radiation is the dominant mode of heat transfer during Stage – I and Stage – II operation of the melter. Discrete Ordinate Method (DOM) is used for solving wall to wall thermal radiation. The radiation from the walls to the cold cap is also substantial. The physics associated with the batch melting process is studied on an industrial scale JHCM. The JHCM used for the experimental investigations in the present study has a melt pool surface area of  $0.82 \text{ m}^2$ . The molten glass is contained in a  $0.9 \times 0.9 \times 0.320$  m cavity in JHCM at the maximum operating level and  $0.9 \times 0.9 \times 0.220$  m at the minimum operating level. Six electrodes, each having a surface cross-section of  $0.2 \times 0.2$  m, are located on opposite ends on two sides of the melter (three electrodes on each face).

### **4.3 Estimation of the Properties of the Materials**

Properties of the glass melt are estimated by using software package SCI GLASS for glass having composition as shown in Table 1. The physical properties based on the composition are estimated as a function of temperature and are used in the model. Various physical properties as a function of temperature for different materials used in the melter are as shown in Table 4.1.

**Table 4.1:** Physical properties of glass and insulation materials used for modelling

Property	Glass*	Refractory**	Backup Refractory**	Insulation-1**	Insulation-2**
Density ( $\rho$ , kg.m <sup>-3</sup> )	$2260 + \frac{158.5}{\left\{1 + \left(\frac{T}{868.64}\right)^{4.01}\right\}}$	4005	1530	220	128
Coefficient of expansion ( $\beta$ , K <sup>-1</sup> )	$5.94 \times 10^{-6}$	-	-	-	-
Specific Heat (C <sub>p</sub> , J.kg <sup>-1</sup> .K <sup>-1</sup> )	$1809.445 - \frac{795.59}{1 + \left(\frac{T}{542.66}\right)^{5.90}}$	768	703	640	612
Thermal conductivity (k, W.m <sup>-1</sup> .K <sup>-1</sup> )	0.96	2.88	$(10^{-6} \times T^2) - (0.0012 \times T) + 1.3617$	0.13	0.1
Viscosity ( $\eta$ , Pa.s)	$exp\left\{-1 + \frac{19723419}{1 + \left(\frac{T}{1.21}\right)^{2.32}}\right\}$	-	-	-	-
Electrical conductivity ( $\sigma$ , S.m <sup>-1</sup> )	$49115.23 - \frac{49133.61}{1 + \left(\frac{T}{1396.36}\right)^{6.98}}$	-	-	-	-

\* Relations obtained from SCI GLASS Software for a given glass composition

\*\* Values given by the manufacturer

#### 4.4 Unit Problems

To facilitate the development and validation of the model, the whole physics associated with vitrification process is broken down to several steps or unit problems. Each unit problem involves simple geometry and only one important feature. Test cases for validation of various modes of transfer are identified within the melter.

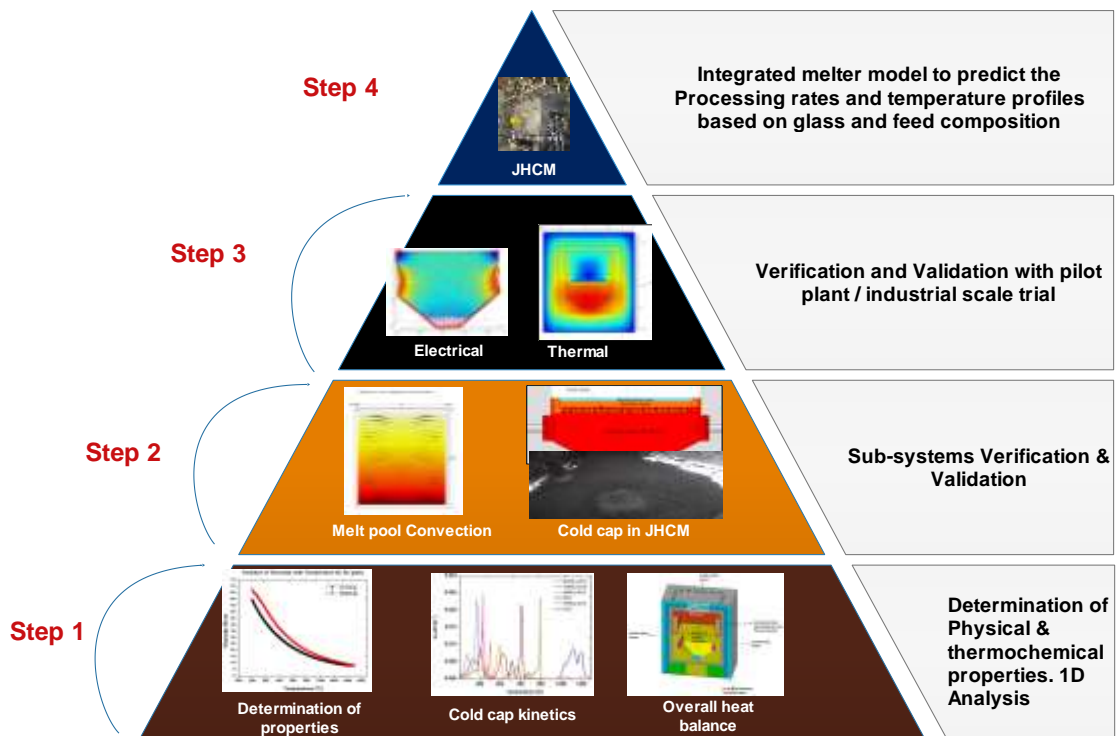


**Figure 4.1:** Pyramidal hierarchy for model development

In building the CFD model for industrial scale melter, validation approach outlined by Guillen et al., (2018) as shown in Figure 4.1 was followed. A validation hierarchy was developed wherein the melter physics is decoupled into sub-systems to validate them individually and build the model methodologically from unit problems to subsystem cases before final integration into the overall model. This approach systematically tests the individual physical models and progressively couples the individual models at increasing levels of complexity until the full model is assessed. Every subsystem of the model is coupled with the grid independency study to quantify the uncertainty in the numerical simulation[83]. The heat loss terms are incorporated

on the outer most surfaces as convective cooling losses and surface to ambient radiation losses.

#### **4.4.1 Electrical**

The physics associated with electrical systems are considered only in the molten glass zone. The electrical potential is specified as boundary conditions on the surface of the electrode. All other spaces are considered as insulators. The Joule heat generated due to the passage of current raises the temperature of the glass pool. The increase of temperature results in an increase of current due to the temperature dependence electrical conductivity. The increased current results in further joule heating.

##### **4.4.1.1 Assumptions:**

- i. The passage of electric current in the glass melt occurs mainly by ionic conduction and is governed by Ohm's law, and conservation of electric charge and ohmic dissipation causes the heating of the glass.
- ii. In electric glass melting operations, the dielectric and the electromagnetic effects (the displacement current and the induced current) are neglected. Thus, it is assumed that the electric current is solely due to conduction.

##### **4.4.1.2 Derivation of the Transport Equation**

As per Ohm's law under conditions assumed above

$$\vec{J} = \sigma \vec{E} \quad (4.1)$$

where,  $\vec{J}$  is the current density ( $A.m^{-2}$ ),  $\vec{E}$  is the electric field intensity ( $V.m^{-1}$ ),  $\sigma$  is the electrical conductivity of the glass melt ( $S.m^{-1}$ )

Neglecting the electromagnetic effect, Faraday's law of induction can be written as:

$$\vec{\nabla} \times \vec{E} = 0 \quad (4.2)$$

Equation (4.2) implies that

$$\vec{E} = -\vec{\nabla}\phi \quad (4.3)$$

where,  $\phi$  is a scalar function called potential having units of volt.

On combining Equations (4.1) and (4.2), we get

$$\vec{j} = -\sigma\vec{\nabla}\phi \quad (4.4)$$

But according to Kirchoff's current law,

$$\vec{\nabla} \cdot \vec{j} = 0 \quad (4.5)$$

On combining Equations (4.4) and (4.5) we get;

$$\vec{\nabla} \cdot \sigma\vec{\nabla}\phi = 0 \quad (4.6)$$

Equation (4.6) is the basic transport equation for calculating electric variables (i.e. voltage, current, joule heat release in the molten glass)

Local rate of heat release per unit volume,  $Q_J$ , is given by:

$$Q_J = \vec{j} \cdot \vec{E} = \frac{j^2}{\sigma} = \sigma |\nabla\phi|^2 \quad (4.7)$$

Distribution of potential  $\phi$  using Equation (4.7) with appropriate boundary conditions is to be determined in order to calculate power dissipation.

#### 4.4.2 Heat Transfer

Heating in the JHCM is carried out in different ways. Start-up heating of pre-formed glass is carried out with silicon carbide resistance heaters. Once the glass reached a conducting temperature heating is carried by Joule heating by passing current between electrodes. The heat input to the system is measured with power supplied to the heaters. Based on the temperature measurements of outer surface heat losses are calculated. The heat losses from the water-cooled jackets and electrode air cooling are calculated based on inlet and outlet temperatures. An overall heat balance for the JHCM presents the boundary conditions to be applied in the model.

### 4.4.3 Cold cap Model

Under optimal steady-state conditions, the slurry feed is charged from above onto the surface of the cold cap to maintain its thickness. Each feed particle travels vertically down through the cold cap, experiencing increasing temperature in response to which its properties like density, dissolution rates of solids, reaction kinetics, keep changing. Thus, as the feed-to-glass conversion proceeds, the temperature, velocity, and extent of feed reactions are functions of the position along the vertical coordinate, and these variables do not change with time.

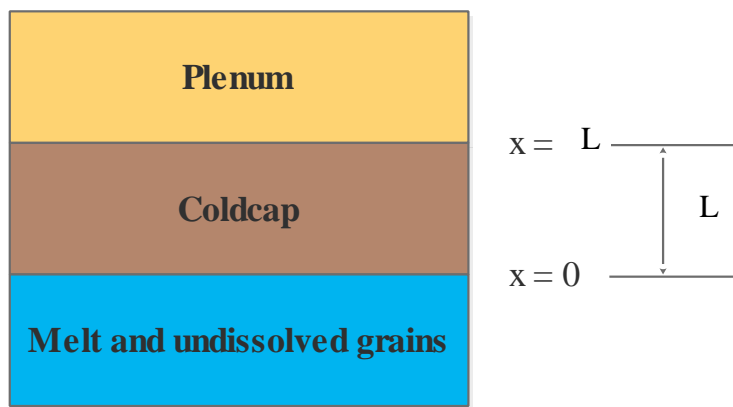


**Figure 4.2:** Cold Cap during Steady State Conditions

#### 4.4.3.1 Mass Balance

Neglecting the diffusion, the mass balance of both condensed phase and gas phase are

$$\frac{\partial \rho_c}{\partial t} + \frac{\partial(\rho_c v_c)}{\partial x} = r_c \quad (4.8)$$

$$\frac{\partial \rho_g}{\partial t} + \frac{\partial(\rho_g v_g)}{\partial x} = r_g \quad (4.9)$$

where,  $\rho$  – density ( $\text{kg/m}^3$ ),  $v$  – velocity ( $\text{m/s}$ ),  $r$  – mass change rate ( $\text{kg.m}^{-3}/\text{s}$ ),  $c$  - condensed phase, and  $g$  – gas phase.

By the mass conservation law, the total mass balance is

$$r_c + r_g = 0 \quad (4.10)$$

The mass fluxes,  $j_c$  and  $j_g$ , are defined as

$$j_c = -\rho_c v_c \quad (4.11)$$

$$j_g = \rho_g v_g \quad (4.12)$$

Because the condensed phase moves in a negative direction, the minus sign is used in Equations (4.11). The integral gas production and the total gas production are

$$N_g(x) = \int_0^x r_g dx \quad (4.13)$$

$$N_{gT} = \int_0^L r_g dx \quad (4.14)$$

where,  $x$  is the vertical coordinate with the origin at the cold-cap bottom (see Figure 4.2), and  $h$  is the total thickness of the cold cap.  $N_g(x)$  represents the gas production at a position  $x$ , and  $N_{gT}$  represents the gas flux leaving the cold cap from the top.

The degree of conversion in terms of gas production is defined as

$$\xi_g(x) = 1 - N_g(x) / N_{gTo} \quad (4.15)$$

With this definition, its value changes from 0 to 1.

According to the mass conversion law, the difference between the mass flux of the condensed phase to and from the cold cap (the mass loss) is:

$$\Delta j_c = j_{cL} - j_{c0} = N_{gTo} \quad (4.16)$$

where,  $j_{cL}$  is the mass flux of the condensed phase entering the cold cap on the top, and  $j_{c0}$  is the mass flux of the condensed phase leaving the cold cap from the bottom.

Accordingly, the mass flux of the condensed phase at any position is related to the degree of conversion in terms of gas and is expressed as

$$j_c(x) = j_{cL} - \Delta j_c \xi_g(x) \quad (4.17)$$

The mass flux of the gas phase can thus be also expressed using the degree of conversion and the mass loss of the condensed phase as

$$j_g(x) = \Delta j_c (1 - \xi_g(x)) \quad (4.18)$$

Satisfying the condition  $j_g(L) = \Delta j_c$

#### 4.4.3.2 Energy Balance

The reaction in the condensed phase involves a change in physicochemical state processes while the batch blanket is melting. Almost all such reactions are endothermic, and the required heat has to be supplied from an external source. Thus, the heating involves more than the total heat needed to raise the temperature of the batch from its feeding temperature to the temperature of glass melt. The process involves evaporation, denitration, the sensible heat of base glass and nitrates, calcination. Heat oxides to fusion temperature, raise the temperature of VWP to pouring temperature. Out of all the reactions, not all the reactions occur in cold cap.

Furthermore, many other processes with an impact on the temperature distribution are present during melting. To calculate the temperature distribution within the cold cap, the energy balance in bulk and gaseous phase was carried out

$$\rho_b C_{pb} \frac{\partial T_c}{\partial t} = \rho_b v_b C_{pc} \frac{\partial T_c}{\partial x} - \frac{\partial q_c}{\partial x} + H + s \quad (4.19)$$

$$\rho_g C_{pg} \frac{\partial T_g}{\partial t} = \rho_g v_g C_{pg} \frac{\partial T_g}{\partial x} - \frac{\partial q_g}{\partial x} - s \quad (4.20)$$

or in steady state form, Equations (4.19) and (4.20) have the form

$$\rho_b v_b C_{pc} \frac{\partial T_c}{\partial x} = - \frac{\partial q_c}{\partial x} + H + s \quad (4.21)$$

$$\rho_g v_g C_{pg} \frac{\partial T_g}{\partial x} = - \frac{\partial q_g}{\partial x} - s \quad (4.22)$$

where,  $T$  – temperature (K),  $C_c$  &  $C_g$  – heat capacities of condensed phase and gas phase respectively ( $\text{J.kg}^{-1}.\text{K}^{-1}$ ),  $H$  – heat source (in case of exothermic reactions) or heat sink (in case of endothermic reactions) ( $\text{W.m}^{-3}$ ),  $s$  – heat transfer between gas phase and condensed phase throughout cold cap ( $\text{W.m}^{-3}$ ).

The conductive heat fluxes can be expressed by the Fourier's law

$$q_c = -\lambda_c \frac{dT_c}{dx} \quad (4.23)$$

$$q_g = -\lambda_g \frac{dT_g}{dx} \quad (4.24)$$

where,  $\lambda_c$  and  $\lambda_g$  represent the effective values of heat conductivity of the condensed and gas phase, respectively, involving both conductive and radiative modes of heat transfer. The values of heat conductivity vary with the change in temperature and composition during melting. The change in temperature is also accompanied by the change in structure (such as porosity).

The same problem also applies to other parameters, e.g., heat capacity, reaction heat, and density. Equation (4.19) can be thus expressed as

$$\rho_b(T, \vec{\epsilon}) C_c(T, \vec{\epsilon}) \frac{\partial T_c}{\partial t} = -\rho_b(T, \vec{\epsilon}) C_c(T, \vec{\epsilon}) V_b \frac{\partial T_c}{\partial x} - \frac{\partial q_c(T, \vec{\epsilon})}{\partial x} + H(T, \vec{\epsilon}) + s \quad (4.25)$$

where,  $\vec{\epsilon}$  denotes the composition vector at each time.

The boundary conditions may be given in the term of fluxes, temperatures or both.

$$\rho_c(0) = Q_{Bo} \quad (4.26)$$

$$\rho_c(L) = Q_U \quad (4.27)$$

$$T(0) = T_{Bo} \quad (4.28)$$

$$T(L) = T_U \quad (4.29)$$

where,  $T_B$  and  $T_U$  represent the temperature on the bottom and the top of the cold cap, respectively, and  $Q_B$  and  $Q_U$  represent the heat fluxes to the bottom and from the top of the cold cap, respectively.

For the solution of heat and mass balance equations, we need to express the properties of the cold cap batch as a function of temperature and composition during melting. For solving the differential, the finite difference has been used as stated by Schill due to the simplicity and accuracy of its solution which is far better than any other method. Here, the explicit finite difference technique is used and the equation being

$$\rho_{bi}^m c_{bi}^m \frac{T_i^{m+1} - T_i^m}{\tau} = (j_{bi}^m c_{bi}^m - j_{gi}^m c_{gi}^m) \frac{T_{i+1}^m - T_{i-1}^m}{2\delta} + j_{i+}^k \frac{T_{i+1}^m - T_{i-1}^m}{\delta^2} - j_{i-}^k \frac{T_i^m - T_{i-1}^m}{\delta^2} + H_i^m \quad (4.30)$$

where,  $i$  - states the distance instance ( $i=2, \dots, N-1$ ),  $k$ - time instance and

$$\lambda_{i+}^k = \frac{\lambda_i^k + \lambda_{i+1}^k}{2} \quad (4.31)$$

$$\lambda_{i-}^k = \frac{\lambda_i^k + \lambda_{i-1}^k}{2} \quad (4.32)$$

The  $\delta$  represent the distance step and  $\tau$  represents the time step for solving the finite difference equation. For solving the above equation, a time step of 0.1s and a distance step of 1mm is considered. The equations were solved.

For solving the differential equations, properties of the material are to be expressed in terms of temperature and composition. Degree of conversion is determined from mass loss fraction and incorporated in the numerical model. The mass loss fraction is obtained from the Thermo-Gravimetric Analysis (TGA) of the glass measuring the condensed and gas phase flow rate for 10 K.min<sup>-1</sup>, 20 K.min<sup>-1</sup>, 30 K.min<sup>-1</sup> and 40 K.min<sup>-1</sup>.

The TGA analysis of the rate of mass loss was high beyond 948 K, it was observed that there was a drastic decrease in the mass of the sample. The condition is the same for all the four temperature rates except for the mass loss rate variation according to the temperature of heat. The obtained results were used to calculate the degree of conversion using the equation

$$\xi_g = \frac{ma(T) - ma_u}{ma_f - ma_u} \quad (4.33)$$

where  $ma(T)$  is the mass of the sample at the particular temperature and  $m_f$  is the initial mass of the sample and  $m_M$  being the final mass of the glass.

#### 4.4.4 Rate Kinetics

##### 4.4.4.1 Model development for thermal decomposition of constituents of feed to the melter

The  $n^{\text{th}}$  order reaction kinetics satisfactorily describes most of solid to solid and gas conversion reaction monitored by TG and Differential Thermogravimetry (DTG). In TG-DTG, the change in mass content and thermal properties of the sample is indicated by a deflection or peak. If the reaction proceeds at a rate varying with temperature, it is evident that it possesses activation energy. The position of the peak varies with the heating rate if experimental conditions are fixed. The variation in peak temperature ( $T_z$ ) is used to determine the activation energy ( $E$ ). The kinetics of reactions in solid-state is described by the equation

$$\frac{d\alpha_d}{dt} = f_d(\alpha_d)A_d \exp\left(-\frac{E_d}{RT}\right) \quad (4.34)$$

where,  $f_d(\alpha_d) = (1 - \alpha_d)^{n_d}$

$\alpha_d$  is the degree of conversion of  $d^{\text{th}}$  reaction,  $t$  time in seconds,  $A_d$  is the pre-exponential factor in  $s^{-1}$ ,  $E_d$  is the activation energy of  $d^{\text{th}}$  reaction in  $J \cdot mol^{-1}$ ,  $R$  is the

universal gas constant in  $\text{J.mol}^{-1}.\text{K}^{-1}$ ,  $T$  is the temperature in Kelvin and  $n_d$  is the order of the reaction of  $d^{\text{th}}$  reaction.

Substituting  $f_d(\alpha_d)$  in Equation (4.34), we obtain

$$\frac{d\alpha_d}{dt} = A_d(1 - \alpha_d)^{n_d} \exp\left(-\frac{E_d}{RT}\right) \quad (4.35)$$

In his seminal paper to determine reaction kinetics, Kissinger developed a method to estimate  $E_d$ , for simple decomposition reaction regardless of reaction order by making differential thermal analysis patterns at several heating rates ( $\theta = dT/dt$ ). Substituting  $dt$  with  $dT/\theta$  in Equation (4.35) [84]. To determine degree of conversion as a function of temperature, Equation (4.35) is integrated, assuming a constant heating rate. The degree of conversion of  $d^{\text{th}}$  reaction is given by the following equation

$$\alpha_d = 1 - \left[1 + \frac{(n_d-1)A_d}{\theta} \int_0^T \exp\left(-\frac{E_d}{RT}\right) dT\right]^{1/(1-n_d)} \quad (4.36)$$

where  $\theta$  is the heating rate in  $\text{K.s}^{-1}$

The resulting integral was exponential integral, and a simple expression cannot be obtained. A satisfactory approximation is obtained using successive integration by parts after considering only first two terms in converging series of Equation by considering the weight of  $i^{\text{th}}$  reaction ( $w_i$ , fraction of mass loss in  $i^{\text{th}}$  reaction [30]).

$$\frac{d\alpha}{dT} = \frac{1}{\theta} \sum_i^y w_i A_i \left[1 + \frac{(n_d-1)A_d}{\theta} \left(1 - \frac{2RT}{E_d}\right) \exp\left(-\frac{E_d}{RT}\right)\right]^{n_d/(1-n_d)} \exp\left(-\frac{E_d}{RT}\right) \quad (4.37)$$

In multiple reaction systems that are mutually independent in a wide temperature range ( $T = T_0 + \theta t$ ), change of conversion concerning temperature  $\frac{d\alpha}{dT}$  is expressed in terms of

$$\frac{d\alpha}{dT} = \frac{1}{\theta} \sum_d^y w_d A_d (1 - \alpha_d)^{n_d} \exp\left(-\frac{E_d}{RT}\right) \quad (4.38)$$

where  $\alpha = \sum \alpha_d$ ,  $w_d$  is the weight-fraction of material reacted in  $d^{\text{th}}$  reaction and  $y$  indicates the major reactions.

As the temperature rises during the reaction, reaction rate  $\frac{d\alpha_d}{dt}$  will rise to a maximum value, then returns to zero as shown in Fig. 3(B). If the temperature rises at a constant rate, differentiating Equation (4.35) with time  $\frac{d^2\alpha_d}{dt^2}$  and equating it to zero provides the maximum reaction rate. Hence, by differentiating Equation (4.35) and applying natural log

$$\ln \frac{E_d \theta}{RT_{dz}^2} = -\frac{E_d}{RT_{dz}} + \ln A_d n_d (1 - \alpha_d)^{n_d} \quad (4.39)$$

where  $T_{dz}$  is the temperature of peak maximum in DTG curve.

According to Equation (4.39), a plot between  $\ln(\theta/T_{dz}^2)$  and  $1/T_{dz}$  should lead to a straight line and slope of Equation (4.39)

$$\frac{E_i}{R} = -\frac{d(\ln(\theta/T_{dz}^2))}{d(1/T_{dz})} \quad (4.40)$$

where, subscript  $z$  denotes the peak maximum.

Activation energy ( $E$ ) is determined from a plot between  $\ln(\theta/T_{dz}^2)$  and  $1/T_{dz}$  for a series of experiments at different heating rates ( $\theta$ ).

Applying Equation (4.37) for a single peak,  $d=1$

$$\frac{d\alpha}{dT} = \frac{1}{\theta} wA \left[ 1 + \frac{(n-1)A}{\theta} \left( 1 - \frac{2RT}{E} \right) \exp\left(-\frac{E}{RT}\right) \right]^{n/(1-n)} \exp\left(-\frac{E}{RT}\right) \quad (4.41)$$

The activation energy obtained from Equation (4.40) is substituted in Equation (4.41) to determine pre-exponential factor, fraction of material reacted, and order of the reaction. To evaluate  $\frac{d\alpha}{dT}$ , all the points in the TG curve are selected to cover complete reaction for each peak. The evaluated  $\frac{d\alpha}{dT}$  is subtracted from the experimentally obtained change of conversion with respect to temperature data. The

resultant error is squared. The sum of the squares of all the errors are partially differentiated with respect to A, w & n and the resultant equations are solved simultaneously. The numerical calculations were solved using non-linear least square solver.

#### **4.5 Mathematical Modelling of Joule Heated Ceramic Melter**

The model uses heat transfer physics with discrete ordinates method (DOM) of evaluation for the surface to surface radiation. It employs hemi cube method of estimating radiation patches as the geometry is highly occluded. The discretisation scheme used for temperature estimation is quadratic while that of surface radiosity is linear. The heat source term (volumetric) is given in the plenum heater socket and the heat loss term is incorporated on the respective surfaces. The losses are mainly by convective cooling and surface to ambient radiation. An off gas nozzle has been created by deleting the volumetric entities at the desired location and sufficient loss terms have been added to the same as using convection. The 16 numbers of probes for estimating the glass pool temperatures are located in the model at the same location as that of the experimental setup.

##### **4.5.1 Assumptions**

The following assumptions were made for developing the model

- 4.5.1.1. Modelling one - half of the melter is sufficient, due to its symmetric nature about a vertical plane in the middle of the electrodes
- 4.5.1.2. Bottom most refractories and draining electrodes are not incorporated in the model, as they are not in the region of interest
- 4.5.1.3. The outermost 6 mm SS layer is neglected to avoid thin layer meshing problems. This layer contributes only 3% of the heat capacity of the system
- 4.5.1.4. The plenum heater is considered to be ideal (100 % efficient)
- 4.5.1.5. There is no air gap between the insulation layers, making them opaque to radiation.

- 4.5.1.6. The variation of specific heat of the insulation layers with temperature is neglected.
- 4.5.1.7. Local cooling effect of PCW is not considered as the losses contribute only after they exit the melter system under study.
- 4.5.1.8. Heap formation of the glass frit in the melter is neglected.

#### **4.5.2 Model Geometry**

The first step in creating a model is to create an appropriate geometry. The 3D geometry was constructed with the dimensions of the ceramic melter as shown in

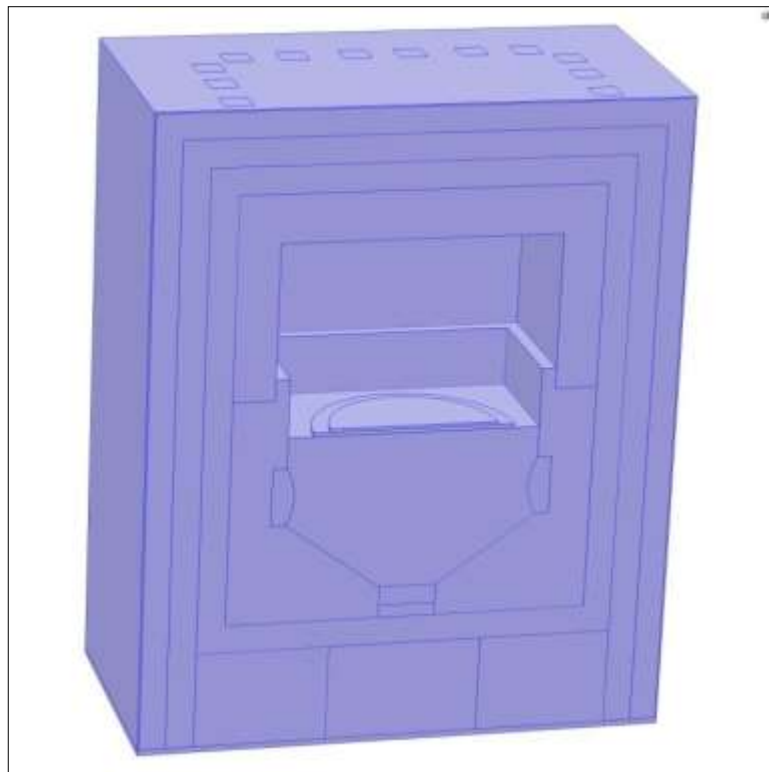


**Figure 4.3:** Geometrical replica of the actual melter used in the model

Figure 4.3. The freeze valves, the lower electrodes in the drain region were not considered into the model as it is out of our region of interest.

#### **4.5.3 Domain Specification of the model**

The following are domain specifications given as input to the software. Each domain is assigned with a specific material property that is used for the computation.

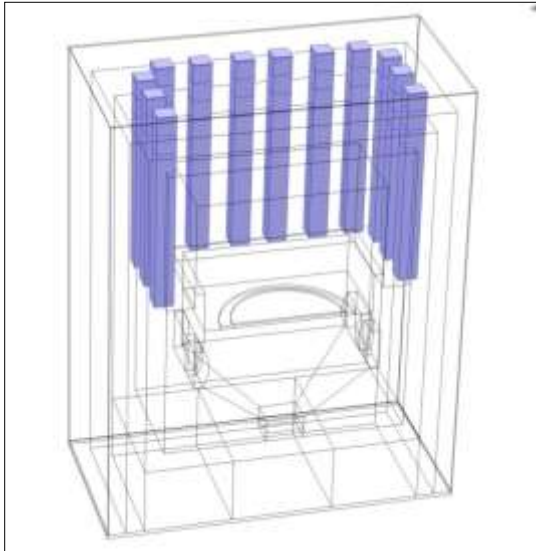


**Figure 4.4:** Silicon Carbide resistance heaters as power source in color

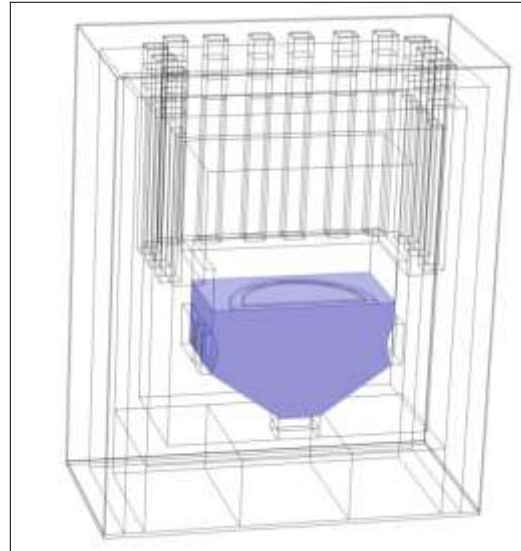


**Figure 4.5:** Cavity of melter

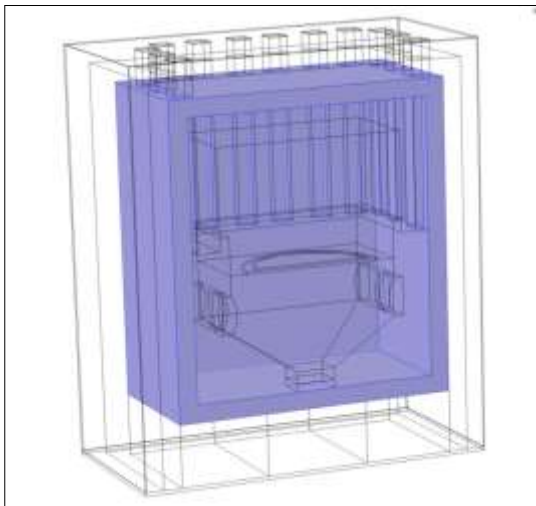


**Figure 4.6:** Refractory layer-1 in color

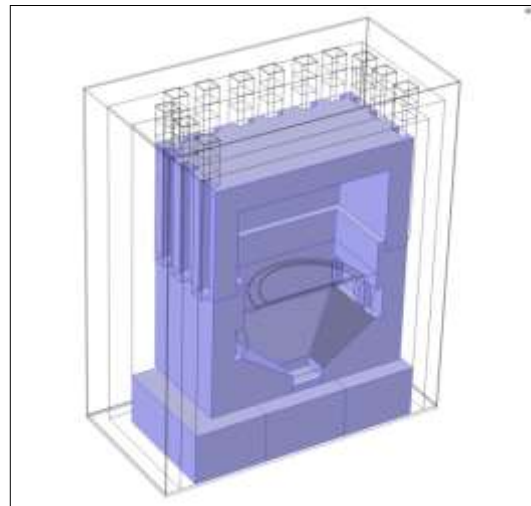


**Figure 4.7:** Insulation layer 1 in highlighted state

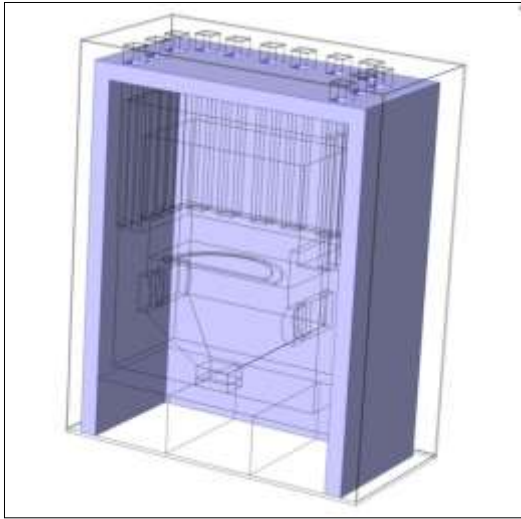


**Figure 4.8:** Insulation layer 2 in highlighted state

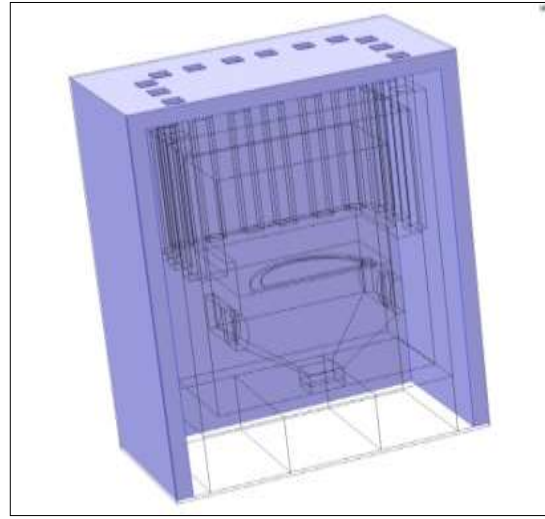


**Figure 4.9:** Insulation layer 3 in highlighted state

The various domains used in the model are shown in Figure 4.3 to Figure 4.9

#### **4.5.4 Mesh independence Studies**

Symmetry boundary condition was incorporated for the open face of the model. The tetrahedral mesh is used for meshing. The 3D geometry is meshed based on the geometry, physics, dimensions and positions. The mesh dependency study is carried out with coarse (mesh elements - 51528), normal (mesh elements - 104980), fine (mesh elements - 187064) and finer mesh (mesh elements - 280904).

The temperature profiles of thermocouple 1 to 16 were compared with 395 W power supply on each heater. It was observed that the values between finer and fine mesh did not vary much whereas, for normal and coarse mesh, the deviation of around 8 % and 15 % was observed compared to the finer mesh as shown in Figure 4.10. Hence, fine mesh is chosen in this study.

COMSOL detects the geometry and predicts the type of mesh suitable for geometry based on physics involved, dimensions and positions. A total number of 187064 tetrahedral elements were created in the model.

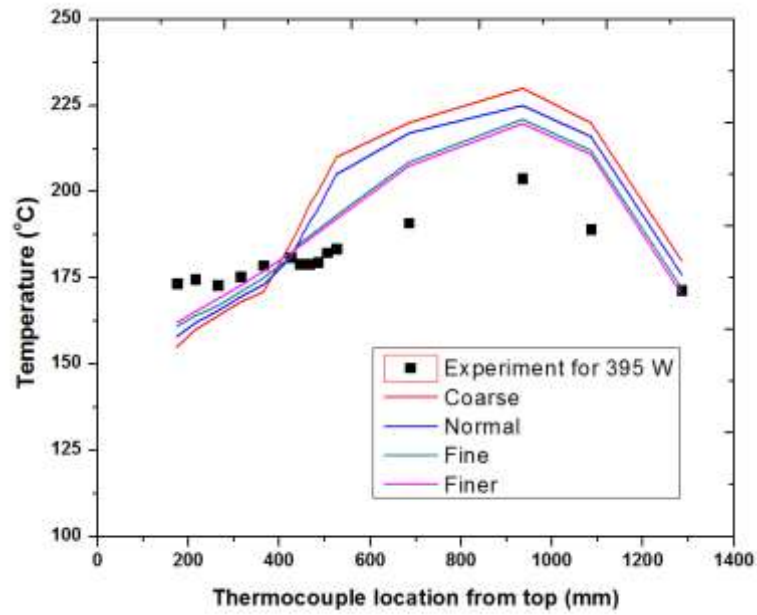


**Figure 4.10:** Mesh independence studies

Minimum element quality is 0.01162, which is present on the cold cap region. An average mesh quality 0.516 was achieved as shown in Figure 4.11. The mesh statistics obtained are given in Table 4.2.

**Table 4.2:** Mesh statistics of the model

<b>Mesh statistics</b>	
<b>Description</b>	<b>Value</b>
<b>Minimum element quality</b>	0.001162
<b>Average element quality</b>	0.516
<b>Tetrahedral elements</b>	187064
<b>Triangular elements</b>	57369
<b>Edge elements</b>	4447
<b>Vertex elements</b>	446

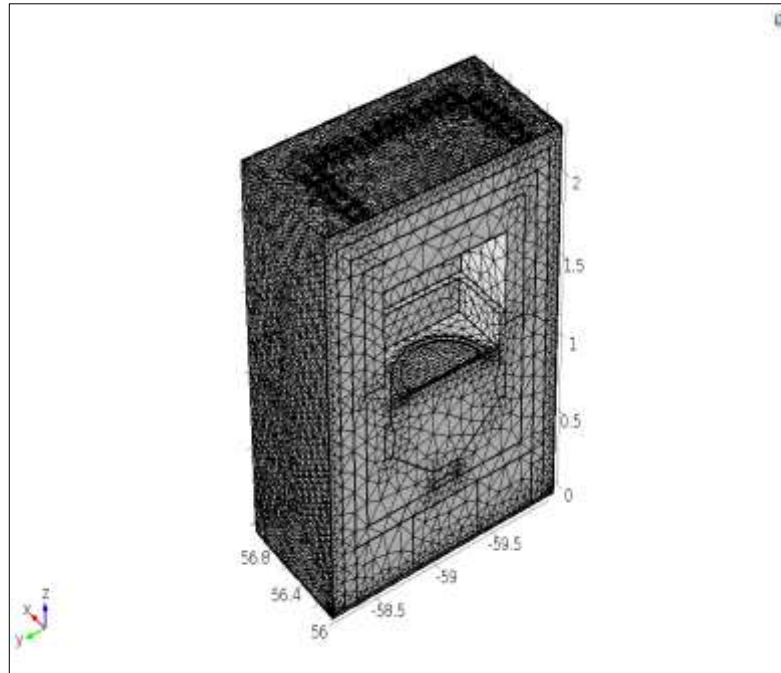


**Figure 4.11:** Meshing of the model

#### **4.5.5 Measurements for validation**

The validation of the model requires temperature estimation inside the cavity. The 16 thermocouples placed inside the melter cavity were used to record the temperature at various heights. The validation by the surface temperature of the melter was done by averaging the temperature plot over the desired surface.

#### **4.6 Model development for Joule Heated Ceramic Melter**

The modelling of Joule melter is an unsteady state heat transfer problem with the surface to surface radiation incorporated on the interior walls of the melter cavity and is constructed using FEM. Surface to Surface model was incorporated to perform computationally effective simulations, it is possible to define planes or sectors of symmetry in this method. When combined with a moving frame, the surface-to-surface radiation interface automatically updates the view factors as the geometrical configuration deforms.

The heat loss terms are incorporated on the outer most surfaces as convective cooling losses and surface to ambient radiation losses. A 3D geometry has been constructed

with dimensions of the actual JHCM, as shown in Figure 4.12. The total heat input is given as a uniformly distributed volumetric heat source, and temperature profiles are generated.

The mathematical model treats the heat balance using the standard parabolic heat equation (Pepper and Heinrich 1992)[85]. The model provides an insight into transient

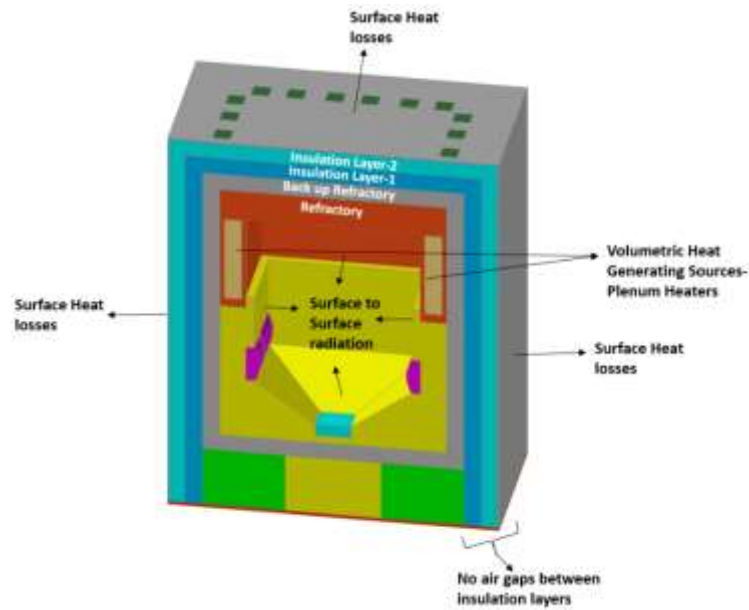


**Figure 4.12:** 3D Geometry of JHCM used in the model and boundary conditions for stage- I & II and steady-state behaviour of the melter from start-up conditions to steady-state operating conditions

#### 4.6.1 Modelling of stage – I and stage – II

The model equation includes surface to surface radiation involved, conduction problem with heat losses by convection and radiation across various insulation layers and the model is specific to Joule melter with PH located at the top. The coupled differential equations were solved numerically for surface Radiosity,  $J$  and temperature,  $T$  using the iterative, robust, memory efficient Parallel Sparse Direct Solver (PARDISO). The developed model provides transient behaviour of Joule Melter from the start-up conditions to the steady-state conditions.

### 4.6.2 Governing Equations

The main governing equation is

$$\rho C_p \frac{\partial T}{\partial t} - \nabla \cdot (k \nabla T) = Q \quad (4.42)$$

where  $\rho$  - density ( $\text{kg.m}^{-3}$ ),  $C_p$  - specific heat capacity ( $\text{J.kg}^{-1}.\text{K}^{-1}$ ),  $Q$  - heat rate ( $\text{J.s}^{-1}$ ),  $k$ - thermal conductivity ( $\text{W.m}^{-1}.\text{K}^{-1}$ ) and  $T$  - Temperature (K).

$$-\hat{n} \cdot (-k \nabla T) = h \cdot (T_{amb} - T) + \varepsilon \cdot \sigma_{sb} \cdot (T_{amb}^4 - T^4) \quad (4.43) \text{ Heat}$$

losses by convection and radiation from the side, top and bottom walls are independently incorporated as given by Equation (4.43).

$$-\hat{n} \cdot (-k \nabla T) = \varepsilon \cdot (G - \varepsilon e_{bl}(T)) \quad (4.44)$$

$$(1 - \varepsilon) \cdot G = J_{su} - \varepsilon e_{bl}(T) \quad (4.45)$$

$$e_{bl}(T) = n^2 \sigma_{sb} T^4 \quad (4.46)$$

Surface to surface radiation for cavity is also incorporated as given by Equations (4.44) to (4.46), where  $h$  is the heat transfer coefficient ( $\text{W m}^{-2} \text{K}^{-1}$ ),  $T_{ext}$  is the external temperature (K),  $\varepsilon$  surface emissivity and  $\sigma$  is the Stefan Boltzmann constant.

### 4.6.3 Boundary Conditions

A three-dimensional coordinate system is used for computation. The initial temperature on all the boundaries is 298 K. Constant heat flux from the Kanthal<sup>®</sup> tubes is assumed for computation. Conjugate heat transfer is given as boundary condition for skin losses from the outer surfaces. Convective heat transfer coefficient of 8, 5, 4  $\text{W.m}^{-2}.\text{K}^{-1}$  is evaluated theoretically for side, top and bottom walls respectively and incorporated in the model.

### 4.6.4 Assumptions made for modelling of stage – I and stage – II

Following assumptions were made for developing the model

- i. The PH module is considered to be ideal, transferring all the heat generated to the surrounding refractory.
- ii. The PH module is smeared out into a volume source, though the heating element is in the shape of a U bar. This is to avoid computational difficulty, as the PH is small in size (1:1000) compared to the JHCM.
- iii. There are no air gaps between the insulation layers, making them opaque to radiation.

The model uses heat transfer physics with discrete ordinates method (DOM) of evaluation for the surface to surface radiation [53]. It employs hemicube method of estimating radiation patches as the geometry is highly occluded. The discretisation scheme used for temperature estimation is quadratic, while that for surface radiosity is linear. The volumetric heat source term is given in the plenum heater socket, and heat loss terms are incorporated on the respective surfaces. The mesh element size distribution of the PH & melter are as shown in Figure 4.14 and Figure 4.13, respectively. The losses are mainly by convective cooling and surface to ambient radiation. An off-gas nozzle has been created at the top surface by deleting the volumetric entities at the desired location, and the loss terms have been added using convection. The heat transfer coefficients of bottom, top and the walls of the melter were estimated and were 1.2, 1.7 and 5  $\text{W}\cdot\text{m}^{-2}\cdot\text{K}$  respectively.

Sixteen numbers of probes are located as shown in the Figure 4.15 in the model for estimating the glass pool temperatures at positions similar to the thermocouples in the experimental set up shown in Figure 3.5

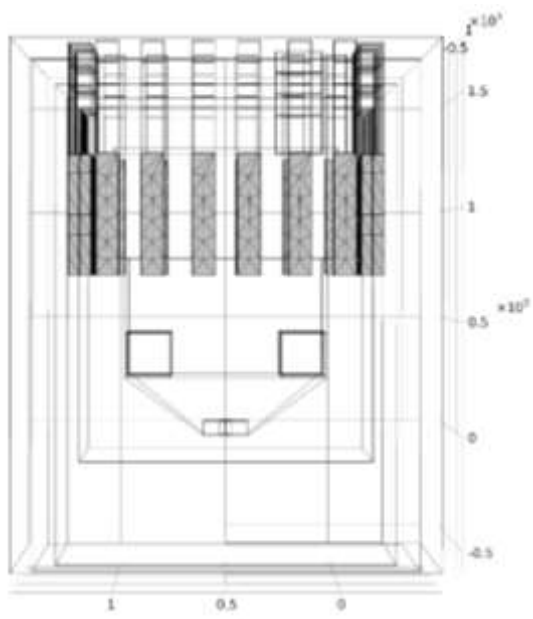


**Figure 4.13:** Finer Meshing for the Plenum heater Domain

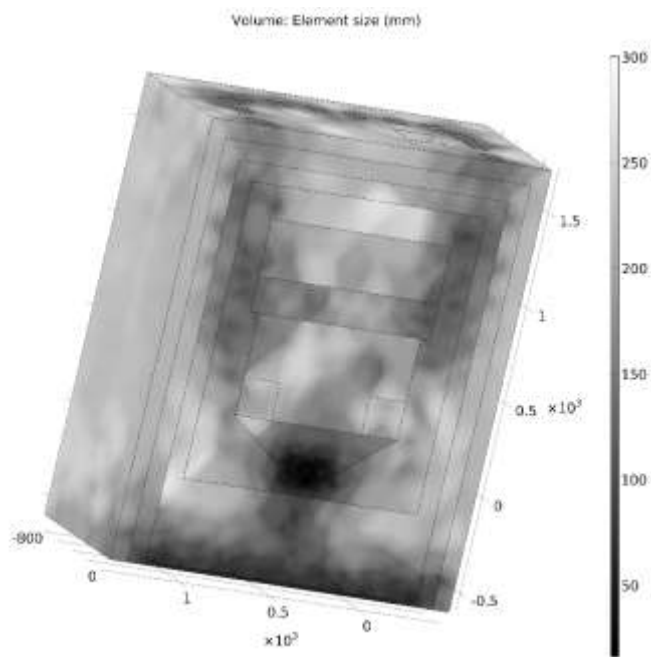


**Figure 4.14:** Mesh Element size distribution

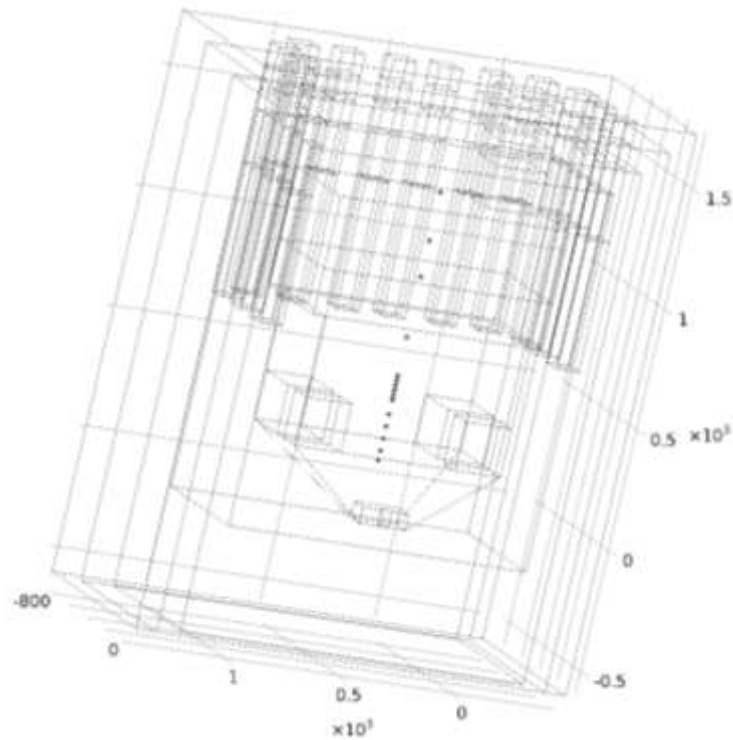


**Figure 4.15:** 16 thermocouples in model used for validation of the model

## **4.7 Modelling of Stage - III**

### **4.7.1 Assumptions made for modelling of Stage – III**

- i. Molten glass is considered as an incompressible Newtonian fluid
- ii. Variation in density due to temperature by Boussinesq approximation
- iii. Viscous heat dissipation effects are negligible
- iv. The cold cap is considered as a heat sink
- v. The thickness of the cold cap is estimated by sub-model given by Pokorný et al., (2012) [43] and incorporated in the model as two different zones. Boiling liquid and calcined mass are considered as two different zones.
- vi. The decay heat is not considered as the experiments were carried out with simulated chemicals. If significant decay heat is present, then this can be incorporated in the model by compensating it with heat input given to the system.

## 4.7.2 Governing equations for the model

The three – dimensional unsteady state mass conservation, Navier – Stokes equation, energy equation, diffusion equation and Laplace equation for the scalar field of electrical potential  $\phi$ . The main focus is to evaluate the governing equations and to obtain the unknown of the system. The focus is to find the unknowns temperature (T), velocity (u), Current density (J) and concentration (c) in the JHCM.

### 4.7.2.1 Electrical

A constant Potential V (volts) is applied between electrodes, based on molten glass electrical properties current density distribution J, which is heating the melt due to Joule effect with the volumetric heat input  $J^2/\sigma$ . The electrical potential is solved in glass melting zone

$$\nabla \cdot \vec{J} = Q_J \quad (4.47)$$

$$\vec{J} = \sigma \vec{E} + \vec{J}_{el} \quad (4.48)$$

$$\vec{E} = -\nabla V \quad (4.49)$$

$$Q_J = \vec{J} \cdot \vec{E} \quad (4.50)$$

Where J is current density ( $A.m^{-2}$ ),  $Q_J$  is current source ( $A.m^{-3}$ ),  $\sigma$  is specific conductivity ( $S.m^{-1}$ ), E is the electric field intensity ( $V.m^{-1}$ ) and V is the voltage (V)

### 4.7.2.2 Heat Transfer

The energy equation is solved to determine the temperature T on the melter structure that includes molten glass, glass contact refractory, plenum region and insulation layers and the outer surface of the melter. The temperature gradient is developed due to heat losses at the surface of JHCM, and temperature gradients develop in the melt.

#### 4.7.2.2.1 Heat transfer in Solids

The heat transfer between the molten glass and other insulation layers are by conduction and heat losses from the outer surface is by convection and radiation

$$\rho C_p \frac{\partial T}{\partial t} + \rho C_p v \cdot \nabla T + \nabla \cdot q = Q_J \quad (4.51)$$

$$q = -k \nabla T \quad (4.52)$$

Convective losses on outer surface

$$-(k \nabla T) \cdot \hat{n} = h(T - T_{amb}) \quad (4.53)$$

Radiative heat losses from hot surfaces

$$-(k \nabla T) \cdot \hat{n} = \varepsilon \sigma_{sb}(T^4 - T_{amb}^4) \quad (4.54)$$

where  $\rho$  is density ( $\text{kg m}^{-3}$ ),  $C_p$  is specific heat capacity ( $\text{J.kg}^{-1}.\text{K}^{-1}$ ),  $u$  is the velocity ( $\text{m.s}^{-1}$ ),  $q$  - heat rate ( $\text{J.s}^{-1}$ ),  $k$ - thermal conductivity ( $\text{W.m}^{-1}.\text{K}^{-1}$ ),  $T$  - Temperature (K)

#### 4.7.2.2.2 Heat transfer in liquids

The heat transfer in the molten glass is by conduction and convection. The heat generated from the electrical currents  $Q_J$ . The molten glass is treated as incompressible Newtonian fluid. Buoyancy forces are considered based on Boussinesq approximation, which is valid for molten glass in the range of 979 to 1473 K with an error of 2.5 % compared with buoyancy force based on density variation [63].

$$\rho C_p \frac{\partial T}{\partial t} + \rho C_p v \cdot \nabla T + \nabla \cdot q = Q_J \quad (4.55)$$

$$q = -k \nabla T \quad (4.56)$$

$T$  is the temperature of molten glass (K).

### 4.7.2.3 Momentum transfer

The three –dimensional transient flow is governed by the mass conversation equation and Navier – Stroke equation. The variation of density of molten glass is considered by Boussinesq approximation

Mass conservation

$$\nabla \cdot (\rho v) = 0 \quad (4.57)$$

Navier-Stokes equation

$$\nabla \cdot \left( \rho v \frac{dv}{dt} \right) = -\nabla \cdot p + [\mu(\nabla v + \nabla v^{Tr})] + J \times B - \rho\beta(T - T_u)g \quad (4.58)$$

### 4.7.2.4 Chemistry

The reaction rate of M<sup>th</sup> species for converting into the product is given below

$$Rr_M = \sum_d Rr_{Md} \quad (4.59)$$

### 4.7.2.5 Mass transfer (Transport of diluted species)

The three –dimensional transient flow is governed by the mass conversation equation and is given by diffusion-convection equation as a time-dependent concentration function

$$\nabla \cdot ((-D_M \nabla c_M) + v \cdot \nabla c_M) + \frac{dc_i}{dt} = Rr_M \quad (4.60)$$

$$N_M = -D_M \nabla c_M + v c_M \quad (4.61)$$

$N_i$  - Concentration flux of i<sup>th</sup> component (mol/m<sup>2</sup>.s),  $D_i$  – Diffusivity of i<sup>th</sup> component (m<sup>2</sup>/s), t-time (s), c - concentration (mol/m<sup>3</sup>), R - Reaction rate.

The thickness of the cold cap is obtained by solving mass and energy balance equations given in Pokorny & Hrma, (2012) coupling with experimental results iteratively[43]. This yields a cold cap containing 2 layers viz., boiling liquid of 4.1 cm and calcined mass of 4.3 cm.

Also, there are heat losses due to radiation from the boundary surfaces of the domains and the equations incorporated in the model accounting the heat losses are given by (Pepper and Heinrich 1992)

$$-nr \cdot q = \varepsilon(G - e_{bl}(T)) \quad (4.62)$$

$$(1 - \varepsilon)G = J - \varepsilon e_{bl}(T) \quad (4.63)$$

$$G = G_{mu}(J) + G_{amb} + G_{ext} \quad (4.64)$$

$$G_{amb} = F_{amb}e_{bl}(T_{amb}) \quad (4.65)$$

$$e_{bl}(T) = n^2\sigma_{sb}T^4 \quad (4.66)$$

In the absence of reliable correlations for heat transfer coefficients incorporating calcined mass and molten glass, the energy distribution is given in the form of boundary conditions to the model.

### **4.7.3 Boundary Conditions for Stage - III**

A three-dimensional time dependent coordinate system is used for computation. The initial temperature on all the boundaries is 298 K. Constant heat flux from outer surface is assumed for computation based on the heat transfer coefficients calculated. Conjugate heat transfer is given as boundary condition for skin losses from the outer surfaces. Heat transfer coefficient of molten glass parametric variable and the initial value is evaluated theoretically and incorporated in the model.

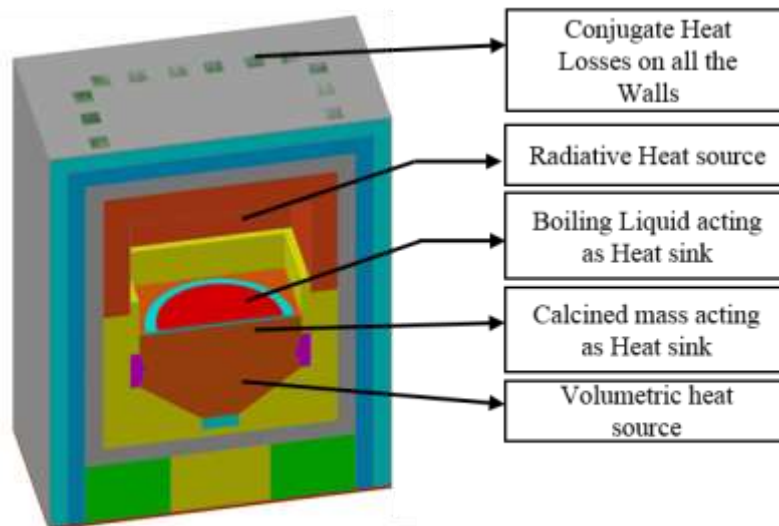


**Figure 4.16:** 3D Geometry of JHCM used in the model and boundary conditions for stage- III

### Numerical Simulations

The calculations were performed for the composition of  $\text{SiO}_2$ -48%,  $\text{B}_2\text{O}_3$ -26.3%,  $\text{Na}_2\text{O}$ -11.7%,  $\text{TiO}_2$ -9.5%,  $\text{Fe}_2\text{O}_3$ -4.5%. The thermo physical properties have been measured and are presented in Table 4.1. All the other parameter settings are in Table 4.2. The coupled effect of Equation. (4.48) to (4.62) were solved using commercial software COMSOL which developed to calcined coupled electrothermohydranamic effects. The discretization of the governing equations was done by finite element method. The pressure and velocity were decoupled by SIMPLE algorithm. Default settings for under relaxation factors (relative tolerance-0.01, absolute tolerance-0.001 and time stepping-0.001s) were used. The calculations were terminated if the residues of the parameters viz., velocity, energy, concentration and electric field are smaller than  $10^{-4}$ . The physics controlled meshing was used. The meshing throughout volume is done using Delaunay-based mesh generator algorithm. The mesh analysis performed results in the usage of fine mesh, which maps all parameters and material properties satisfactorily. The meshes were validated with the experimentally measured temperature profile of GP-01 to GP-16.

#### **4.8 Closure**

A three-dimensional numerical model of JHCM used for vitrification of RLW was developed by solving governing equations. Electrical, heat, flow and mass transfer fields are coupled in the molten glass pool. Mesh dependency studies were carried out, and a fine mesh is used for all the simulations. The model validation with experimental data is presented in the next chapter.

# CHAPTER-5

## RESULTS AND DISCUSSION

# CHAPTER-5

## 5 RESULTS AND DISCUSSION

### 5.1 Estimation of the Physical and Chemical Properties of Glass

The estimation of physical and chemical properties of the materials that make up the system is vital for building a model. These properties influence the accuracy and ability of the model in simulating and predicting the actual performance of the system.

#### 5.1.1 Viscosity

The glass melt is assumed to be Newtonian fluid with constant heat capacity  $C_p$ . The viscosity  $\eta$  (T) being an exponential functions of the temperature, was determined experimentally as described earlier in chapter – 3 and the results are presented in Figure 5.1. The approximated Vogel – Fulcher – Tammann equation model was used for describing the temperature dependence of viscosity. The values have been obtained by fitting the experimental results and the constants A, B, and C have been determined and presented below

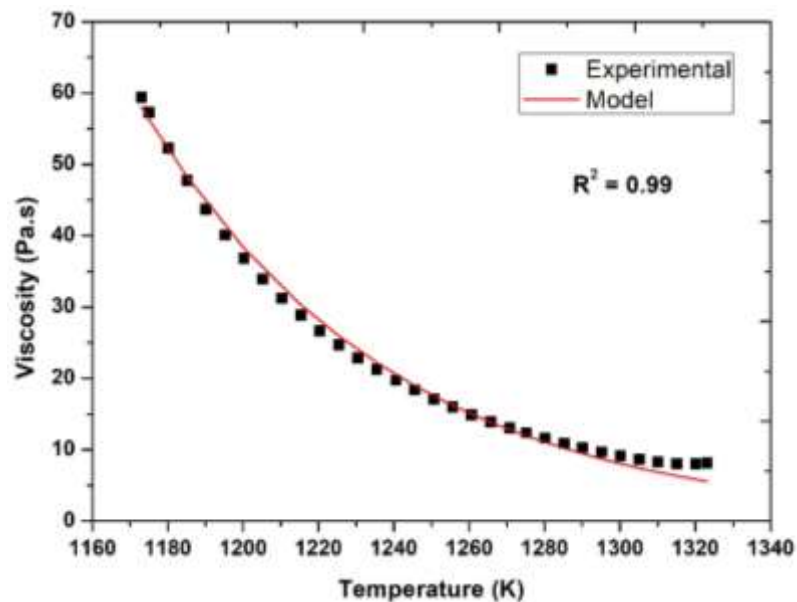
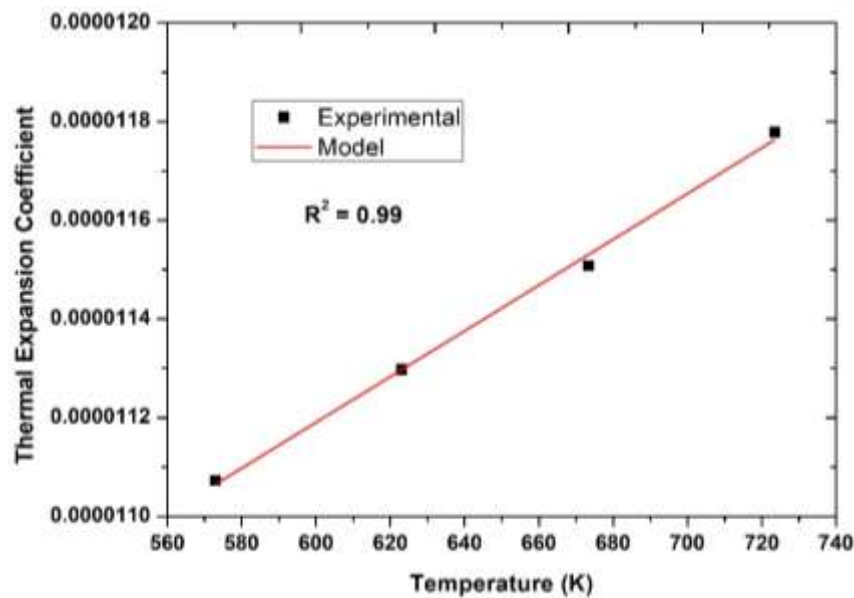


Figure 5.1: Variation of viscosity with temperature

$$\text{Viscosity } (\eta, \text{ Pa.s}) = \exp \left\{ -0.991 + \frac{19723419}{1 + \left( \frac{T}{1.209} \right)^{2.327}} \right\}$$

### 5.1.2 Thermal Expansion of Glass

Dilatometric measurements are carried out to obtain the thermal properties of the glass like transition temperature and coefficient of thermal expansion. The linear thermal expansion measurements were made on pellet (12.20 mm height and 12.95 mm diameter) and were carried out by using a dilatometer, in the temperature range of 570–730 K and the results are presented in Figure 5.2. Linear variable differential transformer (LVDT) was used as the displacement sensor [86].



**Figure 5.2:** Thermal Expansion of Glass in the Temperature Range 570–730 K

### 5.1.3 Resistivity of Glass

Electrical Conductivity in the molten glass is mainly due to the presence of alkali metal ions responsible for electrolytic conduction of ionic species. Glass resistivity influences the design of the melter and the power supply system sizing. Significant variation occurs in the glass resistivity during the treatment of nuclear waste. Studies were carried out to determine the electrical conductivity by four point probe method. An equation was fitted to experimental data and presented in Figure 5.3.

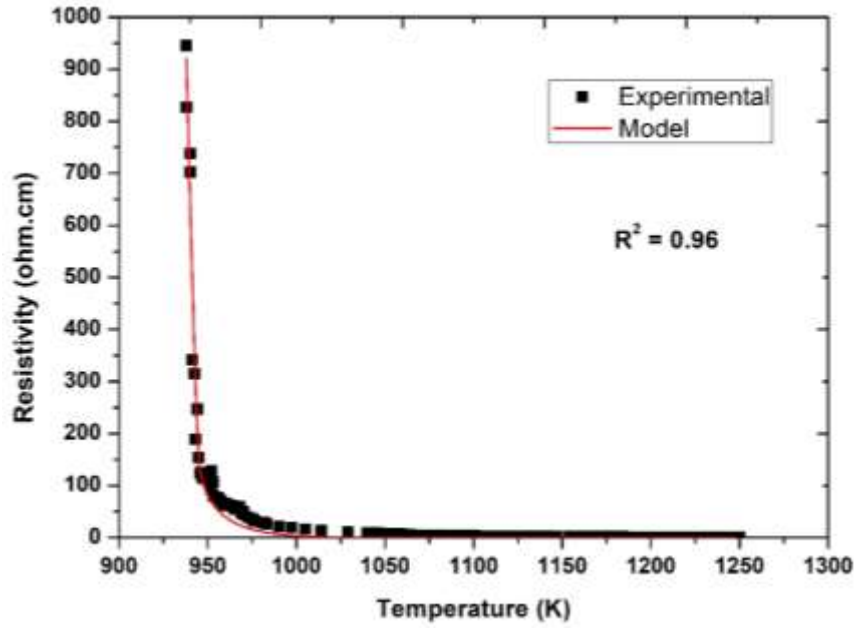


**Figure 5.3:** Variation of Resistivity with temperature

$$\text{Electrical conductivity } (\sigma, \text{ S/m}) = 49115.23 - \frac{49133.613}{1 + \left(\frac{T}{1396.366}\right)^{6.983}}$$

The electrical resistivity is determined as function of Na<sub>2</sub>O concentration and an equation was fitted for change in resistivity as function of Na<sub>2</sub>O in base glass concentration.

$$\text{Electrical resistivity } (\vartheta, \Omega.m) = 31.012e^{-0.088wp}$$

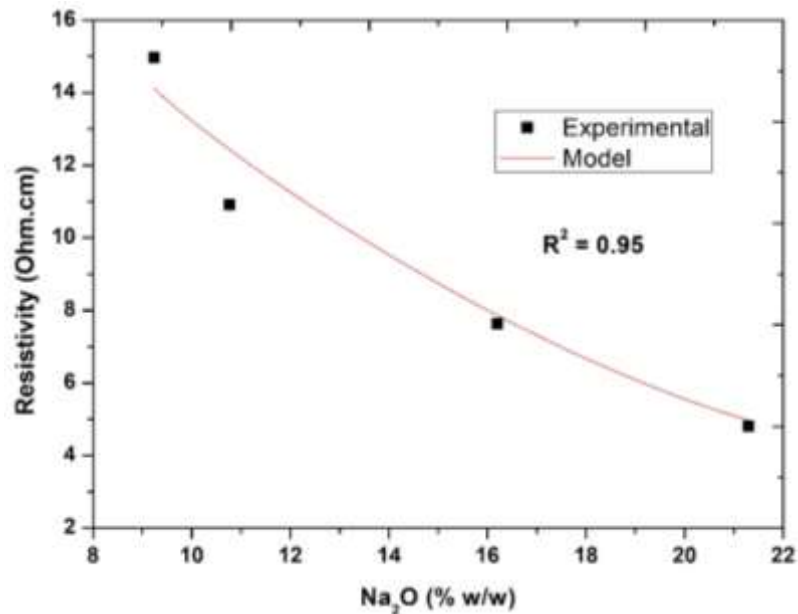


**Figure 5.4:** Variation of resistivity with Sodium concentration

### 5.1.4 Determination of Reaction Kinetics for Vitrification of RLW

In a continuously fed glass melter, RLW processing rate is controlled by the rate of heat transfer from molten glass to the cold cap and also by the kinetics of various chemical reactions and phase transitions within the cold cap [28]. The reaction mechanisms associated with the conversion of melter feed to glass are complex in nature. An understanding of thermal decomposition of the waste constituents is necessary to understand the series of phenomena occurring in cold cap.

In this study, the influence of base glass composition on the decomposition of constituents of sRLW was investigated. When the waste constituents in the form of nitrates are heated to convert to oxides and resultant mass loss can be seen in Figure 5.5 & Figure 5.6. The weight loss with temperature as a result of oxides being formed and subsequent vitrification is presented in Figure 5.6.

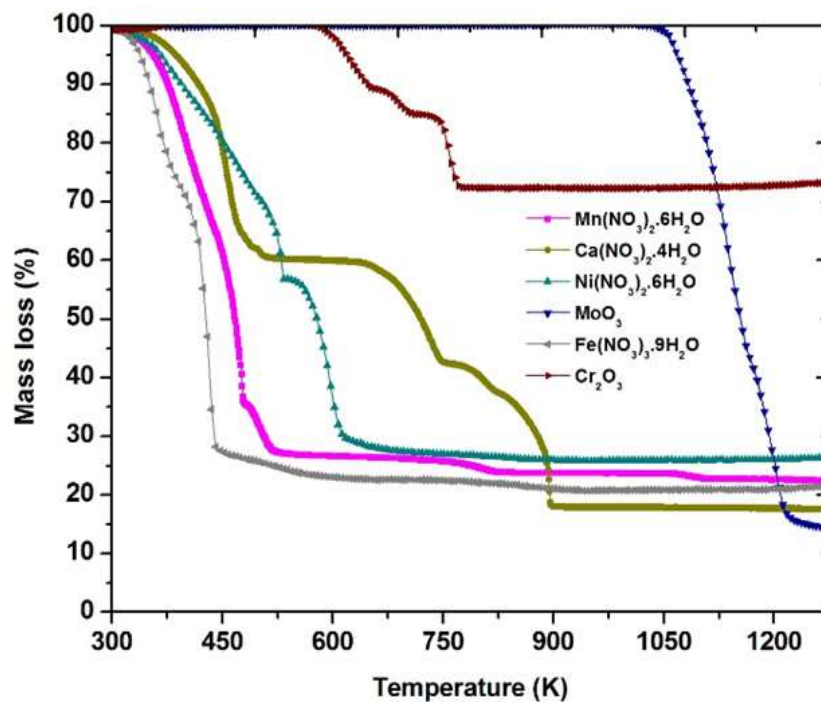
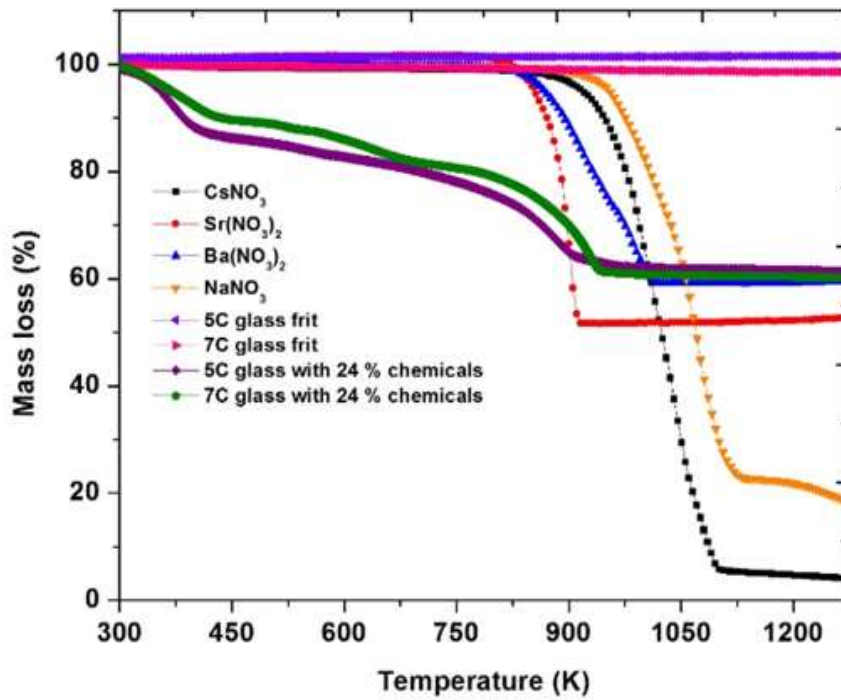
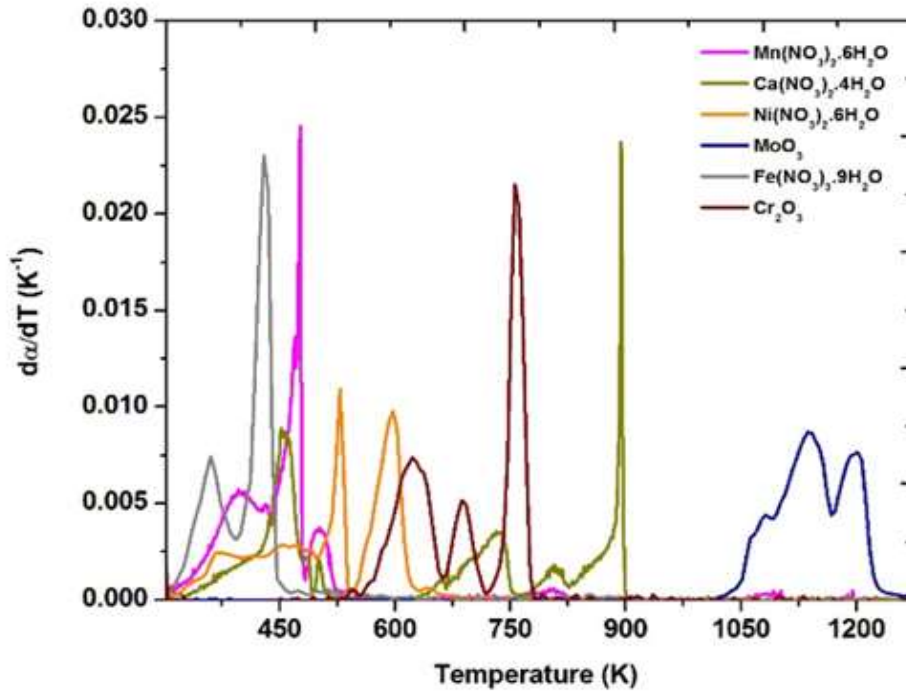


Figure 5.5: Mass loss with temperature for waste constituents in sRLW



**Figure 5.6:** Mass loss with temperature of all the individual waste constituents, 5C & 7C glasses and base glass loaded with sRLW



**Figure 5.7:** DTG Curves of the individual waste constituents using TGA

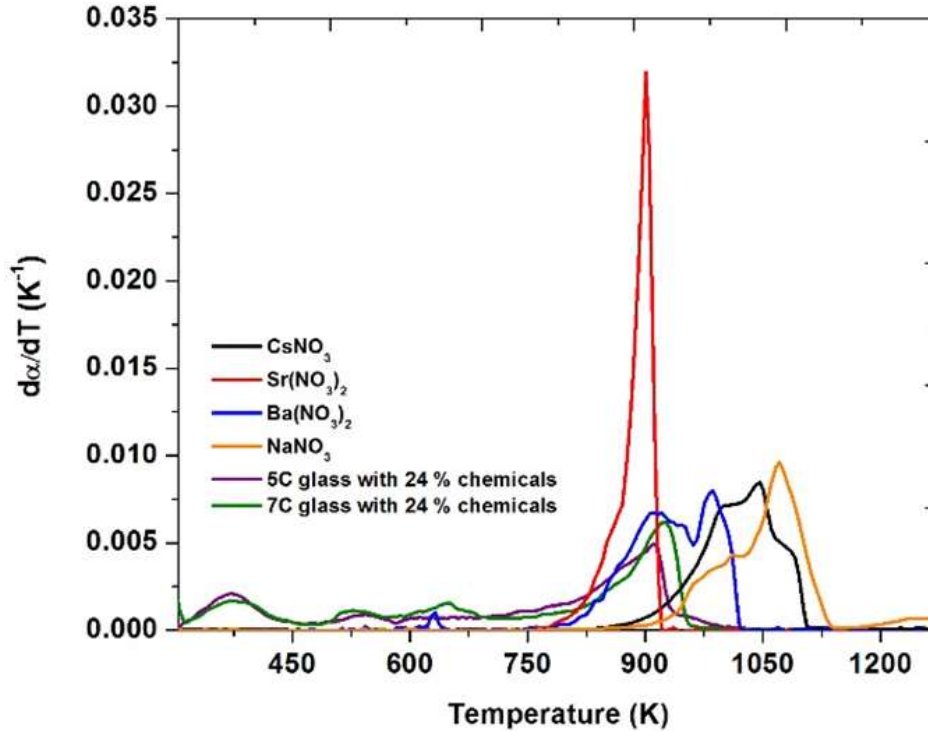


**Figure 5.8:** DTG Curves of the individual waste constituents and 5C & 7C glass with sRLW

#### 5.1.4.1 5C and 7C glasses as base matrices

The influence of temperature on the behaviour of base glasses (5C and 7C) and their interaction with metal salts were analysed in detail. It can be seen from Figure 5.6 that the selected base glass matrices are stable up to 1273 K without any mass loss, which indicates the promising nature of the base matrix in vitrification of RLW. Pure borosilicate glass ( $\text{SiO}_2\text{-B}_2\text{O}_3$ ) has very low electrical conductivity. Addition of alkali oxides as modifiers to the glass formers enhances electrical conductivity and reduces the viscosity of the glass. Basically, in the sodium borosilicate glass,  $\text{SiO}_2$  and  $\text{B}_2\text{O}_3$  form the basic glass network.  $\text{Na}_2\text{O}$  is a modifier oxide, added to achieve a fusion temperature of 1273 K, increase the electrical conductivity of molten glass and achieve a viscosity in the range of 5–10 Pa.s in order to enable pouring of the molten glass in the temperature range of 1223 – 1273 K from the melter.  $\text{TiO}_2$  is added to suppress  $\text{Cs}^{137}$  volatilization, and  $\text{Fe}_2\text{O}_3$  is added to improve the chemical durability and mechanical strength. In the 7C glass,

mixed alkali elements (CaO & K<sub>2</sub>O) are added as an additional constituents to 5C composition by lowering B<sub>2</sub>O<sub>3</sub> in order to increase the concentration of the modifiers beyond their limiting concentrations. CaO and K<sub>2</sub>O reduce the volatilisation of sodium and boron possibly by satisfying the coordination number of the metal ion in a better way as they have different ionic radii. Hence, the addition of CaO & K<sub>2</sub>O stabilises the glass network.

#### **5.1.4.2 TG of sRLW constituents**

In RLW, the waste constituents are present in the form of nitrates. To visualize the temperature zones for the decomposition of waste constituents, the TGA studies were carried out. During the conversion of waste nitrates to oxides and subsequent vitrification, mass loss was observed. The mass loss curves are shown in Figure 5.5 for individual waste constituents and Figure 5.6 shows the mass loss of 5C and 7C glass, 5C & 7C glass loaded with 24 % waste oxide and nitrates of alkali and alkali earth elements.

##### **5.1.4.2.1 TG-DTG of Fission products**

CsNO<sub>3</sub> starts to decompose beyond 850 K. The first peak of the DTG curve for CsNO<sub>3</sub> shown in Figure 5.8 is decomposition of CsNO<sub>3</sub> to CsNO<sub>2</sub>, which occurs between 850 K to 1023 K. Resultant CsNO<sub>2</sub> further decomposes to Cs<sub>2</sub>O from 1023 K to 1123 K. Thermal decomposition of Ba(NO<sub>3</sub>)<sub>2</sub> to Ba(NO<sub>2</sub>)<sub>2</sub> takes place between 798 K to 973 K. Subsequently, it decomposes to BaO between 973 K to 1123 K. Sr(NO<sub>3</sub>)<sub>2</sub> thermally decomposes to SrO between 773-923 K. The thermal decomposition pattern of Ba(NO<sub>3</sub>)<sub>2</sub> and Sr(NO<sub>3</sub>)<sub>2</sub> are also shown in Figure 5.8.

##### **5.1.4.2.2 TG-DTG of Corrosion Products**

Subsequently, Fe(NO<sub>3</sub>)<sub>2</sub> decomposes to Fe<sub>2</sub>O<sub>3</sub> in the temperature range of 373 to 473 K. Ni(NO<sub>3</sub>)<sub>2</sub>.6H<sub>2</sub>O is decomposed to Ni<sub>2</sub>O<sub>3</sub> between 473-540 K. Subsequently, Ni<sub>2</sub>O<sub>3</sub> decomposes to NiO in range of 540-723 K. Mn(NO<sub>3</sub>)<sub>2</sub> decomposes to MnO<sub>2</sub> in the

temperature range of 450-850 K and it further decomposes to  $Mn_2O_3$  between 850-1150 K. The thermal decomposition patterns of corrosion products are also shown in Figure 5.7.

**Table 5.1:** Thermogram of thermal decomposition

Waste Constituent	Temperature (K)								
	373	473	573	673	773	873	973	1073	1173
<b>Fission Products</b>									
$CsNO_3$	Sensible heating					D* to $Cs_2O$		S <sup>#</sup>	
$Sr(NO_3)_2$	Sensible heating					D to SrO			
$Ba(NO_3)_2$	Sensible heating					D to $Ba(NO_2)_2$		D to BaO	
<b>Added Chemicals</b>									
$NaNO_3$	Sensible heating					D to $NaNO_2$		D to $Na_2O$	S
$Ca(NO_3)_2 \cdot 4H_2O$	DH <sup>##</sup>		Sensible heating		D to CaO		Sensible heating		
<b>Corrosion Products</b>									
$Ni(NO_3)_2 \cdot 6H_2O$	DH	D to		D to $Ni_2O_3$	Sensible heating				
$MoO_3$	Sensible heating						M*	D to $MoO_2$	
$Fe(NO_3)_3 \cdot 9H_2O$	DH	D to $Fe_2O_3$		Sensible heating					
$Mn(NO_3)_2 \cdot 6H_2O$	DH		D to $MnO_2$			D to $Mn_2O_3$			
$Cr_2O_3$	Sensible		D to $CrO_x$			Sensible heating			

\* D – Decomposition, \*\* M-Melting, # S-Sublimation, ## DH-Dehydration and x=1 to 1.5

#### 5.1.4.2.3 TG-DTG of Added Chemicals

$NaNO_3$  starts to decompose beyond 900 K. The first stage of decomposition starts at 900 K and is completed at 1023 K.  $NaNO_3$  forms  $NaNO_2$  and subsequently decomposes to  $Na_2O$  before it starts subliming above 1153 K, as shown in Figure 5.8.  $Ca(NO_3)_2$  decomposes to CaO in the temperature range of 773-823 K, as shown in Figure 5.7. The thermal decomposition data is consolidated and presented in Table 5.1.

#### 5.1.5 Determination of kinetic parameters

In this study, to determine rate kinetics, DTG curves for 5C and 7C base glasses with waste constituents equivalent to 24% waste oxide loading in VWP are plotted for different heating rates viz., 10  $K \cdot min^{-1}$ , 20  $K \cdot min^{-1}$ , 30  $K \cdot min^{-1}$  and 40  $K \cdot min^{-1}$  as shown in Figure

5.9 and Figure 5.11. The first three peaks represent the dehydration, thermal decomposition of nitrates of corrosion products and thermal decomposition of nitrates of alkali earth metals respectively while the fourth peak depicts the thermal decomposition of the nitrates of alkali elements present in fission products and added chemicals.

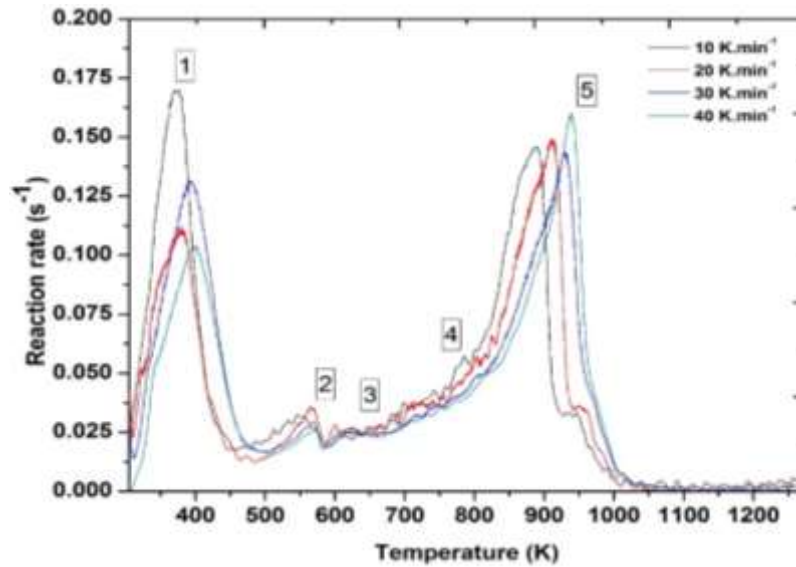


**Figure 5.9:** DTG curves at different heating rates for 5C glass with sRLW

In the present study, the Kissinger method was applied for the determination of activation energy for major reactions [30]. As expected, the curves shift to higher temperatures as the heating rate is increased. Also, the heights of the peaks generally decrease as the

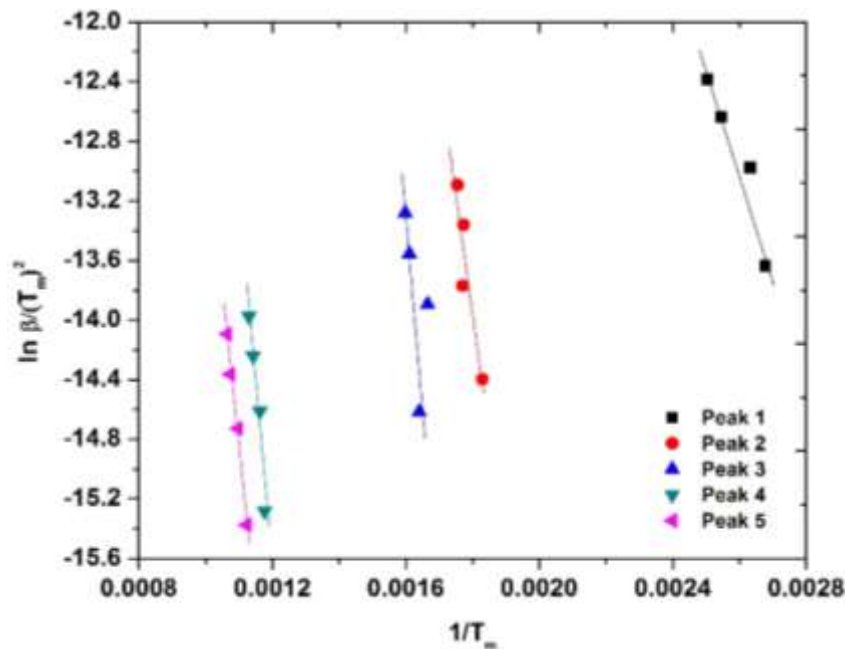


**Figure 5.10:** Kissinger plot for 5C glass with sRLW

heating rates are increased as observed in peak 2, 3 & 4. The shift in peaks is due to different reactions in the waste constituents. Slow-low temperature reactions are bound to get higher time during slower heating rate ( $10 \text{ K}\cdot\text{min}^{-1}$ ), whereas during faster heating rates ( $40 \text{ K}\cdot\text{min}^{-1}$ ) the conversion takes place over a temperature range due to associated lower rate kinetics. Therefore, the height of the peak reduces during faster heating rates and the starting condition of high-temperature reactions are shifted towards higher temperature.

To apply Kissinger's method, the deconvolution of DTG curves is necessary. Four major peaks were chosen, as indicated in Figure 5.9 and Figure 5.11.

A plot between  $\left(\ln \frac{\beta}{T_m^2}\right)$  and  $\left(\frac{1}{T_m}\right)$  yields a straight line. The slope of the line yields the activation energy of that particular reaction. The Kissinger plots for 5C and 7C glasses loaded with waste nitrates corresponding to 24 % waste oxide for all the peaks are shown in Figure 5.10 and Figure 5.12 respectively.

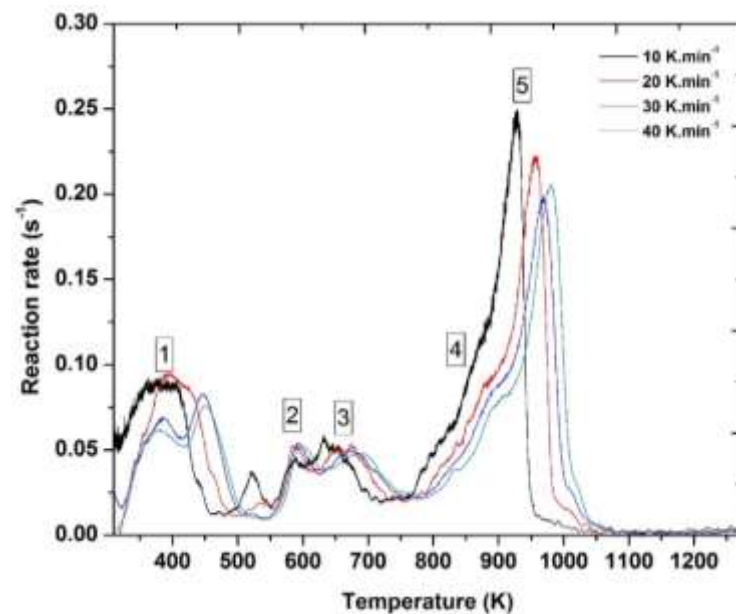


**Figure 5.11:** DTG curves at different heating rates for 7C glass with sRLW

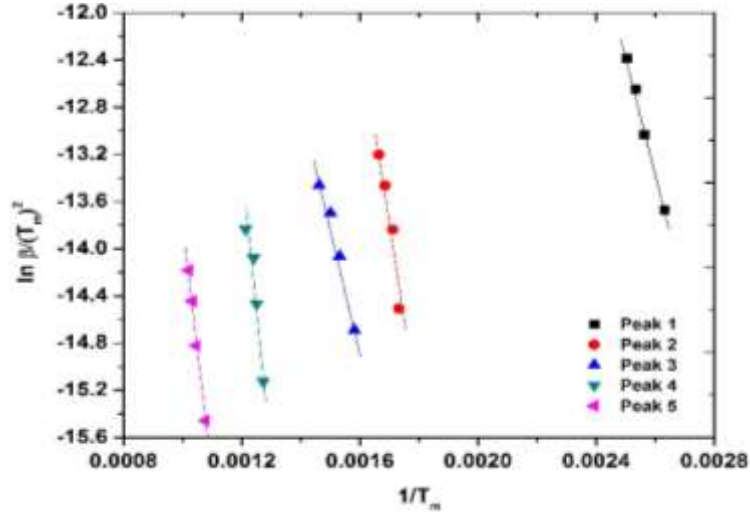


**Figure 5.12:** Kissinger plot for 7C glass with waste constituents

The activation energy obtained from the Kissinger plots facilitated the calculation of the other two important kinetic parameters i.e., pre-exponential factor and order of reaction along with a fraction of weight loss.

Table 5.2 and Table 5.3 show the calculated values of the activation energy, pre-exponential factor, order of reaction and fraction of weight loss due to reactions happening in the peaks. Pre-exponential factor and weight of reactions are independent of the rate of heating. On the other hand order of reaction vary with heating rate by 7%, 11% and 3% for peaks 2, 3 and 4 respectively for 5C and 9%, 0.3% and 12% for peaks 2, 3 and 4 respectively for 7C when compared with an average order of the reaction.

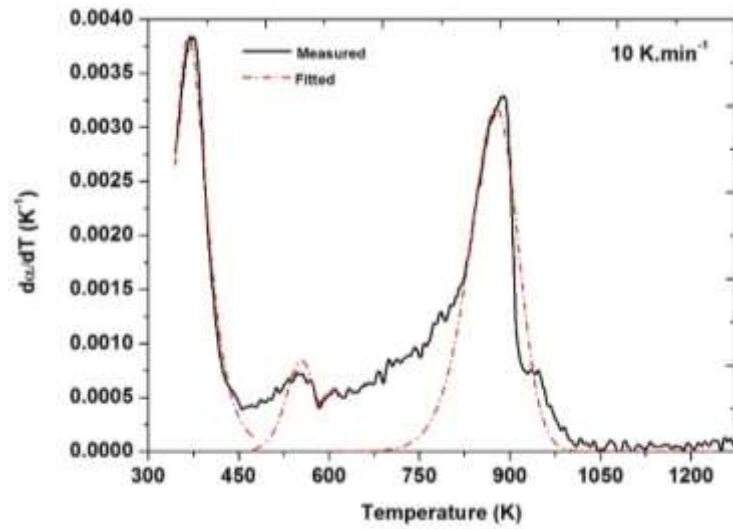
Subsequently, the kinetic parameters determined in this study were substituted in the rate equation mentioned in Equation (4.41), and the plots of measured and fitted values for 5C and 7C were shown in Figure 5.13 and Figure 5.14 respectively. The fraction of weight loss ( $w_i$ ) for the desired peak was obtained from Figure 5.13 and Figure 5.14 for a particular peak. The average values of  $A_i$  and  $n_i$  listed in Table 5.2 and Table 5.3 were used to recalculate  $w_i$  and compared with the experimentally determined fraction of weight loss. The total weight loss determined by fitting is 6.3 % lesser compared to experimentally determined weight loss.

**Table 5.2.** Kinetic parameters of 5C base glass during thermal decomposition

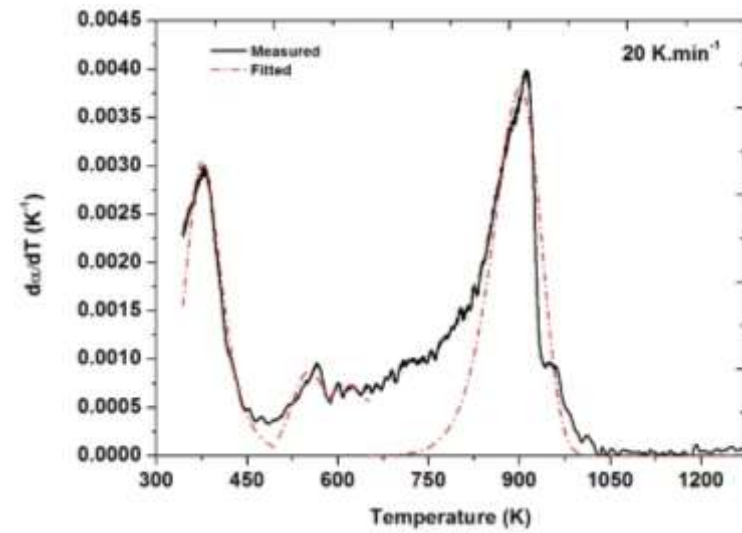
Parameter	logA					n					w				
	Peak														
$\beta$ (K.min <sup>-1</sup> )	1	2	3	4	5	1	2	3	4	5	1	2	3	4	5
10	6.07	10.87	7.17	9.70	8.97	2.03	1.79	1.40	2.78	1.26	0.10	0.03	0.01	0.022	0.22
20	4.18	9.47	5.44	9.80	8.47	2.04	3.36	2.69	2.61	1.10	0.08	0.02	0.02	0.004	0.21
30	6.02	11.40	7.57	7.34	8.46	2.04	2.04	2.80	1.98	1.20	0.11	0.02	0.01	0.046	0.21
40	6.08	11.35	7.78	9.30	8.35	2.04	1.73	3.37	2.52	0.81	0.09	0.02	0.01	0.046	0.21
Average	5.59	10.77	6.99	9.70	8.56	2.04	2.23	2.56	2.78	1.09	0.10	0.02	0.01	0.037	0.21
E (kJ.mol <sup>-1</sup> )	54.40	134.00	101.9	180.8	176.8	54.40	134.0	101.9	180.8	176.8	54.4	134.0	101.9	180.8	176.8

**Table 5.3:** Kinetic parameters of 7C base glass during thermal decomposition

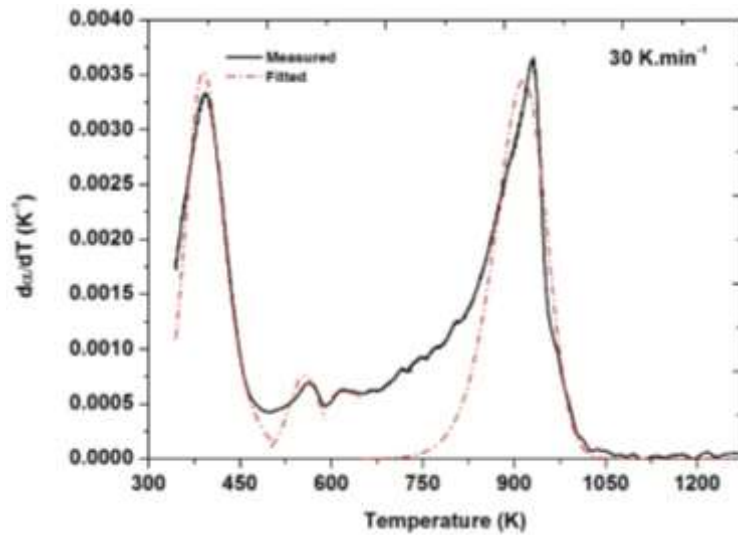
Parameter	logA					n					w				
	Peak														
$\beta$ (K.min <sup>-1</sup> )	1	2	3	4	5	1	2	3	4	5	1	2	3	4	5
10	8.89	12.28	5.86	11.25	8.10	2.65	1.26	1.25	2.09	0.22	0.10	0.03	0.02	0.02	0.31
20	9.57	12.18	5.18	11.01	8.07	4.21	2.81	1.29	2.74	0.34	0.09	0.05	0.05	0.02	0.34
30	8.52	12.45	5.20	11.45	8.10	2.37	2.29	1.23	2.42	0.25	0.10	0.03	0.06	0.03	0.30
40	8.52	12.43	5.20	11.00	9.98	2.40	1.93	1.23	2.42	0.43	0.10	0.03	0.06	0.01	0.32
Average	8.87	12.33	5.36	11.18	8.56	2.91	2.07	1.25	2.4	0.34	0.10	0.03	0.05	0.02	0.32
E (kJ.mol <sup>-1</sup> )	54.40	134.00	101.90	219.61	176.80	54.40	134.00	101.90	219.61	176.80	54.40	134.00	101.90	219.61	176.80



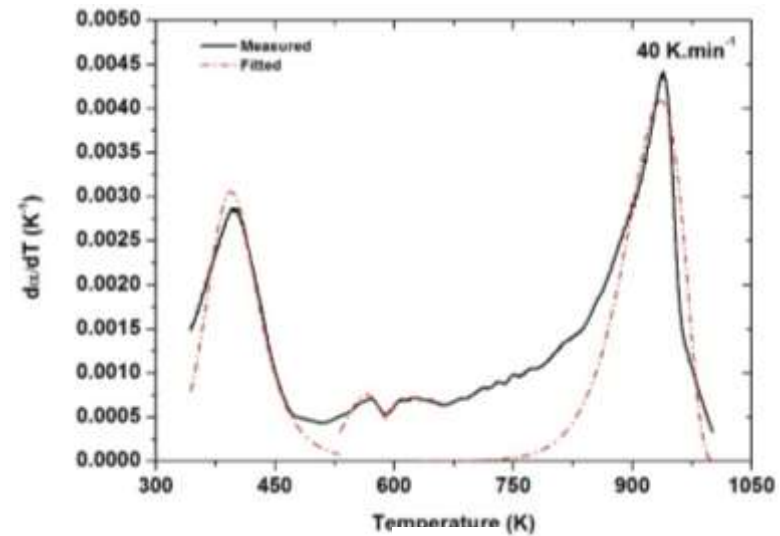
(a)



(b)

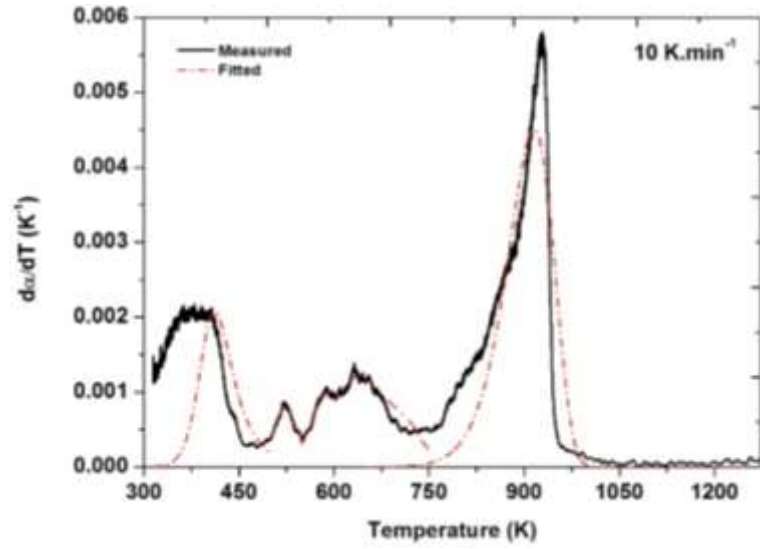


(c)

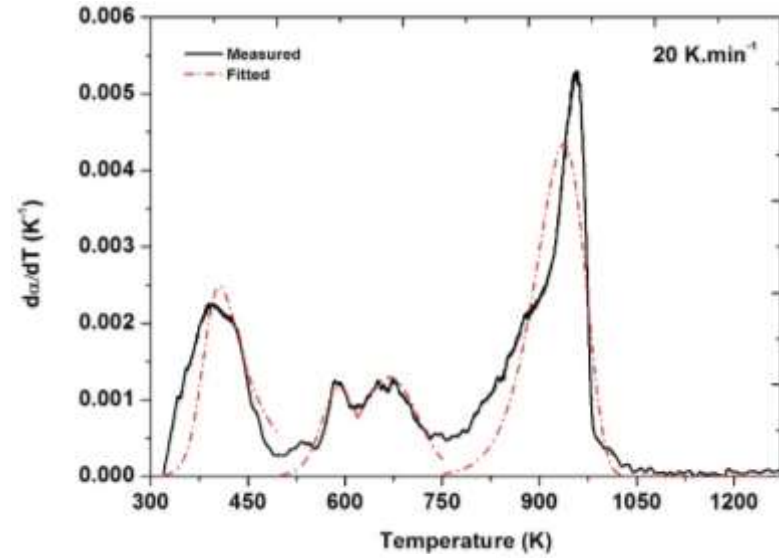


(d)

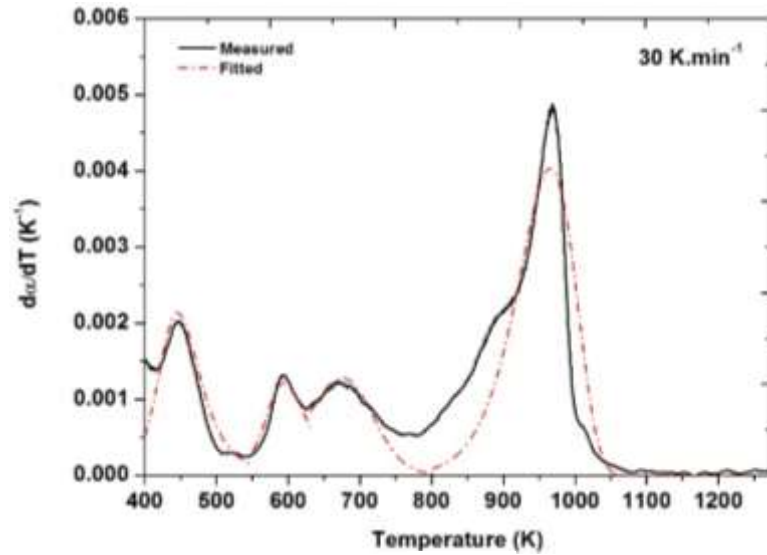
**Figure 5.13:** Measured and fitted TGA curves and deconvolution peaks for individual heating rates for 5C loaded with waste nitrates for different heating rates (a) 10 K.min<sup>-1</sup>, (b) 20 K.min<sup>-1</sup>, (c) 30 K.min<sup>-1</sup> & (d) 40 K.min<sup>-1</sup>



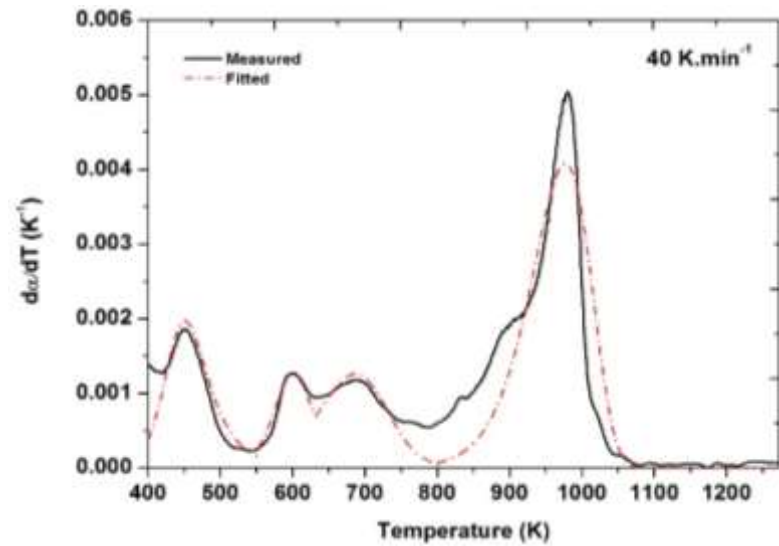
(a)



(b)



(c)



(d)

**Figure 5.14:** Measured and fitted TGA curves and deconvolution peaks for individual heating rates for 7C loaded with waste nitrates for different heating rates (a)  $10 \text{ K.min}^{-1}$ , (b)  $20 \text{ K.min}^{-1}$ , (c)  $30 \text{ K.min}^{-1}$  and (d)  $40 \text{ K.min}^{-1}$

## **5.2 Pilot Plant Studies for Determination of the Contribution of Different Modes of Heat Transfer to the Glass Frit**

Experiments were conducted on pilot scale melter as described in Section 3.3.2, for the determination of dominant modes of heat transfer between refractory and glass beads during the start-up heating of the JHCM.

The temperature was measured at various locations to evaluate the heat transfer mechanism. At plenum heater temperature of 848 K, the maximum face temperature of the refractory block was 673 K. The temperature of the AZS blocks increased linearly with heater power. The rise in temperature of the thermocouples and their steady state temperatures were in line with the position, indicating the absence of any abnormalities. Change in temperature with time predicted from the simulation are compared with experimental data for the thermocouple positions T1-9, as shown in Figure 5.15. Thermocouple-8, which is farthest on the face of the AZS blocks, resembles almost similar values and pattern except for the initial gap. The initial gap is attributed to the transient heat transfer between the blocks and the heat source.

It was observed that Radiation is the dominant mode of heat transfer between the heaters and Kanthal<sup>®</sup> tubes. The transfer from tube to the refractory is also by radiation. The percentage contribution of radiation to total heat dissipation is 74%. The emissivity of the wall surface is 0.58. Radiation contributes 74% of overall heat transfer to glass beads at temperatures up to 773 K. Beyond this, the contribution by radiation increases to ~90%. The overall heat flux decreases drastically if only radiation is considered. If conjugate heat transfer is considered, the heat flux increases by 30%.

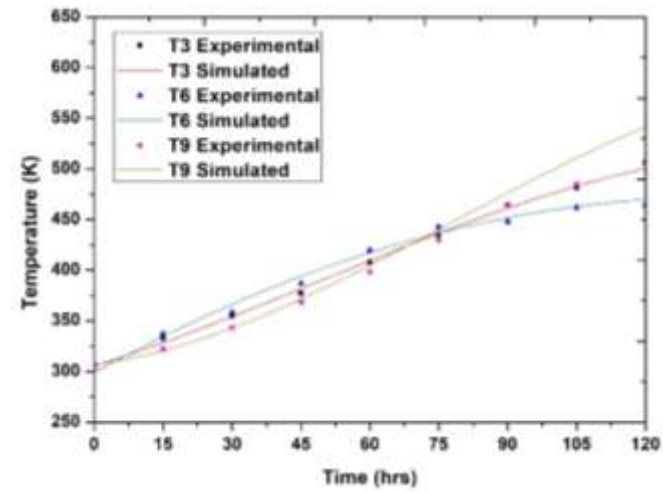
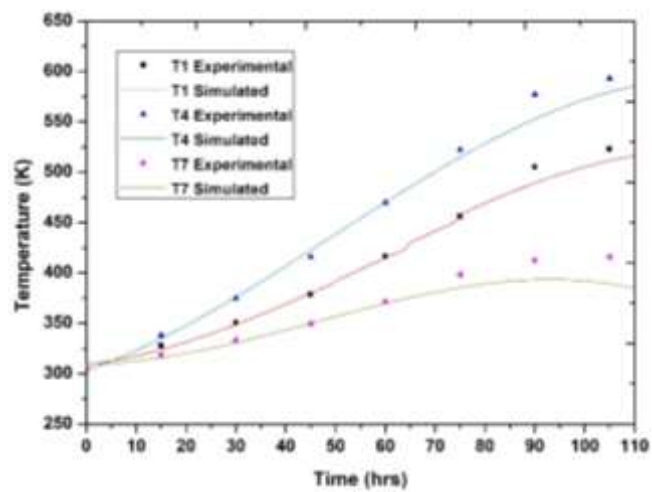
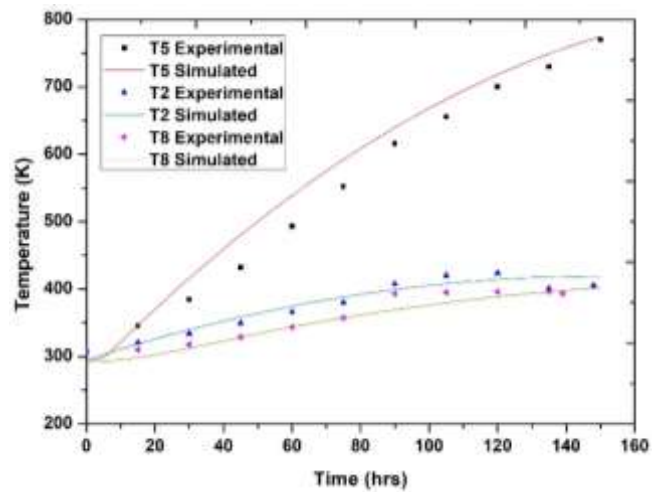


**Figure 5.15:** Validation of model with experimental data on Pilot scale for simulating Stage - II

Deviation of the predicted values from the experimental values is  $\pm 7\%$  for T5 location. For other locations for given power input, the deviation in the predicted values compared to experimental values is  $2\%$ . The variation observed in the rate of change in temperatures for simulated and experimental results is because of the type of heat input given to the heaters, which in actual experiments is changing gradually at a constant rate till it reaches its maximum power of 2.5 kW.

### **5.3 Temperature Profiles in Various Stages of Industrial Scale JHCM Operation**

The objective of the present study was to develop a 3D model of JHCM in order to understand the heat transfer mechanism to propose design modifications of JHCM for better efficiency. The 3D model of JHCM developed as explained in Chapter-4 was validated with the data sets generated during the Stage-I, II & III of melter operation. The experimental measurements of temperatures at different locations in JHCM are interpreted to understand the heat flow in JHCM and are used to validate model.

#### **5.3.1 Temperature Profile for Stage-I Operation of JHCM**

The plenum heaters were powered with different power inputs and the temperature profile of the empty cavity was recorded. For each power input, the system was allowed to achieve a steady state, and the temperature of the empty cavity was recorded using a glass pool and cold cap thermocouples. The temperature on the outer walls was measured to calculate the heat losses from the melter outer body. PCW temperatures, amount of air ingress into melter, and electrode phase temperatures were monitored. The temperature profile of the empty cavity at power inputs of 395 W, 629 W and 776 W is presented in Table 5.4.

As shown in the Table 5.4 that as the power to the plenum heater increases, the plenum heater transmits heat to Kanthal tubes. The Kanthal tubes in turn transmits this heat to

refractory blocks by conduction and radiation. At a power input of 395 W, GP-1, which is at the bottom portion of the melter is at lower temperature compared to the other thermocouples. GP-13, which is located 150 mm above the maximum operating level shows the maximum temperature due to its proximity to the heat source. As we move further to the upper region of the melter, due to losses from the top surface GP-16 temperature reduces. During the experiments, the melter was maintained at negative pressure due to which there was an ingress of air into the cavity through the gaps. This also contributed to lower temperature of GP-14 and GP-15 as compared to GP-13. As thermal conductivity of refractory blocks is  $2.88 \text{ W.m}^{-1}.\text{K}^{-1}$ , the contribution of heat transfer by conduction to the lower part was less.

As the power was increased further, the temperature also increased correspondingly. The surface temperature of the melter was monitored and it was observed that the temperature of the top surface plate was around 343 K for 365 W power input, whereas the temperature of the side surfaces was around 333 K and 313 K at the top and bottom half respectively. The temperature of the bottom plate of the melter was around 309 K. As the power to plenum heaters increases the cavity temperature also increases correspondingly. The resistance between the electrodes was monitored to ascertain complete removal of moisture from the composite refractory walls. The rise in the temperature had resulted in resistance of  $1 \text{ M}\Omega$  at a power input of 629 W indicating that the moisture present in the backup refractory is completely removed at this power. However, the bottom electrodes continued to show lower resistance of about  $1 \Omega$  indicating the presence of moisture in the bottom part of the refractory. Consequently, the power was further increased to 776 W. There was a corresponding increase in the temperature of the cavity as can be seen from Table 5.4. The resistance between the

bottom electrodes was monitored and it was found to be 1 M $\Omega$ , indicating the complete removal of moisture from the lower part of the refractory.

### **5.3.2 Temperature Profile for Stage – II Operation of JHCM**

In stage – II operation melter glass frit was charged and intended to increase the glass temperature to conduction zone. 750 kg of glass frit was charged into the melter and the power to the plenum heater were increased to 1198 W. The temperature of GP-13 increased to 737 K. After adding glass frit the temperature of GP-1 to GP-6 decreased and started increasing after 12 hrs and achieved a temperature rise rate of less than 1 K.hr<sup>-1</sup> after 65 hrs. The subsequent power rise in plenum heaters did not result in corresponding increase of GP-1 to GP-6 temperatures. Hence, the system was allowed to reach the conducting temperature of glass by maintaining the plenum heaters at the power of 1198 W. The JHCM was maintained under these conditions for 160 hours. The temperature on the outer walls was measured to calculate the heat losses from the melter outer body. PCW temperatures, amount of air ingress into melter, and electrode phase temperatures were monitored. The temperature profile of the melter during the stage-II of operation is presented in Table 5.5.

The glass frit charged during this operation was having Na<sub>2</sub>O content of 11.5 %. Glass started conducting at electrode temperature of 948 K. The rise in the sodium content in the base glass will reduce the heating time.

**Table 5.4:** Temperature profile in JHCM during Stage - I

Thermocouple	Thermocouple Location from bottom	P= 395 W	P=629 W	P= 776 W
		Temperature		
No.	mm	K	K	K
1	175	446.4	633.9	709.7
2	215	446.5	633.1	708.7
3	265	447.7	636.2	712.1
4	315	446.0	634.1	710.2
5	365	448.4	638.1	714.2
6	435	451.7	645.1	721.3
7	455	454.0	648.2	725.6
8	475	452.1	646.0	722.2
9	495	452.0	646.5	722.9
10	515	452.6	646.7	722.9
11	535	455.4	650.0	726.4
12	555	456.5	651.9	728.0
13	705	464.0	659.7	737.0
14	955	476.8	659.1	735.9
15	1205	462.1	592.1	643.8
16	1305	444.4	529.0	555.0
<b>Operating Conditions</b>				
Off Gas Flow Rate (m <sup>3</sup> /hr)		93	102	110
Number of hours maintained in steady state (hrs)		64	152	87
Electrode Temperature (K)		425	608	705

P: Power supplied to each heater in a set of 24 No's heaters used for pre heating glass

**Table 5.5:** Temperature profile in JHCM during Stage - II

Thermocouple	Thermocouple location from bottom	P= 1198 W
	mm	K
1	175	637.9
2	215	636.5
3	265	646.4
4	315	660.7
5	365	679.5
6	435	713.8
7	455	733.6
8	475	744.6
9	495	751.4
10	515	759.8
11	535	770.4
12	555	778.9
13	705	841.1
14	955	895.0
15	1205	878.3
16	1305	800.5
Off Gas Flow Rate (m <sup>3</sup> /hr)		109
Number of hours maintained in steady state (hrs)		126
Electrode Temperature (K)		707

P: Power supplied to each heater in a set of 24 No's heaters used for pre heating glass

### **5.3.3 Temperature Profile for Stage – III Operation of JHCM**

Experiments were carried out with Demineralized (DM) Water and solutions having different salt concentrations of 28 g.L<sup>-1</sup> and 56 g.L<sup>-1</sup> is used to study the effect of salt concentration on throughput. The simulated waste and glass frit were fed simultaneously to the melter while continuously monitoring the temperature profile. The feed rate of simulated waste and glass frit was increased stepwise at a rate of 1 L.hr<sup>-1</sup> and 80 g.hr<sup>-1</sup> respectively to attain sustained 90% spread of cold cap on top of the melt. The temperature profiles of glass pool and cold cap thermocouples were monitored and recorded continuously.

#### **5.3.3.1 Boil-up Rate Estimation**

The cold cap was recorded using a bullet camera for every increase in flow rate by 10 L.hr<sup>-1</sup>. The spread of cold cap was limited to a maximum of 90 % to prevent thermal shock to refractories. Cold cap and glass pool temperatures were recorded every hour. A typical cold cap has been shown in Figure 5.16. A maximum evaporation rate of 60 L.hr<sup>-1</sup> was achieved at a cold cap spread of 90 %. The power consumed by JHCM was 45 kW while the maximum glass pool temperature was maintained at 1313 K. Data were collected at different flow rates for the validation of the model were presented in Table 5.6. and Table 5.7.

The melter temperature from GP-01 to GP-10 are higher as these thermocouple are completely inside the glass melt. The temperature from thermocouple GP-11 and GP-12 is less as compared to GP-01 to GP-10 as these thermocouples are in contact with boiling water. The temperature of the thermocouple GP-13 to GP-16 falls drastically due to heat losses from the off-gas nozzles.

**Table 5.6:** Temperature profile of glass pool thermocouples in JHCM during Stage – III for estimating boil up rate

Feed Rate( F): D.M. Water (L.h <sup>-1</sup> )		20	40	60
Glass Frit (kg.hr <sup>-1</sup> )		Frit was not added along with feed during estimation of boil up rate		
Power (kW)		30	35	45
Thermocouple No	Thermocouple Location from bottom Mm	Temperature K		
		K	K	K
1	175	1253	1238	1235
2	215	1250	1235	1231
3	265	1265	1249	1244
4	315	1286	1259	1250
5	365	1286	1253	1243
6	435	1282	1239	1229
7	455	1216	1147	1132
8	475	1169	1069	1057
9	495	1126	1004	998
10	515	1050	884	906
11	535	1010	793	833
12	555	923	674	751
13	705	681	609	566
14	955	621	616	577
15	1205	553	560	535
16	1305	459	494	477

**Table 5.7:** Temperature profile of cold cap thermocouples in JHCM during Stage - III for estimating boil up rate

Feed Rate (F): D.M. Water (L.hr <sup>-1</sup> )		20	40	60
Glass Frit (kg.hr <sup>-1</sup> )		Frit was not added along with feed during estimation of boil up rate		
Power (kW)		30	35	45
Cold Cap Thermocouple	Thermocouple Location from bottom	Temperature		
No	mm	K	K	K
1	455	1234	1192	1162
2	465	1238	1182	1149
3	475	1248	1182	1150
4	485	1262	1163	1129
5	495	1267	1149	1113
6	505	1260	1131	1091
7	515	1196	1114	1071
8	525	1154	1076	1034
9	535	1114	1039	997
10	545	1038	998	960
11	555	991	953	915



**Figure 5.16:** Spread of the cold cap with sRLW - 50 L.hr<sup>-1</sup>, 2.0 kg.hr<sup>-1</sup>

### 5.3.3.2 Processing Capacity Estimation

sRLW of characteristics similar to the radioactive waste, was prepared using stable isotopes of the radioactive species. Two types of sRLW composition with 28 g.L<sup>-1</sup> and 56 g.L<sup>-1</sup> of waste nitrates were used for estimation of processing capacity.

**Table 5.8** Variation of throughput with increased salt content

Salt Content –Total Dissolved Salts (g.L <sup>-1</sup> )	Glass Production rate (kghr <sup>-1</sup> )	Waste Feed rate (lph)
28	2.4	50
56	3.0	30

sRLW and glass frit were fed simultaneously to the melter to study the variation of melter throughput with the salt content. The feed rate of simulated waste and glass frit was increased stepwise at a rate of 1 L.hr<sup>-1</sup> and 80 g.hr<sup>-1</sup> respectively for maintaining waste glass to base glass ratio and to maintain a sustained 90 % spread of cold cap on top of the melt. The variation of melter throughput with salt content is presented in Table 5.8. The temperatures profiles of glass pool and cold cap thermocouples were monitored and recorded continuously and are presented in Table 5.9 and Table 5.10.

**Table 5.9:** Temperature profile of glass pool thermocouples in JHCM during Stage – III for determining processing capacity

Feed Rate( F): D.M. Water (L.hr <sup>-1</sup> )		20	30	40
Glass Frit (kg.hr <sup>-1</sup> )		0.814	1.223	1.633
Power (kW)		40	45	50
Thermocouple	Thermocouple Location from bottom	Temperature		
No	Mm	K	K	K
1	175	1293	1292	1295
2	215	1292	1292	1294
3	265	1292	1287	1295
4	315	1291	1275	1294
5	365	1273	1249	1288
6	435	1226	1187	1278
7	455	1048	912	1195
8	475	943	767	1134
9	495	887	509	1089
10	515	828	526	1013
11	535	797	521	945
12	555	769	492	871
13	705	688	471	606
14	955	668	467	554
15	1205	585	396	476
16	1305	469	353	401

**Table 5.10:** Temperature profile of cold cap thermocouples in JHCM during Stage - III for determining processing capacity

Feed Rate( F): D.M. Water (L.hr <sup>-1</sup> )		20	30	40
Glass Frit (kg.hr <sup>-1</sup> )		0.814	1.223	1.633
Power (kW)		40	45	50
Thermocouple	Thermocouple Location from bottom	Temperature		
No	mm	K	K	K
1	175	1151	1187	1241
2	215	1134	1174	1234
3	265	1129	1181	1237
4	315	1104	1156	1261
5	365	1076	1141	1212
6	435	1047	1113	1196
7	455	723	1088	1182
8	475	969	1029	1156
9	495	922	966	1133
10	515	892	901	1104
11	535	856	826	1067

### 5.3.4 Energy Distribution

The energy consumed by different processes in JHCM was estimated. The external face walls of the melter were divided into grids for temperatures measurement. Based on the temperature of the face walls, the heat transfer coefficients on the walls was estimated, which in turn was used for the development of a mathematical model. The details of energy distribution for different waste compositions are as shown in Figure 5.17.

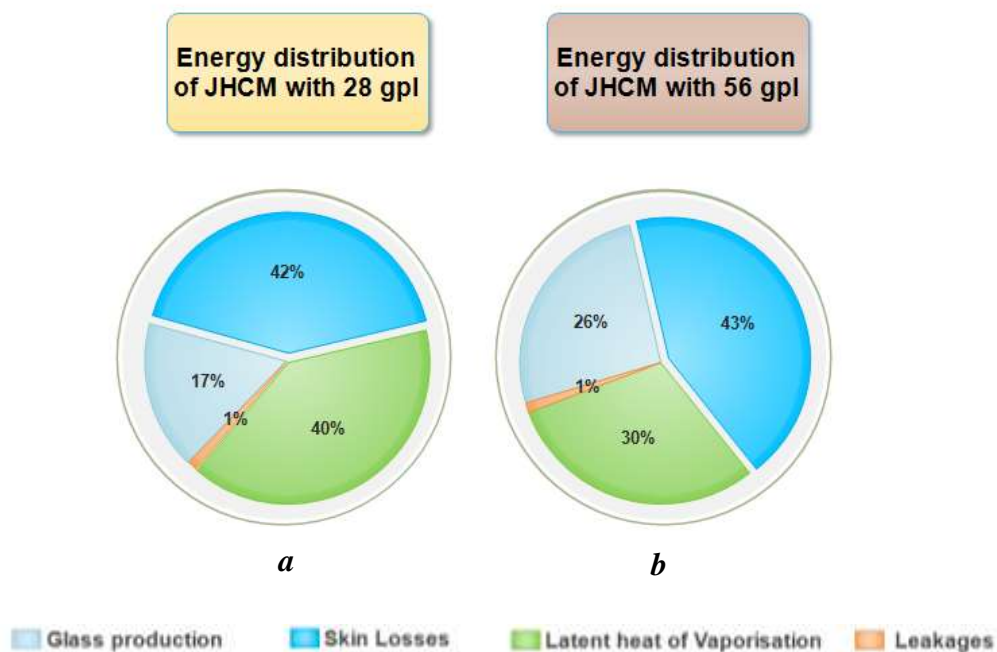


**Figure 5.17:** Energy distribution of JHCM with a) with 28 g.L<sup>-1</sup> and b) with 56 g.L<sup>-1</sup> of total dissolved salt

The power supplied to the melter during the experiments was used for supplying latent heat of vaporization of water. By monitoring the condensed water in the off-gas stream, the rate of evaporation of water is determined. The heat losses are determined by measuring the external temperature. The off-gas losses are determined by measuring the air leakage into the melter and its temperature during the blank run of the melter.

The heat supplied to the melter is used to raise the temperature of the glass pool, to evaporate the liquid associated with the waste, decomposition of nitric acid, to carry out calcination reactions, to heat the calcined mass to fusion temperatures and further to pouring temperatures. Some of the heat supplied to the melter is lost from the system by skin losses.

Experiments were carried out with Demineralized (DM) Water and solutions having different salt concentrations of 28 g.L<sup>-1</sup>, 56 g.L<sup>-1</sup> is used to study the effect of salt concentration on throughput. Based on the experimental results the specific energy required is determined to be 33.67 and 33.68 kJ.g<sup>-1</sup> of salt nitrates for the experiments conducted with waste having a salt content of 28 & 56 g.L<sup>-1</sup> respectively and energy distribution is presented in Table 5.11. The amount of energy required for vitrifying nitrates in simulated waste into the base glass is 33.18 kJ.g<sup>-1</sup> of salt nitrates apart from the evaporation of water as per the theoretical estimates. The theoretical estimates are in close agreement with experimentally determined values with a maximum deviation of +1.6 %, indicating that all the heat losses were accounted.

**Table 5.11:** Off-gas produced for different capacities

<b>TDS</b>	<b>Capacity</b>	<b>Power</b>	<b>Off-gas</b>	<b>NO<sub>x</sub></b>	<b>A</b>	<b>b</b>	<b>c</b>	<b>d</b>
gpl	lph	kW	kg/hr	kg/hr	kW	kW	kW	kW
28	20	31	20.34	0.34	5.1	13	12.5	0.36
56	15	29	15.50	0.50	7.8	13	9.0	0.36

a= Energy for Glass production; b= Energy losses; c=Latent heat of Evaporation of water; d= off gas loses

### 5.3.5 Product Glass Characterisation

Product glass samples collected during the experiments were analysed. Elemental analysis of these samples was also carried out by both Hydrogen Fluoride (HF)

dissolution and sodium carbonate fusion methods. Density and glass transition temperature of glass prepared in the laboratory and that produced in JHCM were comparable. Elemental analysis of the product glass samples collected during the experiments were carried out. Product glass from 5C base glass and simulated waste would have resulted in the sodium concentration of 236.1 mg.g<sup>-1</sup> in the VWP. However, the sodium concentrations in VWP samples were in the range of 229 mg.g<sup>-1</sup>, indicating that sodium from simulated waste has entered into the product glass network. The remaining portion of The narrow range of density of product glasses confirms satisfactory soaking, good homogeneity and absence of any entrapped gas/air. The typical characteristics of VWP after vitrification on plant scale is presented in Table 5.12 and they are in lines with interational standards.

**Table 5.12:** Typical characteristic properties of VWP

S.No.	Simulated trials	Pour Temp. (°C)	Density (g/cc)	Leach rate (g/cm <sup>2</sup> /day )	Na <sub>2</sub> O (g/kg of WWP)
1.	Lab	952	2.7	1.5 x 10 <sup>-5</sup>	236.1
2.	Canister - 1	960	2.66	1.2 x 10 <sup>-5</sup>	192.5
3.	Canister - 2	958	2.65	1.8 x 10 <sup>-5</sup>	209.4
4.	Canister - 3	955	2.66	1.95 x 10 <sup>-5</sup>	225.2
5.	Canister - 4	953	2.67	2.03 x 10 <sup>-5</sup>	229.2

X-ray Diffraction (XRD) analysis of the product glass was also carried out to see the extent of crystallisation. The XRD scan of the product glass was amorphous showing that the glass was homogeneous.

## 5.4 Validation of the Model

### 5.4.1 Temperature Profiles at Various Power Inputs in Stage-I

#### 5.4.1.1 Transient Study: To Estimate Steady State Temperature

The model was validated by estimating the temperatures at a steady state and the time required to achieve steady state, using a transient study for an empty melter cavity. The steady state was considered only when the rate of rise of temperature was less than  $0.5 \text{ K.hr}^{-1}$ . The temperatures profile obtained during experiments was used for the validation of the model.

A step input function as a 'power step input' was defined from 0 to 395 W with a transition period of 1 hour, was given as heat input to the plenum heaters. The response of the system was observed for an empty melter cavity. It took 65 hours for the system to attain a steady state, indicating the huge heat capacity of the system. The slice plot for 65 hours is shown in Figure 5.18.

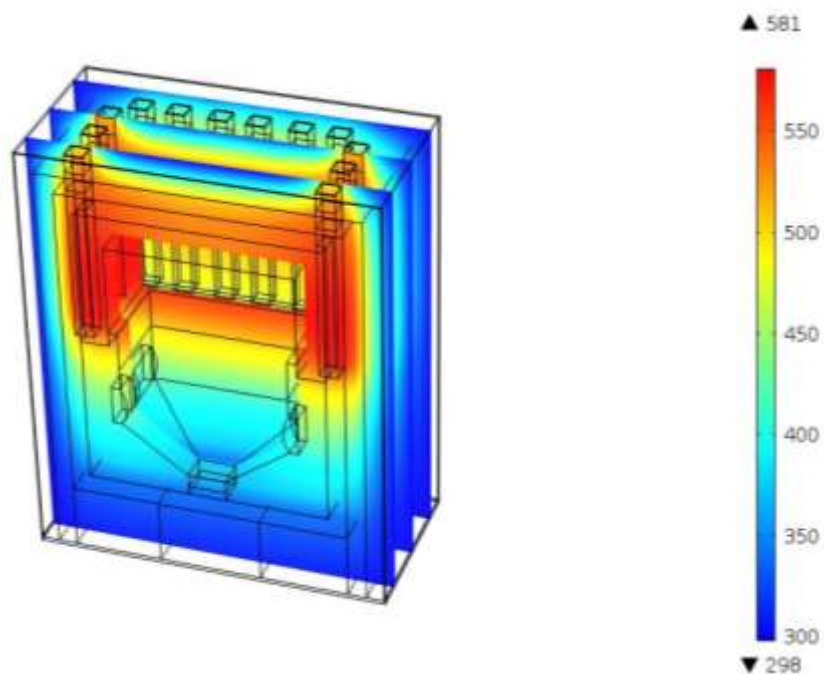


**Figure 5.18:** Slice Plot for transient analysis of empty cavity at  $t = 65 \text{ hr}$  (Kelvin scale)

### 5.4.1.2 Validation and Simulations of Temperature Profiles at Various Power Inputs in stage – I operation

After applying suitable inputs like heat input to the plenum heaters, heat loss from off-gas nozzle, other convective and radiation losses to the model, the temperature profiles across different locations of thermocouples were extracted from the solution set of the entire domain and validated against the experimental data. Temperature profiles at the specified locations in the melter cavity were predicted using the numerical model for plenum heater power inputs of 395 W, 629 W and 776 W and are presented in Figure 5.19 along with the experimental results.

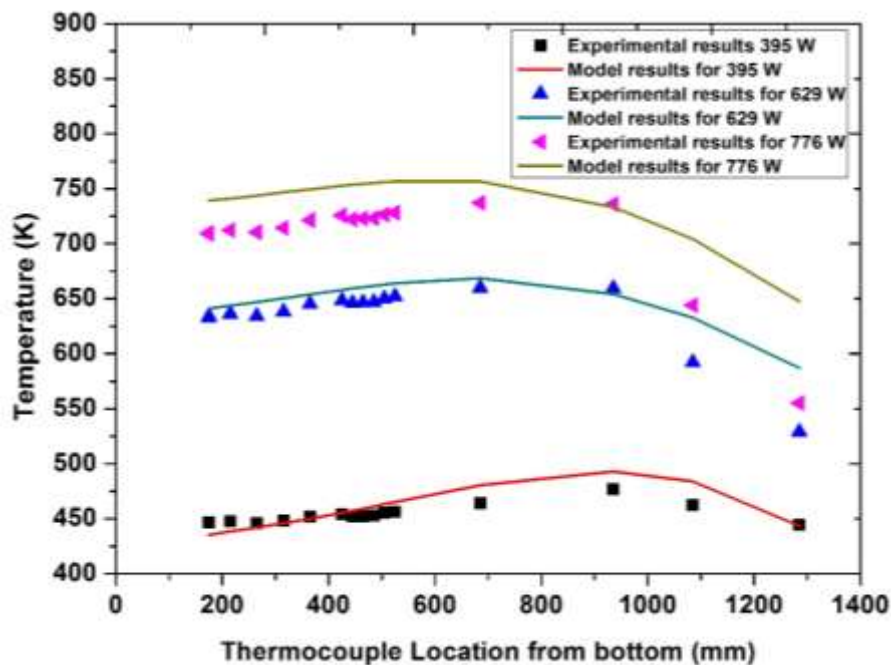


**Figure 5.19:** Validation of model with experimental data for an empty cavity

For plenum heater input of 395 W, the temperature was observed to be maximum at the 14<sup>th</sup> thermocouple because of its proximity to the plenum heater modules. Dip in the temperatures for 15<sup>th</sup> and 16<sup>th</sup> thermocouples is due to the local cooling effect by the off-gases exiting the system. The model could predict the temperatures with an accuracy of  $\pm 8\%$ , up to thermocouple 14. The melter is being operated under a vacuum of  $-30$  mm of water column due to which the air ingresses into melter from the gaps between flanges/refractory blocks. Till 800 mm glass frit was filled beyond

that plenum region starts. The ingressed air causes deviation of temperature beyond 800 mm

For plenum heater power input of 629 W, the temperature is almost uniform in the cavity, as can be seen from Figure 5.20. The peak temperature is again observed at thermocouple 14. However, the dip in temperature after thermocouple 14 is steeper because of the off-gases exiting at a higher temperature. Deviation of the predicted values from the experimental values is  $\pm 4\%$  upto 14<sup>th</sup> thermocouple. For plenum heater power input of 776 W, the predicted temperatures were invariably higher than the experimental values by 5%.

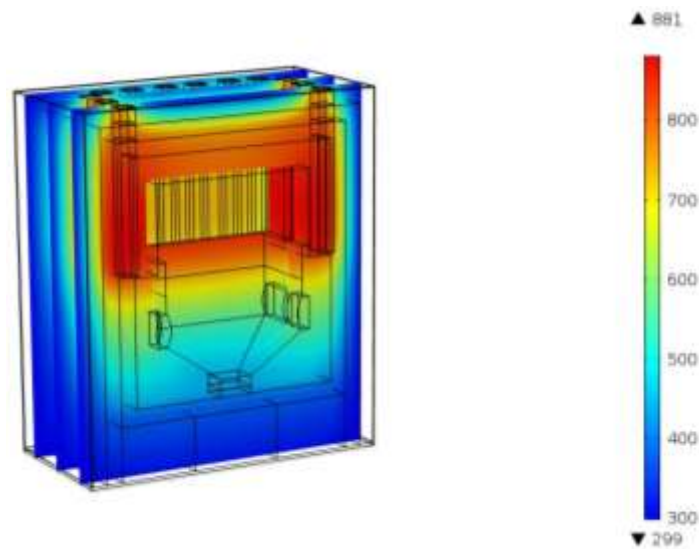


**Figure 5.20:** Slice plot depicting temperature profile inside the melter for 629 W on each heater (Color Legend: Temperature in Kelvin scale)

#### 5.4.2 Temperature Profile in Stage – II Operation of JHCM

The glass frit was charged into melter and the frit added in the form of beads forms a heap based on the angle of repose. The power input to the system increases the plenum heater temperature that transfer heat to the glass frit. The heap consolidates and forms a molten glass as shown in Figure 5.21. Effective thermal conductivity of porous glass beads was modelled for to validate the model

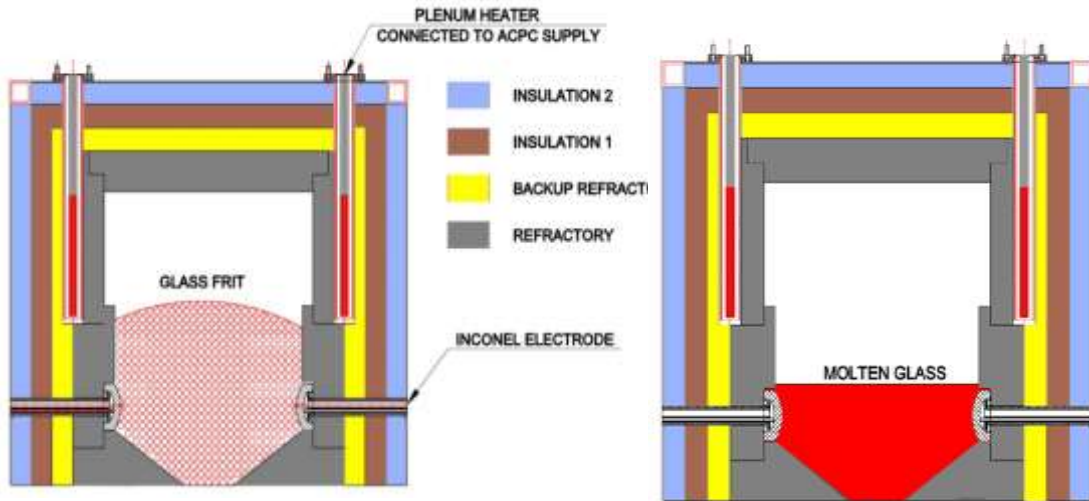


**Figure 5.21** Industrial scale JHCM used for experiments (a) Start-up heating using plenum heaters; (b) Electrode heating

#### 5.4.2.1 Sub model for determination of effective thermal conductivity

A rectangular domain with 66.7 % porosity was constructed along with boundary condition, as shown in Figure 5.22, to estimate the effective thermal conductivity of the packed bed of glass beads. The properties of the porous bed of glass frit were estimated from the properties of glass frit and air.

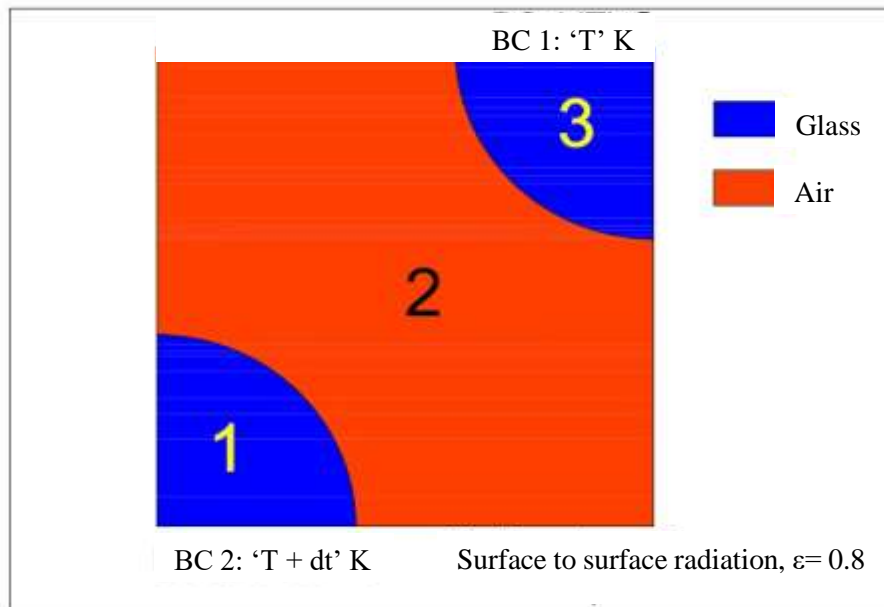


**Figure 5.22:** Model to predict effective thermal conductivity of packed bed of glass

By varying the T and dT values, the effective thermal conductivity of glass was determined at different temperatures and for different temperature gradients. The first case studied was without radiation between the surfaces of the glass particles. The temperature difference between the surfaces of the glass particles, dT was varied as 1, 2, 5, 10, 20, 50, 100 K over a known length of 6.84 mm and the thermal gradient  $\frac{dT}{dx}$  was calculated for each case. Then the average flux was extracted from the model by evaluating,

$$\oint \frac{q}{46.79 [mm^2]}$$

where the value 46.79 mm<sup>2</sup> is the area of the domain over which the value is surface averaged from the value of average heat flux, the effective thermal conductivity is derived by,

$$q = -k \cdot A \cdot \frac{dT}{dx} + \varepsilon \cdot \sigma \cdot (T_{ext}^4 - T^4) \quad (5.1)$$

$$q = -k_{eff} \cdot A \cdot \frac{dT}{dx} \quad (5.2)$$

where,

$$k_{eff} = k + \frac{\varepsilon \cdot \sigma \cdot (T_{ext}^4 - T^4)}{A \cdot \frac{dT}{dx}} \quad (5.3)$$

$$\text{Rearranging, } k_{eff} = \frac{-q/A}{dT/dx} \quad (5.4)$$

The value of q changes with change in all the parameters like T, dT and also by switching on/ off, the radiation between the participating surfaces in heat transfer.

The effect of radiation on thermal conductivity can be determined by a factor f (T) which is defined as follows

$$f(T) = \frac{\text{thermal conductivity with radiation}}{\text{thermal conductivity without radiation}}$$

The model was used to calculate the flux term, q by switching on and off the radiation between the glass particle surfaces. This resulted in a change in the heat

flux term. If this function increases, then radiation begins to dominate among the heat transfer modes. In general, the radiation mode of heat transfer becomes dominant at higher temperatures. The variation of  $f(T)$  concerning a thermal gradient,  $\frac{dT}{dx}$  is almost negligible. The function changes significantly with respect to variation in temperature.

#### 5.4.2.2 Simulation and validation of temperature profiles in stage – II

During the start-up operation of JHCM, only 5% of the heat supplied to the plenum heaters could be utilized for heating the glass frit. As mentioned before, experiments were devised to analyse the effect of different parameters like reducing the skin losses by insulating the top of the melter, reducing the heat losses from the system by optimising the negative pressure of the melter, optimising the gap between heaters and Kanthal<sup>®</sup> tubes and to determine the dominant mode of heat transfer in the system.

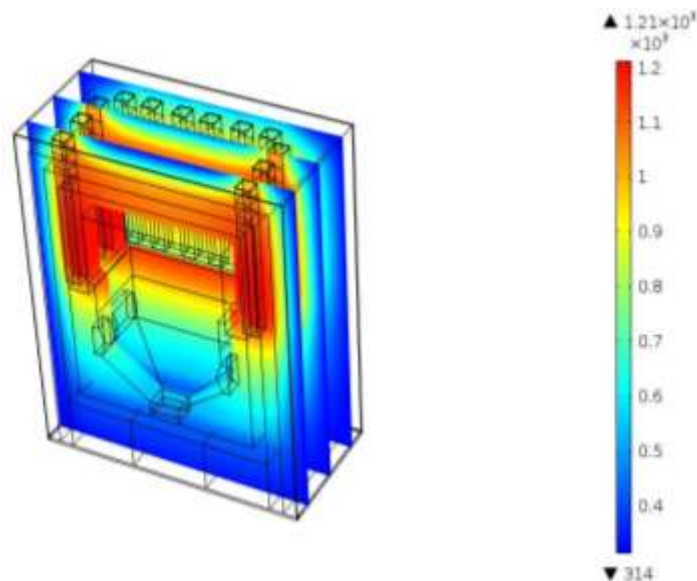


**Figure 5.23:** Slice plot depicting temperature profile inside the melter for 1198 W on each heater (Color Legend: Temperature in Kelvin scale)

After achieving a steady state with a plenum heater power of 776 W, glass frit was charged in the melter up to thermocouple location 12 and plenum heater power was

further raised to 1198 W. This condition was also simulated in the numerical model.

The 3D temperature plot for this case is shown in Figure 5.23.

The surface temperature of the SS enclosure of the melter was monitored with thermal imaging cameras to determine the effectiveness of the insulation layers and detect any point of abnormal heat losses. Based on the temperature of the face walls, the heat transfer coefficients on the walls were estimated. The heat losses in JHCM was apportioned. The off-gas losses were determined by measuring the air leakage into the melter and its temperature. Figure 5.24 shows the heat losses from the melter

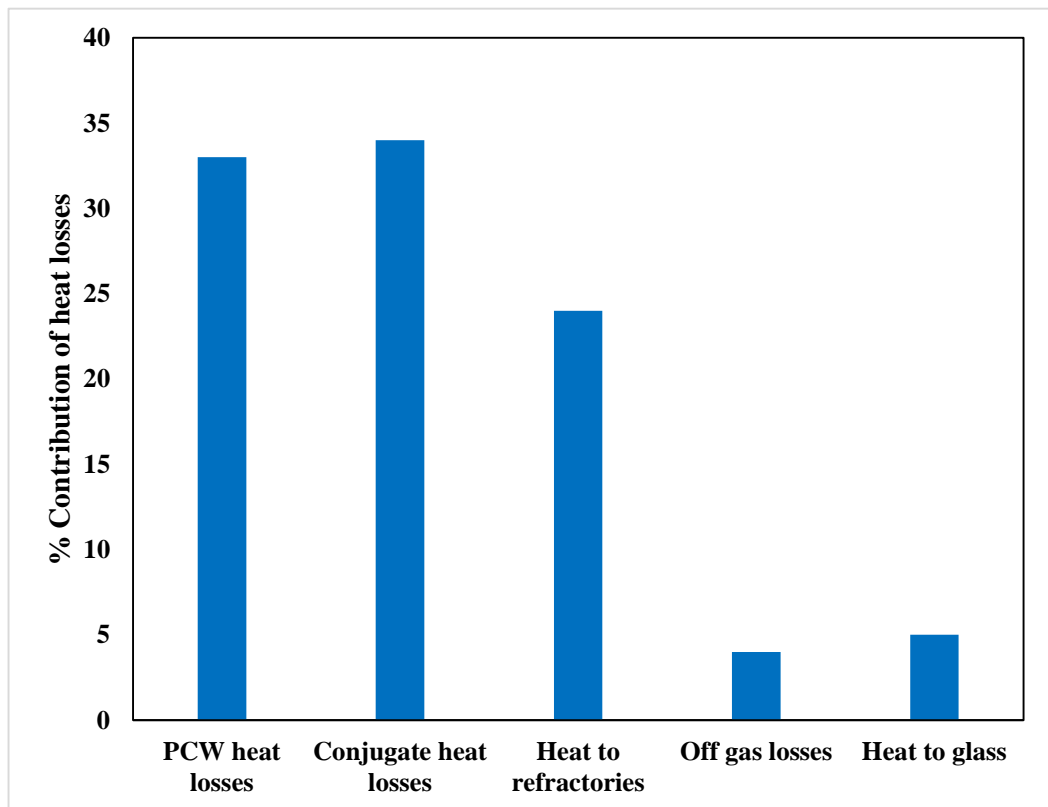


**Figure 5.24:** Apportionment of heat losses from JHCM

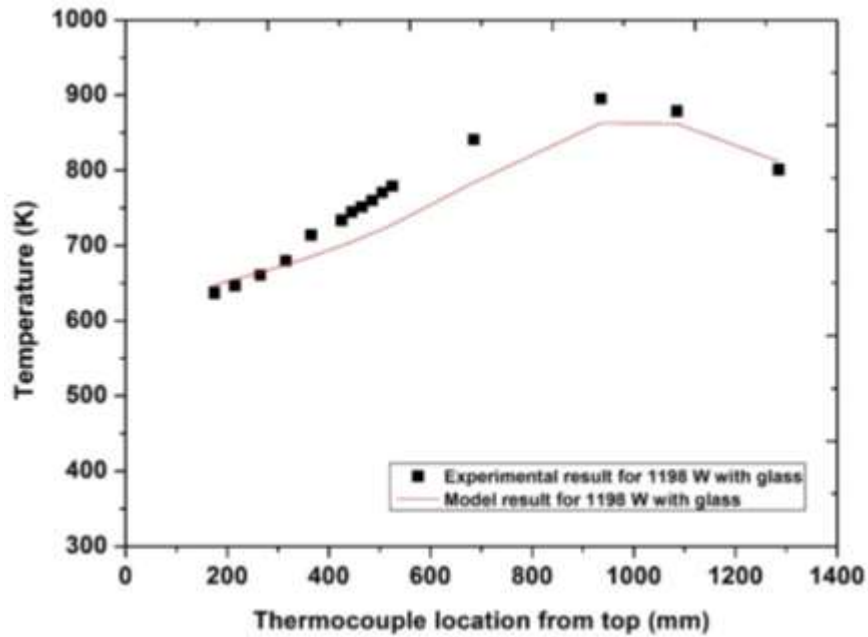


**Figure 5.25:** Validation of model for Temperature profile in Melter charged with packed bed of glass beads

through different media. The model was validated with experimental data, as shown in Figure 5.25. The agreement of the model with experiments is better in the lower portion of the melter,  $\pm 3\%$  up to thermocouple 5, as against  $\pm 5$  to  $\pm 11\%$  for thermocouples 6 to 14. As the temperature increases melting of the glass beads results in consolidation of packed bed in temperature range of 723-873 K. consequently, air in the packed bed escape and porosity of the bed decreases resulting in increase of thermal conductivity. It is seen from computation that thermal conductivity of bed changes from  $0.1 \text{ W.m}^{-1}.\text{K}^{-1}$  to  $1 \text{ W.m}^{-1}.\text{K}^{-1}$  as bed consolidation progresses. A parametric study with thermal conductivity of  $0.1 \text{ W.m}^{-1}.\text{K}^{-1}$  resulted in  $-11\%$  variation whereas  $1 \text{ W.m}^{-1}.\text{K}^{-1}$  resulted in max.  $+8\%$  variation for thermocouples 6-11. The average absolute relative error in the temperature estimated by the model is in the range of  $\pm 5.1\%$ . Parity Plot is shown in Figure 5.26.

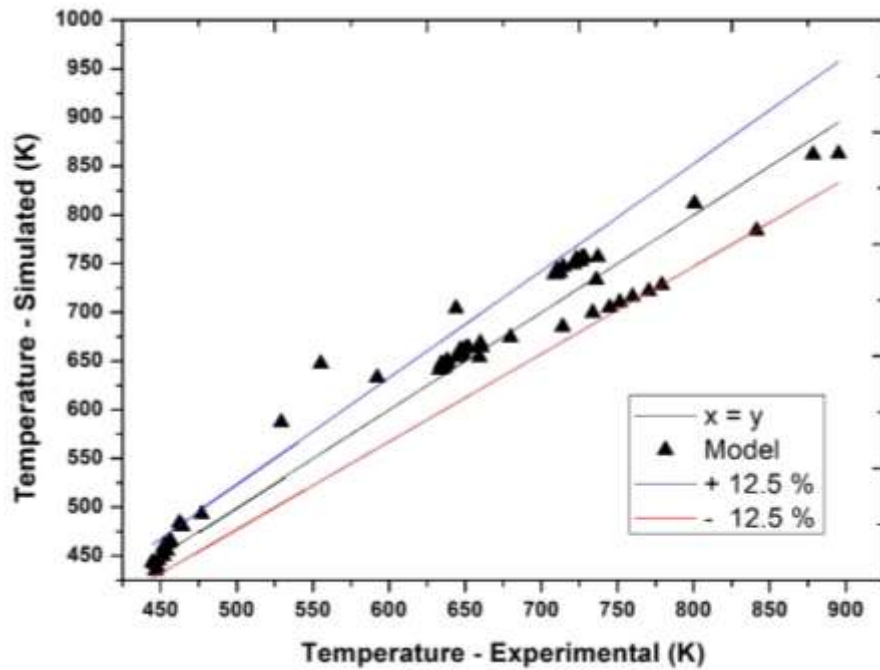


**Figure 5.26:** Parity plot of the experimental values of Temperature and temperature predicted by the Model for stage-I & II

### 5.4.3 Temperature Profiles In Stage – III Of Melter Operation - Simulation and Validation

The glass frit charged was melted and the Joule heat generated in molten glass is used for vitrification. There exists natural convection in molten glass that enhances over all thermal conductivity. Effective thermal conductivity of molten glass was determined based on empirical correlations for validating the model and subsequently this parameter is used for fitting the model.

#### 5.4.3.1 Effective Thermal Conductivity of Molten Glass in Stage - III

The rate of melting is determined by total heat flux to the cold cap. Based on the heat flux, cold cap thickness increases or decreases. Under steady state conditions, the off-gases generated during calcination shall evolve out from glass surface at which heat input balances the glass formation rates. In order to determine heat flux, the effective thermal conductivity of the glass must be determined.

The thermal conductivity of the glass over a wide range of temperature is constant at  $0.96 \text{ W.m}^{-1}.\text{K}^{-1}$ . The convective heat transfer coefficient inside the glass melt in an all-electric glass melter depends on thermally driven flows. This heat transfer coefficient is calculated by finding the effective thermal conductivity for molten glass pool as given in [87] which is

$$k_{\text{eff,mt}} = k\text{Nu} \quad (5.5)$$

where  $k$  is the thermal conductivity of the molten pool, which is constant ( $0.96 \text{ W.m}^{-1}.\text{K}^{-1}$  as shown in Table 4.1) over a wide range of temperature and  $\text{Nu}$  is the Nusselt number.

Nusselt number is a function of Rayleigh Number ( $\text{Ra}$ ) given by [88] as

$$\text{Nu} = 0.195 \text{ Ra}^{1/4} \quad \text{for} \quad 10^4 < \text{Ra} < 4 \times 10^5 \quad (5.6)$$

$$\text{Nu} = 0.068 \text{ Ra}^{1/3} \quad \text{for} \quad 4 \times 10^5 < \text{Ra} < 10^7 \quad (5.7)$$

In the present study  $\text{Ra}$  is in the range of  $4 \times 10^5 < \text{Ra} < 10^7$ , hence, Equation (5.7) was used to find the  $\text{Nu}$  and hence the effective thermal conductivity inside the glass melt pool.

The temperature profiles inside the melter cavity are predicted by incorporating effective thermal conductivity determined by the Equation 5.5 which works out to be  $12.1 \text{ W.m}^{-1}.\text{K}^{-1}$ . The enhancement of thermal conductivity is due to the contribution by natural convection. The glass melt has a Prandtl number of 15900, and the Rayleigh number is  $6.42 \times 10^6$ .

The temperature profiles inside the melter cavity are predicted by incorporating effective thermal conductivity predominantly due to natural convection. The average velocity of natural convection in the molten glass are about  $0.05 \text{ mm.s}^{-1}$ .

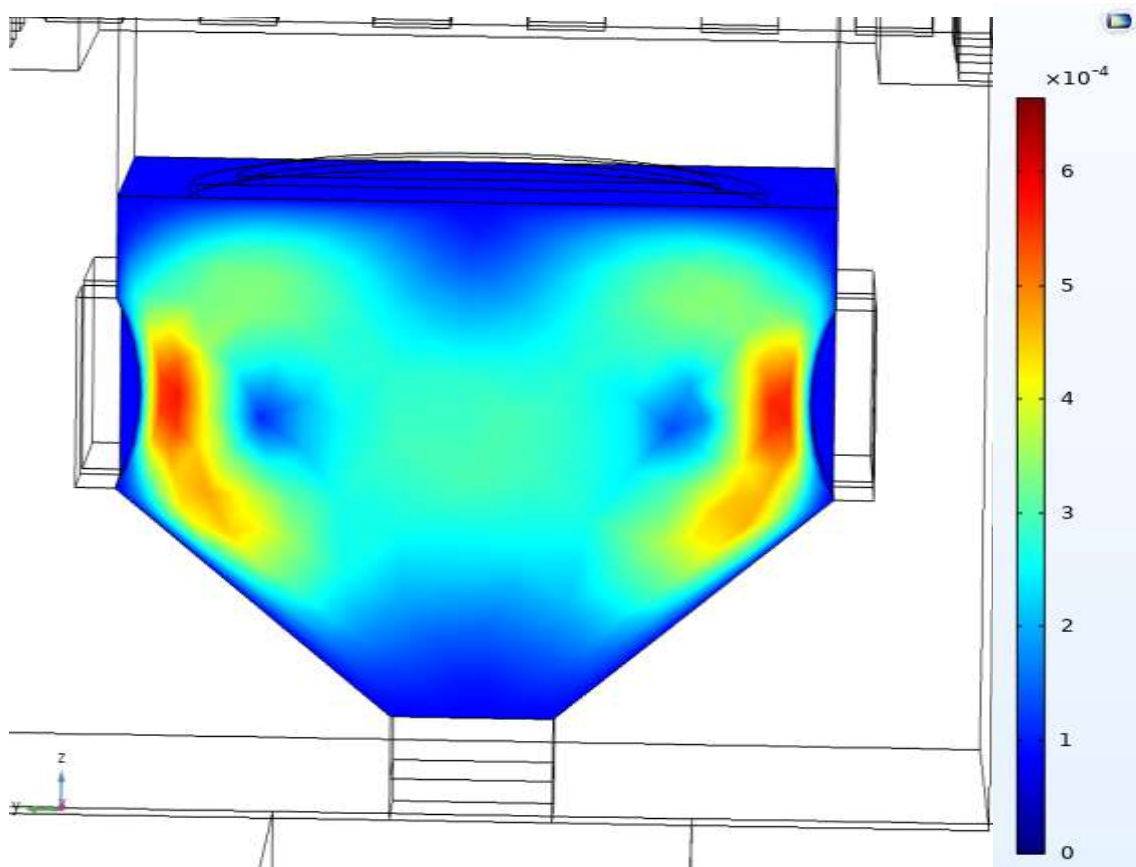


**Figure 5.27:** Velocity distribution in molten glass (Velocity in  $\text{m}\cdot\text{s}^{-1}$ )

The flow is predominantly downward due to natural convection induced by variation in temperature in the molten glass pool. The velocity on top is lesser compared to the centre, as shown in Figure 5.27.

The effective thermal conductivity of the molten glass pool is estimated to be  $11.8 \text{ W}\cdot\text{m}^{-1}\cdot\text{K}^{-1}$  from the model based on the temperature profiles in the melter generated during simulated waste trials carried out with  $28 \text{ g}\cdot\text{L}^{-1}$  salt concentration as shown in Figure 5.28. Based on the thermal conductivity determined from the model, the

temperature profiles generated during the experiments for  $56 \text{ g.L}^{-1}$  and results from the model are compared and depicted in Figure 5.29.

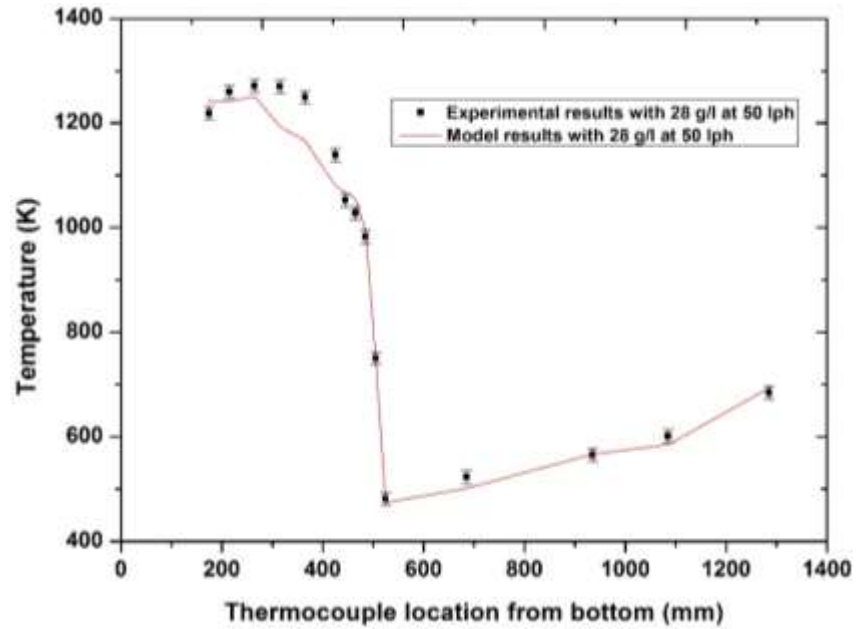


Figure 5.28: Model validation for Stage - III with  $28 \text{ g.L}^{-1}$  at  $50 \text{ L.hr}^{-1}$  feed rate

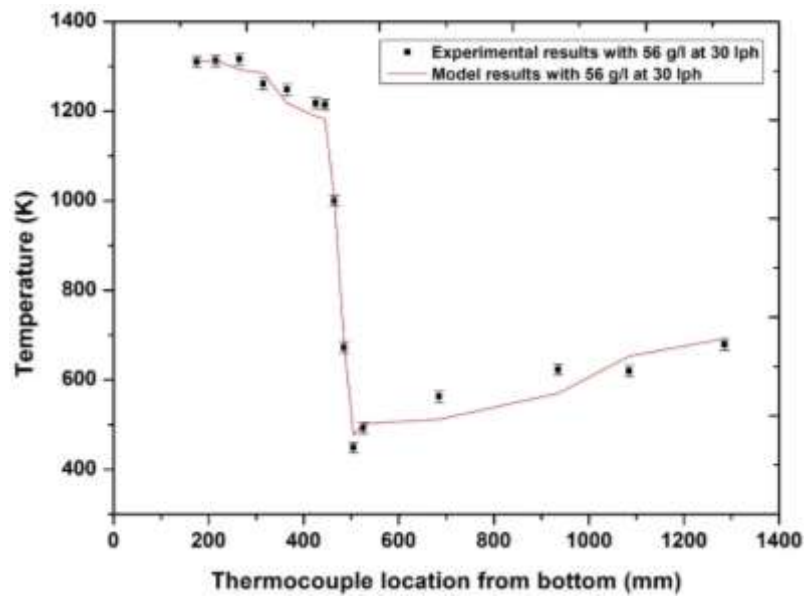
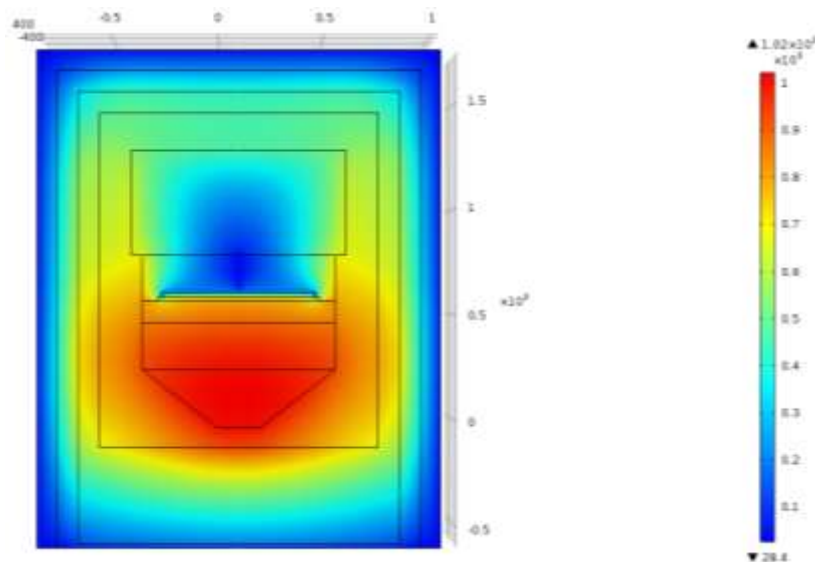


Figure 5.29: Model validation for Stage - III with  $56 \text{ g.L}^{-1}$  at  $30 \text{ L.hr}^{-1}$  feed rate

### 5.4.3.2 Temperature profiles in between insulation layers of the melter

The heat balance between the refractory and insulation layer is done by heat conduction equations giving the boundary condition of the conjugate heat losses from the walls and heat source term is incorporated in the model. Thermal analysis



**Figure 5.30:** 3D Volume plot depicting temperature contours (Rainbow Legend-Celsius scale) inside the JHCM including molten glass and cold cap

of the melter was carried out by FEM. Figure 5.30 shows the 3D Volume plot depicting temperature contours inside the melter for 28 g.L<sup>-1</sup> of salt.

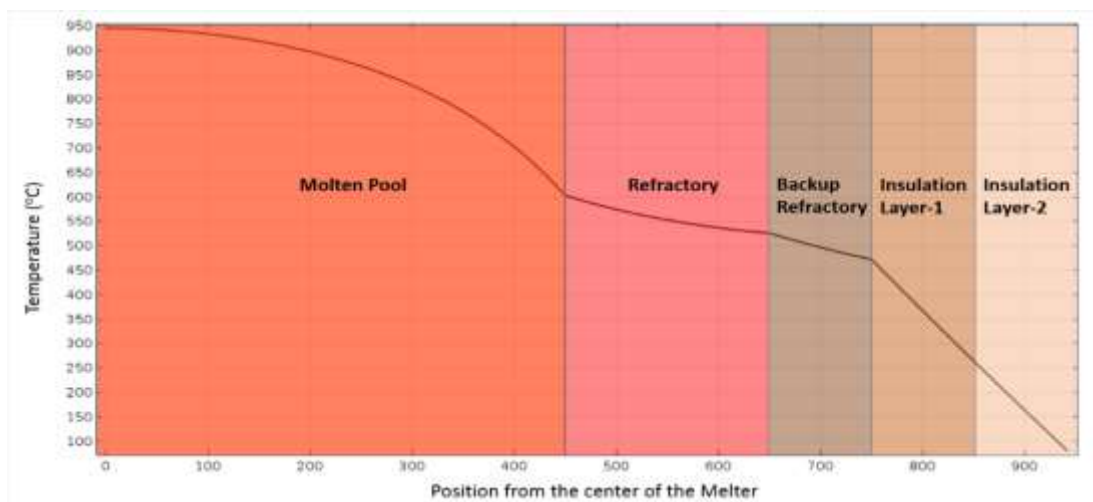


**Figure 5.31:** Temperature profile between the refractory and insulation layers

The temperature profile between the various layers of refractories and insulation is shown in Figure 5.31.

The experimental data were highly reproducible. The error bars in Figure 5.28 & Figure 5.29 represents  $\pm 2\%$  of the first experimental set. The maximum deviation was around  $10\%$  in the region of calcined mass, and the minimum error was less than  $0.5\%$ . Parity plot is shown in Figure 5.32.

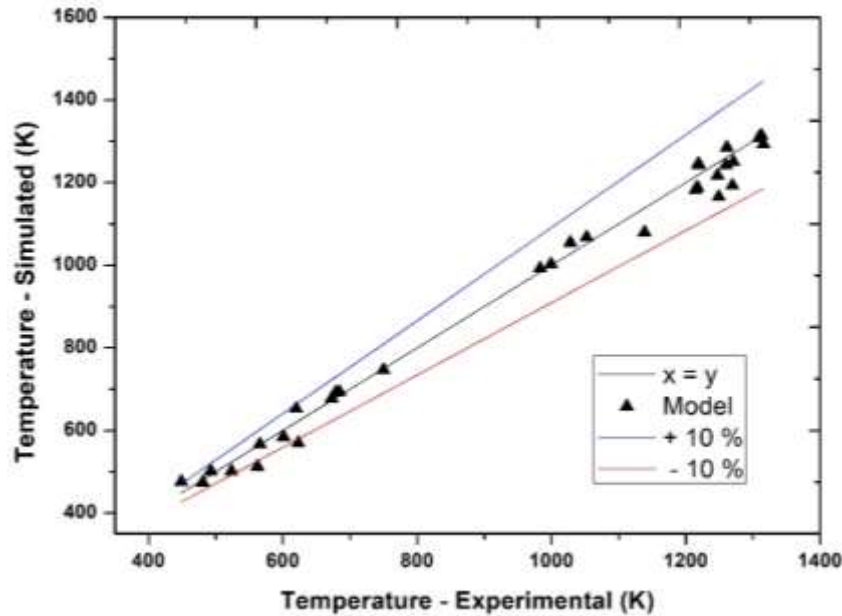


**Figure 5.32:** Parity plot of the experimental values of temperature and temperature predicted by the Model with HLW for stage-3

#### 5.4.4 Electrical Parameters validation in Stage – III operation of JHCM

Electrical parameters such as resistance between the electrodes in an important parameter during the operation of the melter. The glass pool is electrically heated by passing current through the molten glass. The temperature gradient exists in the glass pool as the molten glass, and the cold cap is maintained at different temperature. Glass pool is maintained at  $1273\text{ K}$ , and the cold cap is maintained at boiling liquid temperature. The variation in temperature gradient results in non - uniform electrical heat generation due to the positive temperature coefficient of electrical conductivity of glass.

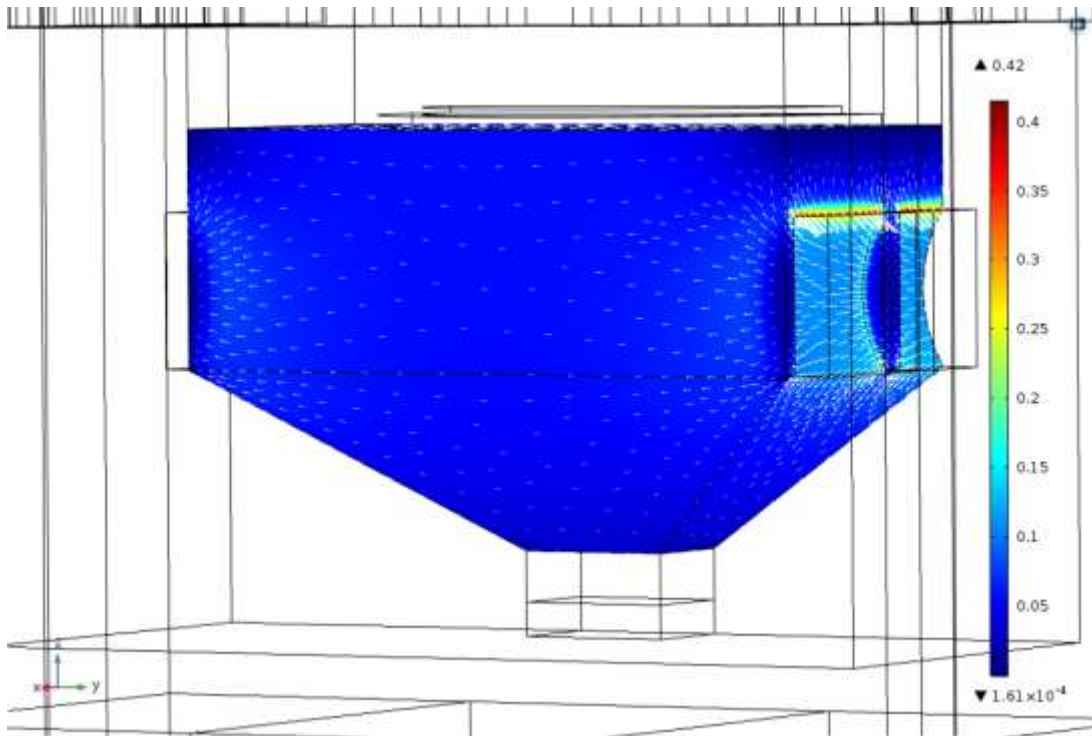


**Figure 5.33:** Current density arrow map for 3D melter model at 60 V potential drop (Rainbow legend current density in  $A.m^{-2}$ )

The current density between the electrodes is presented in Figure 5.33. As the electrodes are always submerged in the molten glass pool and the resistance between electrodes is kept constant.

#### 5.4.4.1 Validation of Electrical parameters

The results are validated with the resistance between electrodes from experimental data. The resistance was plotted as a function of time, resistance has varied as a function of sodium concentration depending amount waste treated. The experimental power was compared with the voltage applied, and the model results indicate a close agreement between measured values and predictions as shown in Figure 5.34. The average absolute relative error in the resistivity estimated by the model is in the range of - 12.1 %

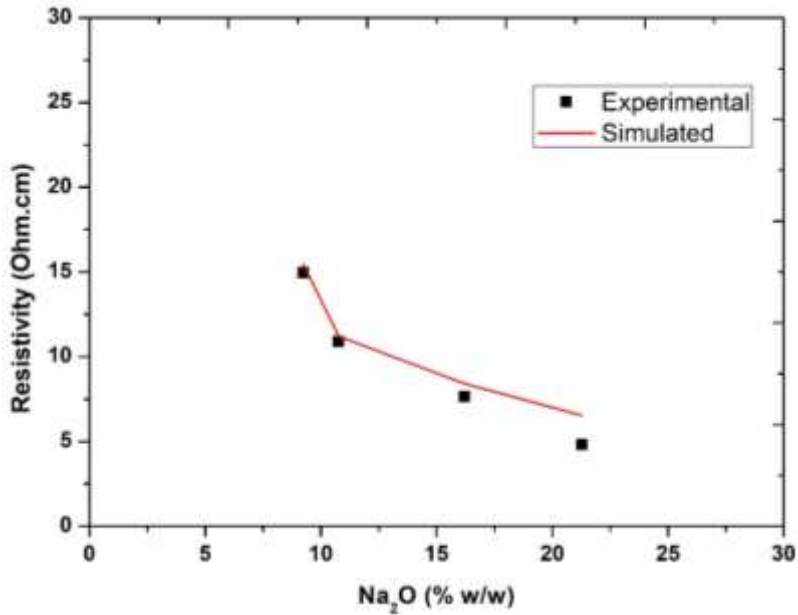


**Figure 5.34:** Validation of model with electrical properties

Electric potential was applied between two electrodes immersed in molten glass. The Joule heat generated by passing the current between electrodes is predicted with model and temperature profiles at different locations were extracted from the solution set and validated against the experimental data. Electrical current distribution in joule melter is simulated and presented in Figure 5.33. The current

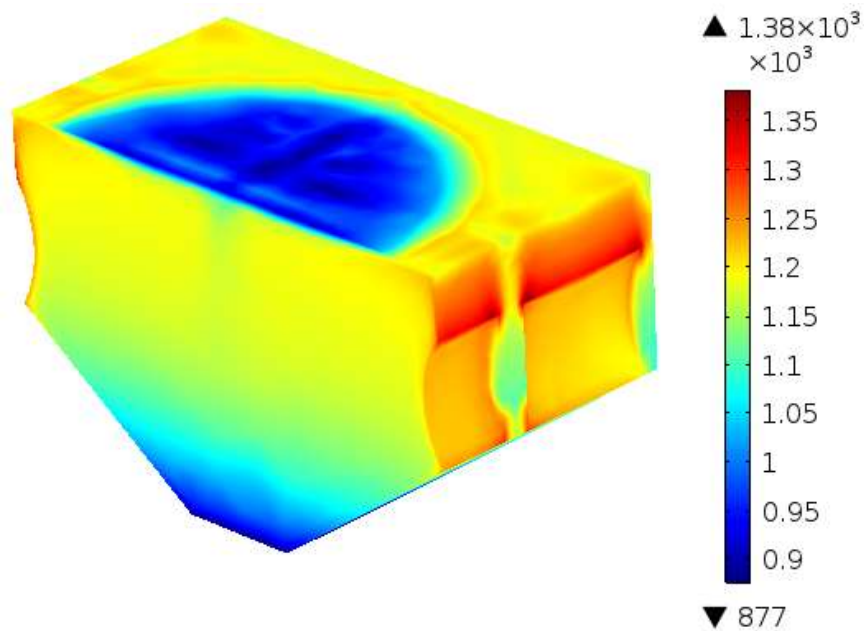


**Figure 5.35:** Temperature profile inside the melter cavity (Rainbow Color legend with Temperature in Kelvin for 60 V input)

distribution is higher at edges of the electrodes. The electrodes are subjected to various voltages and current densities as the electrical conductivity,  $\sigma$  is a function of temperature. Figure 5.35, respectively. The maximum pool temperature is 1381 K. In the hot region, the increase of electrical conductivity leads to increase of electromagnetic convection. The convection currents higher near to electrodes because of enhanced natural convection by electromagnetic convection. The current distribution is higher at edges of the electrodes. The electrode is subjected to various voltages, and current densities are observed to be higher at edges, as shown in Figure 5.33.

#### **5.4.5 Concentration Distribution in Stage – III of JHCM**

Homogenization of molten glass depends on convection mainly generated from non-uniform energy and on glass viscosity. JHCM used for radioactive waste the maximum velocity in literature is  $0.14 \text{ mm.s}^{-1}$  for a given geometry report [44]. The validation of the model is used for distribution of other compositions in the glass. As per DTG, there are five dominant peaks, and rate kinetics was incorporated in the model and plotted the response of these results in molten glass drained. The concentration profile of  $\text{CsNO}_3$  is as shown in Figure 5.36. Diffusivity of  $\text{Cs}_2\text{O}$  in borosilicate glass reported in Nanoka et al [89].

##### **5.4.5.1 Validation of concentration profiles**

In the current study, based on the geometry of the cavity,  $0.07 \text{ mm.s}^{-1}$  is achieved.  $\text{NaNO}_3$  is added in sRLW, and  $\text{Na}_2\text{O}$  was embedded in the glass matrix. The  $\text{NaNO}_3$  added from simulated waste reacts at a higher temperature in the range of 1023 K and decomposes to  $\text{Na}_2\text{O}$ .  $\text{Na}_2\text{O}$  formed diffuses into the glass matrix and embedded in the VWP. Samples from VWP was withdrawn at regular intervals during glass pouring and analysis to determine  $\text{Na}_2\text{O}$  in product glass in VWP.

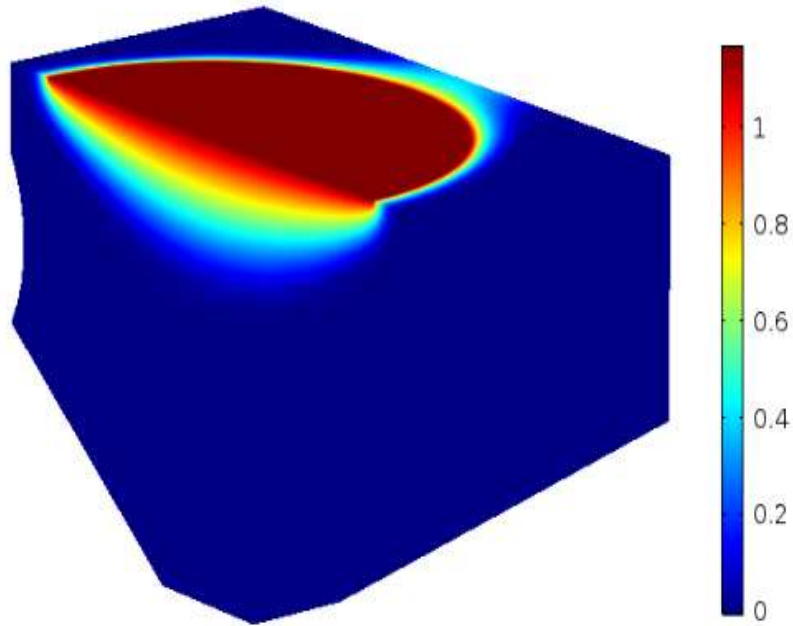


**Figure 5.36:** Concentration profile of  $\text{CsNO}_3$  (Rainbow legend in  $\text{mol.m}^{-3}$ )

Product concentration of  $\text{Na}_2\text{O}$  vs time was plotted for experimental, numerical and analytical and numerical results are in good agreement with experimental. Temperature profiles in JHCM in stage after coupling electrical and decomposition of nitrates. The average absolute relative error in the concentration estimated by the model is in the range of  $\pm 4.4\%$ .

Temperature profiles at GP location in the melter cavity were predicted using the numerical model for 60 %, 80 % 90 % coverage of cold cap and presented in Figure 5.38, Figure 5.39, and Figure 5.40. Boiling nitric acid is at the top of the molten glass pool maintained at 413 K. As shown in Figure 5.41, Figure 5.42 and Figure 5.43, the maximum deviation was observed near the interface.

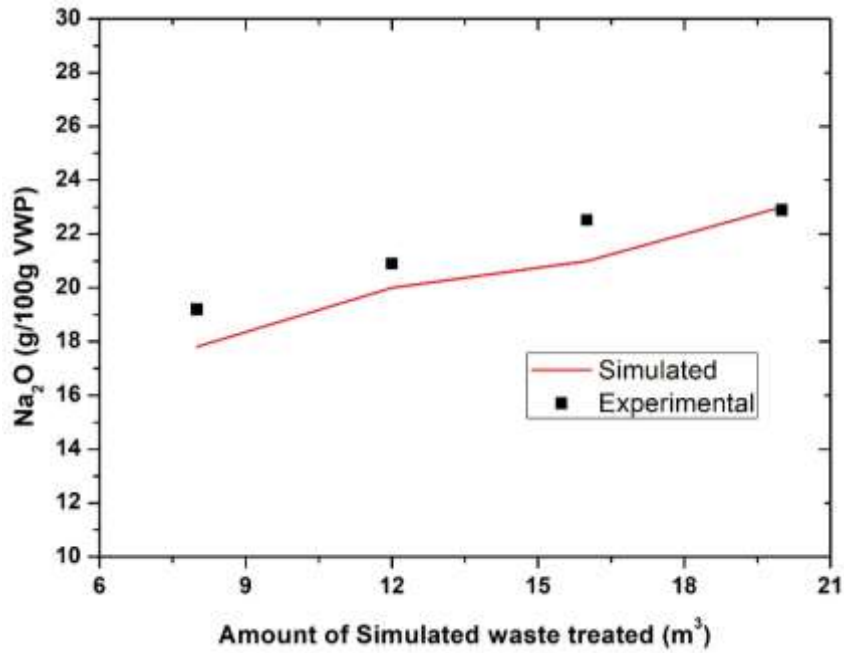


**Figure 5.37:** Validation of model with concentration profiles

The multi-phase prevailing in the cold cap zone is contributing to the deviations at the interface. The electrode are maintained at higher temperature compared to the molten glass. The effect of heat flux at the top of molten glass is transferred to bottom portion. Natural convection in the glass pool is homogenizing the mass. The electrodes are maintained about 200 K higher than the glass pool. The temperatures are monitored off centered in the Figure 3.5. The model could predict the temperature with an accuracy of  $\pm 2\%$  in the molten glass. Whereas in the cold cap region, the prediction is with an accuracy of  $\pm 8\%$  for all the cases. The maximum deviation was around 8% in the region of calcined mass, and the minimum error was less than 0.5%. Parity Plot is shown in Figure 5.44

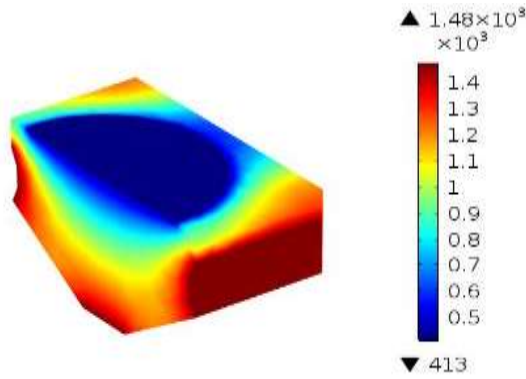


**Figure 5.38:** Cold cap covering 60 % of melter top surface

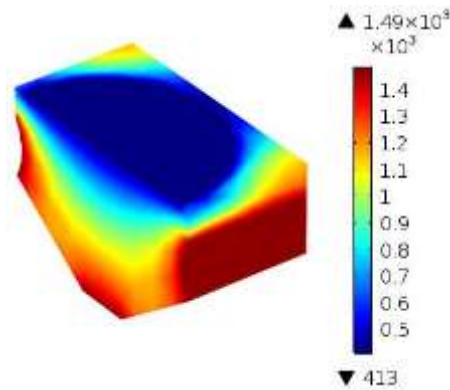


**Figure 5.39:** Cold cap covering 80 % of melter top surface

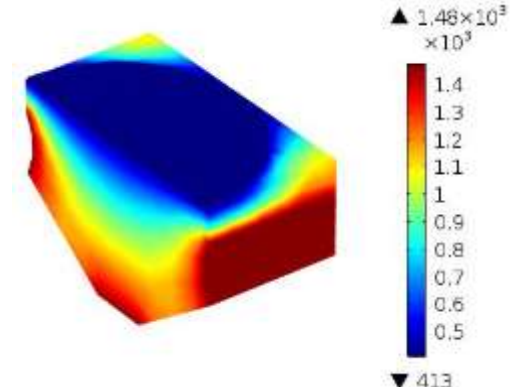


**Figure 5.40:** Cold cap covering 90 % of melter top surface

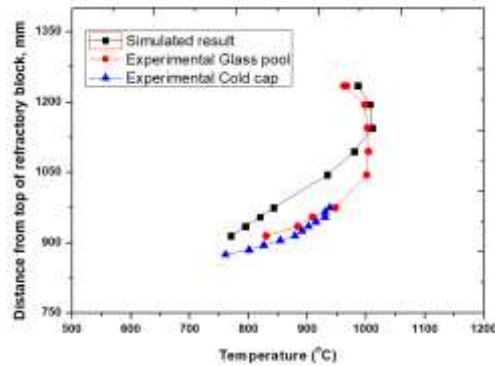


**Figure 5.41:** Comparison of experimental result with simulated result for 60% cold cap spread

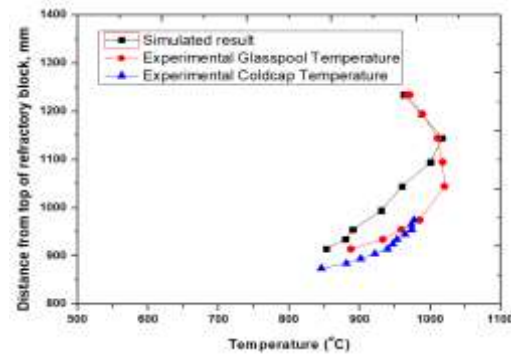


**Figure 5.42:** Comparison of experimental result with simulated result for 80% cold cap spread

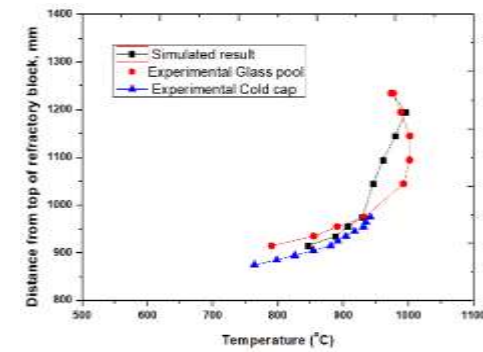


**Figure 5.43:** Comparison of experimental result with simulated result for 90% cold cap spread

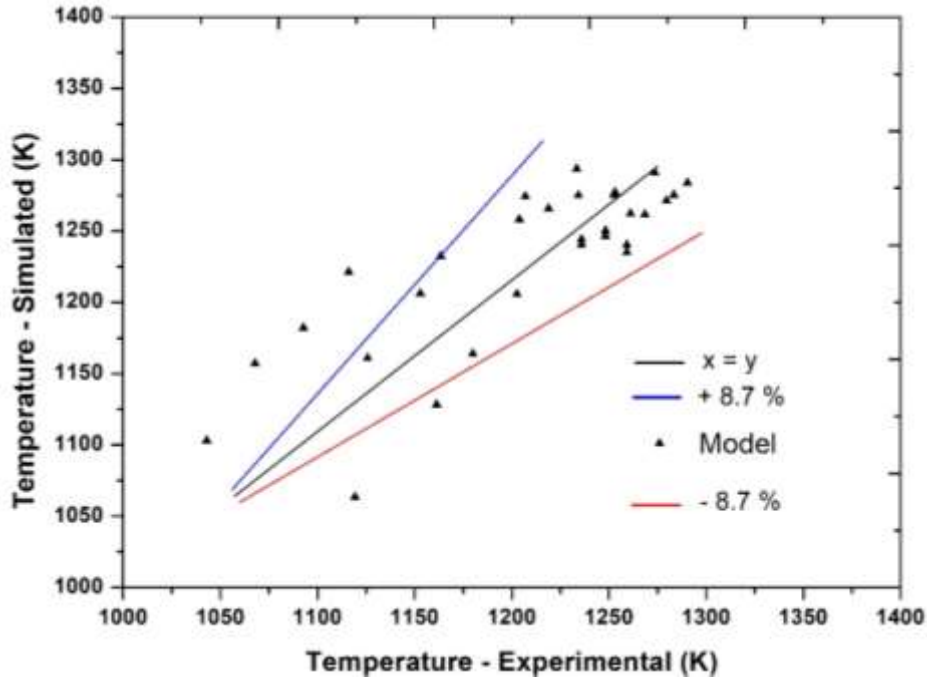


**Figure 5.44:** Parity plot of temperature profile

## 5.5 Study of Design and Operating Parameter Refinements in JHCM Based on Model

JHCM operating and design parameters are studied based on the validated model. The design and operating parameters were studied during start up heating of melter i.e., stage – I and Stage – II of melter operation based on validated model. Subsequently studies were extended to enhance process capacity by using validated model of stage – III operation.

### 5.5.1 Parameters influencing start-up heating efficiency

During the start-up operation of JHCM, it was observed that only 5 % of the heat supplied to the plenum heaters could be utilised for heating the glass frit. Experiments were devised to analyse the effect of different parameters like reducing the skin losses by insulating the top of the melter, reducing the heat losses from the system by optimizing the negative pressure of the melter, optimizing the gap between heaters and Kanthal<sup>®</sup> tubes and to determine the dominant mode of heat transfer in the system.

### 5.5.1.1 Minimizing of the skin losses from the top of melter

The skin losses from the side, bottom and top of the melter were determined and were found to be 3.3, 0.9 and 5.2 kW, respectively. Melter top face and a top half section of side face contributed higher heat losses. The losses can be minimised by providing glass fibre insulation of 50 mm thick, during start-up. Subsequently, these insulations can be remotely removed. The additional insulation will reduce heat losses to 1.5, 0.9 and 3.4 kW. This reduction will allow the plenum heaters to serve their purpose at lower temperatures.

### 5.5.1.2 Optimization of negative pressure of JHCM

In JHCM the pressure must be kept below 50 mm water column below atmospheric pressure to prevent pressurisation of the equipment and subsequent release of radioactivity in the cell. This condition also ensures that gaseous radioactive effluents generated during the process are routed through an elaborate off-gas cleaning system

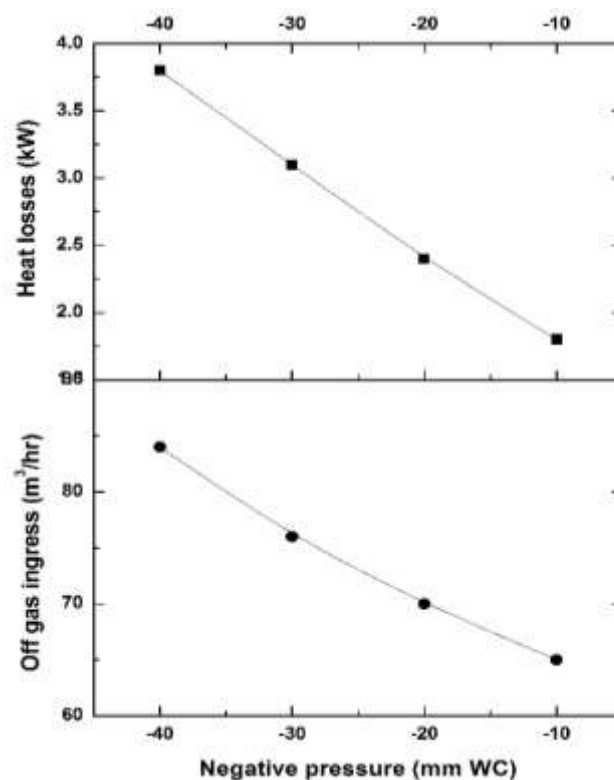


**Figure 5.45:** Off gas ingress and heat losses vs negative pressure in the melter

before finally being discharged it into the atmosphere. To reduce air ingress in JHCM, melter is enclosed by SS sheets as the internal layers of refractory material do not provide sufficient airtightness because of the inherent gaps that exist in the structure.

However various penetrations into the SS casing of the JHCM like electrodes, feed nozzles, off-gas nozzles, level probes, thermowells etc. provides a path for air ingress. The optimised negative pressure of the JHCM is a balance between preventing pressurisation and minimizing air ingress. Increased air ingress will result in heat losses from JHCM. By reducing the negative pressure in melter, the ingress of air into the furnace is reduced. This reduces the heat losses from the equipment. Figure 5.45 shows the heat losses in JHCM concerning air ingress and negative pressure in JHCM.

### **5.5.1.3 Change of the geometry of prefabricated slots from square to circular**

The cylindrical APM Kanthal<sup>®</sup> tubes are placed in prefabricated slots in the refractory. The type of geometry and dimensions of the slots play a very important role in improving or downgrading the thermal performance and hence, the efficiency of the plenum heating.

#### **5.5.1.3.1 Change of the geometry of prefabricated slots from square to circular**

The size of the heaters and minimum clearance limits reduces the dimensions of the slots. However, for any given dimension, the shape of the slots can be square or circular. The validated model was used to study the effect of change in geometry of the prefabricated slot on the overall thermal performance of the plenum heating section. The original square slots have each side of 100 mm length. The slots fabricated in the melter have to provide enough clearance for insertion and removal of APM Kanthal<sup>®</sup> tubes remotely. Remote Handling trials were carried out, and it was realised that a minimum gap of 1.5 mm from both sides was required for insertion and removal of these APM Kanthal<sup>®</sup> tubes where the plenum heaters were placed. Hence

the minimum diameter of the slot was fixed as 93 mm. Studies were carried out to examine the influence of air gap and change in slot geometry by using the validated model as shown in Figure 5.46.

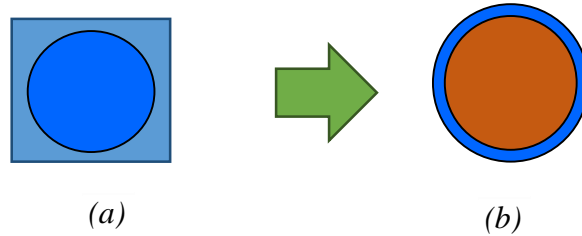


**Figure 5.46:** (a) Prefabricated square slots for placing of PH with a gap 6 – 26 mm.  
(b) Circular Slots for placing of PH

#### 5.5.1.3.2 Variation of the air gap between Kanthal<sup>®</sup> tubes and AZS blocks

The validated model was used to study the effect of change of the air gap thickness between Kanthal<sup>®</sup> tubes and the AZS blocks, on the efficiency of the plenum heating. Simulations were also carried out to study the effect of thickness of the air gap between the Kanthal<sup>®</sup> tubes and the refractory slots. The simulation results shown in Figure 5.47 (a) indicate that as the thickness of the air gap increases, the heat flux dissipated from the inner to the outer cylinder in a concentric cylinders system decreases till a thickness of 100 mm. Thereafter, the heat flux from the Kanthal<sup>®</sup> tubes to the outer

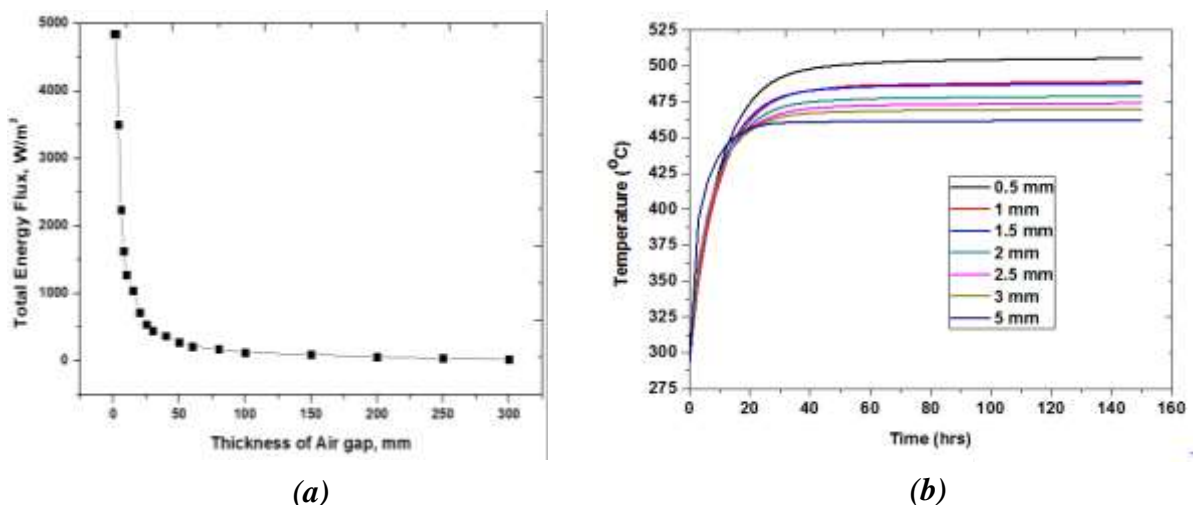


**Figure 5.47:** (a) Total Energy Flux Vs Thickness of the air gap; (b) Change in temperature with time for different air gap thickness between refractories and Kanthal<sup>®</sup> tubes

cylinder is constant even if the thickness of the air gap is increased as the radiation effect decreases substantially after 100 mm gap.

Effect of air gap thickness on the heat loss has been studied and from Figure 13(a) it can be concluded that as air gap increases the heat loss decreases to a particular flux and then it becomes constant. The optimum thickness of the air gap has been determined to be 3 mm from Figure 5.47 (b) to facilitate the remote removal of APM Kanthal<sup>®</sup> tube in the modified design.

The heat flux across the diagonal section of the square slots was determined from simulation. This was then compared with the heat flux in a circular geometry. In this study, it was established that circular geometry results in increased heat flux as compared to square geometry, as shown in Figure 5.48. The effect of geometry on the heating rate was studied using the validated model. The total heat flux of a circular geometry is 44% higher compared to square geometry. The area under the two curves will give power per unit length. The power per unit length for circular and square geometries are 1098.6 W/m and 813.6 W/m respectively. These results reinforce the fact that circular slots provide better heat transfer rates. The results also show that by

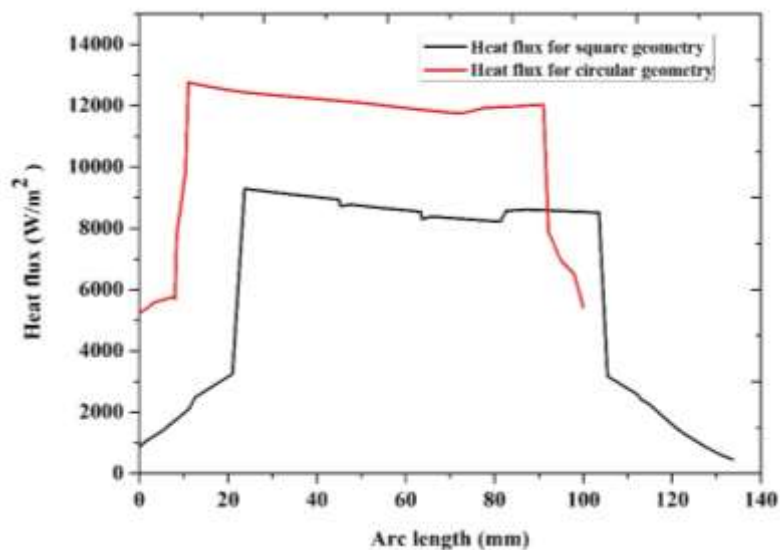


**Figure 5.48:** Heat flux vs Distance in the prefabricated in the square and circular designs

deploying circular geometry design in the prefabricated slots of the refractory, the heat flux, heating rate and thermal efficiency of the melter can be increased by 44%, 10.4%, and 35% respectively. The average absolute relative error in the temperature estimated by the model is in the range of  $\pm 12.5\%$ .

#### 5.5.1.4 Testing of alternate PH design by simulation

The model developed for stage 1, and stage 2 operations were validated in section 5.3. The average absolute relative error in the temperature estimated by the model is in the range of  $\pm 5.1\%$ . The model was used for design refinement of heating system used for stage 1 and stage 2 operation. The U shaped heaters were studied in present study & helical shaped silicon carbide heaters are studied in the validated model. Temperature profile using a helical heater is simulated and given in Figure 5.49.

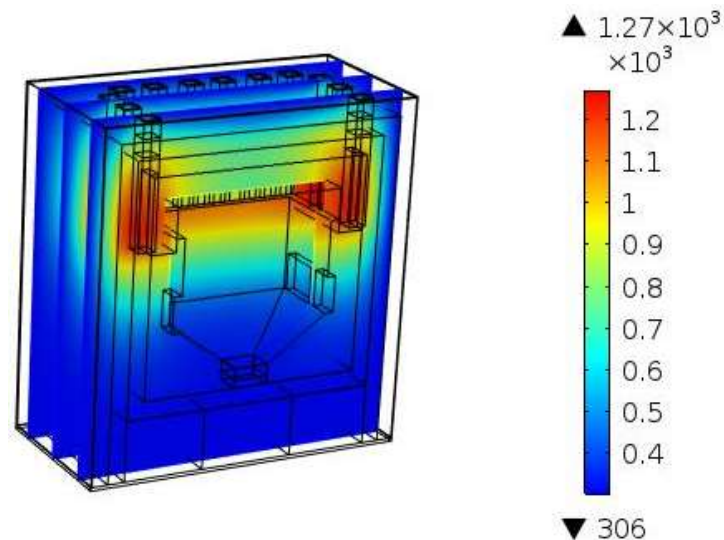


**Figure 5.49:** 3D Volume plot depicting temperature profile (Rainbow Legend – Kelvin scale) inside the melter with modified Plenum Heaters

Helical heaters are found to be the more compact and the desired temperature profiles can be obtained using the helical shaped heater design, that occupy only 60% of the volume compared to that of U tube heaters. A helical element with a pitch of 50 mm and an outer diameter of 20 mm will require 7 (6.87 to be exact) turns to generate the

same power. However, the total height of such a helical heater is approximately 350 mm compared to 550 mm of U bar element. Hence, the size of the domain can be reduced by using helically shaped heaters, and the same power can be delivered by a lesser volume. This will result in a decrease of melter weight by 2 Ton. As the melter is placed in a radioactive cell, it would require an elaborate remote handling facility for decommissioning at the end of its life. This weight reduction will facilitate an easier and more economical design of the decommissioning scheme.

## **5.5.2 Parameters influencing Processing Capacity**

### **5.5.2.1 Salt Concentration**

The throughput of the melter depends upon a) the power fed to the melter b) operating temperature and c) the salt content of the liquid fed to the melter. The operating temperature of the molten glass pool inside JHCM is limited to 1273 K. The molten glass pool surface has a certain heat flux beyond which the power supplied will increase the temperature of the molten glass. Hence, the power fed to the melter depends on the heat transfer to the cold cap. The cold cap is a zone of multiple layers; accumulation of NO<sub>x</sub> gases will reduce the heat flux to the boiling zone. In case of further raise in power instead of increasing the processing capacity, it will lead to raising in operating temperature of glass pool beyond 1273 K. Further increase in the salt concentration will lead to the trapping of more entrapped gases in the calcined zone reducing the heat transfer to boiling liquid, thereby reducing the processing capacity of the melter.

The melter operating capacity is optimized between waste evaporation rate and glass assimilation rate. At higher salt loading, the glass assimilation rate is poor due to low heat transfer through porous media, i.e., through the foam generated during calcination. The throughput at different salt concentrations is given in Table 5.8. As a result, the

throughput of the melter reduces in terms of waste volume at higher salt concentrations, whereas the glass production rate increases due to the decrease of evaporation load.

### 5.5.2.2 Base Glass Composition

7C glass loaded with waste oxides decomposes at a faster rate compared to 5C glass for peaks – 2, 3, 4 and 5 as shown in Figure 5.8, whereas the reaction rate is lower for 7C compared to 5C for peak -1 for all the heating rates.

It was found that the thermal decomposition of  $CsNO_3$  in the presence of borosilicate glasses (5C and 7C) took place at a lower temperature than that of base compound  $CsNO_3$ , as shown in Figure 5.8. Kawai et al., and Banerjee et al., reported a similar phenomenon [28][90]. The decomposition reactions of the waste nitrates shift to lower temperatures in the presence of glass.

### 5.5.2.3 Operating Level above electrodes

The melt level varies as VWP is poured into the canister. The melter is operated between minimum operating levels to maximum operating level. As the joule melters are operated with submerged electrodes in molten glass, the closer the electrodes to cold cap better the heat transfer. As the melter operating level increases for given throughput cold cap spread increases. To maintain the cold cap spread without an increase in the volatilization of radioactive elements, the power is reduced. Throughput variation with operating level is presented in Table 5.13.

**Table 5.13:** Throughput variation with operating level

S.No.	Operating Level above the electrode (mm)	Throughput (lph)
1	10	21
2	90	14.4

#### 5.5.2.4 Influence of electrodes orientation on processing capacity

The electrodes play a vital role in developing convective currents in molten glass. The effect of orientation of electrodes was investigated using the model in order to suggest the design improvements. In an alternate design, two sets of electrodes are placed one above the other, as shown in Figure 5.50. As a result, convective currents increase to 0.14 mm/s from 0.07 mm/s due to an increase in the static head of molten glass and heat flux increases from 15 W/m<sup>2</sup> to 20 W/m<sup>2</sup>. The simulated model is shown in Figure 5.50.

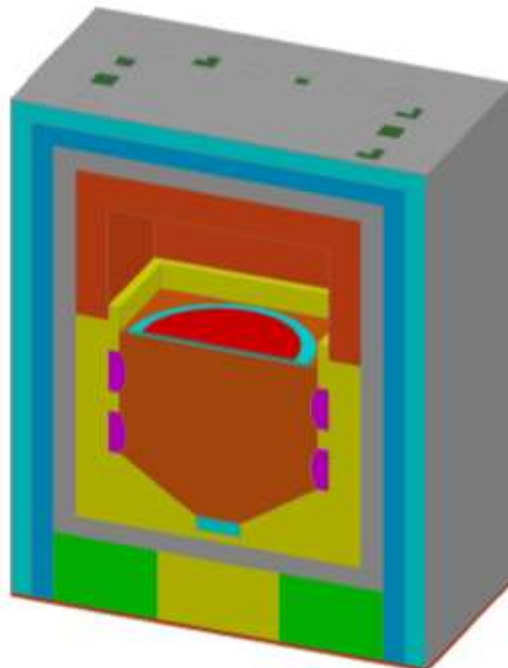


**Figure 5.50:** Melter electrodes one above the other

The model developed was used for assessing the performance of melter by changing electrode orientation also. Electrodes were placed vertically from the top, as shown in Figure 5.52 [91] and simulations were carried out. This particular arrangement makes it possible to replace the electrodes in case of failure remotely. The electrical current density and temperature in the molten glass pool are presented in Figure 5.53 and Figure 5.54. The electrode current density is higher at the interphases. A heat flux of 10 W.m<sup>-2</sup> was achieved.

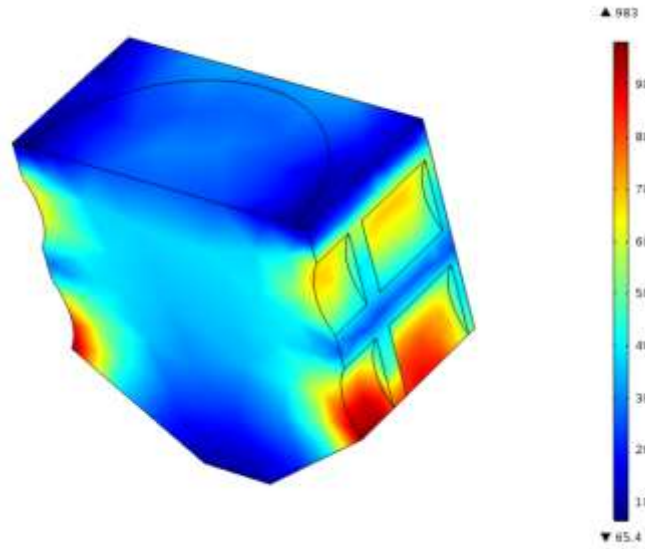


**Figure 5.51:** Simulated model of electrodes placed one above the other

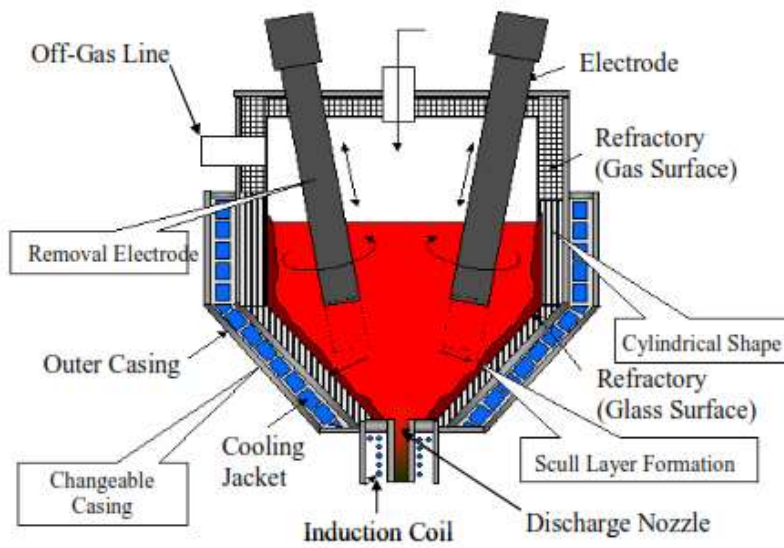


**Figure 5.52:** Vertical orientation of electrodes

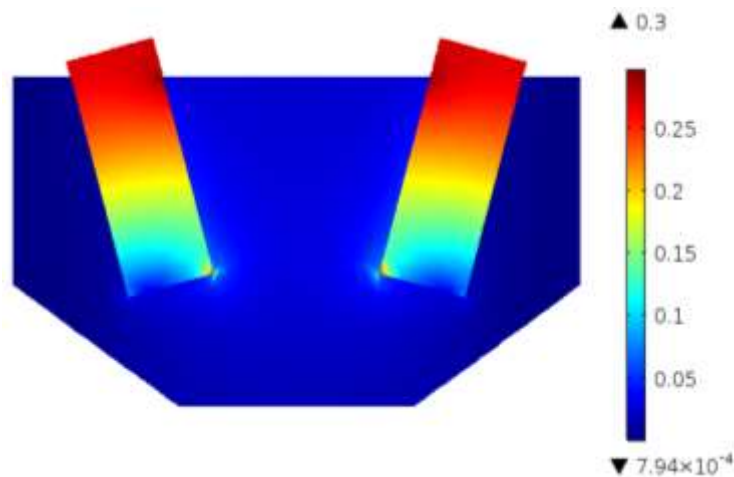


**Figure 5.53:** Simulated model of electrodes immersed vertically (Rainbow legend Current density in  $A.cm^{-2}$ )

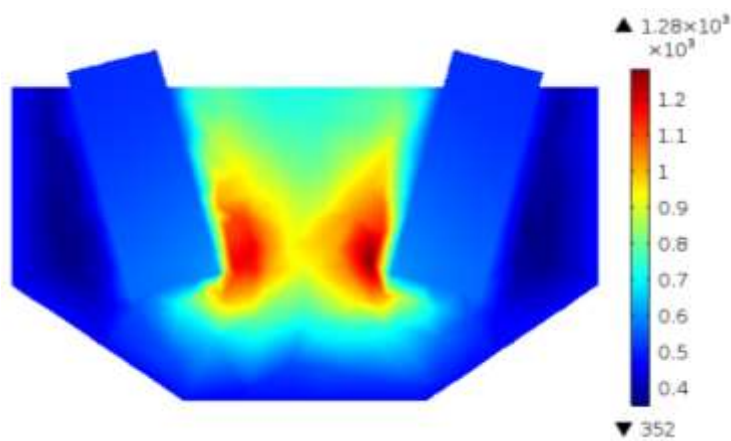


**Figure 5.54:** Simulated model of electrodes immersed vertically (Rainbow legend temperature in K)

## 5.6 Closure

A three-dimensional numerical model of JHCM used for vitrification of Radioactive Liquid Waste (RLW) was obtained using CFD methods. This features a simplified cold cap model at top of the glass pool and appropriate boundary on the wall. Electrical, heat, flow and mass transfer fields are coupled in molten glass pool. The numerical results obtained were compared with experimental results with  $\pm 5\%$  accuracy in molten glass region and  $\pm 10\%$  in the plenum region. The model developed was used for simulation and design refinement studies.

**CHAPTER-6**

**CONCLUSIONS AND**

**RECOMMENDATIONS**

### 6 Conclusions and Recommendations

#### 6.1 Conclusions

The present work is focused on developing an improved JHCM model for treatment of radioactive liquid waste. A numerical, 1:1, 3D model of the glass furnace was developed and heat flow patterns, electrical field, convection pattern and concentration profiles of oxides in JHCM were analyzed using a commercial FEM package COMSOL 5.0. Experiments were conducted on a plant scale melter and the model has been validated using this experimental data.

To generate reliable data as an input to the model, laboratory experiments were carried out for estimating physicochemical characteristics. Thermo-physical and kinetic properties of glass (SiO<sub>2</sub>-48%, B<sub>2</sub>O<sub>3</sub>-26.3%, Na<sub>2</sub>O-11.7%, TiO<sub>2</sub>-9.5%, Fe<sub>2</sub>O<sub>3</sub>-4.5%) with 24 % simulated waste oxides viz., thermal expansion coefficient, viscosity, and electrical conductivity were determined experimentally. Rates of reactions associated with vitrification are estimated from thermogravimetry and this data also has been fed to the model. Kinetic parameters in the presence of other waste nitrates and glass beads were determined for 5C glass determined for 5 peaks observed in TG analysis using the Kissinger method. The kinetic triplet activation energies, pre-exponential factors, and order of reaction of waste nitrates for prominent peak observed are 176.8 kJ mol<sup>-1</sup>, 10<sup>8.56</sup> s<sup>-1</sup>, and 1.2 respectively for 5C base glass reaction with simulated nitrates. The influence of base glass composition on rate kinetics was determined.

Experiments were carried out on industrial scale JHCM and data recorded at every stage of operation including, start up, glass charging & melting and finally

vitrification. Data recorded include temperature profiles at various operating conditions, sodium concentration and electrical parameters and these were used for validating the model. Effect of salt concentration on the throughput of melter was assessed. Energy distribution studies of heat supplied to melter at different stages of operation were carried out. Vitrified products generated during the treatment of 20 m<sup>3</sup> of Simulated High-Level Waste were characterized and qualified for long term storage.

Experiments were carried out on pilot plant scale to determine the dominant mode of heat transfer during stage – I and stage –II operations. A mathematical model that simulated preheating of furnace has been developed. The simulation predicted that apportionment of different modes of heat transfer. Heat transfer by radiation was about 70% at an operating temperature of 973 K.

Radiation is the predominant mode of heat transfer in stage – II, and it was observed that the use of high sodium glass resulted in lowering the conducting temperature of glass and reduces the time of start-up heating. It was observed 5 % of heat supplied to the system was utilized for raising the temperature of glass where remaining heat supplied was utilized for raising the temperature of other materials used in a melter and high skin temperature resulted in higher heat losses. Ingress of air into melter led to heat losses and studied the effect of negative pressure on melter performance.

The numerical model was developed by solving the governing equations of underlying phenomena in JHCM. Suitable boundary conditions, such as the potential difference between electrodes have been applied. The heat generated due to the potential difference results in a temperature profile in molten glass. The non-uniform temperature profile in molten glass due to Joule heat results in convective mixing. The

maximum velocity of molten glass achieved during convective mixing was 0.7 mm/s and the effective thermal conductivity was  $12 \text{ W m}^{-1}\cdot\text{K}^{-1}$ .

Studies carried out for estimating boil-up rate with DM water resulted in a heat flux of  $41.75 \text{ kW}\cdot\text{m}^{-2}$ . The heat flux estimated from the model was  $43 \text{ kW m}^{-2}$ , which is in close agreement with experimental results. The influence of salt concentration in the waste was studied, and it was observed that heat flux decreases as the salt concentration increased. At a salt concentration of  $56 \text{ g}\cdot\text{L}^{-1}$  of waste, heat flux was reduced to  $31.2 \text{ kW}\cdot\text{m}^{-2}$ . The studies carried out concluded that higher salt concentration was preferable as the glass production rate increases at higher salt concentration with lower current densities on electrodes.

In order to couple the chemistry of dissociation of nitrates into oxides and their subsequent vitrification, the rate kinetics determined from experimental studies was incorporated in the model. The diffusion coefficients reported in the literature were also incorporated into the model for solving the diffusion equation in mass transfer. The concentration of individual constituents in product samples and results obtained from simulation were in good agreement. The validated model is used for design refinement studies.

Using the validated model, analysis of the heating mechanisms for operating melter during start-up heating was carried out. During this stage, heat transfer by radiation is predominant. Heat losses are higher as start-up heaters are placed near to the outer surface of the melter. The effect of start-up heaters geometry was studied, and it was observed that circular slots provide better heat flux compared to square slots. Optimization of the gap to be provided between the slot and tube used for start-up heaters was studied. Size optimization of plenum heaters was carried out. Based on the numerical investigations, it was concluded that by adopting helical heaters plenum

space height was reduced. This reduction has resulted in reduced skin losses from the outer surface of JHCM, and lower weight of melter reduces waste generated during decommissioning.

The studies were extended to different electrode configurations reported in the literature. Generated heat flux, electric currents and concentration profiles for the advanced design of melters reported in the literature.

## **6.2 Recommendations**

A mathematical model incorporating the electric, temperature, velocity fields and reaction kinetics in an Industrial scale JHCM was developed, and scope for further investigations in this field of research is outlined. The current study will be used for design refinement tool to improve the efficiency of nuclear waste management for safe and economic management of radioactive waste. The present study provides a basis for predicting the processing capacities based on model-based designs.

The future studies can include the effect of bubbling on JHCM by integrating Multiphase models in the cold cap by coupling with a level set or VOF method and integrating the module with other physics associated with the system is expected to reduce the deviation when compared with experimental results. Modelling of volatilization of Cs and Ru in JHCM is a challenging problem to be solved considering the implication it has on throughput. The spinel concentration's resulting choking of the bottom drain in JHCM is a typical problem that requires dedicated studies for treating the waste that is expected to be generated from fast reactors.

## REFERENCES

- [1] IEA, “2018 World Energy Outlook: Executive Summary,” *Oecd/Iea*, p. 11, 2018.
- [2] R. Pichs Madruga, K. Seyboth, P. Eickemeier, P. Matschoss, G. Hansen, S. Kadner, S. Schlömer, T. Zwickel, and C. Von Stechow, “Renewable Energy Sources and Climate Change Mitigation Special Report of the Intergovernmental Panel on Climate Change Edited by Ottmar Edenhofer Youba Sokona,” 2012.
- [3] D. Caurant, P. Loiseau, I. Bardez, and A. Quintas, *Glasses, Glass-ceramics and Ceramics for Immobilization of Highly Radioactive Nuclear Wastes*. Nova Science Publishers, 2009.
- [4] “Nuclear energy data 2007,” 2007. [Online]. Available: [https://www.oecd-ilibrary.org/nuclear-energy/nuclear-energy-data-2007\\_ned-2007-en-fr](https://www.oecd-ilibrary.org/nuclear-energy/nuclear-energy-data-2007_ned-2007-en-fr). [Accessed: 01-May-2019].
- [5] J. H. Saling, A. W. Fentiman, and Y. S. Tang, *Radioactive waste management*. Taylor & Francis, 2001.
- [6] B. W. Brook and C. J. A. Bradshaw, “Key role for nuclear energy in global biodiversity conservation,” vol. 29, no. 3, pp. 702–712, 2014.
- [7] W. Baehr, “Industrial vitrification processes for high-level liquid waste solutions A technical overview of processes actively being used to treat and solidify liquid wastes in glass,” *IAEA Bulletin*, 1989.
- [8] I. W. Donald, B. L. Metcalfe, and R. N. J. Taylor, “The immobilization of high level radioactive wastes using ceramics and glasses,” *J. Mater. Sci.*, vol. 32, no. 22, pp. 5851–5887, 1997.
- [9] R.K.Bajpai, “Characterization of Natural Barriers of Deep Geological Repositories for High-level Radioactive Wastes in India,” *Indian Nucl. Soc. News*, vol. 5, no. 4, pp. 40–47, 2008.
- [10] M. I. Ojovan and W. E. Lee, *An introduction to nuclear waste immobilisation, second edition*. Elsevier, 2014.
- [11] J. D. Vienna, “Nuclear Waste Vitrification in the United States: Recent Developments and Future Options,” *Int. J. Appl. Glas. Sci.*, vol. 1, no. 3, pp. 309–321, 2010.
- [12] C. P. Kaushik, A. Kumar, G. B. Kale, R. K. Mishra, P. Sengupta, D. Das, and

- K. Raj, "Barium borosilicate glass – a potential matrix for immobilization of sulfate bearing high-level radioactive liquid waste," *J. Nucl. Mater.*, vol. 358, no. 2–3, pp. 129–138, 2006.
- [13] A. A. Cherepanov and D. E. Belokon', "Main technical solutions in the world practice of conditioning of HLW solutions from spent nuclear fuel reprocessing," *Radiochemistry*, vol. 51, no. 4, pp. 433–435, 2009.
- [14] D. Mehta, A. Gangadharan, T. Morzaria, N. S. Tomar, and B. B. Verma, "Industrial Scale Vitrification of High-Level Radioactive Liquid Waste-experience at Waste Immobilisation Plant, Trombay," *Indian Nuclear Society News*, p. Vol-5, 5-10, 2008.
- [15] M. T. Harrison, "Vitrification of High Level Waste in the UK," *Procedia Mater. Sci.*, vol. 7, no. August, pp. 10–15, 2014.
- [16] K. Raj, K. K. Prasad, and N. K. Bansal, "Radioactive waste management practices in India," *Nucl. Eng. Des.*, vol. 236, no. 7–8, pp. 914–930, 2006.
- [17] W. Grünewald, G. Roth, W. Tobie, and S. Weisenburger, "INE's Melter Technology for Vitrification of High-level Liquid Waste," *Nachrichten - Forschungszentrum Karlsruhe*, vol. 36, no. 2, pp. 39–44, 2004.
- [18] G. Sugilal and C. Benny, "Development of Cold Crucible System for Vitrification of High-level Liquid Waste," *Indian Nuclear Society News*, (Vol-5), pp. 19–22, 2008.
- [19] "Country Nuclear Fuel Cycle Profiles - Second Edition," *International Atomic Energy Association*, pp. 83–85, 2005.
- [20] R. Meuleman, "The efficient future for the glass industry is 'all-electric,'" *14th Int. Semin. Furn. Des. Vsetin, Czech Repub.*, 2017.
- [21] Penberthy L, "Electric Melting of Glass," in *The handbook of glass manufacture: Vol I*, Fay VaNisle Tooley, Ed. New York: Books for Industry, 1974, pp. 389–390.
- [22] S. Lee, P. Hrma, R. Pokorny, J. Klouzek, W. C. Eaton, and A. A. Kruger, "Glass production rate in electric furnaces for radioactive waste vitrification," *J. Am. Ceram. Soc.*, Apr. 2019.
- [23] H. xu Gao, F. qi Zhao, R. zu Hu, H. an Zhao, and H. Zhang, "Estimation of the kinetic parameters for thermal decomposition of HNIW and its adiabatic time-to-explosion by Kooij formula," *Def. Technol.*, vol. 10, no. 1, pp. 28–33, 2014.

- [24] D. Ehrt and S. Flügel, “Electrical conductivity and viscosity of phosphate glasses and melts,” *J. Non. Cryst. Solids*, vol. 498, no. May, pp. 461–469, 2008.
- [25] O. K. MI Ojovan, “Synthesis and properties of glass composite materials for solidification of radioactive waste,” *Radiochemistry*, vol. 34, p. 97, 1992.
- [26] G. Suneel, S. Rajasekaran, J. Selvakumar, C. P. Kaushik, J. K. Gayen, and K. V. Ravi, “Determination of reaction kinetics during vitrification of radioactive liquid waste for different types of base glass,” *Nucl. Eng. Technol.*, vol. 51, no. 3, 2019.
- [27] R. F. Taylor, “Chemical engineering problems of radioactive waste fixation by vitrification,” *Chem. Eng. Sci.*, vol. 40, no. 4, pp. 541–569, Jan. 1985.
- [28] K. Kawai, T. Fukuda, Y. Nakano, and K. Takeshita, “Thermal decomposition analysis of simulated high-level liquid waste in cold-cap,” *EPJ Nucl. Sci. Technol.*, vol. 2, p. 44, 2016.
- [29] C. Rodriguez, A. A. Kruger, D. Pierce, J. Chun, M. Schweiger, and P. Hrma, “Kinetics of Cold-Cap Reactions for Vitrification of Nuclear Waste Glass Based on Simultaneous Differential Scanning Calorimetry -Thermogravimetry ( DSC-TGA ) and Evolved Gas Analysis ( EGA ),” *Wm2014*, 2014.
- [30] H. E. Kissinger, “Reaction Kinetics in Differential Thermal Analysis,” *Anal. Chem.*, vol. 29, no. 11, pp. 1702–1706, 1957.
- [31] E. S. Freeman and B. Carroll, “The application of thermoanalytical techniques to reaction kinetics. The thermogravimetric evaluation of the kinetics of the decomposition of calcium oxalate monohydrate,” *J. Phys. Chem.*, vol. 62, no. 4, pp. 394–397, 1958.
- [32] S. Vyazovkin, “Modification of the Integral Isoconversional Method to Account for Variation in the Activation Energy,” *J. Comput. Chem.*, vol. 22, no. 2, pp. 178–183, 2001.
- [33] L. A. Pérez-Maqueda, C. Popescu, S. Vyazovkin, A. K. Burnham, N. Sbirrazzuoli, and J. M. Criado, “ICTAC Kinetics Committee recommendations for performing kinetic computations on thermal analysis data,” *Thermochim. Acta*, vol. 520, no. 1–2, pp. 1–19, 2011.
- [34] T. Liavitskaya and S. Vyazovkin, “Delving into the Kinetics of Reversible Thermal Decomposition of Solids Measured on Heating and Cooling,” *J. Phys. Chem. C*, vol. 121, no. 28, pp. 15392–15401, 2017.

- [35] P. Hrma, A. A. Kruger, and R. Pokorny, "Nuclear waste vitrification efficiency: Cold cap reactions," *J. Non. Cryst. Solids*, vol. 358, no. 24, pp. 3559–3562, 2012.
- [36] C. C. Chapman, "Nuclear Waste Glass Melter Design Including the Power and Control Systems," *IEEE Trans. Ind. Appl.*, vol. IA-18, no. 1, pp. 65–72, Jan. 1982.
- [37] G. Suneel, P. M. Satya Sai, C. P. Kaushik, J. K. Gayen, K. V. Ravi, and A. Roy, "Experimental Investigation and Numerical Modeling of a Joule-Heated Ceramic Melter for Vitrification of Radioactive Waste," *J. Hazardous, Toxic, Radioact. Waste*, vol. 23, no. 1, p. 4018035, 2018.
- [38] C. C. Chapman, "Experience with a joule heated ceramic melter while converting simulated high-level waste to glass." 1976.
- [39] M. Yoshioka, S. Torata, J. Igarashi, T. Takahashi, and M. Horie, "Glass melter and process development for PNC Tokai vitrification facility," *Waste Manag.*, vol. 12, no. 1, pp. 7–16, Jan. 1992.
- [40] G. Roth, W. Grunewald, S. Weisenburger, and J. Fleisch, "Vitrification of high-level waste," *ATW - Int. Zeitschrift fur Kernenergie*, vol. 41, pp. 638–641, 1996.
- [41] A. S. Polyakov, G. B. Borisov, N. I. Moiseenko, V. I. Osnovin, E. G. Dzekun, G. M. Medvedev, V. A. Bel'tyukov, S. A. Dubkov, and S. N. Filippov, "Experience in operating the ÉP-500/1R ceramic melter for vitrification of liquid high-level wastes," *At. Energy*, vol. 76, no. 3, pp. 181–185, Mar. 1994.
- [42] K. S. Matlack, H. Gan, M. Chaudhuri, W. Kot, W. Gong, T. Bardakci, I. L. Pegg, and J. Innocent, "DM100 and DM1200 Melter Testing with High Waste Loading Glass Formulations for Hanford High-Aluminum HLW Streams, VSL-10R1690-1," 2010.
- [43] R. Pokorny and P. Hrma, "Mathematical modeling of cold cap," *J. Nucl. Mater.*, vol. 429, no. 1–3, pp. 245–256, 2012.
- [44] R. L. Curran, "Use of Mathematical Modeling in Determining the Effects of Electrode Configuration on Convection Currents in an Electric Glass Melter," *IEEE Trans. Ind. Gen. Appl.*, vol. IGA-7, no. 1, pp. 116–129, 1971.
- [45] R. L. Curran, "Mathematical Model of an Electric Glass Furnace: Effects of Glass Color and Resistivity," *IEEE Trans. Ind. Appl.*, vol. IA-9, no. 3, pp. 348–357, May 1973.

- [46] R. R. McConnell and R. E. Goodson, "Modelling of glass furnace design for improved energy efficiency," *Glas. Technol.*, vol. 20, no. 3, pp. 100–106, 1979.
- [47] H. Mase and K. Oda, "Mathematical model of glass tank furnace with batch melting process," *J. Non. Cryst. Solids*, vol. 38–39, pp. 807–812, May 1980.
- [48] S. V Patankar and D. B. Spalding, "A Calculation procedure for Heat, Mass and Momentum Transfer in Three-Dimensional Parabolic Flows," Pergamon Press, 1972.
- [49] S V Patankar. V. S. Pratap and D. B. Spalding, "Lammar flow and heat transfer in helically coiled pipes," vol. 62, 1974.
- [50] R. Viskanta, "Review of three-dimensional mathematical modeling of glass melting," *J. Non. Cryst. Solids*, vol. 177, pp. 347–362, 1994.
- [51] Z. Feng, D. Li, G. Qin, and S. Liu, "Study of the Float Glass Melting Process: Combining Fluid Dynamics Simulation and Glass Homogeneity Inspection," *J. Am. Ceram. Soc.*, vol. 91, no. 10, pp. 3229–3234, Oct. 2008.
- [52] P. Hrma, "Thermodynamics of Batch Melting," *Glas. Berichte*, vol. 55, pp. 138–150, 1982.
- [53] P. Schill and J. Chmelar, "Use of computer flow dynamics in glass technology," *J. Non. Cryst. Solids*, vol. 345–346, pp. 771–776, 2004.
- [54] M. K. Choudhary, R. Venuturumilli, and M. R. Hyre, "Mathematical Modeling of Flow and Heat Transfer Phenomena in Glass Melting, Delivery, and Forming Processes," *Int. J. Appl. Glas. Sci.*, vol. 1, no. 2, pp. 188–214, May 2010.
- [55] L. Jacoutot, P. Brun, A. Gagnoud, and Y. Fautrelle, "Numerical modelling of natural convection in molten glass heated by induction," *Chem. Eng. Process. Process Intensif.*, vol. 47, no. 3, pp. 449–455, Mar. 2008.
- [56] C. H. (Chang H. Oh, *Hazardous and radioactive waste treatment technologies handbook*. CRC Press, 2001.
- [57] "Design and operation of off-gas cleaning systems Technical Reports at high level liquid waste conditioning facilities," *IAEA*, no. Technical Report Series. 291, 1988.
- [58] G. Sugilal, P. K. Wattal, and K. Iyer, "Convective behaviour of a uniformly Joule-heated liquid pool in a rectangular cavity," *Int. J. Therm. Sci.*, vol. 44, no. 10, pp. 915–925, 2005.
- [59] A. Fluegel, D. A. Earl, and A. K. Varshneya, "Electrical Resistivity of Silicate

- Glass Melts Calculation Based on the SciGlass Database,” 2007.
- [60] S. Gopalakrishnan and A. Thess, “Chaotic mixing in electromagnetically controlled thermal convection of glass melt,” *Chem. Eng. Sci.*, vol. 65, no. 19, pp. 5309–5319, 2010.
- [61] M. K. Choudhary, “A Modeling Study of Flow and Heat Transfer in an Electric Melter,” *J. Non. Cryst. Solids*, vol. 101, pp. 41–53, 1988.
- [62] L. L. Eyler, “Compilation of Information on Melter n Modeling,” 1996.
- [63] H. UCHIDA, T. Ooba, Y. ISO, S. MATSUNO, T. FUKUI, and I. OONO, “CFD Modeling Coupled with Electric Field Analysis for Joule-Heated Glass Melters,” *J. Power Energy Syst.*, vol. 2, no. 1, pp. 447–455, 2008.
- [64] R. Pokorny, Z. J. Hilliard, D. R. Dixon, M. J. Schweiger, D. P. Guillen, A. A. Kruger, and P. Hrma, “One-Dimensional Cold Cap Model for Melters with Bubblers,” *J. Am. Ceram. Soc.*, vol. 98, no. 10, pp. 3112–3118, 2015.
- [65] B. J. Hardy, “CFD Model for the WSRC Am/Cm Melter,” Westinghouse Savannah River Company, Jun. 1998.
- [66] C. Giessler and A. Thess, “Numerical simulation of electromagnetically controlled thermal convection of glass melt in a crucible,” *Int. J. Heat Mass Transf.*, vol. 52, no. 13–14, pp. 3373–3389, 2009.
- [67] D. P. Guillen, A. W. Abboud, R. Pokorny, W. C. Eaton, D. Dixon, K. Fox, and A. A. Kruger, “Development of a Validation Approach for an Integrated Waste Glass Melter Model,” *Nucl. Technol.*, vol. 203, no. 3, pp. 244–260, Sep. 2018.
- [68] S. Saedodin and M. S. M. Barforoush, “Comprehensive analytical study for convective-radiative continuously moving plates with multiple non-linearities,” *Energy Convers. Manag.*, vol. 81, pp. 160–168, 2014.
- [69] M. S. M. Barforoush and S. Saedodin, “Heat transfer reduction between two finite concentric cylinders using radiation shields; Experimental and numerical studies,” *Int. Commun. Heat Mass Transf.*, vol. 65, pp. 94–102, 2015.
- [70] A. K. Sharma, K. Velusamy, C. Balaji, and S. P. Venkateshan, “Conjugate turbulent natural convection with surface radiation in air filled rectangular enclosures,” *Int. J. Heat Mass Transf.*, vol. 50, no. 3–4, pp. 625–639, 2007.
- [71] P. Teertstra and M. M. Yovanovich, “Comprehensive review of natural convection in horizontal circular annuli,” *ASME Publ. HTD*, 1998.
- [72] M. Torabi and Q. B. Zhang, “Analytical solution for evaluating the thermal

- performance and efficiency of convective-radiative straight fins with various profiles and considering all non-linearities,” *Energy Convers. Manag.*, vol. 66, pp. 199–210, 2013.
- [73] A. H. Malik, A. Shah, and S. Khushnood, “CFD analysis of heat transfer within a bottom heated vertical concentric cylindrical enclosure,” *J. Phys. Conf. Ser.*, vol. 439, no. 1, 2013.
- [74] G. V. Kuznetsov and M. A. Sheremet, “Conjugate natural convection in an enclosure with a heat source of constant heat transfer rate,” *Int. J. Heat Mass Transf.*, vol. 54, no. 1–3, pp. 260–268, 2011.
- [75] M. K. K. Ghauri, A. Shah, M. S. . Alvi, S. Khushnood, F. M. Mahfouz, and A. H. Malik, “Experimental study of conjugate heat transfer within a bottom heated vertical concentric cylindrical enclosure,” *Int. J. Heat Mass Transf.*, vol. 55, no. 4, pp. 1154–1163, 2011.
- [76] M. Rahimi and A. Sabernaemi, “Experimental study of radiation and free convection in an enclosure with under-floor heating system,” *Energy Convers. Manag.*, vol. 52, no. 7, pp. 2752–2757, 2011.
- [77] V. Senve and G. S. V. L. Narasimham, “Effective thermal conductivity of a heat generating rod bundle dissipating heat by natural convection and radiation,” *Nucl. Eng. Des.*, vol. 241, no. 10, pp. 4331–4340, 2011.
- [78] N. A. Roschina, A. V. Uvarov, and A. I. Osipov, “Natural convection in an annulus between coaxial horizontal cylinders with internal heat generation,” *Int. J. Heat Mass Transf.*, vol. 48, no. 21–22, pp. 4518–4525, 2005.
- [79] A. Ungan and R. Viskanta, “State-of-Art Numerical Simulation of Glass Melting Furnaces,” John Wiley & Sons, Ltd, 2008, pp. 203–220.
- [80] R. Pokorný, D. A. Pierce, and P. Hrma, “Melting of glass batch: Model for multiple overlapping gas-evolving reactions,” *Thermochim. Acta*, vol. 541, pp. 8–14, 2012.
- [81] S. V. Patankar, “Numerical Heat Transfer and Fluid Flow.” Taylor & Fracis, Minnesota, 1980.
- [82] R. Pokorny and P. Hrma, “Mathematical Model of Cold Cap-Preliminary One-Dimensional Model Development,” 2011.
- [83] D. P. Guillen, A. W. Abboud, R. Pokorny, W. C. Eaton, D. Dixon, K. Fox, and A. A. Kruger, “Development of a Validation Approach for an Integrated Waste

- Glass Melter Model,” *Nucl. Technol.*, vol. 203, no. 3, pp. 244–260, 2018.
- [84] H. E. Kissinger, “Variation of Peak Temperature with Heating Rate in Differential Thermal Analysis,” *J. Res. Natl. Bur. Stand. (1934)*, vol. 57, no. 4, pp. 217–221, 1956.
- [85] D. Pepper and J. Heinrich, *The Finite Element Method- Basic Concepts and Applications*. London (England): Taylor & Francis, 1992.
- [86] H. Jena, R. Asuvathraman, K. V. G. Kutty, and P. R. V. Rao, “Comparison of electrical conductivity and thermal properties of borosilicate glass with and without simulated radioactive waste,” *J. Therm. Anal. Calorim.*, vol. 115, no. 1, pp. 367–374, 2014.
- [87] Y. A. Cengel, *Heat Transfer: A Practical Approach*, 2nd Editio. Texas: Mcgraw-Hill, 2002.
- [88] M. Jakob and G. A. Hawkins, *Elements Of Heat Transfer And Insulation*, 5th Printing. New York: John Wiley & Sons, Inc., 1942.
- [89] K. Nonaka, H. Nakajima, S. Mitsui, and J.-I. Echigoya, “Self-Diffusion of  $^{22}\text{Na}$  and  $^{137}\text{Cs}$  in Simulated Nuclear Waste Glass,” *Mater. Trans.*, vol. 43, no. 4, pp. 654–659, 2002.
- [90] D. Banerjee, V. K. Sudarsan, A. Joseph, R. Mishra, I. Singh, P. K. Wattal, and D. Das, “Role of  $\text{TiO}_2$  on the physicochemical properties of cesium borosilicate glasses,” *J. Am. Ceram. Soc.*, vol. 93, no. 10, pp. 3252–3258, 2010.
- [91] G. Roth and S. Weisenburger, “Comparison of Advanced Melting Process for HLW Vitrification, Joule-Heated Ceramic-Lined Melter (JHCM) and Cold-Crucible Induction Melter (CCIM),” in *Proceedings of the 2017 25th International Conference on Nuclear Engineering ICONE25*, 2017, pp. 1–12.